Evaluation of FFT Based Cross-Correlation Algorithms for Particle Image Velocimetry

by

Ross A. D. Gilbert

A thesis
presented to the University of Waterloo
in fulfilment of the
thesis requirement for the degree of
Master of Applied Science
in
Mechanical Engineering

Waterloo, Ontario, February 2002

I hereby declare that I am the sole author of this thesis. This is a true copy of the thesis, including any required final revisions, as accepted by my examiners.

I understand that my thesis may be made electronically available to the public.

Acknowledgments

The research that is contained within this work could not have been completed without my Lord and Saviour Jesus Christ who is my life. With him all things are possible, evidenced by the completion of this thesis.

First, I would like to share my sincere gratitude to my supervisor, Dr. David Johnson, for the friendship and guidance that he has shown me. I am truly grateful for the opportunity I have had to work with him for the past two years.

I would also like to give special thanks to Chad Young for the support he has provided me over the last two years.

To my friends Chris Salisbury, Jeffrey Baschuk, Bryan Sperandei, Teo Dabov, Rachel Fu, Paul Deslauriers and John Costa who have made the past two years not only possible, but truly enjoyable. Through your caring, I have learned so much. I hope to be able to return the same gift of friendship that each of you have given me.

Finally, I am forever in debt to my parents, Les and Carolyn, my brothers and sisters, Michael, Jan, Paul and Nicole, for their everlasting support in everything I do. To my family, I dedicate this thesis.

Abstract

In the current study, the four most common Particle Image Velocimetry (PIV) cross-correlation algorithms were evaluated by measuring the displacement of particles in computer generated images. The synthetic images were employed to compare the methods since the particle diameter, density, and intensity could be controlled, removing some of the uncertainty found in images collected during experiments, *e.g.*, parallax, 3-D motion *etc.* The most important parameter that was controlled in the synthetic images was the particle motion. Six different displacement functions were applied to *move* the particles between images: uniform translation, step, sawtooth, sinusoid, line source and line vortex.

The four algorithms, which all use the fast Fourier transform (FFT) to perform the cross-correlation, were evaluated with four criteria; (1) spatial resolution, (2) dynamic range, (3) accuracy and (4) robustness. The uniform translation images determined the least error possible with each method, of which the deformed FFT proved to be the most accurate. The super resolution FFT and deformed FFT methods could not properly measure the infinite displacement gradient in the step images due to the interpolation of the displacement vector field used by each method around the step. However, the predictor corrector FFT scheme, which does not require interpolation when determining the interrogation area offset, successfully measured the infinite displacement gradient in the step images. The smaller interrogation areas used by the super resolution FFT scheme proved to be the best method to capture the high frequency finite displacement gradients in the sawtooth and sinusoid images. Also shown in the sawtooth and sinusoid images is the positional bias error introduced by assuming the measured particle displacement occurs at the centre of the interrogation area. The deformed FFT method produced the most accurate results for the source and vortex images, which both contained displacement gradients in multiple directions.

Experimentally obtained images were also evaluated to verify the results derived using the synthetic images. The flow in a multiple grooved channel, using both water and air as the fluid medium in separate experiments, was measured and compared to DNS simulations reported by Yang [1]. The mean velocity, average vorticity and turbulent fluctuations determined from both experiments using the deformed FFT method compared very well to the DNS calculations.

Contents

List of Tables

List of Figures

Chapter 1

Introduction

1.1 Motivation and Scope of Research

Flow visualisation is one of the most fundamental techniques employed to study the motion of a fluid. Particles placed in a flow can produce qualitative information about a fluid flow on a large scale and the results can be used to produce valuable insight into the mechanics governing flow behaviour. The desire to quantify this behaviour brought about the development of various velocity measurement tools, such as the three-cup anemometer, pitot-static probe, cobra probe, hot-wire anemometer and non-intrusive laser based techniques, such as Laser Doppler Velocimetry (LDV).

LDV was developed to measure the velocity of particulate within a small control volume. The ability to provide temporal velocity information and its compatibility with the turbulent nature of flows through Reynolds averaging made LDV a common fluid measurement technique. The LDV technique [2, 3, 4] improved with time as the errors were identified and were either corrected or minimised to allow for its use in complex flows. To this day it is generally accepted as being one of the most accurate techniques available to measure the velocity of a fluid flow.

LDV allows for the measurement of velocity at a single point so the average vector field can only be determined after the individual measurements are assembled. As such, each measurement

point becomes independent in time and the entire vector field can only be assembled for steady flows. The desire to measure instantaneous spatial velocity data over an entire flow field prompted the development of Particle Image Velocimetry (PIV).

1.2   Particle Image Velocimetry

PIV is a natural extension of the flow visualisation techniques typically used to qualify the nature of a flow. The premise behind PIV has existed for some time but it wasn't until the required technology matured that it could be realistically applied to measure the velocity of a fluid flow.

With PIV, a planar light sheet is used to illuminate a nearly two-dimensional cross-section of a flow, which contains tiny particles (Figure 1.1). As particles pass through the light sheet they are illuminated and imaged using a digital or film based recording device placed normal to the
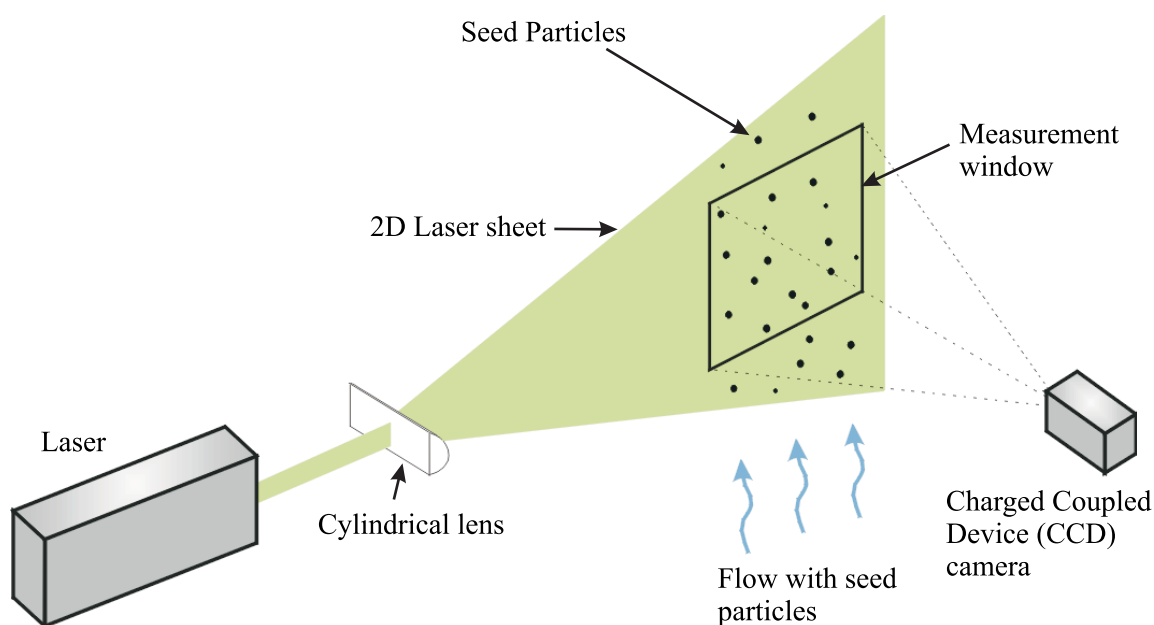
Figure 1.1: PIV Overview

light sheet. Figures 1.2a and 1.2b show typical images for experiments conducted in water and in air respectively.

Two or more successive images are recorded by a camera that *captures* the positions of the *seed* particles at two instances in time. The distances traveled by the particles between the two images are determined. These seed particles are generally assumed to follow the flow so the velocity of the flow is then determined by dividing the measured particle displacement with the time separation of the two images. Multiple velocities are found throughout the image, creating an instantaneous 2-D velocity vector field.

1.2.1 Different Types of Pulsed Laser Velocimetry

Many different methods may be used to determine the displacement of the seed particles. The choice of methodology typically depends on the number of seed particles contained within an image. Adrian [5] divided the methods into three different groups: laser speckle velocimetry (LSV), low density PIV and high density PIV. Due to the relative accuracy of low and high density PIV, as well as the difficulty in obtaining the necessarily high seeding density required for LSV, it is no longer widely used, but has been described in detail by other authors [5, 6].

Low Density PIV - Particle Tracking Velocimetry

Low density PIV, also known as particle tracking velocimetry (PTV), is employed when the seeding density is low enough that individual particles can be identified. With PTV, individual particles are tracked between images and a velocity vector is produced for each particle. For PTV to work effectively, the seeding density must be below a set limit, which is based on two criteria. The first is that the neighbouring particles do not occlude, *i.e.* overlap, in the image plane. This ensures that individual particles can be identified. The second criteria for the density limit of PTV is that the displacement between images by the particles must be less than the mean spacing between the particles. This allows the assumption that the particle in image 1 will be matched to its closest particle in image 2.
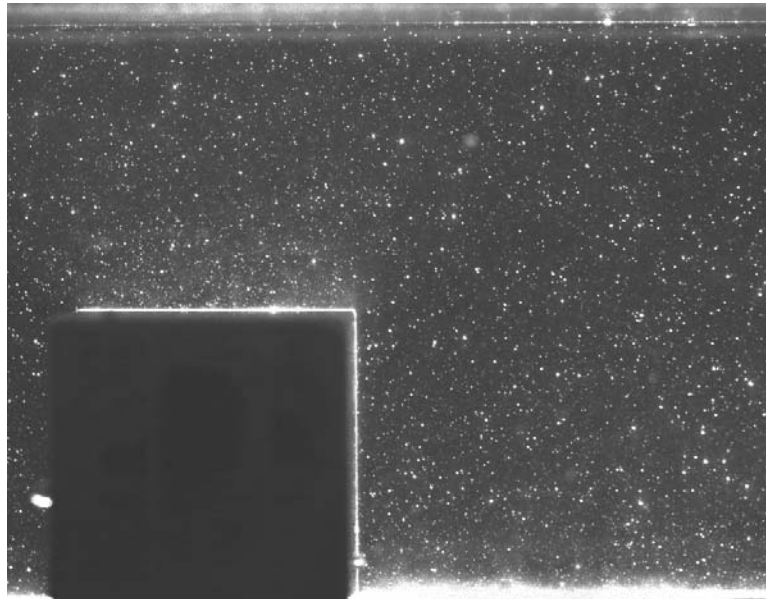
(a) Water
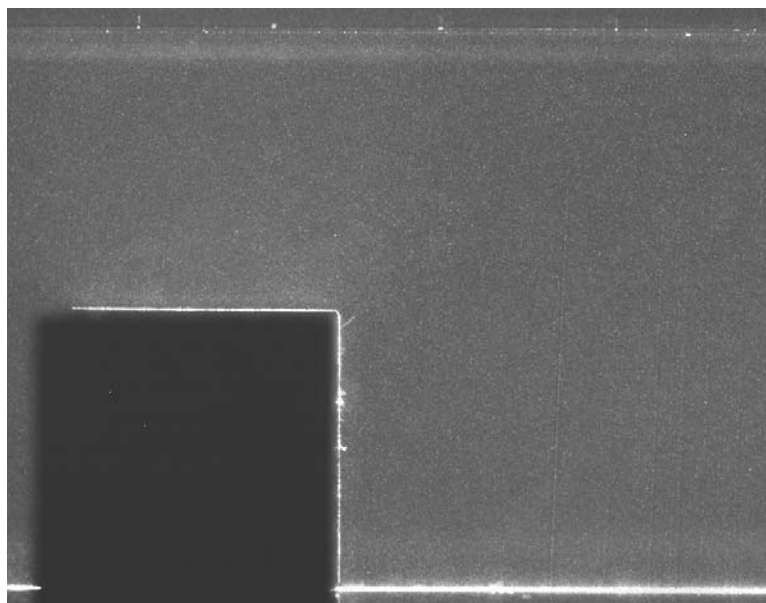
(b) Air

Figure 1.2: Typical seeded PIV images (60mm x 40mm) for (a) water using Pliolite as seed particles and (b) air using mineral oil for seed particles

Some PTV algorithms use a hybrid of PTV and high density PIV [7, 8, 9, 10, 11, 12]. High density PIV is first performed to determine an estimate of the large scale velocity. PTV is then performed to find the exact displacement of each individual particle using the large scale velocity as an estimate when searching for the matching particle in the second image.

High density PIV

High density PIV is applied when the seeding density is too high to apply PTV effectively. Either individual particles cannot be identified or the mean spacing between the particles is below the average displacement, making the tracking of individual particles too difficult. As a result, the representative displacement of a cluster of particles is measured.

1.2.2 Three dimensional PIV

With PIV, the motion of an individual or a group of particles within an illuminated plane is measured, *i.e.* the velocity can only be determined in the two dimensions of the plane of illumination. However, it is possible to measure the fluid velocity in the third dimension by using holographic techniques [13], multiple-plane light sheets [14] or a common method called stereo PIV [13, 15, 16, 17].

Stereo PIV is similar to regular PIV in that a 2-D laser light sheet isolates a cross-section of the flow field. The difference between regular PIV and stereo PIV is the presence of a second camera. Instead of having one camera placed perpendicular to the laser sheet, as in regular PIV, stereo PIV uses two identical cameras are placed at angles to the laser sheet that are focused onto the same area, as shown in Figure 1.3. Due to the thickness of the laser sheet and the angle between the light sheet and the optical axes of the cameras, a portion of the velocity field measured with each camera is influenced by the velocity normal to the light sheet. The different velocity components are resolved through the simultaneous analysis of 2-D images captured by both cameras. The velocity in all three dimensions can then be resolved by relating the 2-D results from each camera [13]. Therefore, the techniques used to measure the displacement of

Displacement seen from left

True displacement

Displacement seen from right

Focal plane = Centre of light sheet

45°   45°

Left camera

Right camera
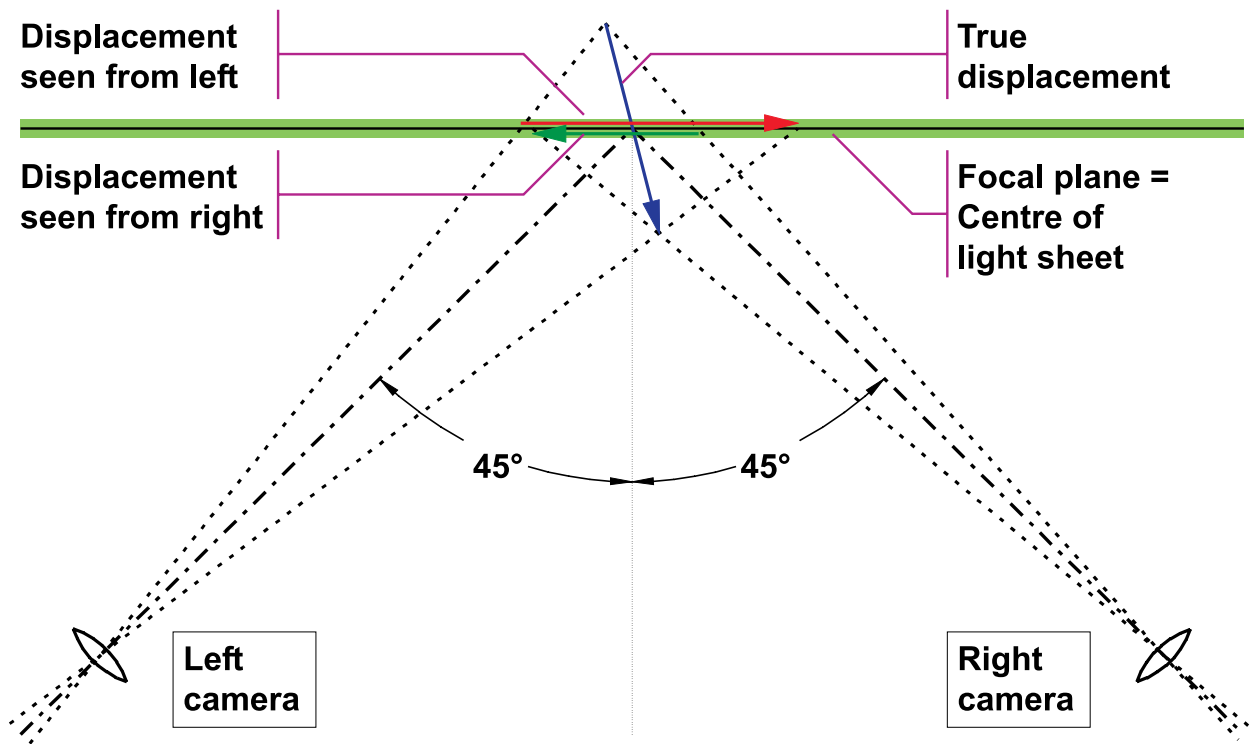
Figure 1.3: Stereo PIV Setup [18]

the particles for stereo PIV are the same as those used for regular PIV and so any improvements made to the 2-D PIV can be applied to stereo PIV.

1.3 Objectives

Since the methods used in 2-D PIV to measure the particle displacements are the same as those used with stereo PIV, this thesis will concentrate only on 2-D PIV. Determining the displacements of the particles between images is the most difficult and critical task in the PIV process. In practice, it is typically difficult to meet the two criteria required for the successful application of PTV and therefore the focus of this thesis will be high density PIV, hereafter referred to as PIV.

Since PIV is still maturing as an experimental method there are many different algorithms available to measure the particle displacements. The most common technique, and the focus of this thesis, is the cross-correlation method. With the cross-correlation method, computer algorithms are used to determine the displacement of a group of seed particles within a smaller subsection of the image called an interrogation area.

Much of the literature on the recent developments of the PIV technique is devoted to the introduction of different adaptations of the cross-correlation technique to improve the measurement accuracy. The objective of the work described in this thesis is to:

1. define the most common cross-correlation based algorithms,

2. implement the algorithms,

3. evaluate the algorithms to examine their strengths and weaknesses using computer generated synthetic images,

4. identify the algorithm best suited for a particular flow condition and

5. verify the conclusions based on the analysis of the synthetic images through the use of *real* images collected from an experiment.

To evaluate each algorithm, synthetic images will be used. Synthetic images are mathematically generated images where a function representing a particle is displaced by a specific amount, depending on the simulated flow conditions. Synthetic images are used so that the exact displacement of the particles between the images is known, allowing the error in the processing methods to be quantified.

The quality of the images collected during experiments is not as *ideal* as that found in the synthetic images, *i.e.* parameters such as seed density cannot be easily controlled. Therefore, images collected from two experiments (one with water as the fluid medium and the other using air) will also be used to verify the conclusions formed based on the results from the synthetic images.

1.4 Thesis Outline

The following chapter, Chapter 2, reviews the literature pertaining to PIV. Specifically, the different algorithms to be implemented and tested as well as the major sources of error that exist within PIV will be examined. How the methods were implemented for this research programme is detailed in Chapter 3. Chapter 4 describes the methodology used to generate the synthetic images. In Chapter 5 the results of the analysis of the synthetic images are presented and discussed to explore the strengths and weaknesses of each algorithm. The experimental setup and results from the water and air trials are summarised in Chapter 6. Finally, in Chapter 7, the conclusions and recommendations pertaining to the different algorithms are presented.

Chapter 2

Literature Review

2.1 Introduction

The literature involving PIV can be divided into three categories; (1) those works that introduce new methodologies to determine the displacement of the seed particles, (2) those which examine the error of different methodologies and (3) those which describe the application of PIV to particular experiments. The literature that examines the errors associated with different PIV techniques is usually presented by the creator of an algorithm to proclaim the capabilities of the method for a flow with a specific motion, *i.e.* rotation or shear, *etc.* This thesis will provide an unbiased comparison and assessment of the most common algorithms for different transport mechanisms that can be found in most fluid flows. Before discussing the issues pertaining to the accuracy and limitations of the algorithms, an overview of the PIV technique will be presented, including the major sources of error that exist within PIV. Summaries of the PIV technique can be found in [5, 6, 13, 19, 20, 21, 22, 23, 24, 25].

2.2   Overview of PIV

An overview of PIV must be provided before discussing the specific details of the different algorithms that were examined. A flowchart of the three steps involved in the application of the PIV technique is shown in Figure 2.1. The first step is to record images of a cross-section of a flow that has been seeded with particles, which are assumed to follow the flow. Current experiments typically use a charged-coupled device (CCD) camera to capture digitised images of the location of the seed particles within the flow, at two sequential instances in time. The CCD image is a discrete matrix where particle locations are represented by the intensity on the image array. After the images have been recorded, they are stored on a computer where they can be analysed to determine the particle displacements.

The particle displacements between images are estimated by dividing the images into smaller subsections called interrogation areas. The local displacement of the particles within each interrogation area is determined through the use of statistical tools, such as a cross-correlation. This results in a 2-D map of particle displacement vectors.

The measured displacements, $(\Delta x, \Delta y)$, are translated into local velocity vectors (u, v) by dividing the measured displacement by the time separation between images, Δt, and multiplying by a magnification factor, M, which relates the image size to the physical dimensions of the area being recorded.

$$u = M\frac{\Delta x}{\Delta t} \quad , \quad v = M\frac{\Delta y}{\Delta t} \tag{2.1}$$

The calculated velocity vector is then located at the centre of each interrogation area to create a 2-D vector field. The velocity field can then be further processed to obtain flow attributes such
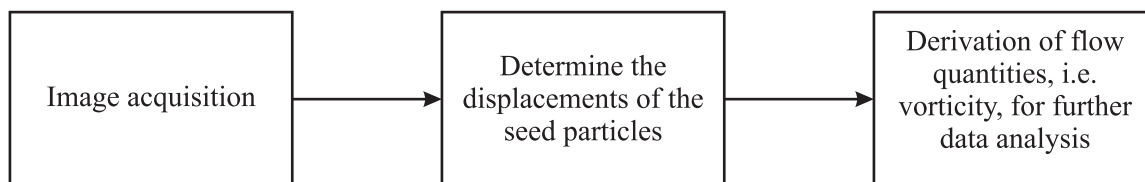
Figure 2.1: Flowchart of the steps in PIV

as vorticity, 2-D streamlines, *etc.* The accuracy of these derived quantities depends on the size of the error in the original estimates of the velocity vector field.

2.3   Particle Displacement Extraction

The precision of the flow quantities derived from a velocity vector field depends on the accuracy of the measured displacement (represented as the second step shown Figure 2.1) relative to the actual fluid motion in the vicinity of the seed particle. The magnitude of this error depends largely on the algorithm employed to determine the particle displacement between images, neglecting any errors introduced by the experimental setup.

Rather than finding the displacement of a single seed particle, the PIV technique tracks the movement of a group of particles within an interrogation area. The motion of a cluster of particles can be described with a linear digital signal processing model as shown in Figure 2.2 [20]. The positions of the particles within an interrogation area of the first image recorded at time t can be represented by the function $f(m,n)$, where m and n are locations within a sampled region of the image. Image 1 undergoes a spatial shift causing the seed particles to move, *i.e.* the motion of the fluid, that can be represented by the image transfer function $s(m,n)$. A noise function $d(m,n)$ is added to represent the signal deterioration due to any source, *e.g.*, the movement
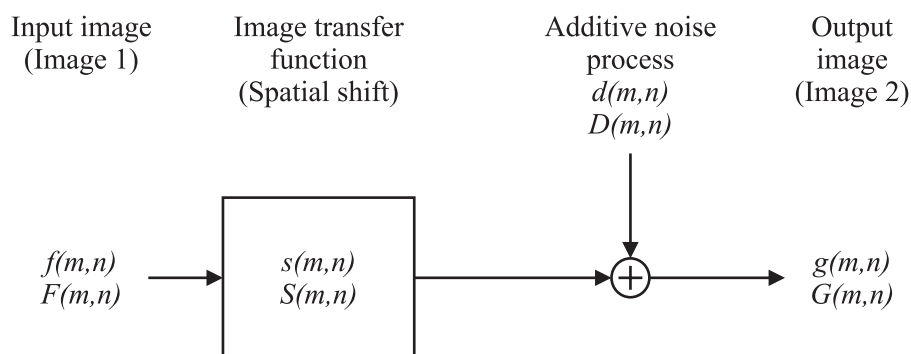
Figure 2.2: Image displacement function [20]

of the seed particles through the image plane between the recordings. The resulting function $g(m,n)$ is the output image, or the second image of the image pair, which represents the particle positions recorded at time $t + \Delta t$. If the spatial shift is assumed to be by translation only, *i.e.* the seed particles within an interrogation area all move the same distance in the same direction, and the noise function is negligible, the displacement can be estimated through a statistical *cross-correlation* of the two images. Equation 2.2 shows the mathematical representation of Figure 2.2 [20].

$$g(m,n) = [f(m,n) * s(m,n)] + d(m,n) \tag{2.2}$$

The $*$ represents a spatial convolution between the input function $f(m,n)$ and the image transfer function $s(m,n)$. However, the noise function is not negigible and thus must be added to the convolution.

Since the images are discrete, the cross-correlation operation will also be discrete. Between two regularly sampled regions, $f(m,n)$ and $g(m,n)$, the discrete cross-correlation, $\phi_{fg}(m,n)$, is given by the expected value E [20]:

$$\phi_{fg}(m,n) = E[f(m,n), g(m,n)] \tag{2.3}$$

The displacement is found by shifting the particles in the first image by a discrete value, comparing them to the particles in the second image and determining the correlation. The values produced by each possible displacement will create the *cross-correlation plane*. An example of a typical cross-correlation plane is shown in Figure 2.3. When particles in the first image match the same particles in the second image, for a given spatial shift, the value of the correlation will be the maximum in the cross-correlation plane (represented by the yellow in Figure 2.3). The maximum value is referred to as the *displacement peak*, while the other local maxima are referred to as noise peaks. These noise peaks are created due to the random matching of particles between the two interrogation areas.

The distance of the displacement peak from the centre of the correlation plane represents the spatial shift of the particles during the time separation betweeen images. This is illustrated in
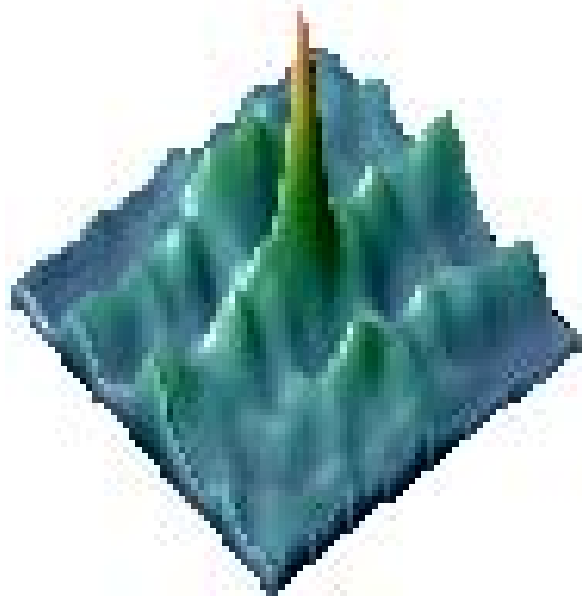
Figure 2.3: Typical cross-correlation plane

Equation 2.5 by substituting Equation 2.2 into Equation 2.3 and neglecting the noise effects [20]:

$$\phi_{fg}(m,n) = E[f(m,n), f(m,n) * s(m,n)] \tag{2.4}$$

$$\phi_{fg}(m,n) = \phi_{ff}(m,n) * s(m,n) \tag{2.5}$$

where ϕ_{ff} is the self-correlation of $f(m,n)$, referred to as the auto-correlation and will have its maximum correlation at the origin, *i.e.* the centre of the cross-correlation plane. Since the displacement function is assumed to represent a translation of the particles only, the convolution of the input function with the displacement function $s(m,n)$ moves the correlation peak away from the origin by an amount equal to the spatial shift.

To determine the correlation value for each displacement, *i.e.* to create the cross-correlation

plane, the convolution between $f(m,n)$ and $g(m,n)$ can be rewritten as [20]:

$$\phi_{fg}(m,n) = \frac{\displaystyle\sum_{k=-\infty}^{\infty}\sum_{l=-\infty}^{\infty} f(k,l)g(k+m,l+n)}{\sqrt{\displaystyle\sum_{k=-\infty}^{\infty}\sum_{l=-\infty}^{\infty} f^2(k,l)}\sqrt{\displaystyle\sum_{k=-\infty}^{\infty}\sum_{l=-\infty}^{\infty} g^2(k,l)}} \tag{2.6}$$

where k and l are locations within the image. Equation 2.6 is referred to as the *spatial cross-correlation* and is normalised to values between 0 and 1 by the denominator. This is necessary to compare the cross-correlation for different displacements since the sampled area g varies with m and n.

If the motion of the particles within the interrogation area is uniform, as assumed earlier, and there are no particles moving out of plane, the maximum value of the correlation will be unity. This does not occur in most flows as turbulence, shear, vorticity, diffusion, *etc.*will create velocity gradients, which negate the assumption of uniform motion within the interrogation area. In the case of a velocity gradient, not all the particles within an interrogation area of the first image will have identical displacements, so they will match best with their corresponding particles in the second image at different spatial shifts. The cross-correlation technique as described above cannot properly measure these velocity gradients. As a result, the maximum value within the cross-correlation plane will be less than unity and the width of the displacement peak will broaden [5, 20, 26].

Discrete Fourier Transform

Calculating the cross-correlation for each interrogation area as presented in Equation 2.6 is computationally expensive due to number of operations required, $O[N^4]$ where N is the length of the side of the interrogation area. Rather than performing a sum over all the elements in a sampled region for each possible displacement, the correlation theorem can be used to reduce the number of computational operations. The correlation theorem states that the cross-correlation of two functions, *i.e.* the convolution of f and g, is equivalent to a complex conjugate multiplication of

their Fourier transforms [25]:

$$\Phi_{fg} \Longleftrightarrow F \cdot G^{\star} \tag{2.7}$$

where F and G are the Fourier transforms of the images f and g respectively. Hence, the efficiency of the correlation algorithm can be further increased by computing the Fourier transforms of the two input images followed by their complex-conjugate multiplication. The resulting Fourier coefficients are inversely transformed to produce the cross-correlation plane, as shown in Figure 2.4.

Since the images are discrete, the Fourier transform can be performed using the fast Fourier transform (FFT) which reduces the number of operations to $O[N^2 log_2 N]$ compared to $O[N^4]$ operations required for the spatial cross-correlation. The most common implementation of the FFT routine requires the interrogation area to have a base-2 dimension, *i.e.* 32x32 pixels, 64x64 pixels, *etc.*, however Gui *et al.* [27] suggested a method allowing the use of any sized interrogation window by padding the interrogation area with zeros until it has a base-2 dimension.

The Fourier transform, by definition, is the integral summation over a domain which ranges from negative infinity to positive infinity, *i.e.* the interrogation areas need to be boundless to apply the Fourier transform. However, the interrogation areas used in PIV are of finite dimension. To create an infinite signal, the image is *wrapped* to create a *periodic continuation* [21]. By wrapping the interrogation area, the infinite signal requirement for the cross-correlation is removed but the maximum measurable displacement is limited to half the length of the interrogation area dimension, due to the Nyquist sampling criterion [20]. Due to the periodic continuation of the cross-correlation, fewer particle pairs correlate as the particle displacement increases. This causes
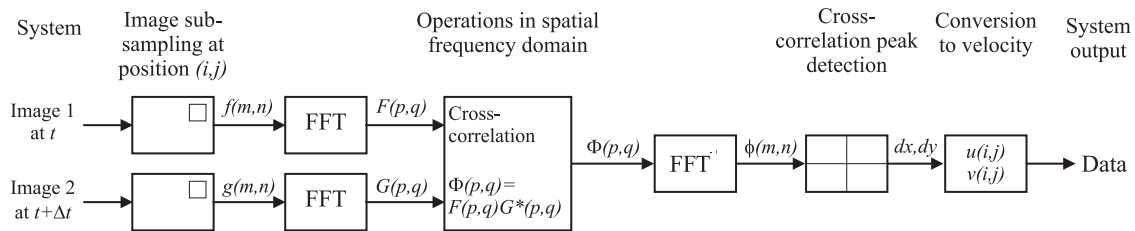
Figure 2.4: Flow chart for discrete Fourier transform cross-correlation [20]

the signal-to-noise ratio (SNR) to decrease with increased displacement reducing the probability that the largest peak represents the average spatial shift. To account for this SNR degradation, the true maximum measurable displacement is closer to one-third the length of the interrogation area [5, 20, 28].

The periodic continuation of the FFT cross-correlation induces an error when the size of the sampled region in the first image is equal to that in the second image. The contribution to the correlation plane by the particles near the edge of a interrogation area will decrease as the displacement increases, see Figure 2.5, as they begin to correlate with the opposite edge of the interrogation area. As a result, the magnitude of the correlation peak will decrease as the displacement increases and bias the peak towards the centre (zero-displacement) of the correlation
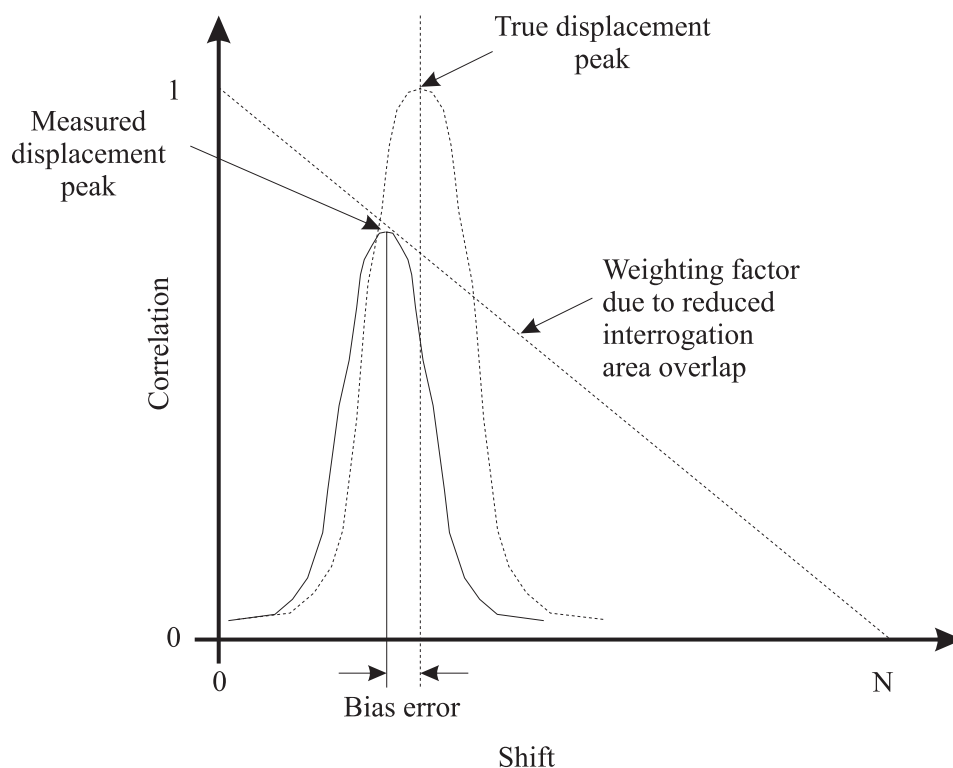
Figure 2.5: Correlation bias for FFT [25]

plane, *i.e.* zero-bias the measured displacement [25, 29]. To minimise the bias, the recommended displacement of the particles within an interrogation area is further reduced from one-third to one-quarter of the length of the side of the interrogation area. This is commonly referred to as the *one-quarter rule*.

One method used to reduce the zero-velocity bias caused by large displacements is to employ a window filter, as shown in Figure 2.6 [25, 30]. By dividing the correlation plane by the filter, the magnitude of the edges of the correlation plane are increased relative to the centre. However, filters such as those shown in Figure 2.6 do not account for the contribution of noise that occurs when the particles at the edge of one interrogation area match with particles at the opposite edge of the second interrogation area. Therefore, the shape of the filter required should be different for every interrogation area.

The cross-correlation planes produced by the discrete Fourier transform method shown in Figure 2.4 are not equal that produced using the spatial cross-correlation in Equation 2.6 due to the periodic continuation used for the Fourier transform. However, the results of the cross-correlation plane are similar since the Fourier transform is only another method of determining the expected values for Equation 2.5. Similar to the spatial cross-correlation, the discrete Fourier method is also incapable of resolving velocity gradients, *i.e.* the particles are assumed to move uniformly within an interrogation area.
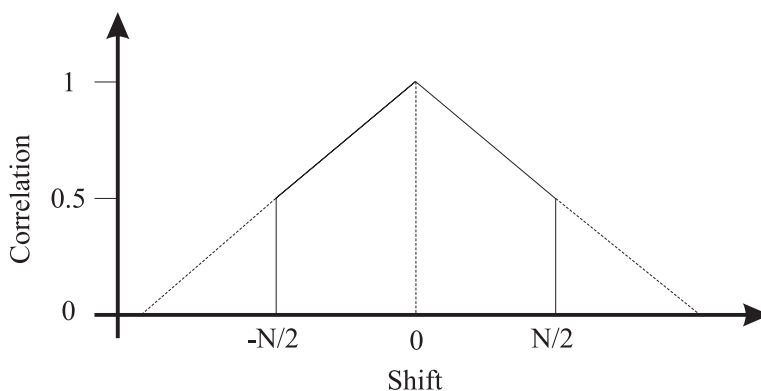
Figure 2.6: Typical window filter used to account for zero-velocity bias [25]

2.3.1 Sub Pixel Interpolation

The cross-correlation plane, produced by either the spatial or FFT method, is discrete. Therefore the measured displacement of the particles within an interrogation area will always be an integer value (in pixels). The actual spatial shift of the particles typically is a non-integer value so the maximum error from the true location of the highest peak within the cross-correlation plane is $\pm$ 0.5 pixels. For a 32x32 pixel interrogation window the recommended displacement is 8 pixels (one-quarter rule) so the error would be $\pm$ 6% of full scale, which is not considered accurate enough for most research applications.

If the correlation peak is broader than one pixel, the error can be significantly reduced by estimating the true location of the peak with a *sub pixel interpolation* strategy. Table 2.1 shows the three most common methods used to determine the sub pixel location of the displacement peak, (x_0, y_0) [25]. The locations of the values used are shown in Figure 2.7.

The peak centroid estimator is based on the assumption that the centroid of a symmetric object is the location of that object [29]. Figure 2.8 shows the four discrete peaks which are centered about different displacement values away from the origin (0.0 pixels, 0.1 pixels, 0.25 pixels and 0.5 pixels). The discrete peaks are only symmetric for the 0.0 pixels and 0.5 pixels displacements. Therefore, for other displacements, the centroid method will become strongly biased towards integer pixel displacements [29]. This phenomenom is termed *peak-locking*.

Another method that can be used for sub pixel interpolation, which is less susceptible to peak-locking than the centroid method, is to fit a curve to the correlation peak. The shape of the displacement peak can be represented by a function and the maximum location found analytically. The most common functions used to mimic the shape of the displacement peak are the Gaussian and parabolic functions. The Gaussian curve fit has proven to be more accurate than the parabolic fit since it provides a better approximation to the actual shape of a correlation peak [31].

Depending on the choice of sub pixel interpolation strategy, the error (in estimation of the displacement) can be reduced to approximately 0.1 pixels [12, 20, 29, 32, 33]. This means for a 32x32 pixel interrogation area the error due to the peak finding can be reduced to $\pm$ 1%.

Fitting function	Estimators
Peak centroid	$x_0 = \dfrac{(i-1)\phi_{(i-1,j)} + i\phi_{(i,j)} + (i+1)\phi_{(i+1,j)}}{\phi_{(i-1,j)} + \phi_{(i,j)} + \phi_{(i+1,j)}}$
$f(x) = \dfrac{first\ order\ moment}{second\ order\ moment}$	$y_0 = \dfrac{(j-1)\phi_{(i,j-1)} + i\phi_{(i,j)} + (j+1)\phi_{(i,j+1)}}{\phi_{(i,j-1)} + \phi_{(i,j)} + \phi_{(i,j+1)}}$
Parabolic peak fit	$x_0 = i + \dfrac{\phi_{(i-1,j)} - \phi_{(i+1,j)}}{2\phi_{(i-1,j)} - 4\phi_{(i,j)} + 2\phi_{(i+1,j)}}$
$f(x) = Ax^2 + Bx + C$	$y_0 = j + \dfrac{\phi_{(i,j-1)} - \phi_{(i,j+1)}}{2\phi_{(i,j-1)} - 4\phi_{(i,j)} + 2\phi_{(i,j+1)}}$
Gaussian peak fit	$x_0 = i + \dfrac{\ln\phi_{(i-1,j)} - \ln\phi_{(i+1,j)}}{2\ln\phi_{(i-1,j)} - 4\ln\phi_{(i,j)} + 2\ln\phi_{(i+1,j)}}$
$f(x) = C\exp[\frac{(-x_0-x)^2}{k}]$	$y_0 = i + \dfrac{\ln\phi_{(i,j-1)} - \ln\phi_{(i,j+1)}}{2\ln\phi_{(i,j-1)} - 4\ln\phi_{(i,j)} + 2\ln\phi_{(i,j+1)}}$

Table 2.1: Three point estimators for determining sub pixel location of displacement peak [25]
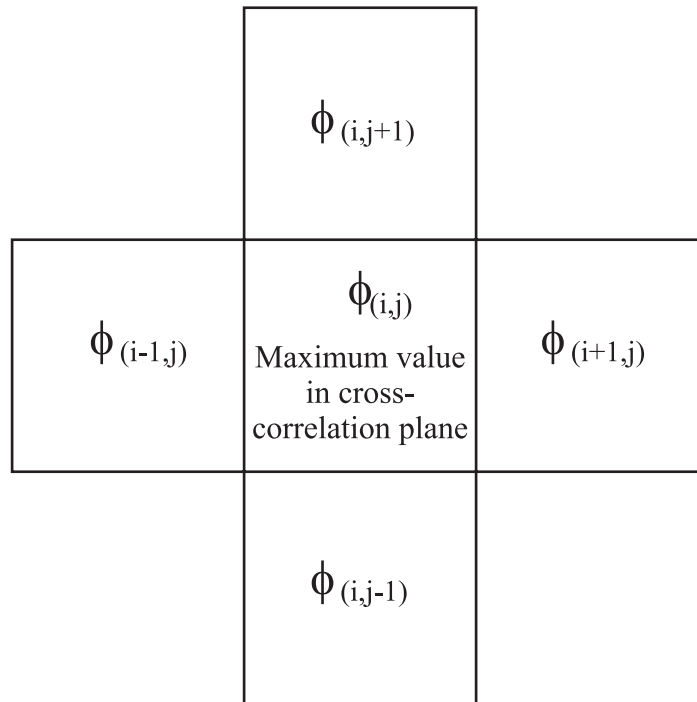
Figure 2.7: Locations of points used for sub pixel interpolation
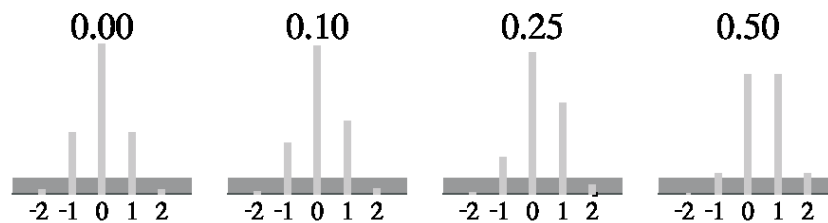
Figure 2.8: Correlation peaks for different pixel displacements [29]. Note that the peaks are only symmetric for displacements of 0.0 pixels and 0.5 pixels.

2.3.2 Vector Validation

The largest peak in the correlation is assumed to represent the spatial shift of the group of particles in the interrogation area and the second largest peak is a noise peak, *i.e.* random matching between particles. If the signal is poor, a noise peak may become larger than the correlation peak and the estimated displacement becomes false, *i.e.* invalid. The procedure of separating invalid measurements from those based on the true displacement peak is termed *validation*.

Not enough detail about the flow exists to use physical validation strategies, such as the continuity equation. Rather, validation can be done by comparing the *quality* of the measurements against some threshold. Young [34] separated the validation strategies into three general categories: (1) nearest-neighbour, (2) intrinsic methods and (3) global methods.

Nearest-neighbour validation strategies compare the estimated displacements from one interrogation area to those in its spatial neighbours [5]. If the difference between a displacement vector and its neighbours is too large, the displacement vector is determined to be invalid. The accuracy of this scheme is strongly based on the threshold value used to compare the results as well as the *smoothness* of the displacement vector field.

Intrinsic validation strategies determine the validity of a velocity vector without regard to its neighbours. Instead, the magnitude of the displacement peak and/or the width of the displacement peak are used to determine the *strength* of the cross-correlation by comparing some/all of the aforementioned criteria to one or more threshold values [5, 20, 28].

Global schemes utilize segmentation of pixel intensities, velocities, or intermediate scalar parameters to separate the *bad* from the *good* measurements [34]. These methods are more sophisticated and implementation and computational time are key factors.

The nearest-neighbour and the intrinsic methods are the most common validation strategies, used for their simplicity and ease of implementation. However, the number of user defined factors required by these methods, *e.g.*, threshold limits, kernel sizes, *etc.*, make their proper execution difficult.

2.4   Types of Error in PIV

Before describing the other cross-correlation algorithms that are employed in an effort to reduce the error of the previously described standard FFT method, how these errors occur must be explained. Muste *et al.* [35] divided the errors associated with PIV into two categories (1) *random* and (2) *mean bias*.

2.4.1   Random Error

Random errors result in values above and below the true value but will average to zero if the sample size is large. Random errors are typically estimated with the root-mean-square (RMS) method. In this work the RMS and the standard deviation are the same and for a discrete signal the RMS is defined as:

$$RMS = \frac{1}{A} \sqrt{\sum_{i=0}^{A} (u_i - \bar{u})^2} \tag{2.8}$$

where A is the number of measurements.

The SNR ratio can be used as a gauge to measure the random error within the cross-correlation. The SNR will decrease when fewer particles contribute to the correlation for a given displacement, *i.e.* fewer particles have a corresponding particle for a given spatial shift. Therefore it is easier for the displacement peak to shift from the true value due to noise in the interrogation area when the SNR is low compared to when the SNR is high. For example, if the background noise is high and the SNR is low, the multiplication of a particle with the background noise during the correlation may cause a noise peak to become the highest peak. Since the background noise is random, the error would average to zero with a large sample size, and the RMS would be high. Thus for PIV, the random error can loosely be interpreted as anything that reduces the SNR and increases the RMS.

Adrian [5] conjectured that if the particle imaged was greater than 2 pixels in diameter, the random error, ε_{rdm}, could be consolidated into a single term proportional to the imaged particle diameter d_p:

$$\varepsilon_{rdm} = c \cdot d_p \tag{2.9}$$

Prasad *et al.* [36] found the proportionality constant c was dependent on the experimental conditions but typically varied from 0.05 to 0.10. However, Westerweel [32] created a model to predict the measurement error and showed the RMS was proportional to d_p^2, see Figure 2.9.

2.4.2 Mean Bias Error

Unlike random errors, mean bias errors are not reduced by averaging. They tend to change the measured value by a consistent amount in the same direction, *i.e.* always increase or always decrease the measured value from the true value. Bias errors are defined as:

$$mean\ bias\ error = average\ value - true\ value \qquad (2.10)$$

For PIV, mean bias errors can be interpreted as anything that consistently shifts the displacement peak in a direction, within the correlation plane, relative to the true displacement, as shown in Figure 2.10.
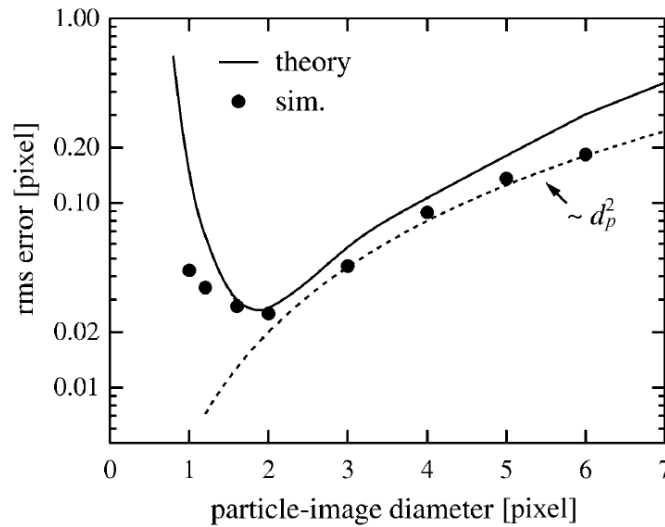
Figure 2.9: RMS error as a function of particle displacement [32]

2.5 Sources of Error in PIV

Table 2.2 shows the major sources of error that exist within PIV and by which type of error they are best represented. Each of them will be examined in turn.

2.5.1 Image Recording

When the particles are imaged onto a recording medium, photographic film or a CCD camera, error will exist due to noise in the recording device. Pickering and Halliwell [6] examined the error caused by film grain noise when film was used to record the particle positions. Prasad *et al.* [36], Adrian [37] and Huang *et al.* [38] compare film to digital recordings. Although they determined film is more accurate due to its higher resolution, the difficulty in processing the images makes it impractical for most cases. (Incidentally, this error only exists for experimentally collected images, not synthetic images. Therefore it is important to validate any results determined based on synthetic images with similar results from experimentally collected images.)
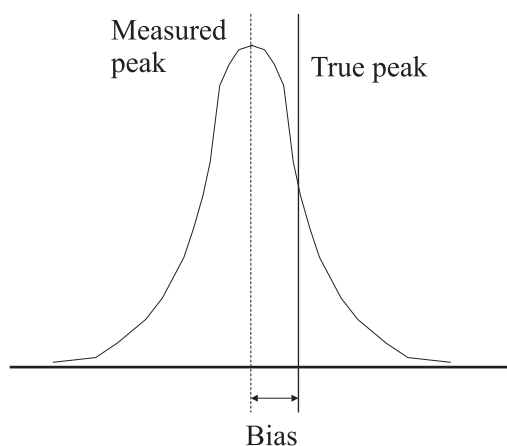
Figure 2.10: displacement peak shift due to mean bias error

Error	Type
Image recording	Random
Contrast between particle and background noise	Random
Particle density	Random
Loss of pairs due to out-of-plane motion	Random
Parallax	Random
Tracking error	Bias
Acceleration error	Bias
Velocity gradients	Random and Bias
Sub pixel interpolation	Bias

Table 2.2: Major sources of error in PIV

2.5.2 Contrast Between Particle and Background Noise

Within the recorded images there exists a difference between the intensity of the background noise and the particles, defined as the contrast. The intensity of the background noise and of the imaged particle depends on the camera and laser setup. Guezennec and Kiritsis [12] performed a statistical analysis on the effect of the contrast between the particles and the background noise on the measurement error using a combination of PIV and PTV. For their particle displacement measurements, PIV was first used to determine the displacement vectors, then individual particles were tracked with a PTV algorithm.

It was found that when the contrast was greater than 100 counts the error was insensitive to the background noise, for an 8-bit image. However, when the contrast was below 100 counts the error quickly increased with the background noise level. The reason is that the particles in one interrogation area will multiply with noise in the second interrogation area. If the background noise is small the contribution to the correlation plane of this multiplication will be small, but as the background noise increases (with a constant contrast) so does its contribution to the correlation. This will reduce the SNR, which will increase the probability of an error in the displacement measurement. Therefore, if the contrast between the particles and the background

cannot be increased, it is better to lower the overall intensity of the image.

2.5.3 Particle Number Density

Particle number density is defined as the number of particles within an interrogation area. Huang *et al.* [38], using a standard PIV algorithm, found that as the number of particles increased, the RMS error decreased, as shown in Figure 2.11. This is a result of more particle pairs matching and *strengthening* the displacement peak in the correlation plane, thus improving the SNR. Adrian [5] and Grant [13] both recommend having greater than 10-20 particles within an interrogation area in order to reduce the measurement error due to the particle number density to an acceptable level.
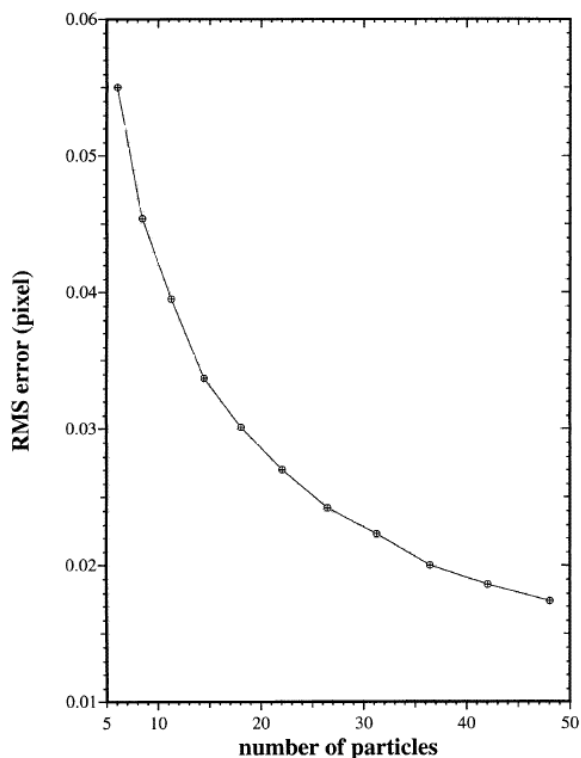
Figure 2.11: RMS as a function of particle density [38]

2.5.4 Loss of Pairs Due to Out-of-Plane Motion

Another advantage of a higher particle number density is the reduced error due to the *loss of pairs* from out-of-plane motion. Loss of pairs refers to the condition where a particle fails to correlate with its matching particle in the second image. This results in a diminished value for the displacement peak in the correlation, reducing the SNR [5, 13]. Although PIV is typically used for flows that are predominately 2-D in nature, the flow will still contain small velocity components in the direction normal to the light sheet. If the light sheet is too thin and/or the velocity normal to the light sheet is too high, a particle which exists in the first image may move out-of-plane by the time the second image is recorded. Alternatively, a particle may move into the image plane after the first image has been recorded. Since these particles do not have a matching particle in the corresponding interrogation area in the second image, the SNR will be reduced, resulting in an increase in the error. Adrian [5] recommends the particle displacement normal to the image plane between image recordings be less than one-quarter the thickness of the laser sheet.

2.5.5 Parallax

The motion of particles normal to the light sheet may cause an error in the particle displacement measurement, even if the particle exists within both images. The light sheet used to create a 2-D slice in the flow field has a thickness and it is possible to transpose the motion normal to the light sheet into a displacement parallel to the image plane, *i.e.* Δz is measured as Δx and Δy, thus reducing the accuracy.

The measured motion of the particle $(\Delta x_{measured}, \Delta y_{measured})$ can be determined by [17]:

$$\Delta x_{measured} = -(x_{axis} + \Delta x)[1 + \Delta z/(D_0 - \Delta z)] + x_{axis} \qquad (2.11)$$

$$\Delta y_{measured} = -(y_{axis} + \Delta y)[1 + \Delta z/(D_0 - \Delta z)] + y_{axis} \qquad (2.12)$$

where (x_{axis}, y_{axis}) is the distance the particle is from the optical axis, D_0 is the distance between the lens and the image plane and $(\Delta x, \Delta y, \Delta z)$ is the true displacement of the particle, as shown in Figure 2.12. The obvious solution to reduce the error due to parallax is to limit the displacement

of the particle in the direction normal to the image plane. However, this is not always possible, so the error can also be minimised by increasing D_0, the distance between the image plane and the camera lens.

2.5.6 Tracking Error

The function of the PIV technique is to measure the motion of particles that have been seeded within a flow. The assumption is that the seed particles follow the flow perturbations exactly and hence the particle velocity mimics the flow velocity. This is not always true. The seed particles will not exactly follow the flow if there is a large difference in density between the particles and
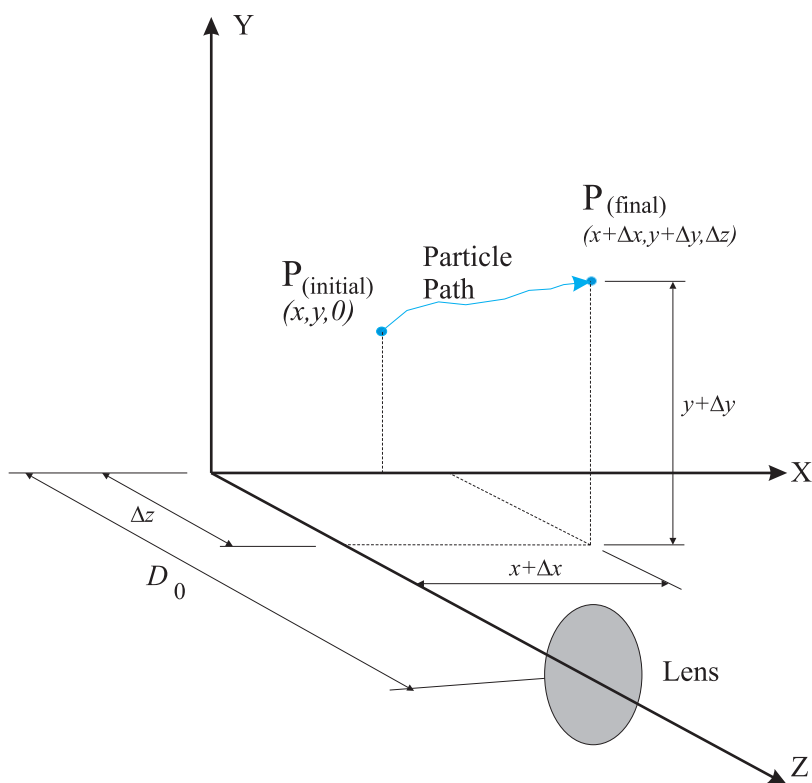
Figure 2.12: Error in 2-D measurements of 3-D flows due to parallax [17]
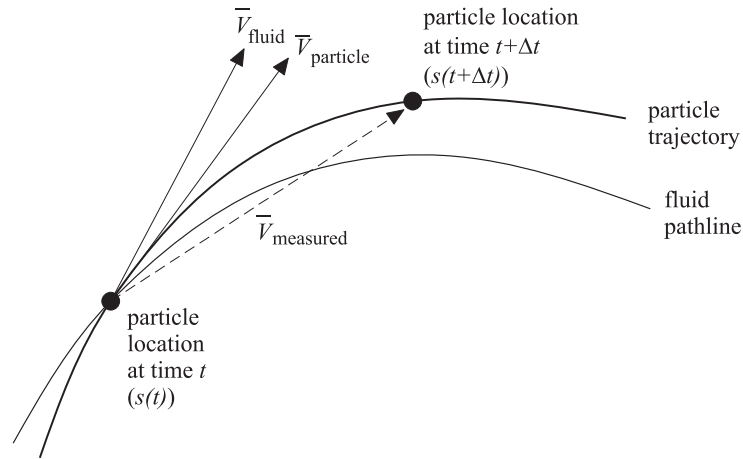
Figure 2.13: Velocity streamline of a particle [42]

fluid medium. Alternatively, a time lag may exist between the acceleration of the fluid and the response of the particles. The time lag of the particle response will damp/hide some of the turbulent nature of the flow.

Melling [39] used a simple Stokes flow analysis to model the reaction of different seed particles to an oblique shock, using air and water as the fluid medium. For a more accurate analysis Hinze [40] uses the equation derived by Basset, Bossinesq and Ossen (BBO) to model the flow of a particle within a fluid.

2.5.7 Acceleration Errors

For the standard PIV technique, the estimated velocity of a particle is an approximation of the Eulerian velocity from a Langrangian motion, assuming the acceleration of the flow is zero between the images [41]. PIV determines the average velocity over the pulse separation, which may be different from the actual instantaneous velocity. Figure 2.13 shows the measured velocity compared to that of the particle velocity and the fluid velocity. The difference between the particle and fluid velocity is the tracking error described in Section 2.5.6. However, the difference

between the measured velocity and the particle velocity is due to the particle accelation during the time separation between the images.

Boillet and Prasad [41] modelled the error due to the acceleration of the flow. In general, fluid flows can be unsteady and have non-zero acceleration of the form:

$$\frac{d\vec{V}}{dt} = \frac{\partial \vec{V}}{\partial t} + \vec{V} \cdot \nabla \vec{V} \tag{2.13}$$

where $\vec{V}$ is the velocity of the particle.

Assuming the particle follows the flow exactly (*i.e.* no tracking errors) and neglecting higher order terms, the particle trajectory may be approximated by:

$$s(t + \Delta t) = s(t) + \frac{ds}{dt}\Delta t + \frac{d^2 s}{dt^2}\frac{\Delta t^2}{2} \tag{2.14}$$

where $s(t)$ is the particle position at time t. The *relative* error due to acceleration is then the difference between the actual and measured displacement, divided by the measured displacement:

$$\varepsilon_{accel} = \frac{|\Delta s - \vec{V} \cdot t|}{\Delta s} \tag{2.15}$$

$$\varepsilon_{accel} = \frac{d\vec{V}}{dt}\frac{\Delta t^2}{2|\Delta s|} \tag{2.16}$$

Note, as the limit $\Delta t \to 0$, the velocity measurement becomes instantaneous and the error due to acceleration approaches zero, as expected.

Reducing the laser pulse separation will reduce the error due to acceleration but the overall error may increase since the displacement of the particles between images also goes to zero, increasing the error relative to the particle displacement. Wereley and Meinhart [43] suggested placing the vector at a location other than the centre of the interrogation area at time t. The vector is placed at the location the center of the interrogation area would be at time $t + \frac{1}{2}\Delta t$ changing the order of the acceleration error from $O[\Delta t]$ to $O[\Delta t^2]$.

If the acceleration of the flow needs to be measured, more than two instances in time need to be recorded. Jakobsen *et al.* [44] used four cameras to measure the acceleration in a flow involving waves impinging against a wall.

2.5.8 Velocity Gradient Errors

The cross-correlation approach assumes that all the particles move uniformly within an interrogation area. When velocity gradients exist within an interrogation area, as they typically do in fluid flows, not every particle will have a corresponding match in the second image for a given spatial shift. Examples of this condition are shown in Figure 2.14 [45]. This is sometimes referred to as loss of pairs due to in-plane motion and causes the displacement peak in the cross-correlation plane to broaden [5, 20, 26]. This increase in the width of the peak is due to the cross-correlation routine finding particles and their corresponding matching particles at different spatial shifts. The increase in the width of the displacement peak may increase the error associated with the sub pixel interpolation since the peak is no longer as well defined.

The error due to velocity gradients within an interrogation area has both a random and a mean bias component. When more than one displacement exists within the interrogation area, the cross-correlation operation may randomly select any of them as the displacement peak, causing the RMS, *i.e.* the random error, to increase.

The mean bias error from velocity gradients results from two different mechanisms: (1) the range of velocities within an interrogation area and (2) the shape of the velocity profile. The range of
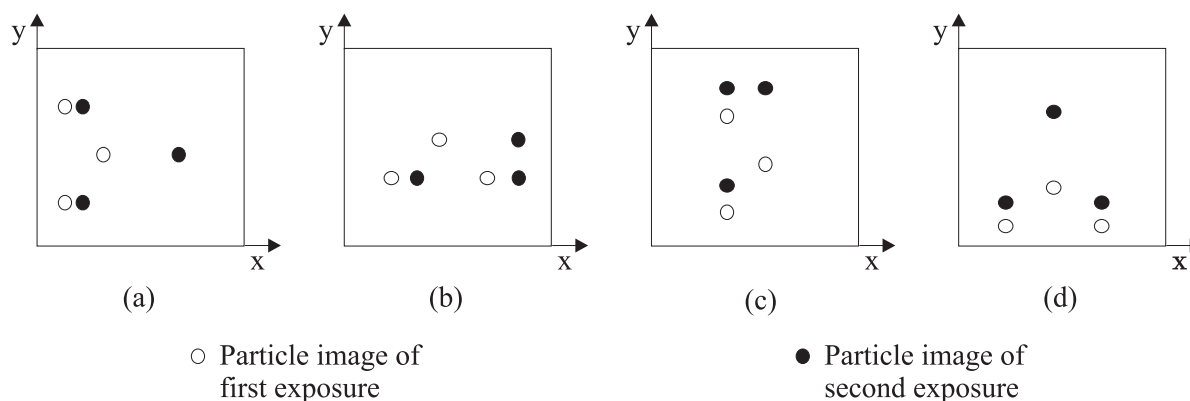
Figure 2.14: Typical gradients within an interrogation area (a) $\partial u/\partial x > 0$, (b) $\partial u/\partial y > 0$, (c) $\partial v/\partial x > 0$, (d) $\partial v/\partial y > 0$ [45]
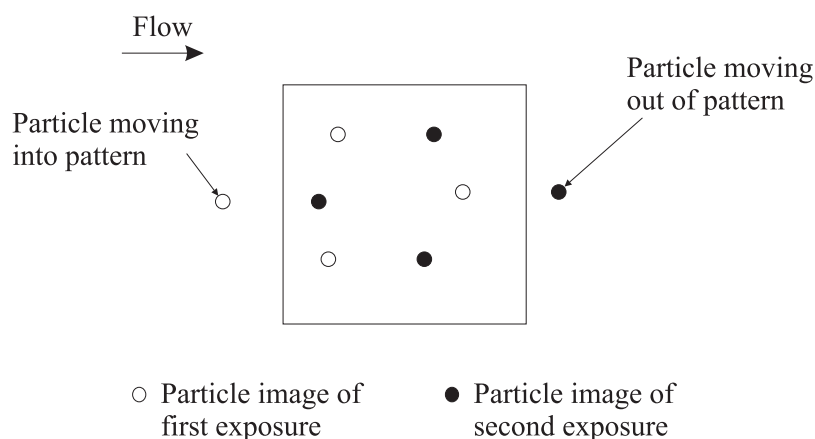
Figure 2.15: Loss of pairs due to particles moving out of the interrogation area [46]

velocities within an interrogation area affects the measurement results since the faster moving particles travel a greater distance within an interrogation area compared to the slower moving particles. Over the duration of the time separation, more fast moving particles will leave the interrogation area than slow moving particles, as shown in Figure 2.15. Hence, there will be more matching particle pairs for the slower moving particles and the displacement peak will become biased towards those particle displacements.

The second mechanism that biases the displacement peak due to velocity gradients is a result of the shape of the velocity gradient. Figure 2.16 shows a possible velocity gradient and its histogram of velocities within the interrogation area. In this case the mean velocity does not equal the velocity that exists at the centre of the interrogation area, instead it is shifted towards the lower velocities within the interrogation area. Since the velocity vector is placed at the centre of the interrogation area the measurement contains a mean bias error. For the special case shown in Figure 2.17, the mean bias error would be zero since the expected mean velocity is equal to the velocity at the centre of the interrogation area.

It is important to note that the error associated with velocity gradients is not solely a result of the cross-correlation procedure, but also where the vector is placed within the interrogation area. The displacement peak still measures a velocity within the interrogation area, it just may not

Interrogation area

Velocity at centre
of interrogation area

Expected value

Velocity

(a)

(b)

Figure 2.16: (a) Velocity gradient within an interrogation area and its (b) histogram of velocities
and expected value

Interrogation area

Expected value
and velocity at the
centre of interrogation
area

Velocity

(a)

(b)

Figure 2.17: (a) Special case of a velocity gradient within an interrogation area and its (b)
histogram of velocities

correspond to the velocity at the centre of the interrogation area as assumed when the vector is placed there. The velocity measured may exist away from the centre of the interrogation area and if the vector was properly placed within the interrogation 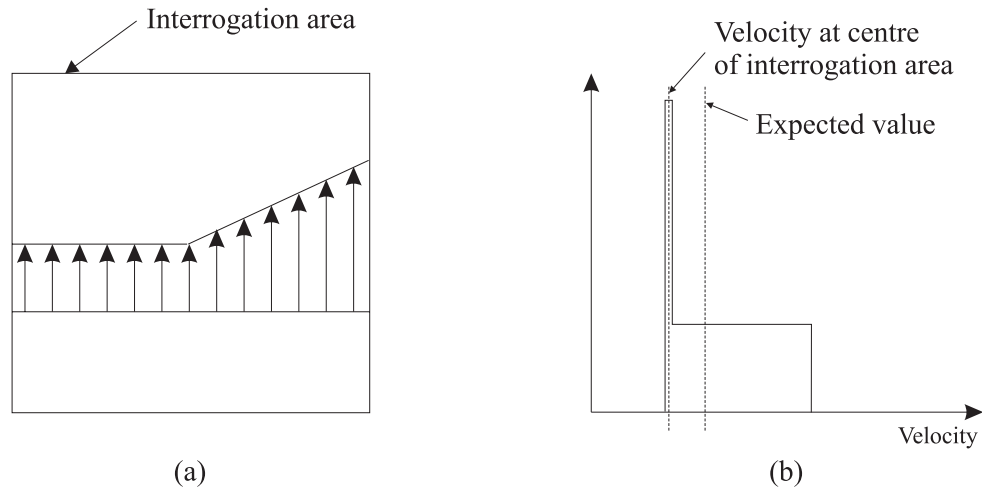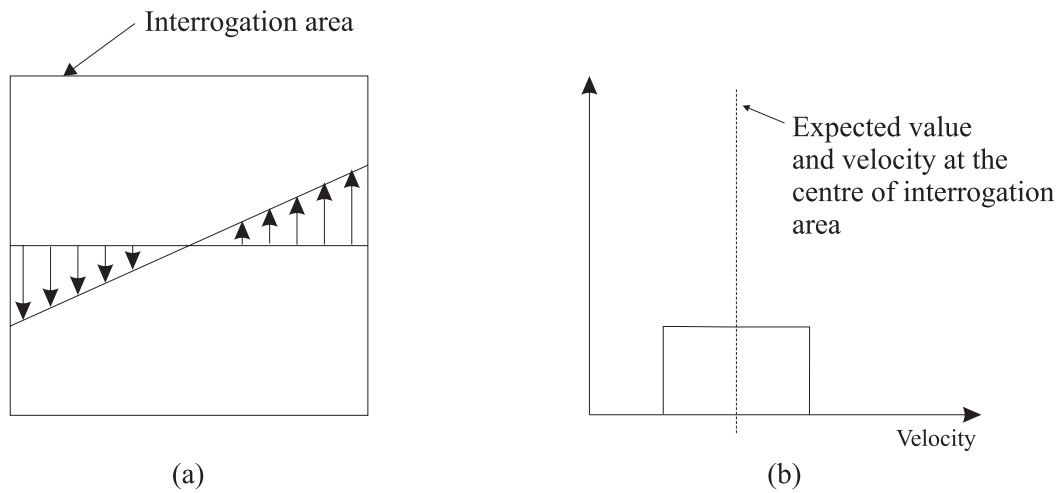area the bias and random error would both be zero. Young *et al.* [47] determined which particle contributed the most to the displacement peak in the correlation plane and placed the velocity vector at the position of the particle, reducing the overall error.

Smaller interrogation areas can also be used to reduce the error due to velocity gradients since the distance from the centre of the interrogation area to the proper location of the vector will be less for smaller interrogation areas.

2.6 Improved Cross-correlation Strategies

Modifications of the standard FFT method have been introduced to reduce the magnitude of the aforementioned errors. The three most common cross-correlation based algorithms are (1) predictor corrector FFT, (2) super resolution FFT and (3) interrogation area deformation FFT. Each method will be described in turn.

2.6.1 Predictor Corrector FFT Correlation

The accuracy of the cross-correlation technique is highest when there is no particle displacement between images. With zero displacement, the errors due to the zero-bias of the FFT routine and the peak-locking in the sub pixel interpolation become zero. This is illustrated in Figure 2.18 [48], which shows that for displacements less than 0.5 pixels the RMS error is significantly reduced, and is zero when there is no displacement. Based on this observation, Westerweel *et al.* [48] suggested a modification to the standard PIV algorithm in order to take advantage of the accuracy inherent with small displacements. If one of the interrogation areas of an image pair is offset by the integer amount of the particle displacement, the cross-correlation will only be measuring the residual displacement, which can be made less than 0.5 pixels. Consequently, the accuracy of the displacement estimate will be greater than the analysis without a window offset.
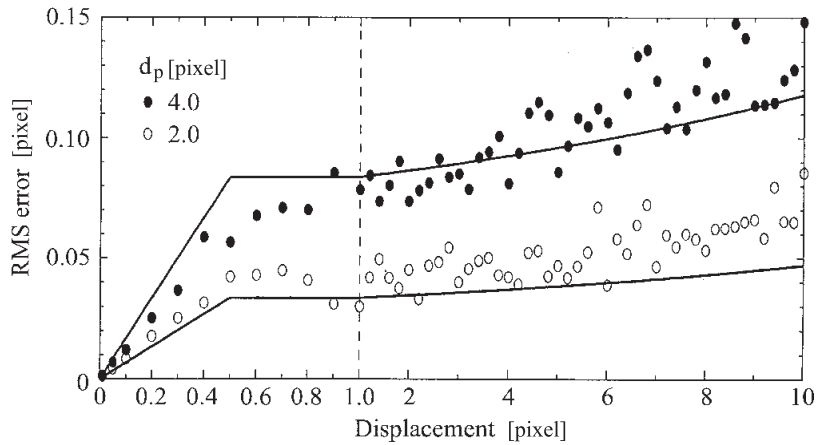
Figure 2.18: RMS estimation error for the displacement [48]

For most flows, the integer offset of the interrogation area will vary throughout the image plane due to velocity gradients. Therefore the integer offset must be determined locally for each interrogation area. Generally, the approach is to first apply the standard PIV technique as described earlier. Then the cross-correlation is repeated using the integer value of the previously measured displacement as the window offset for the interrogation area. The cross-correlation can then be repeated with the new integer offset determining a more accurate displacement iteratively. The number of iterations can be based on a user specified value or on the magnitude of the displacement peak in the cross-correlation plane. Since the magnitude of the displacement peak represents the accuracy of the displacement estimate, as long as the magnitude of the largest peak in the correlation plane increases the procedure is repeated. This method is referred to as *predictor corrector FFT* since it corrects the previous estimate of the particle displacement. Figure 2.19 shows the algorithm for the predictor corrector FFT method.

2.6.2 Super Resolution FFT Correlation

The cross-correlation method contains two assumptions; (1) the effect due to noise is negligible and (2) the particles within the interrogation area move uniformly in a single direction. The first

Figure 2.19: Predictor corrector FFT algorithm [48]

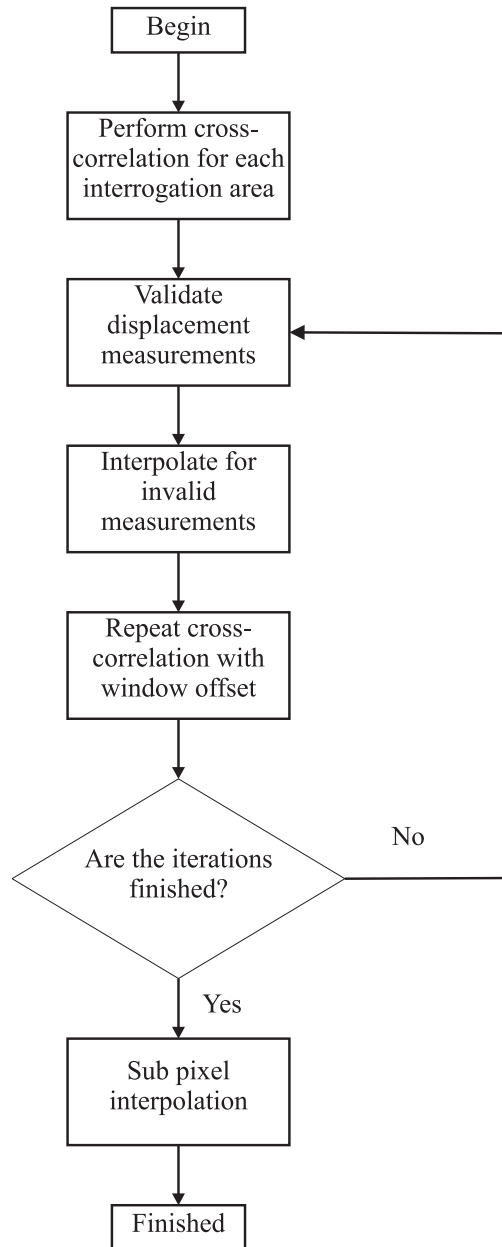assumption is valid for most experiments. With respect to the second assumption, velocity gradients will exist within all flows, especially turbulent flows. Velocity gradients will prevent every particle within an interrogation area from corresponding to its matching particle in the second image for a single spatial shift, thus broadening and diminishing the value of the displacement peak [10, 29, 45]. Adrian [5] recommended that $|\Delta \vec{V}|/|\vec{V}| < 0.2$, where $|\Delta \vec{V}|$ is the velocity variation over the interrogation area due to the velocity gradients to reduce the displacement error associated to velocity gradients.

The guideline recommended by Adrian for velocity gradients puts an upper limit on the size of the interrogation area, *i.e.* reduces the size of the interrogation area. Within this guideline, velocity gradients will still exist within each interrogation area but the difference between the maximum and minimum velocity will be reduced. Smaller interrogation areas will also lower the spacing between velocity vectors, which may enable the measurement of some length scales present in turbulent flows.

Unfortunately, utilising smaller interrogation areas limits the maximum measurable displacement (since the one-quarter rule must still be adhered to). With the smaller particle displacement, the relative error will increase. If the error in the displacement measurement was ± 0.5 pixels, the relative error would be greater when the displacement is 4 pixels than when the displacement is 8 pixels.

Scarano and Riethmuller [49] proposed a method that would allow for the use of small interrogation areas without reducing the maximum measurable particle displacement. Similar to the predictor corrector FFT method, an iterative approach is used to determine the displacement of the particles by offsetting the interrogation area. However, after estimating the integer offset with the standard FFT technique and validating the displacement vectors, the size of the interrogation area is reduced by a factor of 2 (see Figure 2.20). The cross-correlation is then determined with the smaller interrogation areas, along with an integer offset, creating a finer mesh of velocity vectors, while maintaining the necessary particle displacement, over the time separation Δt, required for higher accuracy. The procedure can then be repeated by further dividing the size of the interrogation area. The number of iterations can be based on a user specified value or on the magnitude of the displacement peak in the cross-correlation plane. Since the magnitude of the
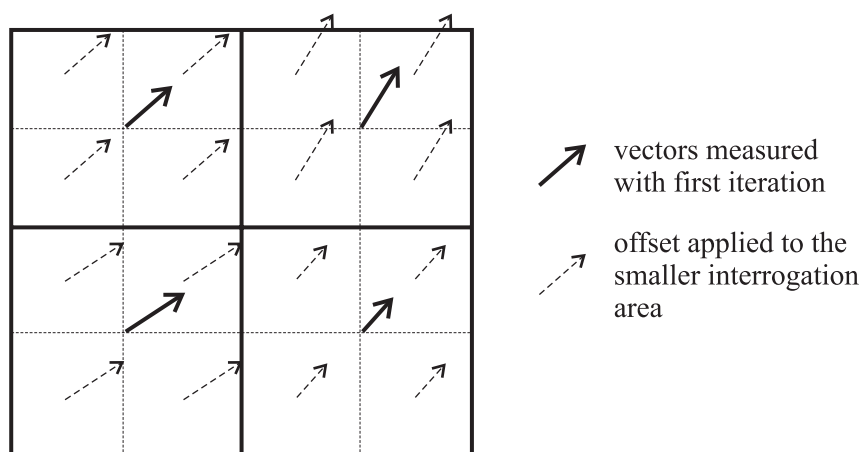
Figure 2.20: Halving of interrogation windows for super resolution FFT - application of an interrogation result (solid line) to build a finer mesh (dotted line)

displacement peak represents the accuracy of the displacement estimate, as long as the magnitude of the peak increases the procedure is repeated.

The smaller interrogation areas will obey the one-quarter rule since the cross-correlations after the initial estimate are only *fine tuning* the measurements. This method is called *super resolution FFT* and Figure 2.21 shows its algorithm.

2.6.3   Interrogation Area Deformation Correlation

The standard cross-correlation method can accurately measure pure translation in a flow but there are two other transport mechanisms within fluid flows,

$$fluid\ motion = convection + stretching + rotation \tag{2.17}$$

where convection is pure translation, stretching is expressed by $\partial u/\partial x$ and $\partial v/\partial y$ and rotation is expressed by $\partial u/\partial y$ and $\partial v/\partial x$. Both stretch and rotation create velocity gradients within an interrogation area. These cannot be measured properly with the cross-correlation, resulting in a reduced value for the maximum cross-correlation peak. Although the super resolution FFT
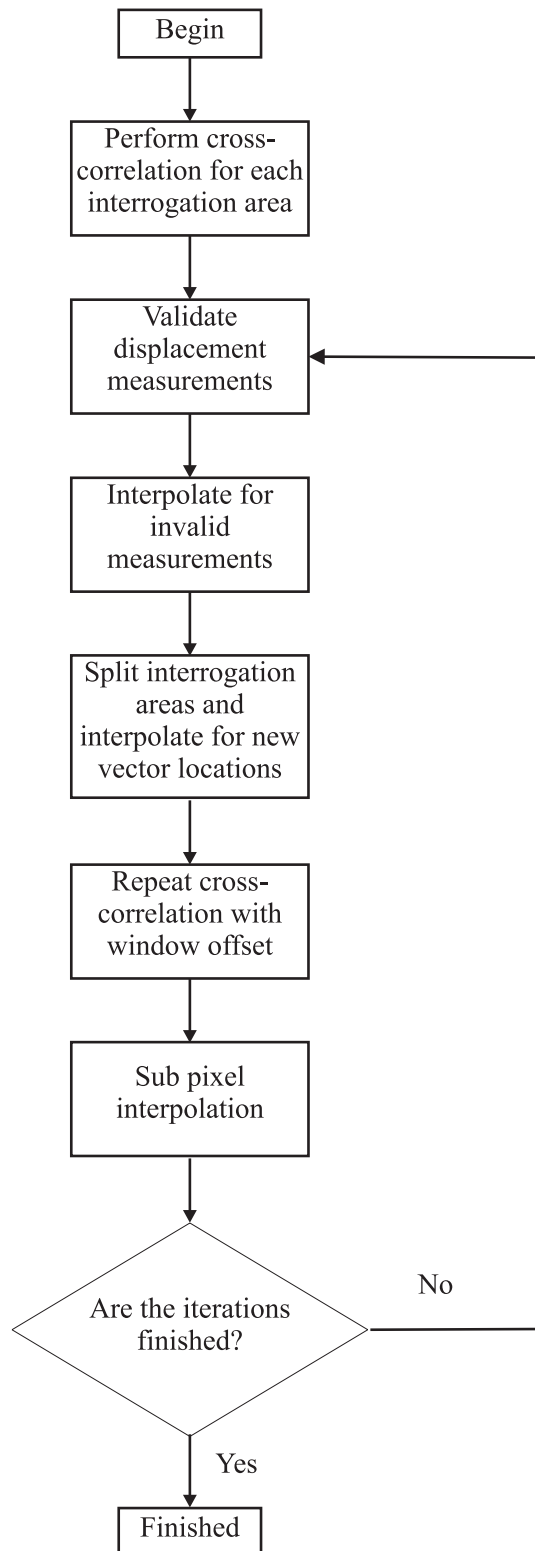
Figure 2.21: Super resolution FFT algorithm [49]

method was designed to reduce the error due to velocity gradients within an interrogation area [49], the methodology still relies upon the measurement of pure translation.

Methods that reconstruct the interrogation area to account for stretch and rotation have been proposed by Huang *et al.* [46, 50], Ashforth-Frost *et al.* [51], Jambunathan *et al.* [52] and Weng *et al.* [53]. The method is called *interrogation area deformation PIV*, hereafter referred to as deformed FFT, and an algorithm is shown in Figure 2.22.

If the displacement vectors of each particle $(\Delta x, \Delta y)$ are known, it is possible to determine the particle positions in the second image from the first image by [52]:

$$x_2 = x_1 + \Delta x \quad , \quad y_2 = y_1 + \Delta y \tag{2.18}$$

where (x_1, y_1) is the position of a particle in the first image, at time t and (x_2, y_2) is the position of the same particle in the second image, at time $t + \Delta t$. The images are digitized so a particle image is represented by the pixel's grey level distribution, *i.e.* $I_1(x_1, y_1, t)$ for image 1 and $I_2(x_2, y_2, t + \Delta t)$ for image 2.

A new image $2'$ can be created using the particle positions in image 2 and subtracting the displacement vectors, $(\Delta x, \Delta y)$.

$$I_{2'}(x_2 - \Delta x, y_2 - \Delta y, (t + \Delta t) - \Delta t) \tag{2.19}$$

The cross-correlation is then performed between images 1 and $2'$. If the displacement vectors are correct, image $2'$ will be identical to image 1 and the cross-correlation will measure zero particle motion, which is the displacement where the cross-correlation technique is the most accurate. As well, there are no longer any velocity gradients within the interrogation area since they have been *subtracted*, *i.e.* removed. Thus the assumption of uniform flow within an interrogation area used for the cross-correlation becomes valid.

Rather than identifying individual particles, each pixel within the image can be treated as a displaced particle. Since the image is discrete, each particle location in image 2 is an integer value but Δx and Δy are usually non-integer values. Therefore interpolation is used to determine the grey-level intensity of the image $2'$.
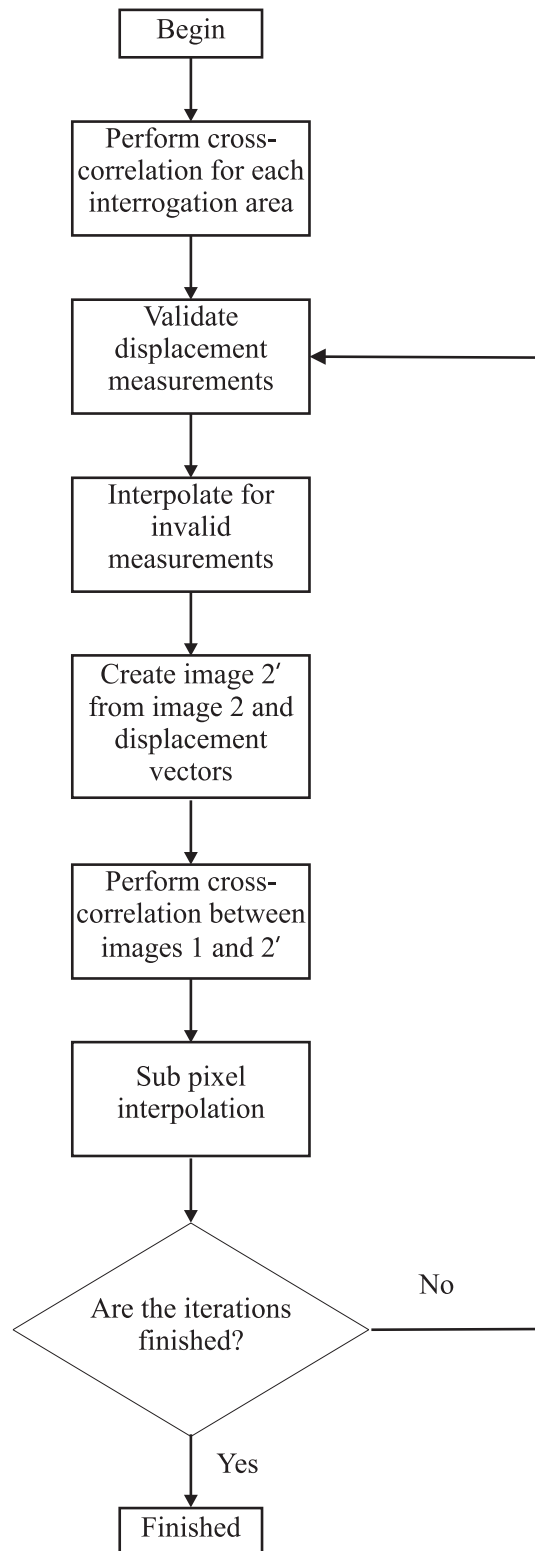
Figure 2.22: Interrogation area deformation algorithm [52]

Similar to the predictor corrector FFT and super resolution FFT methods the displacement vectors are unknown but can be estimated with the standard FFT technique and then validated. This will create a field with a displacement vector located at the centre of each interrogation area. To determine the displacement vector of each pixel that is not at the centre of an interrogation area, interpolation of the displacement field is performed.

If the displacement vectors are not exact, *i.e.* the magnitude of the displacement peak in the correlation plane is below unity, the procedure can be iteratively repeated using the previous measurement for the displacement vectors. In the case where the magnitude of the displacement peak never reaches unity, the procedure is stopped when the magnitude of the displacement peak does not increase from the previous iteration.

Chapter 3

Implementation of FFT Cross-Correlation Strategies

3.1   Introduction

Chapter 2 described the four FFT based cross-correlation algorithms evaluated; standard FFT, predictor corrector FFT, super resolution FFT and deformed FFT. This chapter describes the implementation of the cross-correlation along with how the peaks within the correlation plane were determined. Also, the super resolution FFT and deformed FFT were implemented slightly differently than described in Chapter 2. The rationale behind these differences is discussed in turn.

3.2   Constructing the Correlation Plane

Section 2.3 described how the cross-correlation method is used to determine the displacement of a group of particles within an interrogation area. A Visual C++ program was created to implement the four cross-correlation algorithms. Each of the four methods evaluated differ in

how the interrogation areas are constructed, but they all apply the cross-correlation similarly. That is, in all of the examined cross-correlation strategies, an FFT algorithm is employed to produce the cross-correlation plane [54].

For each of the algorithms, the correlation plane was determined using the procedure shown in Section 2.3 and values were normalised between 0 and 1. The normalisation of a cross-correlation calculated with an FFT is similar to that of the spatial cross-correlation described in Equation 2.6. The cross-correlation [ϕ_{fg}] was normalised by dividing each value by the geometric average of the self-correlations [ϕ_{ff}, ϕ_{gg}] for each interrogation area at zero displacement, as shown in Equation 3.1.

$$\phi_{fg} = \frac{\phi_{fg}}{\sqrt{\phi_{ff}}\sqrt{\phi_{gg}}} \tag{3.1}$$

3.3 Locating the Peaks Within the Correlation Plane

Depending on the contrast between the particles and the background within the image, the difference in magnitude between the displacement peak and noise peaks may be very small on the cross-correlation plane, even though the maximum correlation may be close to 1. Due to this relatively high *noise floor*, the ratio of the maximum peak to the largest noise peak will be very small. The small ratio between peaks will not affect the location of the displacement peak, but may influence the results if peak validation is employed. In an attempt to alleviate this problem, the noise floor was removed by subtracting the lowest value within the correlation plane from every value. The correlation plane was then multiplied by a factor to *stretch* the maximum peak such that its maximum height was the same as before the noise floor was removed.

After the correlation plane was normalised, the first and second largest peaks were found, presumably the displacement peak and largest noise peak, respectively. Finding the maximum value was easily done but generally the second highest value was found next to the maximum value, *i.e.* it was part of the same peak. To ensure that the peaks were independent, the second largest peak must have been greater than two pixels away from the maximum peak.

3.4 Super Resolution FFT

The super resolution FFT implemented in the Visual C++ program was slightly different than that described in Section 2.6.2. When moving to smaller interrogation areas, Scarano and Riethmuller [49] would use the closest displacement vector to the center of the new interrogation area for the integer offset. In the Visual C++ program, the vector used for the interrogation area offset was determined using a bi-linear interpolation of the surrounding displacement vectors determined from the previous iteration, providing a better estimate for the interrogation area offset.

3.5 Deformed FFT

The deformed FFT method was applied by warping one of the interrogation areas such that the cross-correlation ideally only measured pure translation, *i.e.* the particles within the interrogation area move with a uniform motion between images. The amount of the deformation was determined by the displacement measurements from the previous iteration. Since every pixel does not contain a displacement vector, bi-linear interpolation was used where there was no displacement information. Often, deforming the interrogation area resulted in moving a pixel by a non-integer amount, *i.e.* the new location existed between pixels. To determine the grey level intensity for the displaced pixel, bi-linear interpolation was used.

Some methods described in Section 2.6.3 used the magnitude of the correlation to determine the number of iterations required. Presumably, the greater the magnitude of the displacement peak in the correlation plane, the greater the number of particles that were correlated, thus the accuracy of the displacement vector field used to deform the interrogation area would improve the accuracy of the displacement estimate. Therefore, as long as the magnitude of the correlation was increasing, the procedure was repeated. This criteria for the number of iterations was not included in the Visual C++ program. Rather, a fixed number of iterations (determined by the user) was applied, regardless of the change in magnitude of the displacement peak between iterations.

Chapter 4

Synthetic Image Generation

4.1 Introduction

When evaluating the different cross-correlation algorithms, the amount of error introduced to the measurements due to the cross-correlation analysis is an important factor. One way of examining the error is through the creation of synthetic images where the exact displacement of the particles between images is known. This chapter discusses the creation of synthetic images used to ascertain the bias and random errors for the different cross-correlation algorithms analysed.

The exact velocity of the fluid in an experimental flow is generally unknown. Other measurement techniques can be employed to compare against the results obtained with PIV but these results would also contain some amount of experimental error, so accurately determining the error of the PIV measurements would be impossible.

Synthetic images were created where the exact displacement of the particles was known. Therefore, the amount of bias in the measurement can be found with Equation 2.10. As well, experimental flows contain transient effects, such as turbulence, which will cause the flow to fluctuate about a mean value. This will increase the value of the RMS making it difficult to determine the size of the random error. The synthetic images were created without a fluctuating velocity

component so an RMS value in the results greater than zero resulted only from the random error of the measurement technique.

4.2   Synthetic Image Generation Algorithm - Overview

The synthetic images were created using a MATLAB [55] program written at the University of Waterloo by Chad Young [56]. The images created were 8-bit Tagged Image File Format (TIFF), *i.e.* the pixel intensities ranged from 0 to 255. The computer program used to generate the synthetic images allowed different image parameters to be controlled: particle size, particle number density, background noise, contrast between the background and the particle. Different flow conditions: translation, rotation, shear, or different combinations, could also be implemented with the advantage that the displacement of the particles is known exactly. The algorithm employed to generate the synthetic images is shown in Figure 4.1.

The first step in the synthetic image generation program was to create an image that was *seeded* with particles. The program allows control of the particle number density, the size of the particles and their intensity. Table 4.1 shows the values of the parameters used to generate the synthetic images.

After the initial image had been created, the displacement of each pixel was calculated based on

Parameter	Value
Particle density (number of particles within a 32x32 pixel area)	4, 7, 11, 15, 20
Mean particle diameter (pixels) $[d_{mean}]$	2, 3, 4, 5, 6, 8, 10
Fluctuation of particle diameter (pixels) $[d_{fluct}]$	0.5
Mean particle intensity (counts) $[I_{mean}]$	200
Fluctuation of particle intensity (counts) $[I_{fluct}]$	10
Background noise (counts)	0
Image size (pixels)	480x480

Table 4.1: Parameters used for synthetic image generation

the applied displacement function to determine its new position. For some of the displacement functions, the particle displacement was dependent on the particles location within the image, therefore the motion of the particles was determined incrementally, for all the images. One-hundred steps were used to displace the particles from their initial positions in image 1 to their final positions in image 2. If a particle moved off the image during the incremental motion, it was discarded without creating a new particle. After one-hundred steps, an image was created showing the final positions of the particles. Figure 4.2 shows a typical synthetic image with a particle density of 11 particles per 32x32 pixel area and a mean particle diameter of 10 pixels. Comparing Figure 4.2 to Figure 1.2, the computer generated image more closely resembles images captured during an experiment using water as the fluid medium than air.

4.2.1   Particle Number Density

The particle number density is defined as the number of particles within a 32x32 pixel area rather than the total number of particles within the entire image. This prevented a region of the image from having a high local particle density. Although the particle number density may vary greatly throughout an experimentally recorded image where seeding the flow may be difficult, quantifying the impact of the particle number density with respect to the cross-correlation algorithms would be arduous. To quantify the influence that the particle number density has on the different cross-correlation routines, five different particle number densities were examined ranging from 4 to 20 particles within a 32x32 pixel area. These values are typical in a water based experiment [39].

4.2.2   Particle Size

The particle itself was represented with a 2-D Gaussian profile, and had a mean diameter that was equal in the two directions. The mean particle diameter was defined as four times the standard deviation of the distribution. However, as typical for most seed particles used in experiments, the synthetic particle diameter, d_p, was programmed to fluctuate about the mean particle diameter, d_{mean}, as a function of the parameter *fluctuation of particle diameter*, d_{fluct}, and a random

number, $randn$, which had a mean of 0 and standard deviation of 1.

$$d_p = d_{mean} + d_{fluct} \cdot randn \qquad (4.1)$$

The program also allowed the fluctuation to vary independently in both principle axes. This created seed particles that were non-circular and varied in both shape and size, as shown in Figure 4.3. To quantify the influence of the mean particle size on the different cross-correlation routines, seven different mean particle sizes were examined ranging from 2 to 10 pixels in diameter.

4.2.3 Particle Intensity

The maximum intensity of the synthetic particle, I_p, occured at the particle centre. Similar to seed particles used in experiments, the intensity varied between particles about a mean value, I_{mean}. For the synthetic images, individual particle intensity fluctuated as a function of the *fluctuation of the particle intensity*, I_{fluct}, and a random number, $randn$, which had a mean of 0 and standard deviation of 1.

$$I_p = I_{mean} + I_{fluct} \cdot randn \qquad (4.2)$$

Since it was possible to create a particle with an intensity greater than 255 counts (the upper limit of an 8 bit image), the image was normalised such that the brightest pixel was 255 counts.

A continuous 2-D Gaussian distribution was used to represent the intensity distribution for each synthetic particle, but the particles shown in Figure 4.3 appear as discrete values. This was due to the discrete pixel locations in the image. To determine the intensity of each pixel, the Gaussian function was integrated over the pixel area to determine the average value for the pixel. Figure 4.3 also shows particles that occlude or overlap, which is common for experimental flows. Instead of adding the intensities of the particles that overlap, the brighter pixel intensity was used. As such, the brighter and/or bigger particles always appeared in front of the smaller and/or dimmer particles.

4.3   Displacement Functions

After the initial image was created at $t = 0$, the synthetic particles were *moved* via a displacement function. To evaluate the different flow mechanisms, six different displacement functions were employed. They are shown in Table 4.2; uniform translation, step, sawtooth, sinusoid, vortex and source.

4.3.1   Uniform Translation Images

In the uniform translation, particles in the image were displaced by pure translation of equal magnitude in the horizontal (x) and vertical (y) directions.

$$u = \text{constant}, \quad v = \text{constant} \tag{4.3}$$

Since the displacement was independent of position, every particle undergoes the same displacement and there was no displacement gradient anywhere in the image.

$$\frac{\partial u}{\partial x} = 0, \quad \frac{\partial u}{\partial y} = 0 \tag{4.4}$$

$$\frac{\partial v}{\partial x} = 0, \quad \frac{\partial v}{\partial y} = 0 \tag{4.5}$$

4.3.2   Step, Sawtooth and Sinusoid Images

The particle displacement functions in the step, sawtooth and the sinusoid images were applied only as functions in the x-direction, *i.e.* the displacement was constant in the y-direction.

$$u = 0, \quad v = f(x) \tag{4.6}$$

Therefore displacement gradients existed in the form of a shear in the x-direction only.

$$\frac{\partial u}{\partial x} = 0, \quad \frac{\partial u}{\partial y} = 0 \tag{4.7}$$

$$\frac{\partial v}{\partial x} = g(x), \quad \frac{\partial v}{\partial y} = 0 \tag{4.8}$$
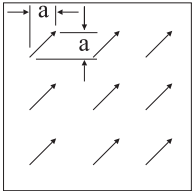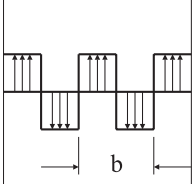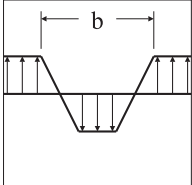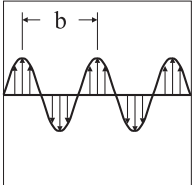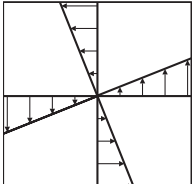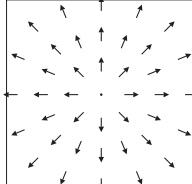
Displacement Function		Description
Uniform translation		Uniform translation of each particle by 'a' pixels in both directions
Step displacement profile		Infinite displacement gradient. Maximum displacement is 2a and period b.
Sawtooth displacement profile		Finite displacement gradient. Maximum displacement is 2a and period b.
Sinusoid displacement profile		Sinusoidal function with amplitude a and period b
Vortex displacement profile		Line vortex about the centre of the image. Displacement of 'a' pixels at the edges of the image.
Source displacement profile		Line source emanating from the centre of the image.

Table 4.2: Different displacement functions examined

where $g(x)$ depended on the displacement function. The step and sawtooth contained infinite and constant displacement gradients, respectively, between regions of zero displacement gradient. The displacement gradient varied throughout the sinusoid images since the displacement profile was in the shape of a sine wave.

4.3.3 Vortex and Source Images

The vortex displacement function was generated using a *free* vortex of vorticity ω and rotated about the centre of the image, such that:

$$u = \omega y, \quad v = -\omega x \tag{4.9}$$

$$\frac{\partial u}{\partial x} = 0, \quad \frac{\partial u}{\partial y} = \omega \tag{4.10}$$

$$\frac{\partial v}{\partial x} = -\omega, \quad \frac{\partial v}{\partial y} = 0 \tag{4.11}$$

The source displacement function was that for a line source at the centre of the image with a source strength, m, or:

$$u = m\frac{x}{\sqrt{x^2 + y^2}}, \quad v = m\frac{y}{\sqrt{x^2 + y^2}} \tag{4.12}$$

$$\frac{\partial u}{\partial x} = \frac{m}{\sqrt{x^2 + y^2}} - \frac{mx^2}{(x^2 + y^2)^{3/2}}, \quad \frac{\partial u}{\partial y} = -\frac{mxy}{(x^2 + y^2)^{3/2}} \tag{4.13}$$

$$\frac{\partial v}{\partial x} = -\frac{mxy}{(x^2 + y^2)^{3/2}}, \quad \frac{\partial v}{\partial y} = \frac{m}{\sqrt{x^2 + y^2}} - \frac{my^2}{(x^2 + y^2)^{3/2}} \tag{4.14}$$

Unlike the step, sawtooth and sinusoid displacement functions, the displacements in the vortex and source images were functions of both x and y, so displacement gradients existed in both directions.

4.4 PIV Errors and the Synthetic Images

The synthetic images were created using the computer program described in Section 4.2 specifying the parameters as shown in Table 4.1 [56]. The control of these parameters allows some of the

errors that exist in images collected during experiments to be eliminated. The synthetic images were not recorded with a camera so any error due to the particles imaging onto a medium (film or a CCD array) could be neglected. The particles follow the flow exactly so there was no tracking error. The effect of the background noise could also be ignored since the background was set to 0 for the synthetic images. Also, the displacement of the particles was specified so the displacement normal to the image was set to 0, eliminating any error from loss-of-pairs due to out of plane motion, as well as the error from parallax effects. The only errors that still existed in the synthetic images were those caused by the sub-pixel interpolation and displacement gradients.

4.4.1 Displacement versus Velocity

Although all the flows evaluated were steady, individual particles accelerated between images for the vortex and source displacement functions since the displacement vector was a function of position. However, in analysing the PIV results one must take care to separate the errors associated in estimating the displacement of particles and the errors associated with the calculation of the velocity via Equation 2.1. In the analysis of the synthetic images, only the errors associated with the displacement measurements are directly analysed. The uncertainty of the velocity measurement caused by the first order approximation in Equation 2.1 is left to future work. As such, the error due to acceleration could be neglected since the particle displacement was considered instead of the particle velocity.

Create image 1 (controlling parameters for particle density, particle size and particle intensity)

Calculate the displacement at each pixel location based on the type of flow (vortex, source, linear, step, sawtooth, sinusoid)

Determine the new position of each pixel

Has the 100 steps occured

Yes

Create image 2 with the new seed positions

No

Increment the time step
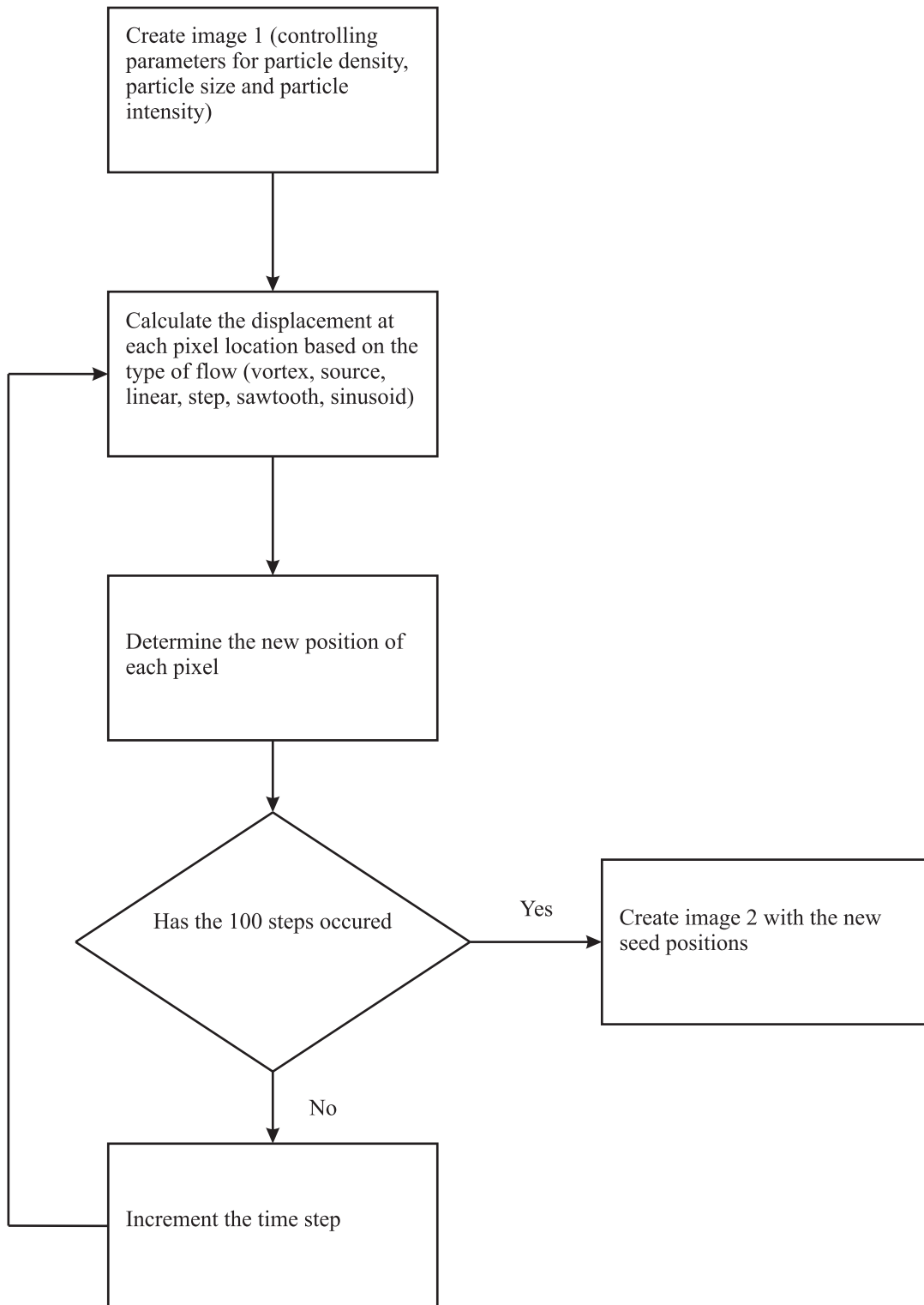
Figure 4.1: Synthetic image generation algorithm
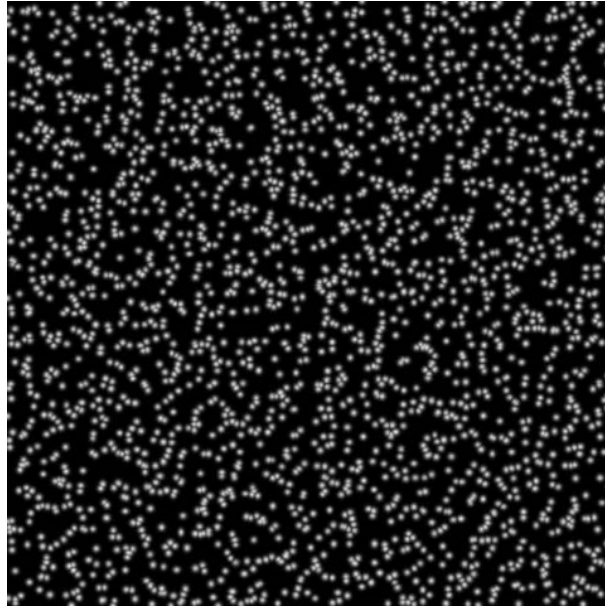
Figure 4.2: Typical synthetic image with particle number density of 11 particles per 32x32 pixel area and a mean particle diameter $[d_{mean}]$ of 10 pixels, 480x480 pixel image size
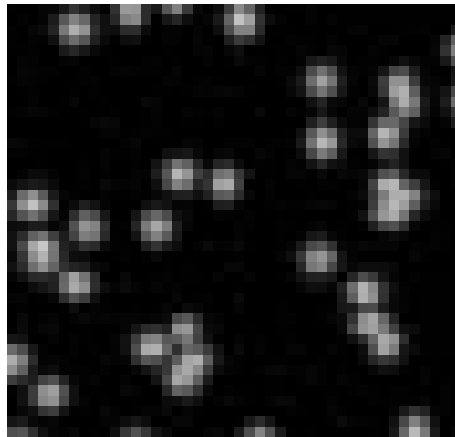
Figure 4.3: Typical synthetic particles with a mean particle diameter $[d_{mean}]$ of 6 pixels and a particle number density of 15 particles per 32x32 pixel area

Chapter 5

Synthetic Image Analysis

5.1   Introduction

Synthetic images were created using the techniques described in Chapter 4 and were evaluated with the four FFT based displacement measurement algorithms discussed in Chapters 2 and 3. Synthetic images were used to compare particle displacements estimated using the different cross-correlation algorithms since the exact particle displacements were known. Furthermore, the use of synthetic images allowed certain sources of error to be isolated and other sources of error to be removed entirely, as discussed in Chapter 4.

This chapter will discuss the criteria used to compare the four methods evaluated, followed by the results. The results have been divided into three sections based on the motion of the particles within the synthetic images. In the first section, the results from the uniform translation images are detailed along with a comparison of two sub-pixel interpolation schemes. The next section compares the results from the images generated using the step, sawtooth and sinusoid displacement functions, which contained displacement gradients only in the horizontal direction. The third section presents the results from the images generated using the source and the vortex displacement functions, used to assess the effect of displacement gradients in both the vertical

and horizontal directions. A short summary of the synthetic results is provided at the end of each section.

5.2 Comparison Methods

Before the results from the synthetic images are presented, the standards with which the cross-correlation algorithms were evaluated must be considered. The criteria used to assess each cross-correlation strategy were as follows:

1. spatial resolution (density of the vectors in the resulting displacement field)

2. dynamic range (range of displacements that are detected)

3. accuracy (error relative to the exact displacement)

4. robustness (number of valid measurements)

The importance of each criterion will be discussed in turn below.

5.2.1 Spatial Resolution

The number of displacement vectors contained within the vector field produced by the cross-correlation method is defined here as the spatial resolution. When the spacing between vectors is smaller, *i.e.* a higher spatial resolution, more details of a flow field can be determined, such as smaller turbulent length scales. One way to *artifically* increase the spatial resolution is by increasing the interrogation area overlap. Interrogation overlap refers to the amount by which the neighbouring interrogation areas overlap. Figure 5.1 shows an interrogation overlap of 50% in the horizontal direction and 75% in the vertical direction. The interrogation area overlap could be such that there is a displacement vector for each pixel. However, when interrogation area overlap is used, the displacement vectors are no longer independent. This may cause the same displacement vector to be measured in neighbouring interrogation areas. To prevent this
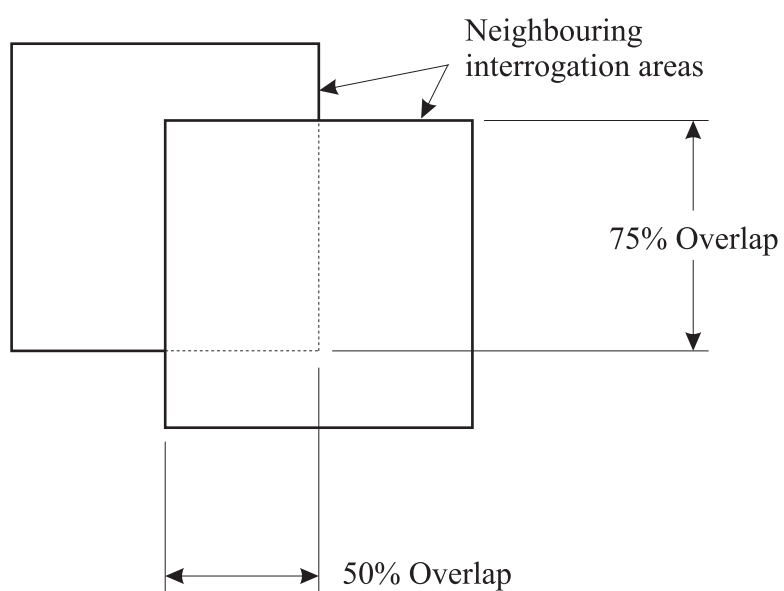
Figure 5.1: Example of interrogation area overlap - 50% in the horizontal direction, 75% in the vertical direction

from happening the largest interrogation area overlap used was 75%, which is typical for most experiments. Therefore it was important to determine if the increased spatial resolution was a result of a higher interrogation area overlap or a result of the method applied. This was achieved by using the same interrogation area overlap wherever possible.

5.2.2 Dynamic Range

Dynamic range refers to the range of displacements the technique is capable of measuring, *i.e.* the minimum and maximum displacements that can be measured. This is important for flows that consist of large displacement gradients. A method that is capable of measuring a large range of displacements is more versatile, since it is able to measure the entire flow field with the same algorithm. However, for flows with uniform or near-uniform displacements a cross-correlation method with a large dynamic range may not be necessary, especially if it has other limitations, such as accuracy.

5.2.3 Accuracy

The accuracy of each method will be determined by comparing the total error and wherever possible the mean bias and random error. The total error is defined as the difference between the measurement and the actual displacement for a single vector.

$$total\ error = U_{measured} - U_{actual} \tag{5.1}$$

The mean bias error is the average difference between all the measurements from the actual displacement.

$$mean\ bias\ error = \overline{U_{measured} - U_{actual}} \tag{5.2}$$

Since the applied particle displacements do not fluctuate about a mean value the random error is the RMS of A measured data points.

$$random\ error = \frac{1}{A} \sqrt{\sum_{i=0}^{A} (U_i - \bar{U})^2} \tag{5.3}$$

For the source and vortex cases the mean bias and RMS errors could not be determined. Therefore, the 10th, 50th and 90th percentiles of the total error were compared to evaluate the accuracy of the different cross-correlation methods.

5.2.4   Robustness

Robustness refers to the ability of the cross-correlation algorithm to produce the *correct* displacement peak as the maximum peak in the correlation plane, regardless of the measurement accuracy. The displacement vectors were determined to be correct by applying the validation strategies described in Section 2.3.2. By comparing the number of displacement vectors that were discarded by the validation strategies, the robustness of each method could be evaluated. The more vectors that passed the validation limits, the more robust the method. A robust cross-correlation method is important since a method that discards 90% of its data may not be advantageous.

5.3   Algorithm Parameters

Before discussing the results of the analysis for the synthetic images for the cross-correlation algorithms it is important to declare the values of the parameters for each of the four methods, *i.e.* the size of the interrogation area, number of iterations, the validation between iterations, *etc.* Table 5.1 shows the values used for the processing of the synthetic images for each of the four cross-correlation algorithms. In an effort to make equal comparisons, the parameters were held constant for the analysis of each of the images unless the effect of a specific parameter was being investigated.

To investigate the spatial resolution of the cross-correlation methods the interrogation area overlap used was the same for all the images evaluated. Since the displacements of the particles for the step, sawtooth and sinusoid images change in the horizontal direction only, a horizontal overlap of 75% and a vertical overlap of 0% was used to increase the resolution of the measurements in the desired direction. However, for the deformed FFT algorithm it was found that a high resolution of vectors was required in both directions to achieve reasonable results. Therefore, an

interrogation area overlap of 75% in both directions was applied for the deformed FFT method only.

The size of the interrogation area on the initial iteration was chosen to obey the *one-quarter rule* (Section 2.3). For the results shown below, unless otherwise stated, the size of the interrogation area for the standard FFT, predictor corrector FFT and the deformed FFT algorithm was 32x32 pixels. For the super resolution FFT algorithm a larger initial interrogation area of 64x64 pixels was used such that the final interrogation area would not be too small. Using a factor of 2 to reduce the size of the interrogation area and three iterations, the final interrogation area size for the super resolution FFT method was 16x16 pixels.

Each evaluated case contained two image pairs to increase the number of possible measurements, reducing the effect a single measurement would have on the overall conclusions. Therefore, the

Parameter	Standard FFT	Predictor Corrector FFT	Super Resolution FFT	Deformed FFT
Horizontal interrogation area overlap [%]	75	75	75	75
Vertical interrogation area overlap [%]	0	0	0	75
Sub-pixel interpolation	Gaussian	Gaussian	Gaussian	Gaussian
Number of iterations	1	4	3	4
Type of validation between iterations	-	Peak	Peak	Peak
Value of validation between iterations	-	1.3	1.3	1.3
Initial size of interrogation area	32x32	32x32	64x64	32x32
Super resolution factor	-	-	2	-
Type of validation of results	Peak	Peak	Peak	Peak
Value of validation of results	1.3	1.3	1.3	1.3

Table 5.1: Parameters used for each cross-correlation algorithm (unless otherwise specified)

results of both image pairs were included in the plots and all the calculations for the mean bias and RMS errors.

5.4 Uniform Linear Translation Images

The uniform linear translation images contain a uniform translation of the particles. The distance the particles moved between images ranged from 0 to 2.0 pixels in 0.1 pixel increments, with identical displacements in both the horizontal and vertical directions. Figure 5.2 shows the vector plot of particle displacements for an applied displacement of 2.0 pixels in both the horizontal and vertical directions.

As mentioned in Section 2.3, the cross-correlation assumes the particles move with a uniform motion. Since all the particles move with a uniform translation between images, the *best* possible
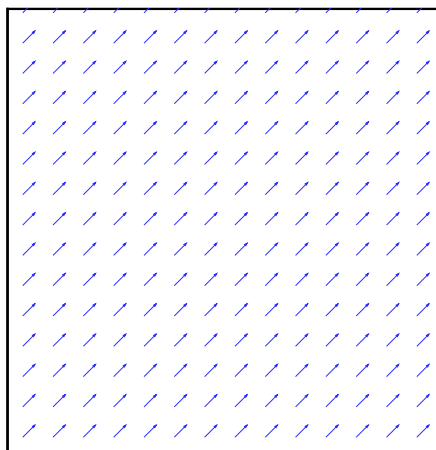
Figure 5.2: Vector plot for the linear translation images with a displacement of 2 pixels in each direction

estimate of the particle displacement, *i.e.* the least error, was made by each cross-correlation method for the uniform translation images. The error due to the choice of sub-pixel interpolation scheme could therefore be evaluated, since other sources of error, such as displacement gradients, were eliminated from the images.

5.4.1   Effect of Particle Number Density on Linear Translation Results

To investigate the effect the number of particles has on the accuracy of the results, five different particle number densities were evaluated for the linear translation case; 4, 7, 11, 15 and 20 particles within a 32x32 pixel area. For the linear translation images, the same displacement exists within each interrogation area. This allowed every vector within both image pairs to be ensemble averaged to determine the mean bias error according to Equation 5.2 as well as determine the RMS error according to Equation 5.3.

A contour plot of the mean bias error in pixels for each of the four cross-correlation methods is shown in Figure 5.3 as a function of the particle number density and the applied displacement, with a constant particle diameter of 2 pixels. For each cross-correlation method, when the particle displacement is greater than 0.5 pixels, the mean bias error shows a slight improvement as the particle number density increases up to 10 particles per 32x32 pixel area. Nevertheless, there appears to be very little change in the mean bias error with the particle number density as the contours are all nearly vertical.

However, the random error shows an improvement as the particle number density increases, as shown in Figure 5.4. For each cross-correlation method examined, the RMS error decreased as the particle number density increased. Since more particles contributed to the displacement peak, the peak became better defined within the cross-correlation plane. This resulted in an improvement of the sub-pixel interpolation accuracy, thus reducing the random error.

The only method which had an RMS error greater than 0.1 pixels, when there were more than 14 particles per 32x32 pixel area, was the super resolution FFT method. The reason for the higher error was the smaller number of particles used within a single interrogation area. The super resolution FFT method only uses a 16x16 interrogation area on the final iteration so the number
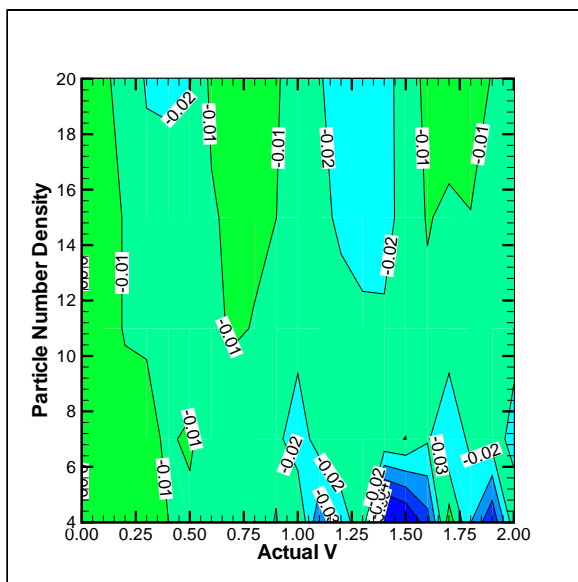
(a) Standard FFT
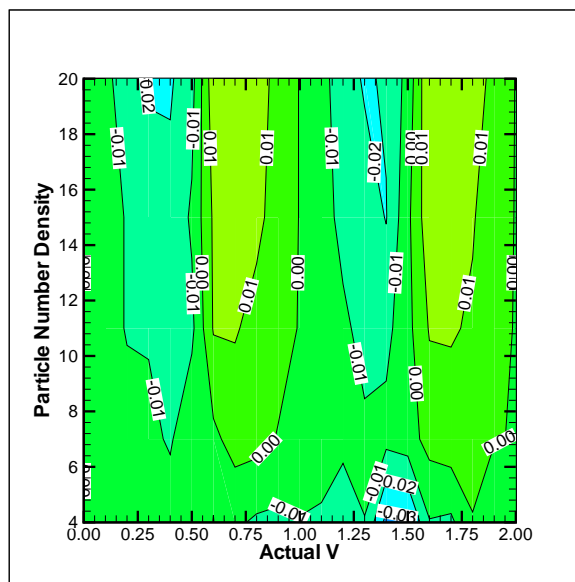
(b) Predictor Corrector FFT
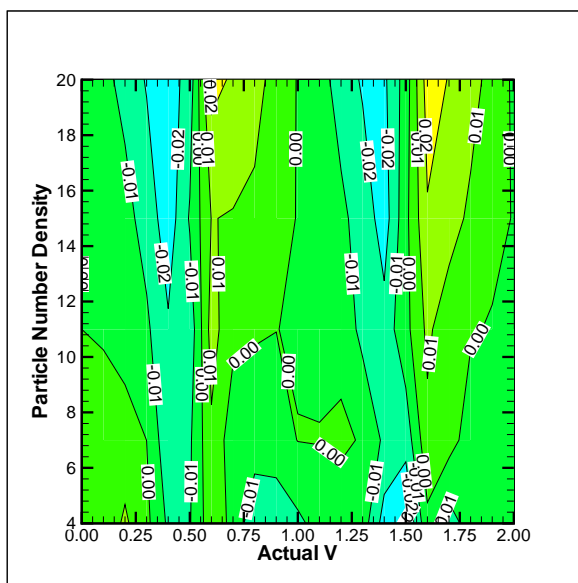
(c) Super Resolution FFT
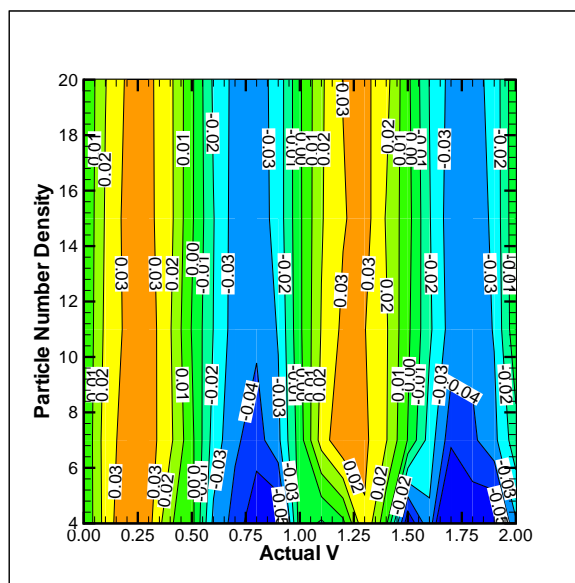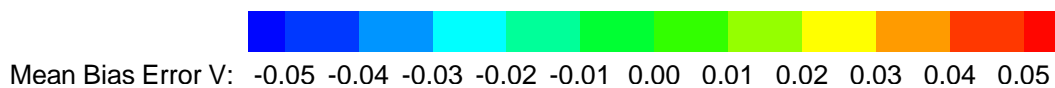
(d) Deformed FFT

Figure 5.3: Contour plot of mean bias error as a function of particle number density and displacement with a constant particle diameter of 2 pixels (a) Standard FFT (b) Predictor Corrector FFT (c) Super Resolution FFT (d) Deformed FFT
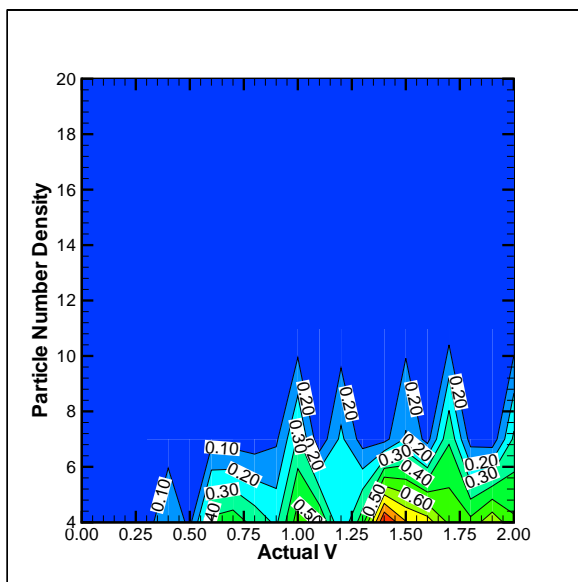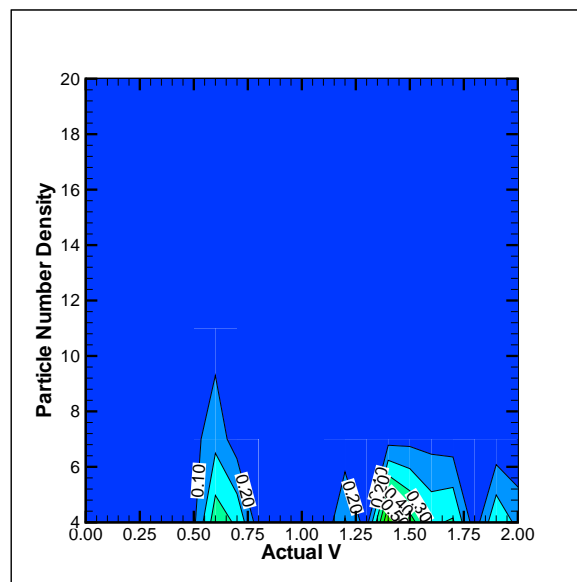
(a) Standard FFT

(b) Predictor Corrector FFT
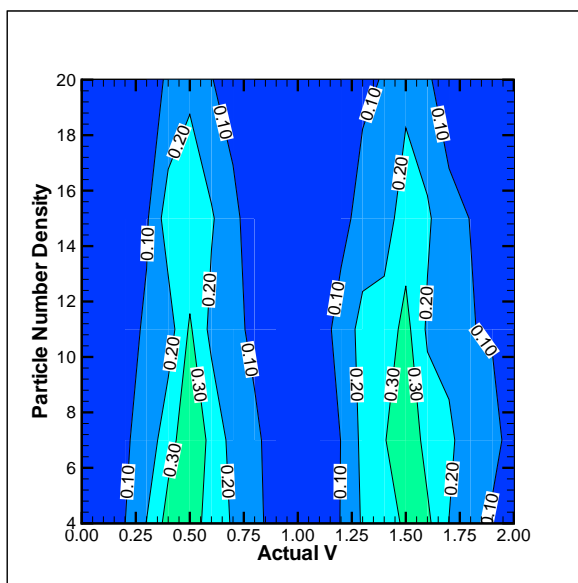
(c) Super Resolution FFT
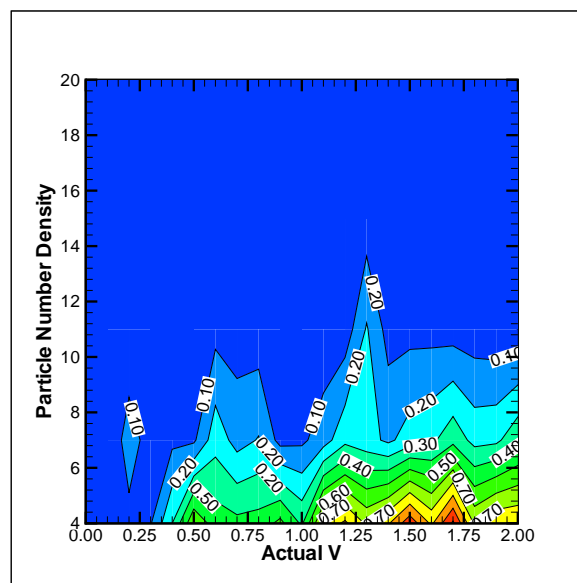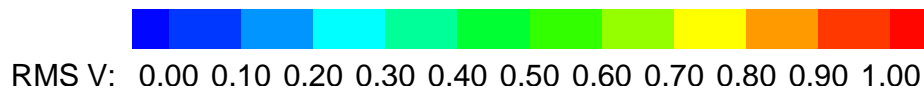
(d) Deformed FFT

Figure 5.4: Contour plot of the RMS error as a function of particle number density and displacement with a constant particle diameter of 2 pixels (a) Standard FFT (b) Predictor Corrector FFT (c) Super Resolution FFT (d) Deformed FFT

of particles within an interrogation area was only one-quarter of the particle number density. Therefore less particles were contributing to the displacement peak within the cross-correlation plane. This effect will be shown in greater detail later. Nonetheless, the super resolution FFT algorithm shows the same trend of improved results with increased particle number density as do the other three cross-correlation methods.

5.4.2 Effect of the Particle Diameter on the Linear Translation Results

To investigate the effect that particle size had on the accuracy of the different cross-correlation methods, seven different particle diameters were examined; 2, 3, 4, 5, 6, 8 and 10 pixels. Typical particle diameters in experiments range from 2 to 6 pixels. However, the particle size is usually determined by other factors, such as the type of seed particle, the area of interest being examined, illumination and focus.

Figure 5.5 shows a contour plot of the mean bias error as a function of the particle diameter and the applied displacement, with a constant particle number density of 20 particles per 32x32 pixel area. The mean bias error in the standard FFT method increased with the size of the particle except when the displacement between images was zero, which produced zero mean bias error. This is shown in Figure 5.5a with the dark blue contour in the upper half of the figure, signifying that the bias error was greater than -0.1 pixels.

The mean bias error for the predictor corrector FFT and super resolution FFT schemes is shown in Figures 5.5b and 5.5c, respectively. In both plots the range in the mean bias error increases as the particle size increases. This can be seen from the blue and green contours in Figure 5.5b above mean particle diameters of 6 pixels and in Figure 5.5c with the blue and red contours also above mean particle diameters of 6 pixels. Also seen in Figures 5.5b and c is the mean bias error switching from a negative to a positive value at half and full integer particle displacements. This phenomena will be discussed in further detail later.

Unlike the other three cross-correlation schemes, the mean bias error in the deformed FFT method decreased with larger particle diameters. This suggests that when the interrogation area was warped due to the displacement gradients, larger particles *deformed* better than the smaller
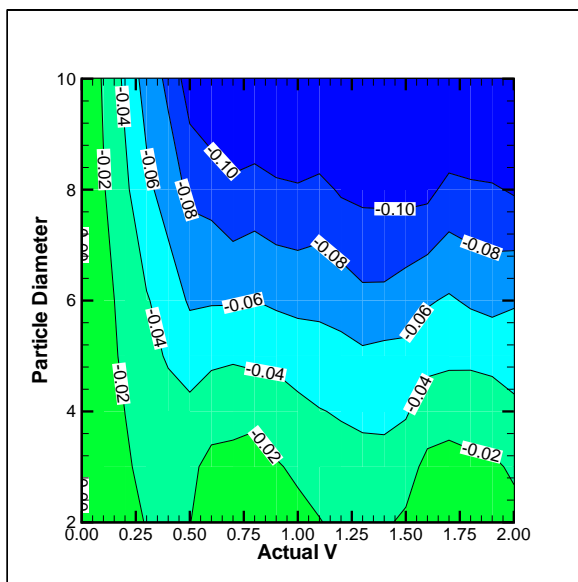
(a) Standard FFT
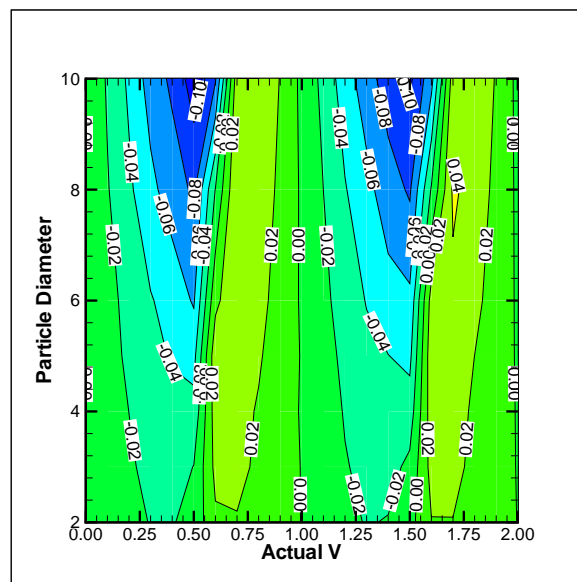
(b) Predictor Corrector FFT
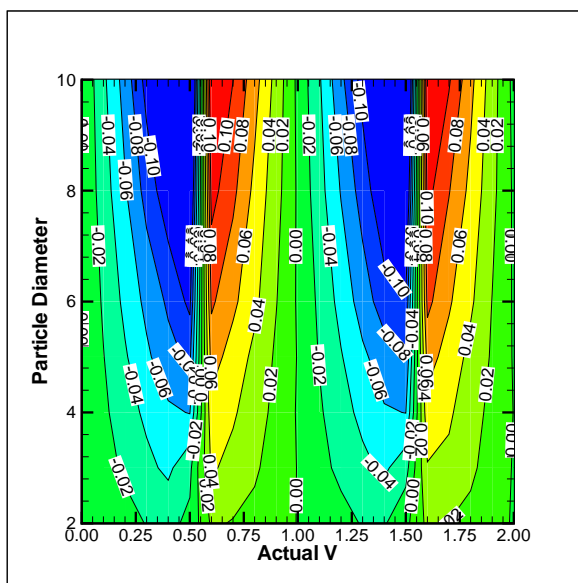
(c) Super Resolution FFT
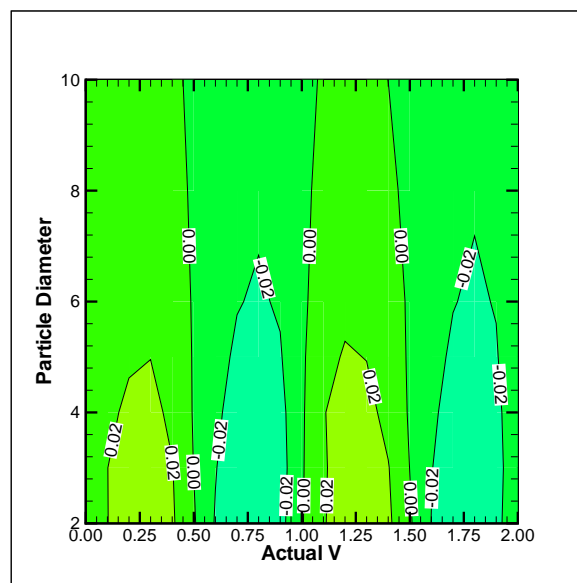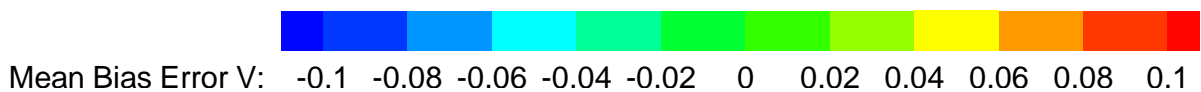
(d) Deformed FFT

Figure 5.5: Contour plot of mean bias error as a function of particle diameter and displacement (a) Standard FFT (b) Predictor Corrector FFT (c) Super Resolution FFT (d) Deformed FFT

particles. This may have been a result of the bi-linear interpolation required to create the new interrogation area.

Unlike the mean bias error, the RMS error followed the same trend for each of the four cross-correlation methods. Figure 5.6 is a contour plot of the RMS error as a function of the particle diameter and the particle displacement between images. For each cross-correlation method the RMS error was a minimum when the particle diameter was approximately 3 pixels, as evidenced by the increased blue contour in Figure 5.6 for a mean particle diameter of 3 pixels. This can be explained with the Gaussian sub-pixel interpolation scheme, which is a three point estimator as described in Section 2.3.1, used to approximate the displacement peak in the cross-correlation plane. With the larger particles, the peak was not as well defined by using only three points compared to the peaks created with the smaller particles, as shown in Figure 5.7. This suggests that the sub-pixel interpolation scheme should be based on the particle size. However, in practice this may be difficult due to the wide range of particle sizes usually found in an experimentally obtained image.

5.4.3   Robustness

Peak validation was applied to the data to remove any spurious vectors and to test the robustness of the four cross-correlation methods. Every vector was considered to be valid for each cross-correlation method. This was due to the simple uniform motion of the particles, which all contributed to the same peak in the correlation plane for the same applied displacement.

5.4.4   Parabola vs Gaussian Sub-Pixel Interpolation

In this section the errors produced with the parabolic and Gaussian sub-pixel estimators are discussed. Only the case with 15 particles per 32x32 pixel area and a particle diameter of 4 pixels is shown since the results are typical for all the other combinations in Table 4.1. This specific combination of the particle size and particle number density was chosen since it was close to the ideal combination. The ideal combination was a particle size of 3 pixels in diameter and a particle number density of 20 particles per 32x32 pixel area as was shown earlier.
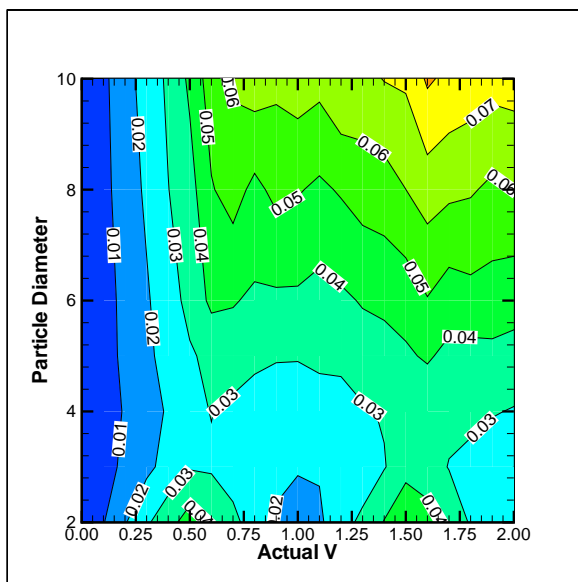
(a) Standard FFT
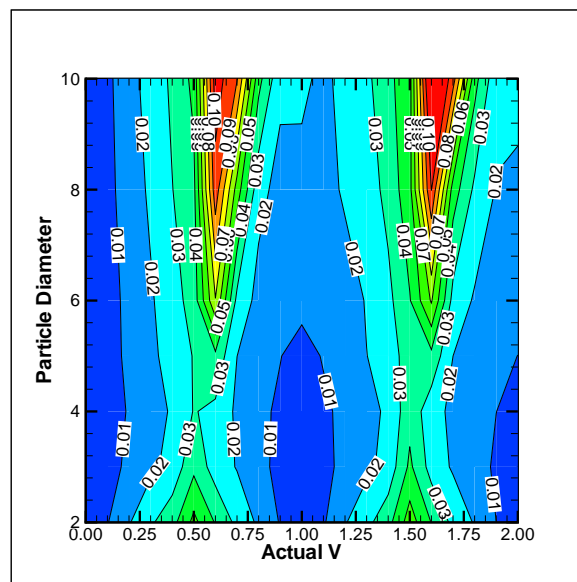
(b) Predictor Corrector FFT
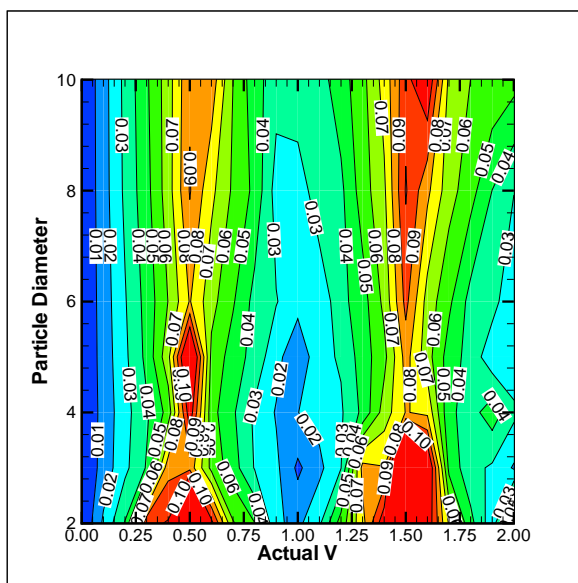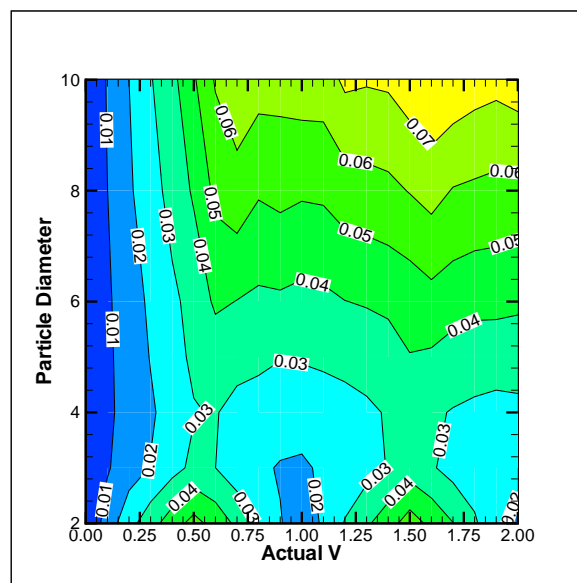
(c) Super Resolution FFT

(d) Deformed FFT

Figure 5.6: Contour plot of RMS error as a function of particle diameter and displacement (a) Standard FFT (b) Predictor Corrector FFT (c) Super Resolution FFT (d) Deformed FFT

(a)   (b)
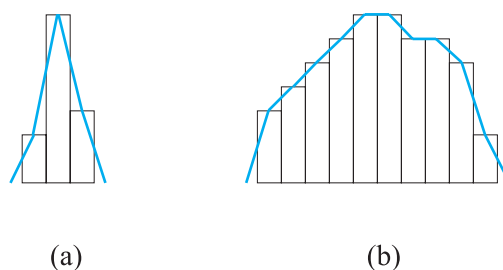
Figure 5.7: Three point estimator applied to a cross-correlation peak with a particle diameter of (a) 3 pixels (b) 10 pixels

The mean bias error and the RMS error are shown in Figure 5.8, as a function of the applied displacement for the standard FFT and predictor corrector FFT methods, using both the parabolic and Gaussian sub-pixel interpolation schemes. The same information is shown in Figure 5.9 for the super resolution FFT and deformed FFT methods.

From Figure 5.8 the oscillatory nature of the peak locking is evident for the standard FFT method. The oscillations are not about a constant value, rather about a line which decreases as the applied displacement increases for both the parabolic and Gaussian sub-pixel interpolation schemes.

Figure 5.8 also shows the RMS error for the parabolic and Gaussian sub-pixel interpolation schemes for the standard FFT method. The RMS error has local maxima at half integer displacements, which shows that both sub-pixel interpolation methods are susceptible to peak locking. The Gaussian sub-pixel interpolation scheme is the more accurate of the two methods with a maximum mean bias error of approximately 0.05 pixels compared to the 0.075 pixels with the parabolic method. This is not surprising since the synthetic particles were generated having a Gaussian particle intensity distribution since, as discussed in Section 2.3.1, particles typically used in experiments have been shown to have a Gaussian intensity distribution [57].

Graphs (c) and (d) of Figure 5.8 show the mean bias error and RMS error for the predictor corrector FFT algorithm using the parabolic and Gaussian sub-pixel interpolations, respectively. The results are similar to those obtained using the standard FFT algorithm since the error increases until a particle displacement of 0.5 pixels. Then, unlike the standard FFT method, the
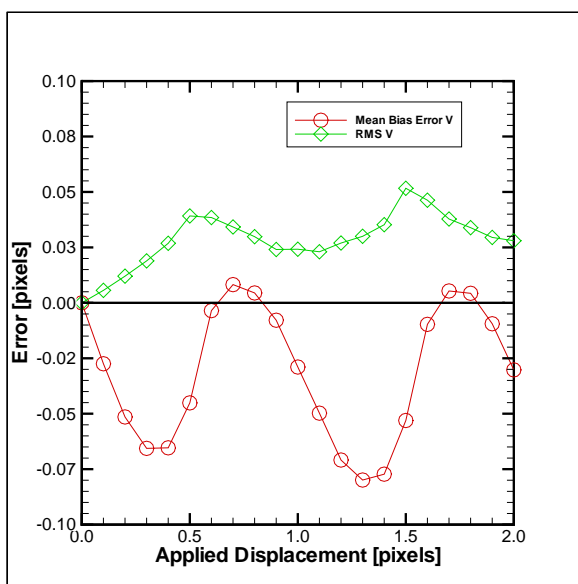
(a) Standard FFT with parabolic interpolation
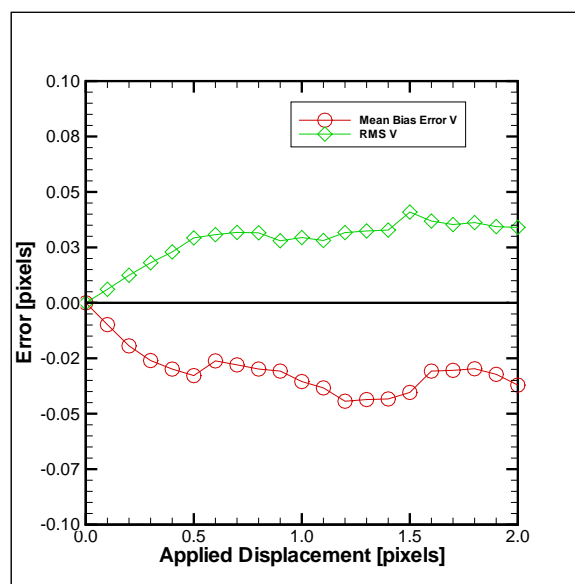
(b) Standard FFT with Gaussian interpolation
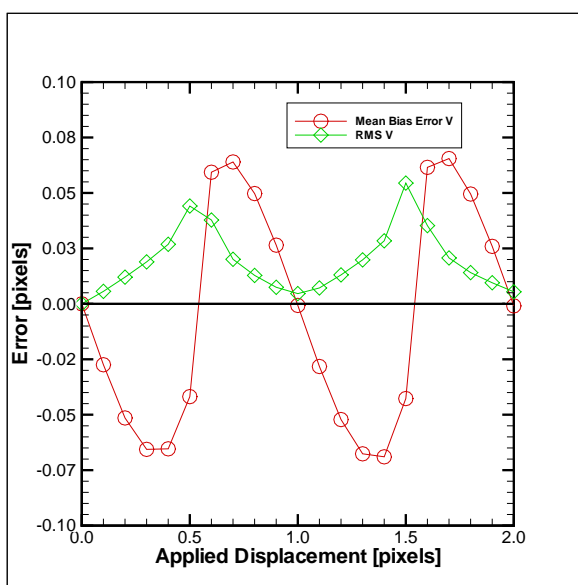
(c) Predictor Corrector FFT with
parabolic interpolation
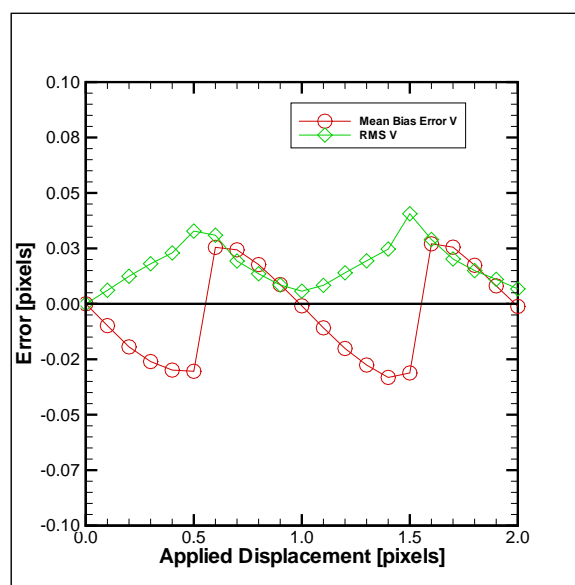
(d) Predictor Corrector FFT with
Gaussian interpolation

Figure 5.8: Mean bias error and RMS error as a function of applied displacement with 15 particles per 32x32 pixel area and a particle size of 4 pixels in diameter a) Standard FFT with parabola sub-pixel estimator b) Standard FFT with Gaussian sub-pixel estimator c) Predictor corrector FFT with parabola sub-pixel estimator d) Predictor corrector FFT with Gaussian sub-pixel estimator
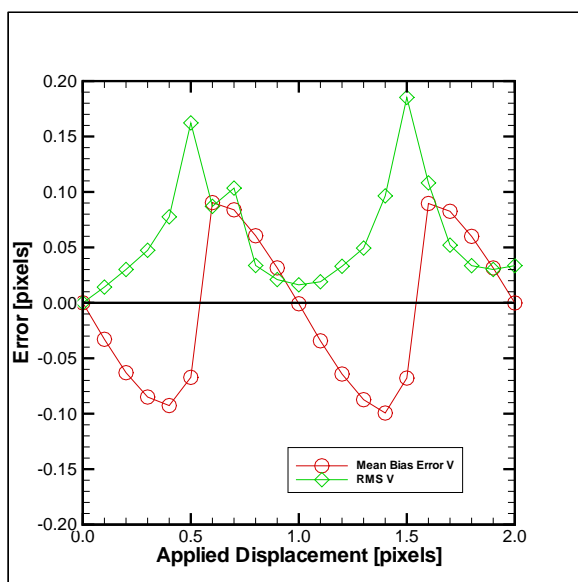
(a) Super Resolution FFT with
parabolic interpolation
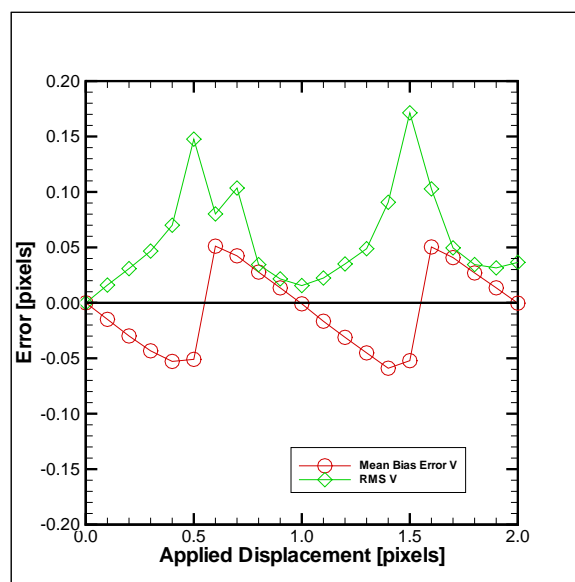
(b) Super Resolution FFT with
Gaussian interpolation
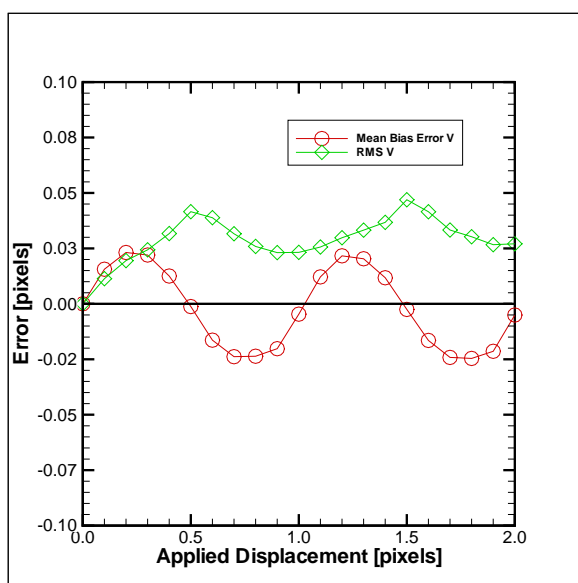
(c) Deformed FFT with parabolic interpolation
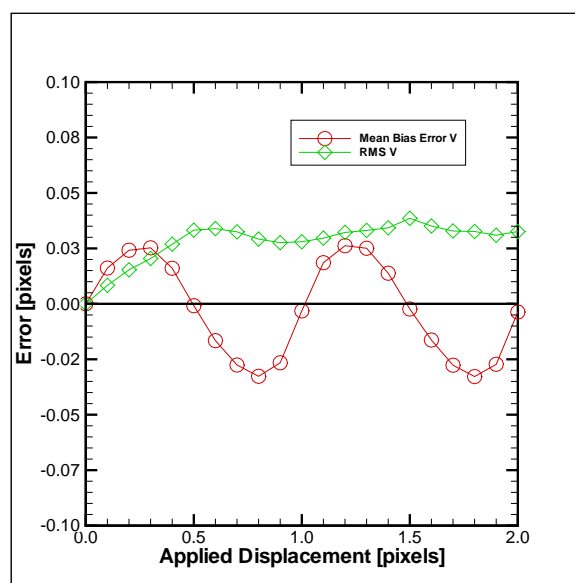
(d) Deformed FFT with Gaussian interpolation

Figure 5.9: Mean bias error and RMS error as a function of applied displacement with 15 particles per 32x32 pixel area and a particle size of 4 pixels in diameter a) Super resolution FFT with parabola sub-pixel estimator b) Super resolution FFT with Gaussian sub-pixel estimator c) Deformed FFT with parabola sub-pixel estimator d) Deformed FFT with Gaussian sub-pixel estimator

sign of the mean bias error switches, *i.e.* the method goes from under predicting the particle displacement to over predicting the particle displacement. This is due to the integer offset used by the predictor corrector FFT method. When the estimated displacement is between 0.5 and 1 pixel, the interrogation area is moved by 1 pixel, so the displacement being measured becomes negative. As a result, the mean bias error and the RMS error both exhibit an oscillatory behaviour which repeats after 1 pixel, with a maximum value of approximately 0.04 pixels for both sub-pixel interpolation schemes. Similar to the standard FFT method, the Gaussian scheme is more accurate than the parabolic interpolation for the predictor corrector method with maximum mean bias errors of approximately 0.03 pixels and 0.075 pixels, respectively.

The results for the super resolution FFT method for the uniform translation images are shown in Figure 5.9a-b. The shape of the mean bias error and RMS error for both the parabolic and Gaussian schemes are very similar to those obtained using the predictor corrector FFT algorithm. This is expected since both cross-correlation methods use an integer offset when the displacement is greater than 0.5 pixels. However, the mean bias error was greater with the super resolution FFT method compared to the predictor corrector FFT method. The parabolic scheme had a maximum mean bias error of 0.1 pixels while the Gaussian method produced a maximum mean bias error of 0.05 pixels. As well the RMS error was approximately 4 times greater with the super resolution FFT compared to the predictor corrector FFT algorithm. The increase in error is attributed to the smaller interrogation areas used for the final iteration of the super resolution FFT and will be discussed in greater detail in Section 5.4.5.

Graphs (c) and (d) of Figure 5.9 show the mean bias error and RMS error for the deformed FFT method using the parabolic and Gaussian methods, respectively. Both sub-pixel interpolation schemes exhibit an oscillatory shape, similar to a sine wave. Unlike the previous three cross-correlation schemes, there is little difference in the mean bias error between the parabolic and Gaussian methods with a maximum value of approximately 0.025 pixels. This is attributed to the bi-linear interpolation used to determine the pixel intensity for sub-pixel displacements. The shapes of the particles no longer exactly represent a Gaussian profiles, thus the parabolic and Gaussian interpolation schemes produce similar results. However, the RMS error is slightly lower for the Gaussian method compared to the parabolic.

Of the four cross-correlation methods applied to the uniform translation images the deformed FFT produced the most accurate results. The reasons for the improved performance of the deformed FFT over the other algorithms is the improved accuracy when measuring small displacements as well as the ability of the deformed FFT method to offset the interrogation area by a non-integer offset, *i.e.* a sub-pixel offset can be applied between iterations. An example would be an applied displacement of 0.4 pixels measured with each cross-correlation algorithm. The predictor corrector FFT and super resolution FFT must attempt to measure the entire 0.4 pixel displacement for each iteration. For the same 0.4 pixel displacement, assume the first iteration of the deformed FFT method measured a displacement of 0.3 pixels, the next iteration only has to measure 0.1 pixels. Assuming the next measured displacement was still less than 0.1 pixels, the following iteration would only need to measure a displacement smaller than 0.1 pixels. This would continue until the error is due entirely to the pixel value interpolation scheme and the sub-pixel accuracy. As seen in all the previous figures, for each of the four cross-correlation methods, the error decreases as the particle displacement becomes smaller between 0 and 0.5 pixels, until there is no applied displacement, where the error is zero. Therefore, the deformed FFT method allows for smaller measured displacements for each subsequent iteration, which improves the accuracy.

If the predictor corrector FFT and super resolution FFT were capable of non-integer interrogation area offsets their accuracy would improve and the error may be less when compared to the deformed FFT scheme. For the deformed FFT scheme, the pixels within an interrogation area are displaced by different amounts, albeit the differences are small for the linear translation images. This would not be the case for the predictor corrector FFT and super resolution FFT methods, where the entire interrogation area would have a uniform translation. The assumption of a uniform pixel offset is advantageous for this case since the particle displacement is constant within the uniform translation images.

5.4.5 Effect of Interrogation Area Size on Accuracy of Results

To determine if the larger error produced by the super resolution FFT method, compared to the other three strategies, was a result of the smaller interrogation area used in the final iteration, different sized interrogation areas were examined for each cross-correlation algorithm. Figure 5.10

shows the mean bias error as a function of the applied displacement for the four cross-correlation methods for interrogation areas ranging in size from 16x16 to 64x64 pixels area. Since the super resolution FFT changes the size of the interrogation area with each subsequent iteration, the size for the final iteration (16x16 pixel area) was used for reference purposes.

From Figure 5.10b and c the mean bias error for the 32x32 super resolution FFT was approximately equal to that seen for the same sized interrogation area using the predictor corrector FFT method. This confirms the earlier hypothesis that the increased error for the super resolution FFT was due to the smaller interrogation areas. In fact, the other three cross-correlation schemes show a small improvement between the 32x32 and 64x64 pixel areas but a significant decrease in accuracy for the 16x16 interrogation area case. This was due to a combination of the smaller number of particles within each interrogation area for the 16x16 pixel area case, as well as the bias towards smaller displacements since the displacement peak was generated with the FFT based cross-correlation, as mentioned earlier in Chapter 2. For the smaller interrogation areas this error tends to become magnified. The super resolution FFT does not exhibit the same degree of error with the 16x16 pixel area, due to the larger interrogation areas used in previous iterations. When the interrogation area has been reduced to 16x16 pixels the super resolution FFT only needs to measure a displacement less than 0.5 pixels so the bias error is less appreciable. The other three cross-correlation methods must attempt to measure the entire displacement with an interrogation area of 16x16 pixels for the first iteration. This exhibits the importance of achieving an accurate first step in all iterative methods since each subsequent iteration will be based on the initial displacement estimate.

5.4.6 Uniform Translation Images Summary

Spatial Resolution

Since the particle displacement was uniform throughout the entire image it was difficult to gauge the spatial resolution of each cross-correlation method. Therefore, no conclusions regarding the spatial resolution of the algorithms examined could be made from the uniform translation images.

(a) Standard FFT

(b) Predictor Corrector FFT

(c) Super Resolution FFT

(d) Deformed FFT
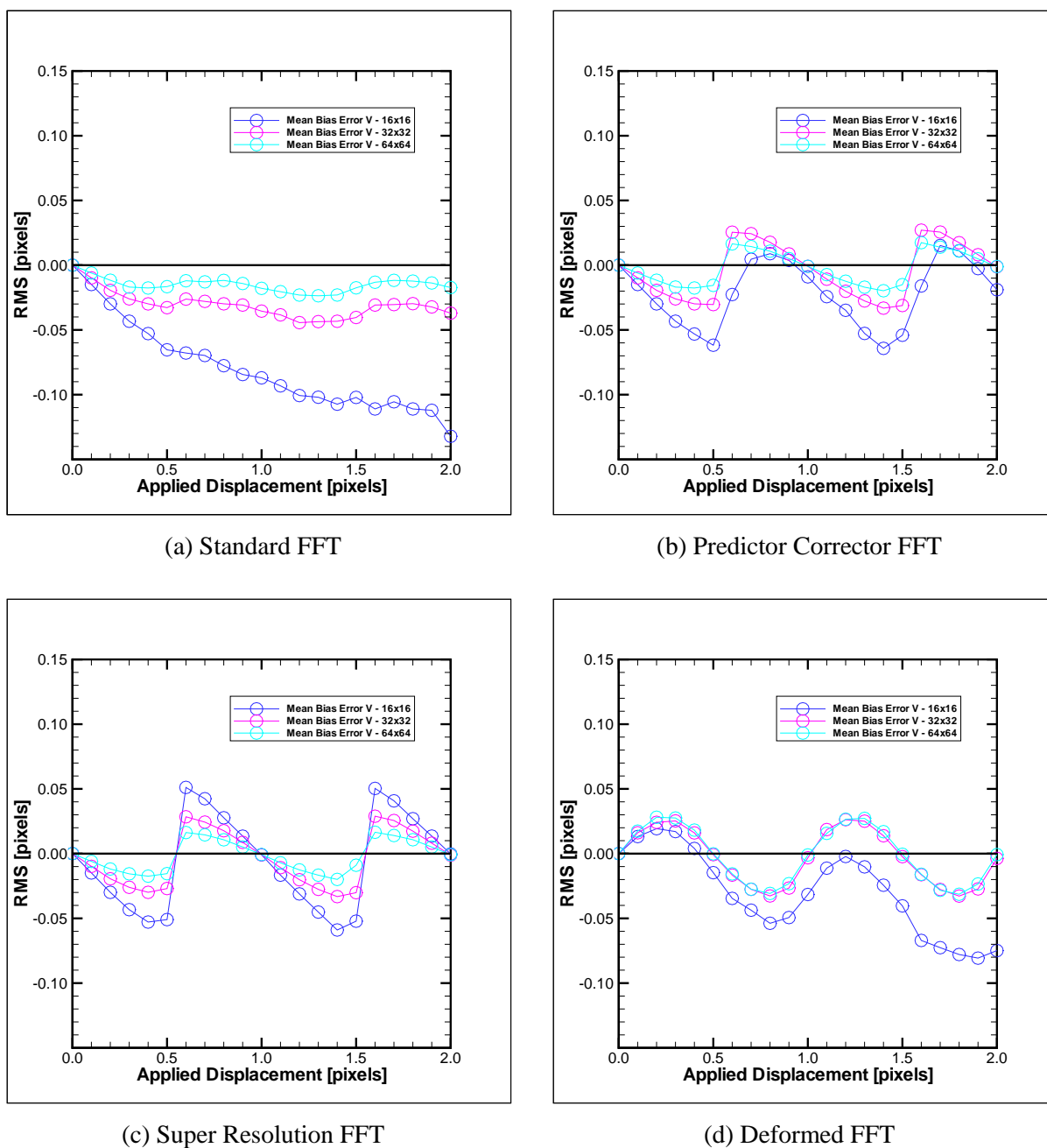
Figure 5.10: Mean bias error as a function of applied displacement with 15 particles per 32x32 pixel area and a diameter of 4 pixels for different interrogation area sizes a) Standard FFT with Gaussian sub-pixel estimator b) Predictor corrector FFT with Gaussian sub-pixel estimator c) Super resolution FFT with Gaussian sub-pixel estimator d) Deformed FFT with Gaussian sub-pixel estimator

Dynamic Range

The dynamic range refers to the range of displacements each method can accurately measure. Similar to the spatial resolution, the uniform particle displacements within the image prevented any judgments concerning the dynamic range of each cross-correlation method from being made.

Accuracy

The linear translation images were used to determine the highest accuracy capable with PIV, when using a cross-correlation strategy, *i.e.* to establish the least amount of error possible. The accuracy of the linear translation images was measured by the mean bias and RMS errors. The most accurate results were produced by the deformed FFT method with a mean bias error of 0.03 pixels and an RMS error of 0.03 pixels. The deformed FFT algorithm produced the least amount of error since it was capable of sub-pixel offsets between iterations. If the predictor corrector FFT method were capable of sub-pixel offsets, it may produce better results since it would enforce the uniform flow condition, as opposed to the deformed FFT method which allowed for the skewing of the interrogation area. Larger interrogation areas were also determined to be more accurate, although little improvement was seen between 32x32 and 64x64 pixel areas.

The Gaussian sub-pixel interpolation scheme was determined to be more accurate than the parabolic scheme, due in part to the particles being modelled with a Gaussian distribution. It was also determined that a particle diameter of 3-5 pixels produced the smallest RMS error for all four methods, while each method also contained less error with higher particle number densities.

Robustness

The applied uniform displacement in the uniform translation images was very simple so it was difficult to measure the robustness of the cross-correlation methods. Each method used over 99% of the vectors available so no conclusions can be made about the robustness of the algorithms from the uniform translation images.

5.5   Step, Sawtooth and Sinusoid Images

The step, sawtooth and sinusoid images were similar flows, each containing displacement gradients in a single direction. The major difference between the flows, other than the displacement profile used to create the flows, was the magnitude of the displacement gradient. The step images contained an infinite displacement gradient, *i.e.* a step, between two regions of constant displacement, as shown in Figure 5.11. The sawtooth images were similar to the step images since they also contained a displacement gradient between two regions of constant velocity, however the sawtooth images contained a constant finite displacement gradient. The magnitude of the displacement gradient depended on the size of the period, as shown in Figure 5.12. Figure 5.13 shows a vector plot for the applied displacement for the sinusoid images, which was in the shape of a sine wave. This created a displacement gradient that varied in magnitude in the horizontal direction.

For the results shown, the maximum displacement for each of the step, sawtooth and sinusoid
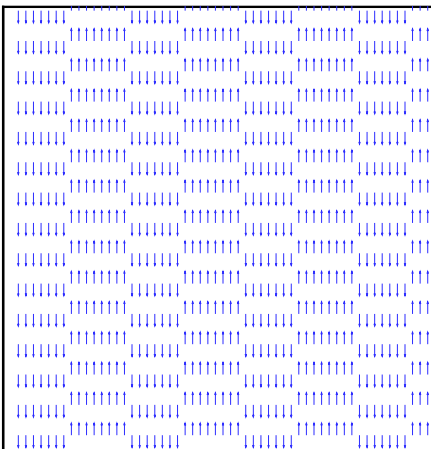
Figure 5.11: Vector plot for a step image
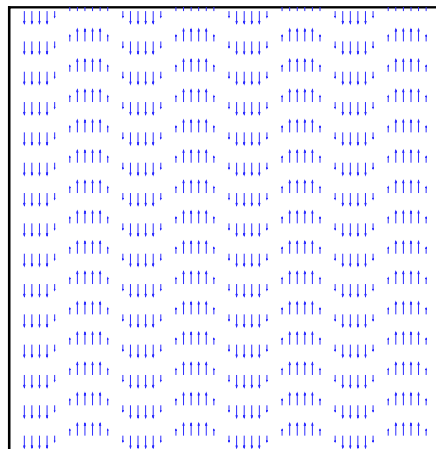
Figure 5.12: Vector plot for a sawtooth image
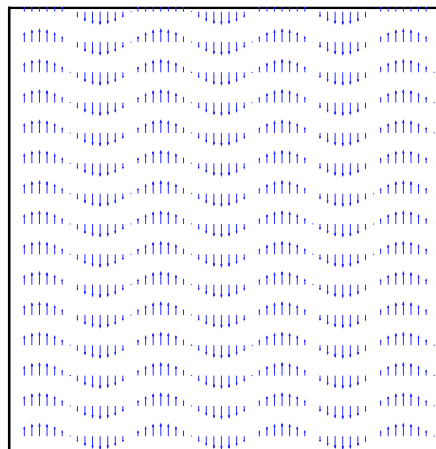
Figure 5.13: Vector plot for a sinusoid image

images was 8 pixels while different periods of 64, 128 and 256 pixels were evaluated. Since the trends are similar for all the periods examined, only the results for the period of 128 pixels are shown to reduce the number of plots. However, the results for the periods of 64 and 256 pixels are included in Appendices A, B and C for the step, sawtooth and sinusoid images respectively. As well, the same range of particle diameter size (2 to 10 pixels) and particle number densities (4 to 20 particles per 32x32 pixel area) as the uniform translation images were investigated. Only the results for the images with a particle diameter of 4 pixels and 15 particles per 32x32 pixel area are shown in this section with a period of 128 pixels since they are representative of the other cases. The Gaussian sub-pixel interpolation scheme was used for all the results since it was determined to be the most accurate sub-pixel scheme from the uniform translation image results.

Since the displacement profiles were repeating functions with a well defined period, the displacement results were normalised by using the remainder of the horizontal location $[x]$ divided by the period, as shown in Equation 5.4.

$$x_{index} = remainder(x/Period) \tag{5.4}$$

This collapsed the results into a single period of the displacement function.

5.5.1 Infinite Gradient - Step Velocity Profile Results

Unlike the uniform translation images, the step images contained a displacement gradient. From $0 < x_{index} < 0.5$ the particles move with a constant 8 pixels displacement in the negative vertical direction $[v]$. Then at $x_{index} = 0.5$ there is an infinite displacement gradient, *i.e.* a step, after which the particles move with another uniform displacement of 8 pixels, this time in the positive vertical direction.

All Measurement Results

The results for every individual validated measurement are shown in Figure 5.14, along with the exact displacement, for the four cross-correlation schemes. The difference between results for the
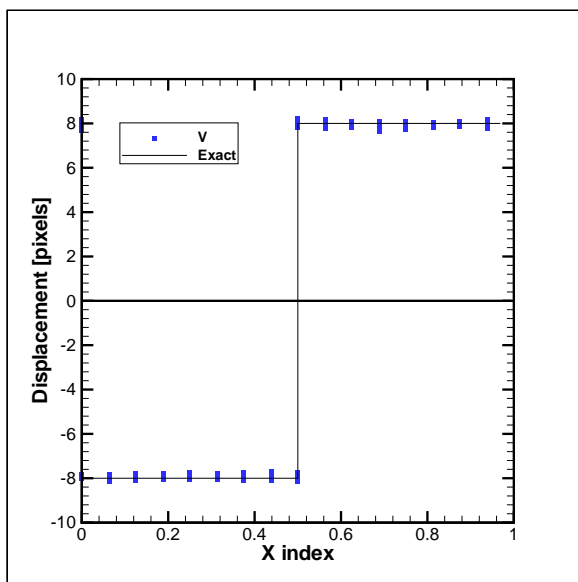
(a) Standard FFT
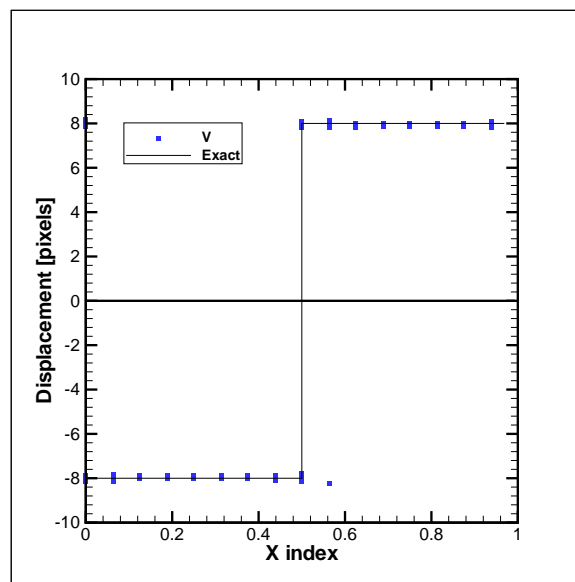
(b) Predictor Corrector FFT
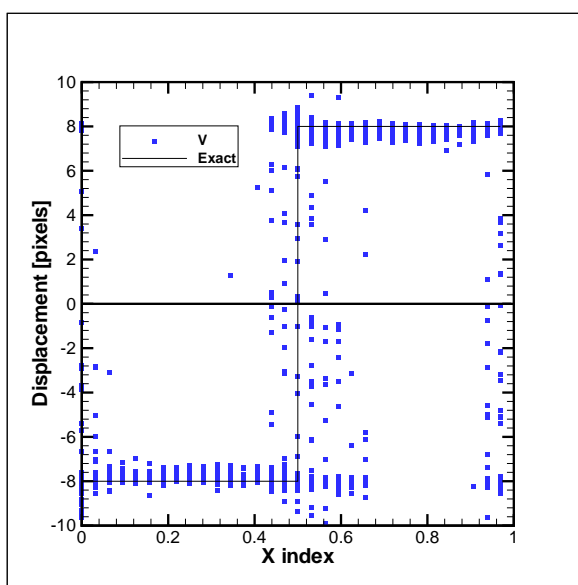
(c) Super Resolution FFT
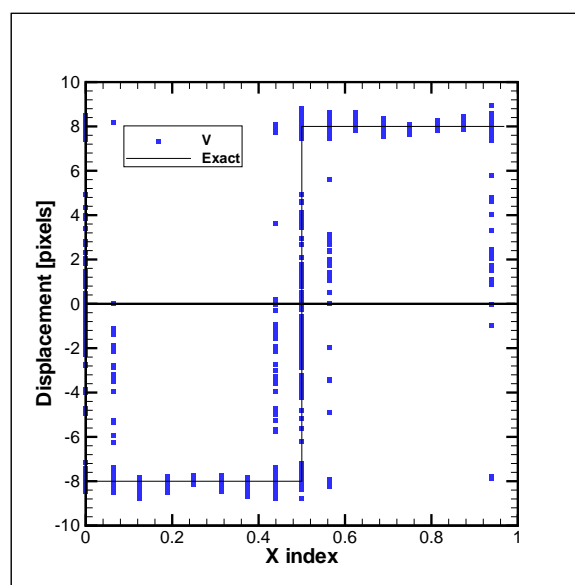
(d) Deformed FFT

Figure 5.14: Validated displacement measurements for step displacement function of period 128, particle size 4 pixels in diameter and a particle number density of 15 particles per 32x32 pixel area (a) Standard FFT (b) Predictor Corrector FFT (c) Super Resolution FFT (d) Deformed FFT
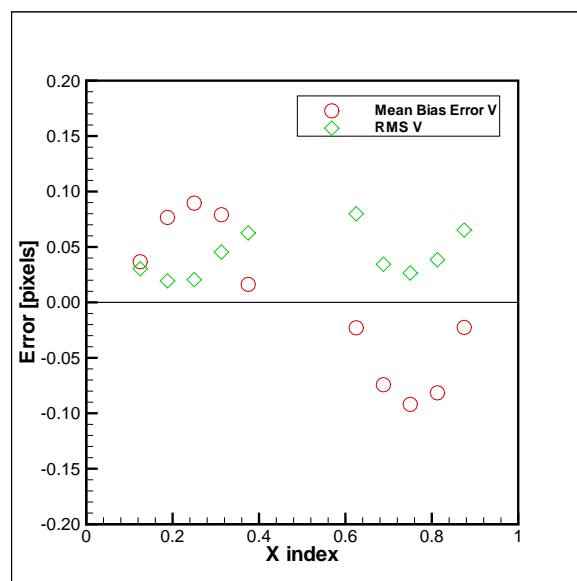
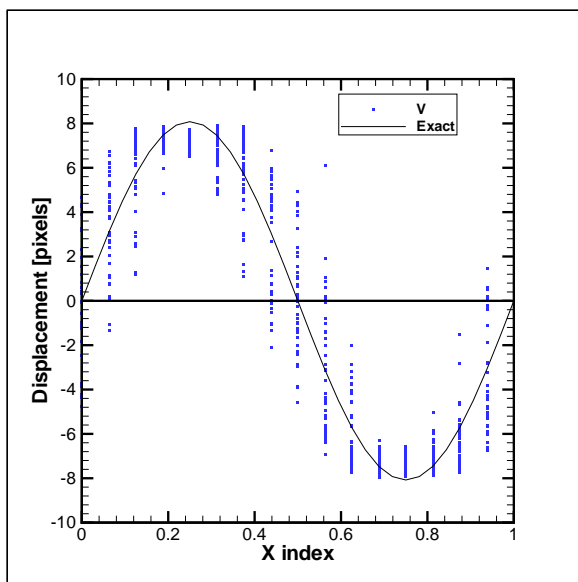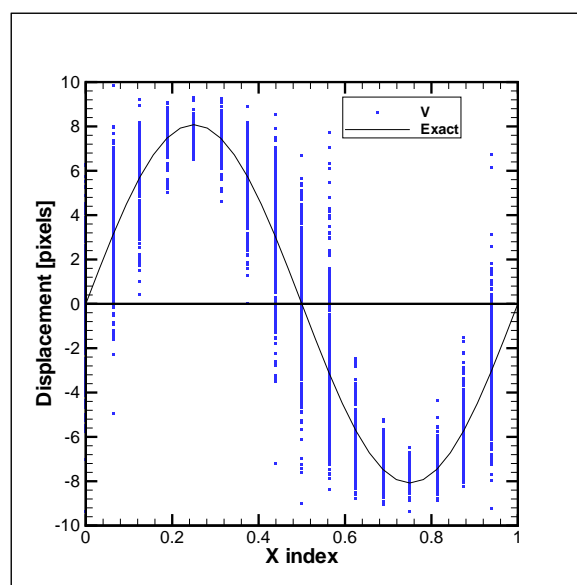standard FFT and predictor corrector was small compared to the other schemes, as they matched the exact profile well (with the exception of one outlier for the predictor corrector FFT method) for all of x_{index}.

However, the measurements produced using the super resolution FFT and deformed FFT methods do not have the same accuracy as the standard FFT or the predictor corrector FFT algorithms. Away from the step, the measurements for the super resolution FFT and deformed FFT methods produced a *wavy* profile with the variation in the displacement measurements as much as $\pm$ 1 pixel for both schemes. Near the step, the variation of the measurements and their deviation from the exact displacement profile increased. This was due to the interpolation used by both the super resolution FFT and deformed FFT algorithms.

Within the super resolution FFT method, interpolation was used to determine the interrogation area offset vector between iterations. The first iteration was performed without any offset and produces results similar to the standard FFT shown in Figure 5.14, but not exactly the same since the first iteration uses an interrogation area of 64x64 pixels. The second iteration reduced the interrogation area by a factor of two, to 32x32 pixels area. The amount by which these new interrogation areas are then offset must be determined using interpolation of the displacement field. In this case, bi-linear interpolation was used. Since the bi-linear interpolation cannot properly represent the displacement discontinuity that existed at the step, the interrogation area offset was incorrect. Sometimes the cross-correlation produced the correct displacement peak despite the inaccurate offset. This is seen with the measurements that lie on or near the exact displacement profile. For other measurements, the error in the offset was too great and an erroneous displacement measurement results. The error then tends to expand as it affects the entire vector field with subsequent iterations, due to the interpolation scheme, resulting in the wavy displacement profile in the regions of constant displacement. A similar problem (the inability of the interpolation scheme to accurately represent the step) existed with the deformed FFT method, which used interpolation to offset the individual pixels within an interrogation area.

Averaged Measurement Results

Figure 5.15 shows an ensemble average of the results shown in Figure 5.14. There was little
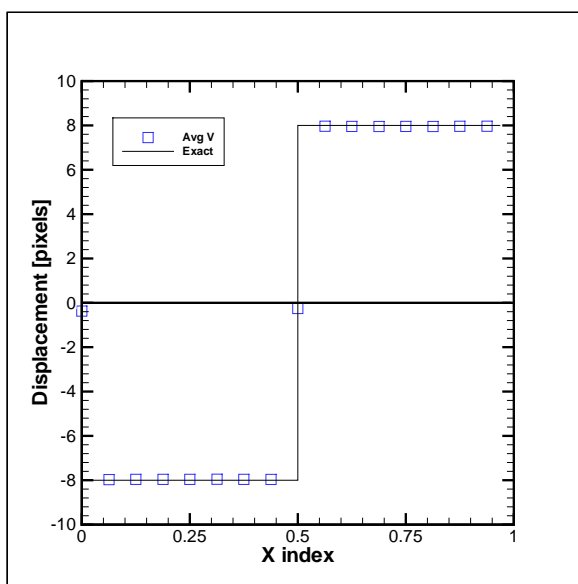
(a) Standard FFT
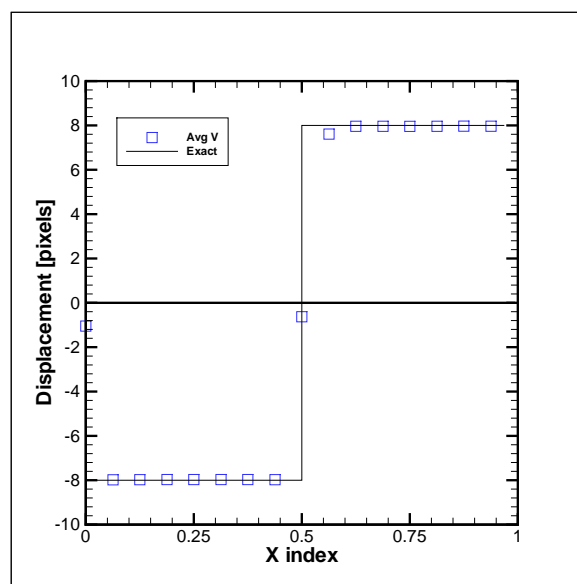
(b) Predictor Corrector FFT
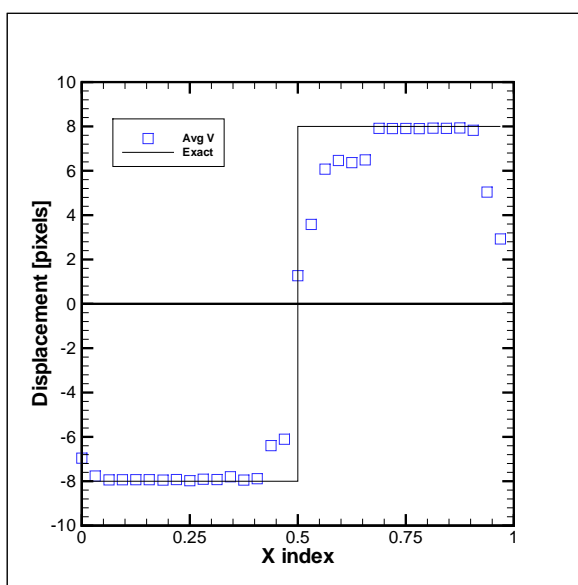
(c) Super Resolution FFT
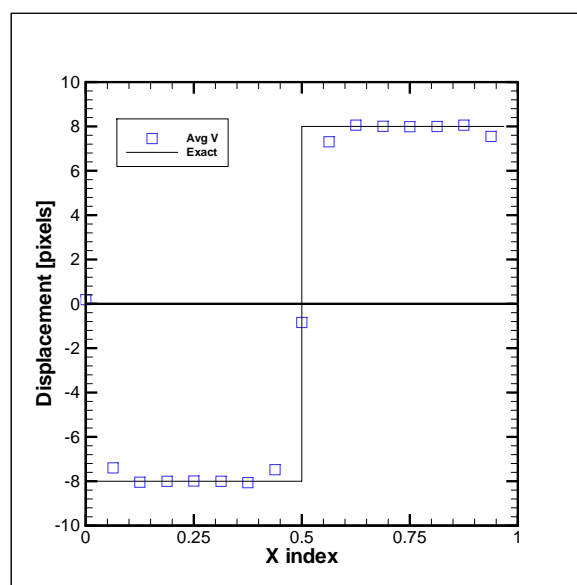
(d) Deformed FFT

Figure 5.15: Ensemble averaged measurements for step displacement function of period 128, particle size 4 pixels in diameter and a particle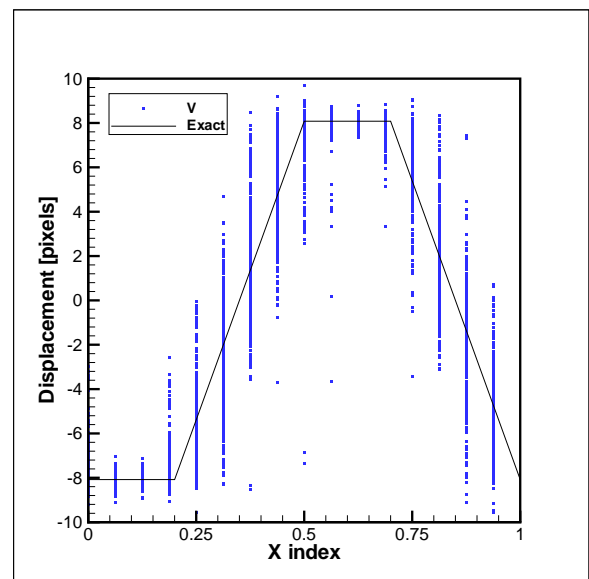 number density of 15 particles per 32x32 pixel area (a) Standard FFT (b) Predictor Corrector FFT (c) Super Resolution FFT (d) Deformed FFT

difference between the standard FFT and predictor corrector FFT, with the slight deviation in the predictor corrector FFT at $x_{index} = 0.56$ attributed to one outlier. Due to the interrogation area overlap, a displacement vector exists where the interrogation area was bisected by the step ($x_{index} = 0.5$). The displacement measured with the cross-correlation method depended strongly on the location of the particles within the interrogation area. If more particles existed in the positive displacement half of the interrogation area then the positive displacement would be measured, and vice versa if more particles were in the negative half. Since the location of the particles within the interrogation area is random there should be an equal number of vectors measuring the positive displacement as measuring the negative displacement, with enough displacement vectors. This was seen with the average displacement at the step, which is almost zero for both the standard FFT and predictor corrector FFT methods.

The ensemble averaged results for the super resolution FFT and deformed FFT schemes show the effects of the interpolation near the step. The step in the average displacement profile was *rounded*, with the super resolution FFT scheme exhibiting more rounding than the deformed FFT method. Note however that compared to the results in Figure 5.14c-d the wavy displacement profile in the regions of constant displacement disappeared with averaging.

Figure 5.16 shows the mean bias error and RMS error as a function of x_{index} for the four cross-correlation algorithms. The mean bias and RMS error were both larger near the step for the super resolution FFT and deformed FFT algorithms compared to the other methods, as expected. However, due to the scale of the errors near the step it was difficult to determine the difference between the methods in the regions of constant displacement.

Figure 5.17 is the same plot as Figure 5.16 except the error scale has been changed to highlight the error in the regions of constant displacement. There was little difference between the mean bias error of the standard FFT and the predictor corrector FFT methods, less than 0.15 pixels for each, suggesting there was little improvement in the measurements after the first iteration.

Although the deformed FFT method had difficulty measuring the particle displacements near the step, in the region of constant displacement the mean bias error was the lowest, below 0.1 pixels, while the super resolution FFT method had the largest mean bias error, between 0.1 and 0.2 pixels. This agrees with the results from the uniform translation images and was not surprising since
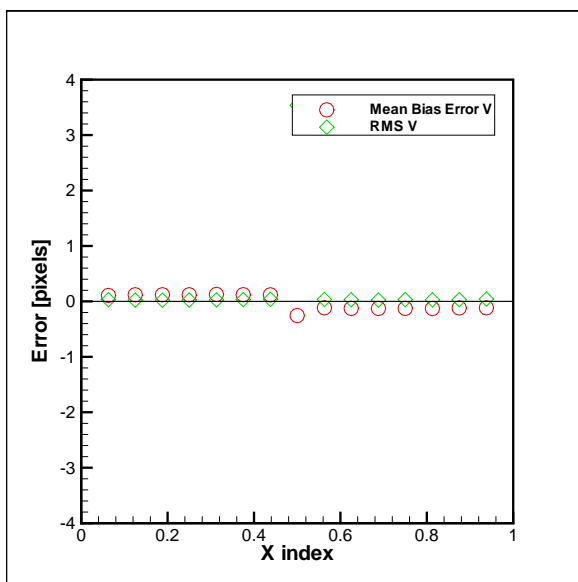
(a) Standard FFT
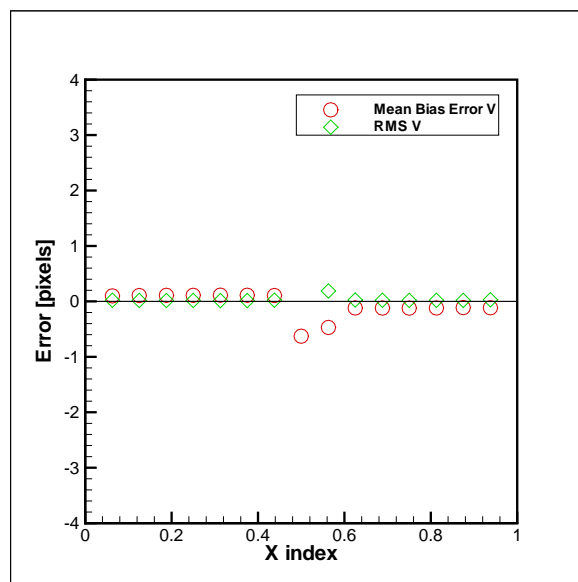
(b) Predictor Corrector FFT
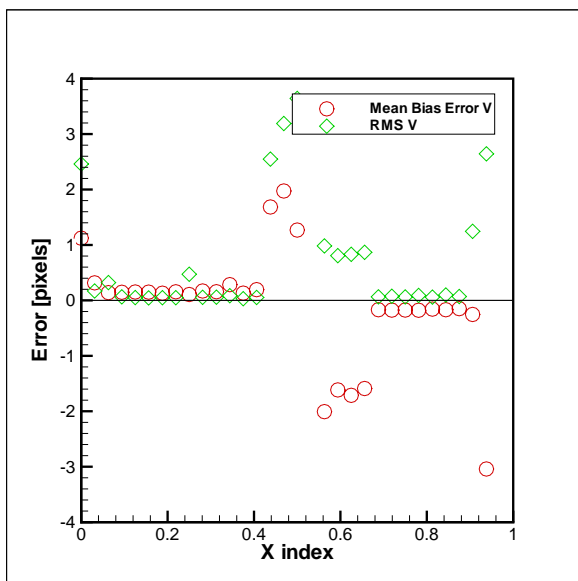
(c) Super Resolution FFT
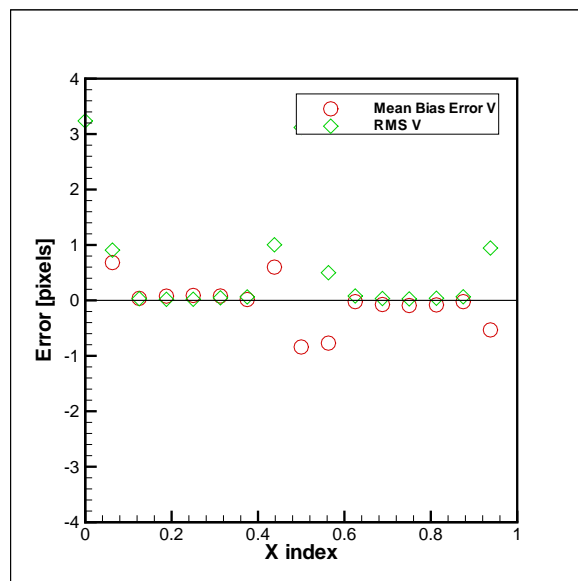
(d) Deformed FFT

Figure 5.16: Mean bias and RMS error for step displacement function of period 128, particle size 4 pixels in diameter and a particle number density of 15 particles per 32x32 pixel area (a) Standard FFT (b) Predictor Corrector FFT (c) Super Resolution FFT (d) Deformed FFT
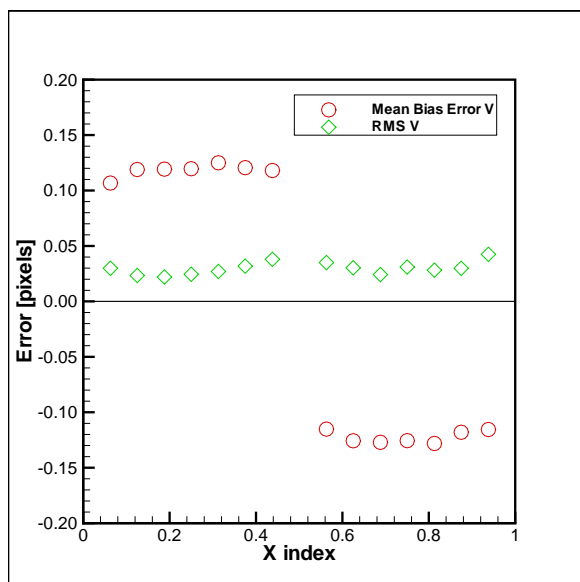
(a) Standard FFT
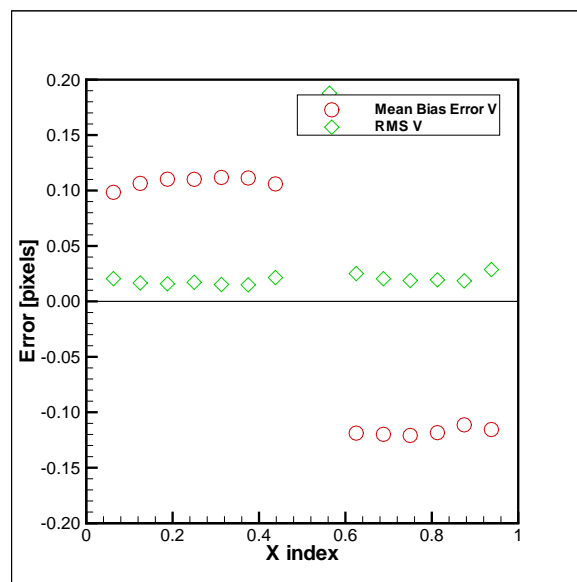
(b) Predictor Corrector FFT
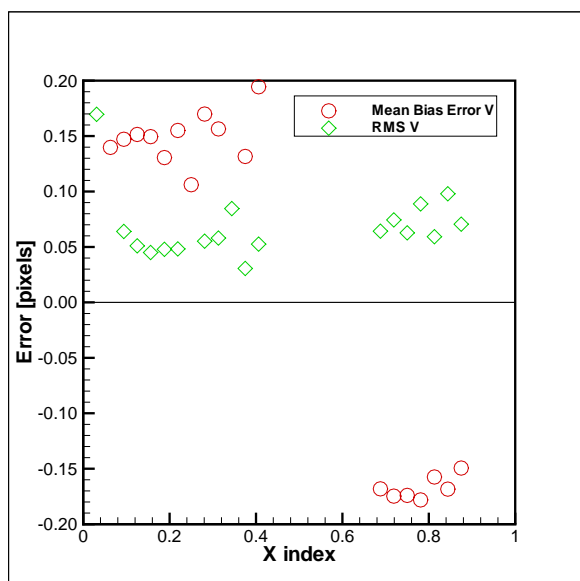
(c) Super Resolution FFT

(d) Deformed FFT

Figure 5.17: Mean bias and RMS error for step displacement function of period 128, particle size 4 pixels in diameter and a particle number density of 15 particles per 32x32 pixel area (zoom) (a) Standard FFT (b) Predictor Corrector FFT (c) Super Resolution FFT (d) Deformed FFT

in the regions of constant displacement the step and uniform translation images were essentially identical. As for the RMS error, it was the lowest for the displacements measured using the predictor corrector FFT method, below 0.02 pixels, while the super resolution FFT method also had the largest RMS error of 1 pixel (not including the measurements at the location of the step).

5.5.2 Finite Gradient - Sawtooth and Sinusoid Profile Results

Unlike the step images, the displacement gradients in the sawtooth and sinusoid images were finite. The sawtooth images contained regions of constant displacement gradients while the displacement gradients were never constant throughout the sinusoid images. However, the results were similar for the sawtooth and sinusoid images. Therefore, to reduce the number of plots, only the sinusoid profile images are presented for some parts of the discussion with the corresponding plots for the sawtooth images included in Appendix B.

All Measurements Results

Figure 5.18 shows every individual validated displacement plotted against the appropriate scaled x-value for one period of the sine displacement function as estimated by the four cross-correlation algorithms. The exact displacement profile of the sinusoid images is also shown. The results produced using the super resolution FFT method contained many outliers that the validation routine did not remove. The outliers were due to the smaller interrogation areas used with the super resolution FFT method, 16x16 versus 32x32 pixel area for the other three schemes. As a result, the number of particles within any interrogation area for the super resolution FFT method was approximately one-quarter the number of particles present in the interrogation areas for the three other algorithms. As seen with the uniform translation images, smaller particle number densities will contribute more error since there are fewer particles contributing to the true displacement peak in the correlation plane. In the case of the outliers in the super resolution FFT results, the noise peak must have been more than 1.3 (the value used by the peak validation) times greater than the true displacement peak. To remove these outliers a higher value for the peak
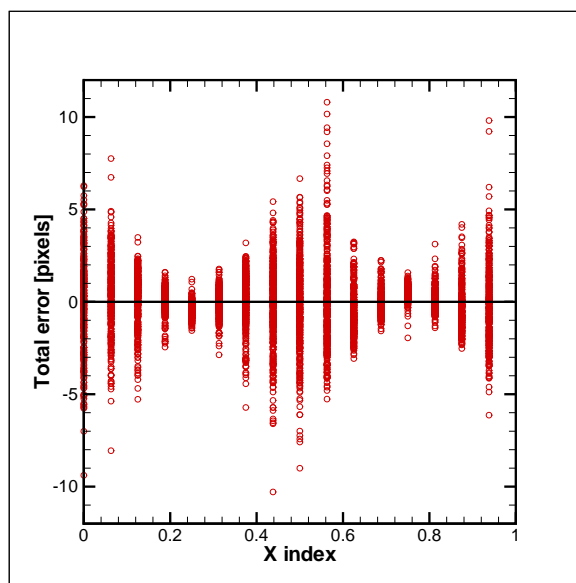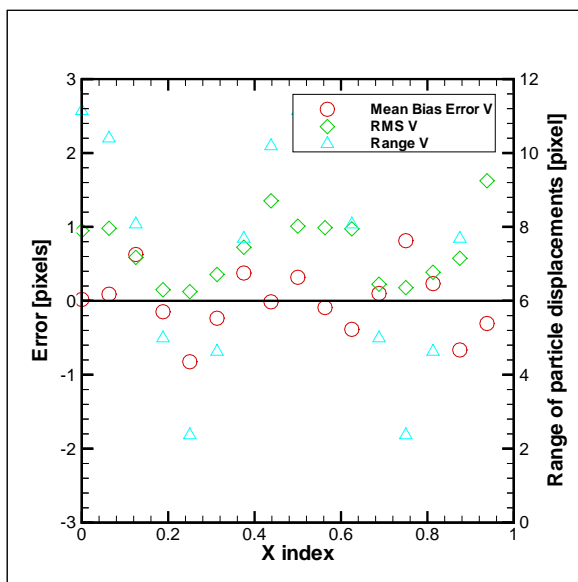
(a) Standard FFT
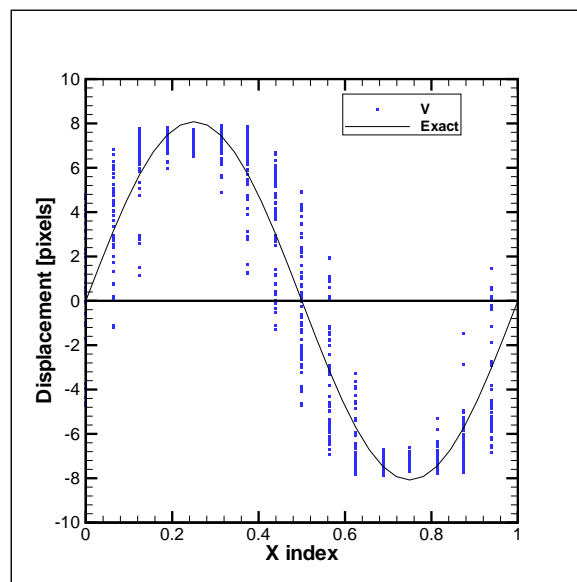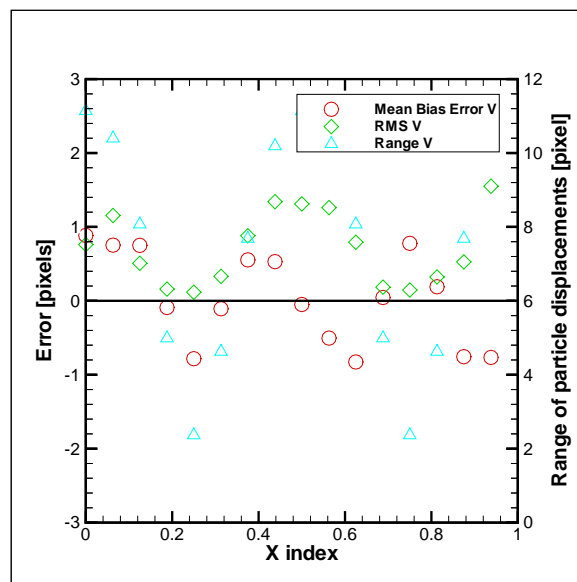
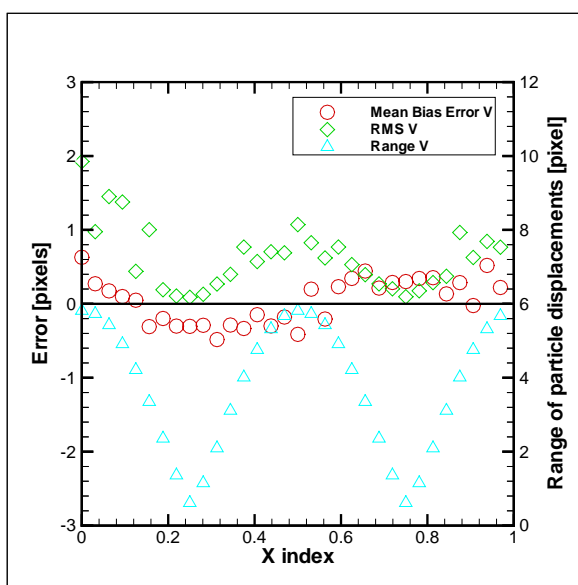(b) Predictor Corrector FFT
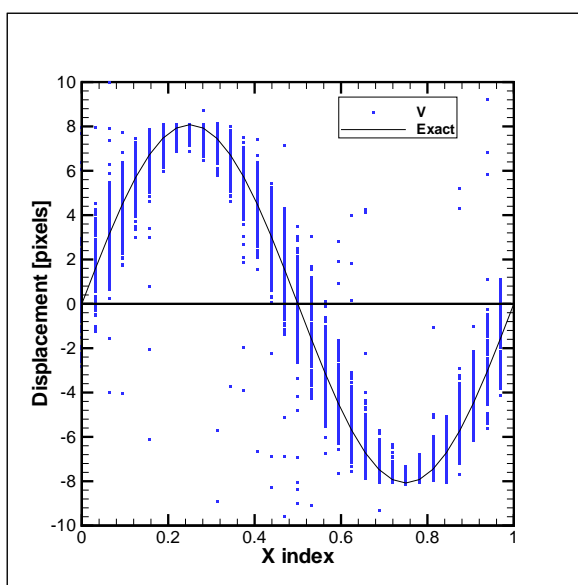
(c) Super Resolution FFT

(d) Deformed FFT

Figure 5.18: Validated displacement measurements for sinusoid displacement function (a) Standard FFT (b) Predictor Corrector FFT (c) Super Resolution FFT (d) Deformed FFT

validation could have used or another validation strategy such as comparing each displacement vector to its neighbours could be applied, as described in Section 2.3.2.

Figure 5.18 also shows that three of the cross-correlation methods under estimated the maximum particle displacements, while the deformed FFT method did not. The deformed FFT algorithm resolved displacements that were greater than those which existed within the image, probably due to the bi-linear interpolation used to deform the second interrogation area. The fact that a method was producing measurements that do not exist anywhere within the image appears to be worse than not being able to measure the maximum particle displacements. However, this error may result in a smaller mean bias error for the deformed FFT method with the same RMS error as the other three cross-correlation strategies. Figure 5.19 shows similar results for the sawtooth images.

Another important result shown in Figures 5.18 and 5.19 was the large variation in the individual particle displacement measurements. In the standard FFT, predictor corrector FFT and deformed FFT schemes the variation in the displacement measurements at a single x_{index} was as much as 10 pixels. The variation also increased as the displacement gradient increases.

The variation in the displacement measurements for the super resolution FFT method was as high as 6 pixels (omitting the outliers), which was smaller than for the other cross-correlation methods. This variation was due to the displacement gradients in the images, more specifically, the different displacements of the particles within a single interrogation area.

Figure 5.20 shows every validated measurement along with lines representing the maximum and minimum actual particle displacements that existed within each interrogation area at each displacement vector location. The maximum line was constructed by determining the true maximum displacement within the interrogation area at each measurement location. The minimum line was determined in a similar manner.

Nearly all the displacement measurements for the standard FFT, predictor corrector FFT and super resolution FFT methods lie between the maximum and minimum particle displacement limits, neglecting the outliers. This suggests that the cross-correlation algorithms were measuring particle displacements that exist within the interrogation area, only they are not always located
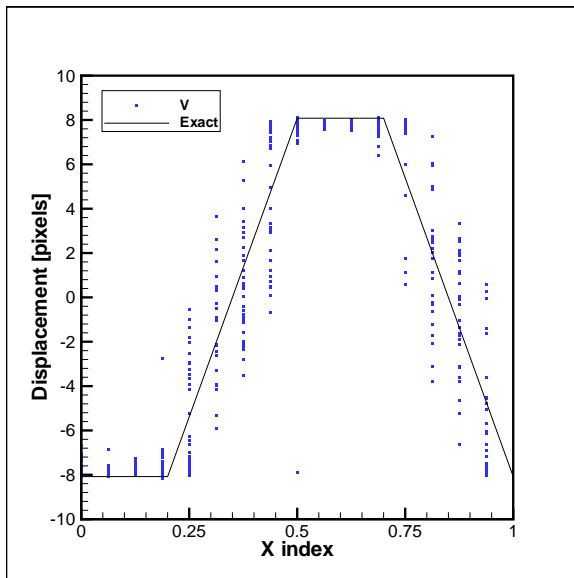
(a) Standard FFT
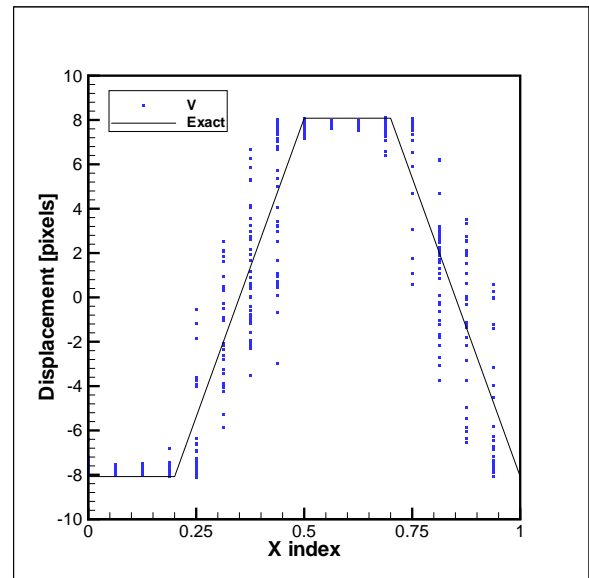
(b) Predictor Corrector FFT
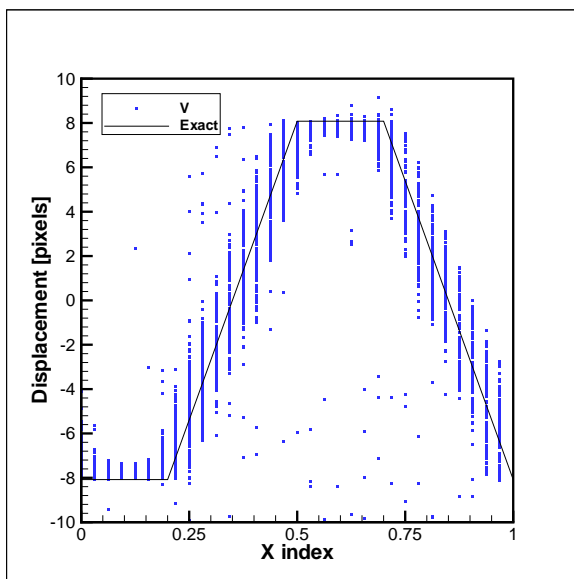
(c) Super Resolution FFT

(d) Deformed FFT

Figure 5.19: Validated displacement measurements for sawtooth displacement function (a) Standard FFT (b) Predictor Corrector FFT (c) Super Resolution FFT (d) Deformed FFT
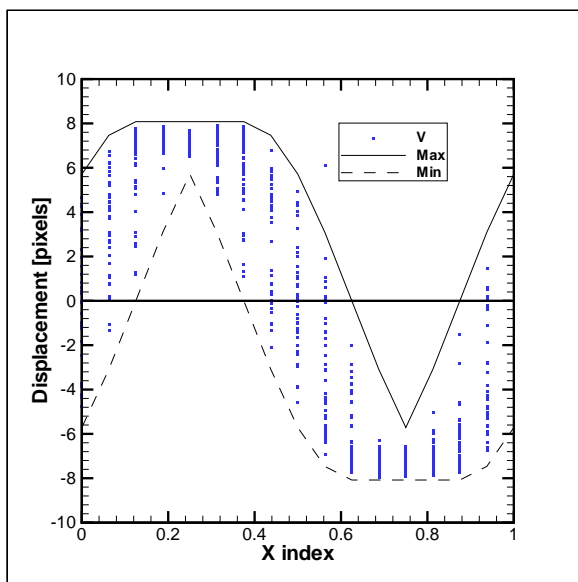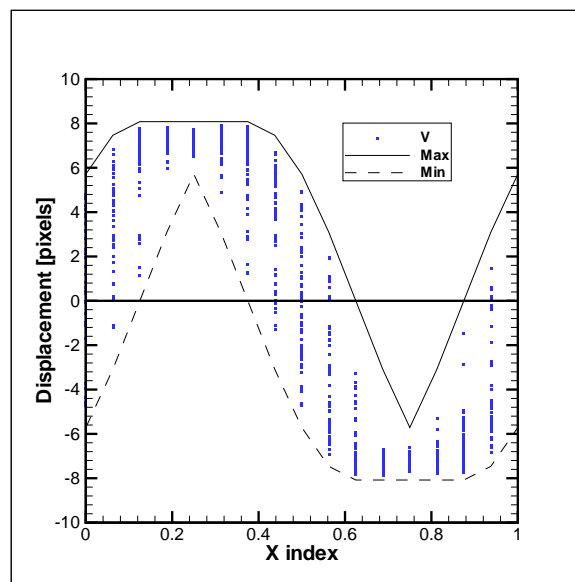
(a) Standard FFT

(b) Predictor Corrector FFT
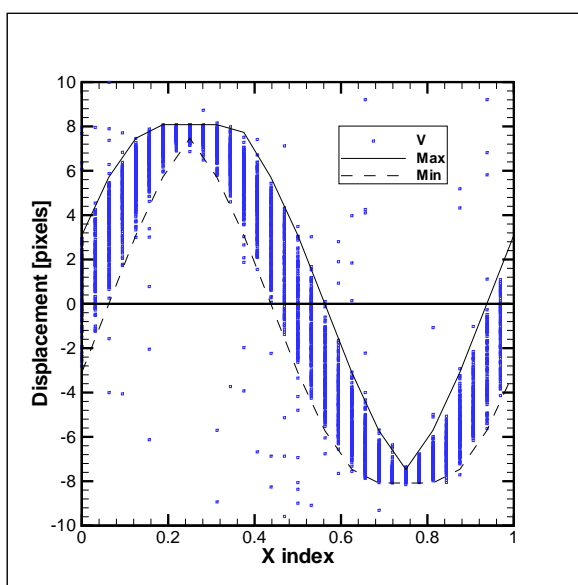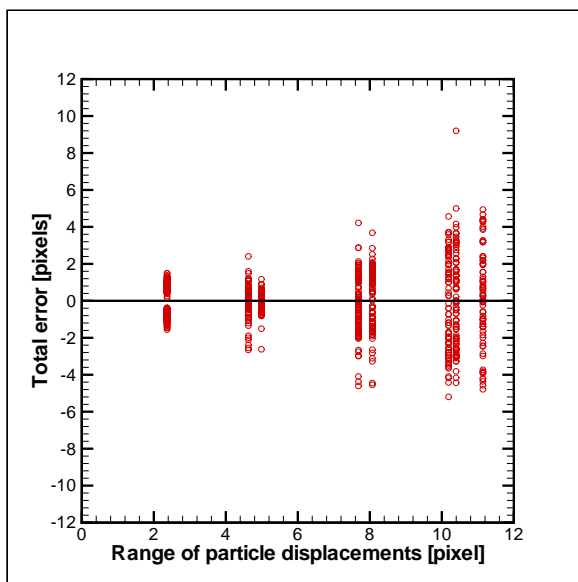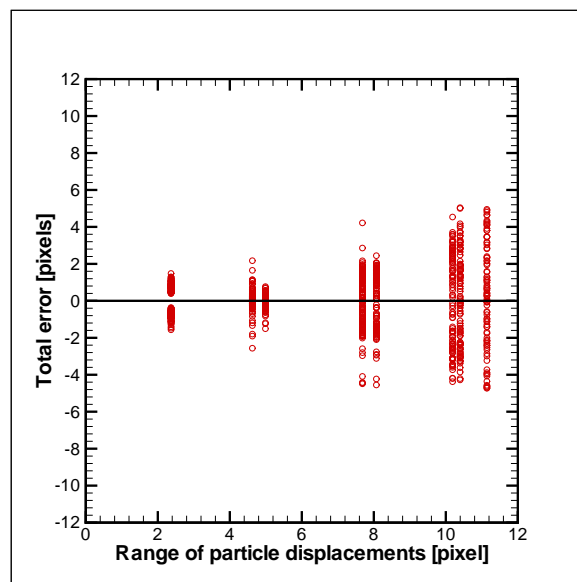
(c) Super Resolution FFT
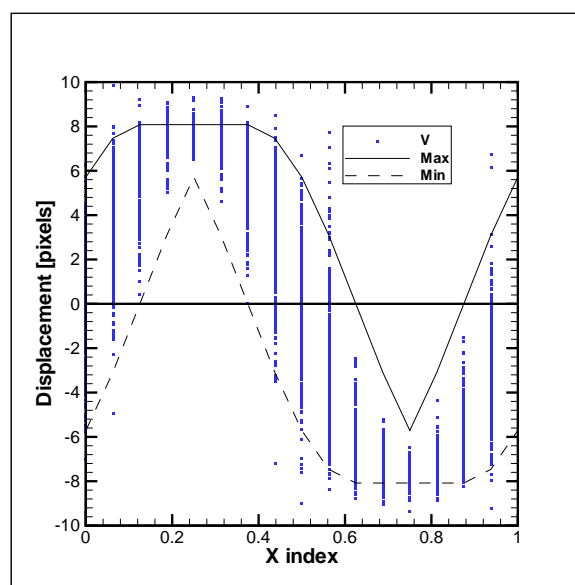
(d) Deformed FFT

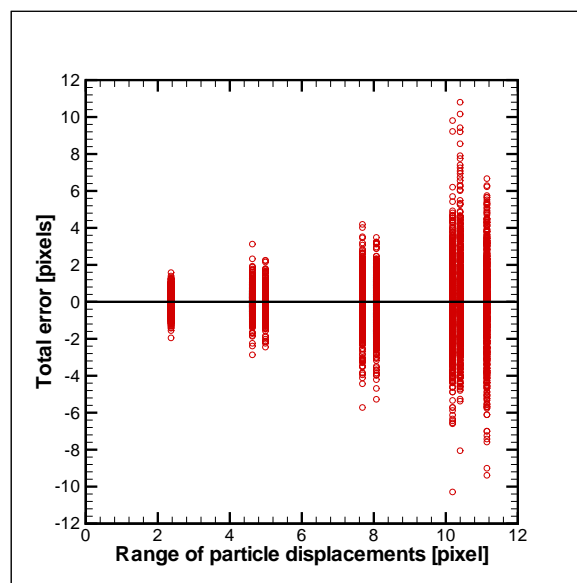Figure 5.20: Validated displacement measurements for the sinusoid displacement function with minimum and maximum displacements for each interrogation area (a) Standard FFT (b) Predictor Corrector FFT (c) Super Resolution FFT (d) Deformed FFT

at the centre of the interrogation area. The error was introduced when the vector result was placed at the centre of the interrogation area, rather than somewhere else inside the interrogation area, creating a positional bias error. For flows where there are small gradients, this positional bias error is generally small. However, for flows with large gradients the positional bias error can begin to dominate the total error. By properly assigning the vector within the interrogation area the error will be reduced, as shown by Young *et al.* [47].

Figure 5.20 also shows the smaller range between the maximum and minimum actual particle displacements within an interrogation area for the super resolution FFT method, compared to the other algorithms. This smaller range of particle displacements was due to the smaller interrogation area used by the super resolution FFT method, 16x16 versus the 32x32 pixel area used by the other three methods. This was the reason the variation in the measured displacements was smaller for the super resolution FFT method than the other three algorithms.

Averaged Measurement Results

The ensemble averaged results for the sinusoid displacement are shown in Figure 5.21, which shows the higher definition of the sinusoidal shape of the particle displacement as a result of the increased number of vectors produced using the super resolution FFT method, compared to the other algorithms. This was a result of the increased number of vectors achieved with the smaller interrogation areas, not a result of the interrogation area overlap, which was the same for all four cross-correlation methods.

Also shown in Figure 5.21 is that the standard FFT, predictor corrector FFT and super resolution FFT methods all appear to underestimate the maximum displacements, which occur at $x_{index} = 0.25$ and $x_{index} = 0.75$. This was not surprising since every individual displacement measured by those methods was smaller than the maximum displacement. The deformed FFT scheme, which had displacement measurements greater than the maximum displacements, also under-estimates the maximum displacements, but the bias error was smaller than in the other methods. There are many reasons why these methods inherently underestimate the maximum displacement. As mentioned earlier, the mean bias error may be due to the wrapping of the interrogation area
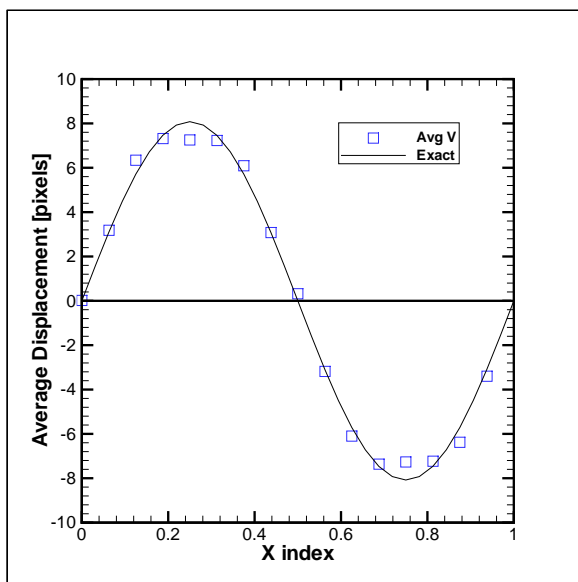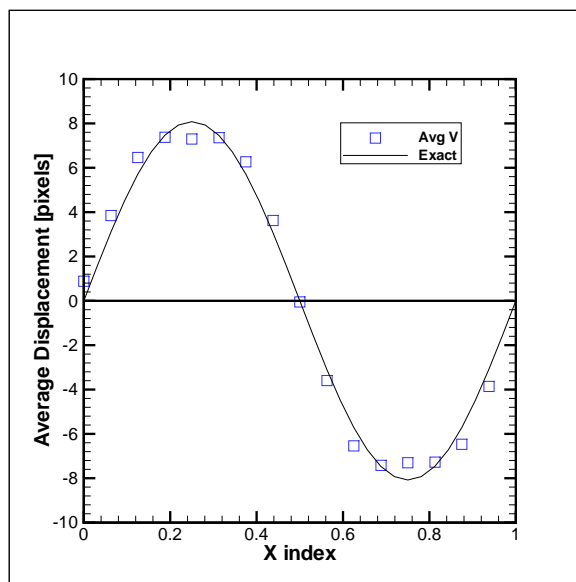
(a) Standard FFT

(b) Predictor Corrector FFT
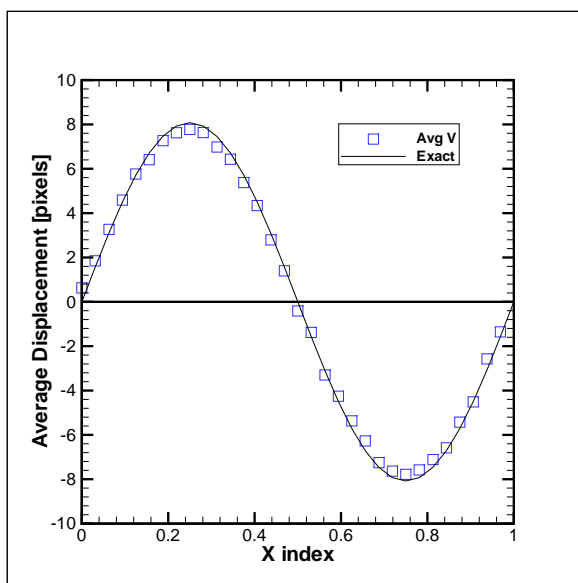
(c) Super Resolution FFT
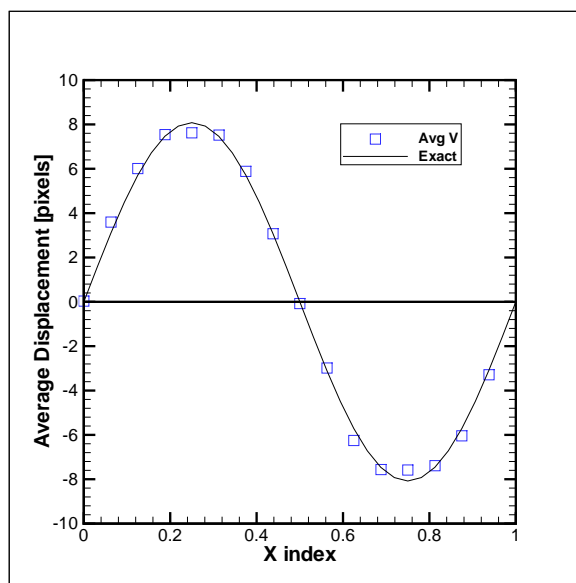
(d) Deformed FFT

Figure 5.21: Ensemble averaged measurements for sinusoid displacement function (a) Standard FFT (b) Predictor Corrector FFT (c) Super Resolution FFT (d) Deformed FFT

discussed in Section 2.3. Another possible reason was that the cross-correlation analysis was biased towards particles which have a higher intensity. Therefore, a measurement less than the maximum displacement may be a result of the brightest particle within the interrogation area moving a distance less than the maximum displacement. As a result, the measured displacement vector would not exist at the centre of the interrogation area.

Relationship between the error and range of particle displacements

To better show the errors associated with the various cross-correlation strategies the total error versus x_{index} is shown in Figure 5.22. The total error was defined as the difference between the individual displacement measurement and the actual displacement. All the measurements for the standard FFT, predictor corrector FFT and super resolution FFT show the bias in the maximum displacement measurements at $x_{index} = 0.25$ and $x_{index} = 0.75$. While the deformed FFT method produced measurements that were both less than and greater than the maximum displacements.

Also shown in Figure 5.22 was the variation in the total error as a function of x_{index}, for all four cross-correlation methods. The variation in the total error was smallest at the peak particle displacements while the variation was largest at $x_{index} = 0.5$, where the displacement gradient was largest.

The mean bias error, RMS error and the range of actual particle displacements within the interrogation area at each x_{index} measurement location is shown in Figure 5.23. The range of actual particle displacements was defined as the difference between the maximum and minimum displacement of the particles in the interrogation area. The mean bias error for the standard FFT and predictor corrector FFT method were both approximately 1 pixel, while the mean bias errors for the super resolution FFT and deformed FFT schemes were smaller ($\sim$ 0.5 pixels).

The RMS error was the smallest for the super resolution FFT scheme, approximately 0.75 pixels, while the other three methods have a maximum RMS error slightly above 1 pixel. Also shown in Figure 5.23 was the relationship between the RMS error and the range of particle displacements within the interrogation area, as they increase and decrease together.
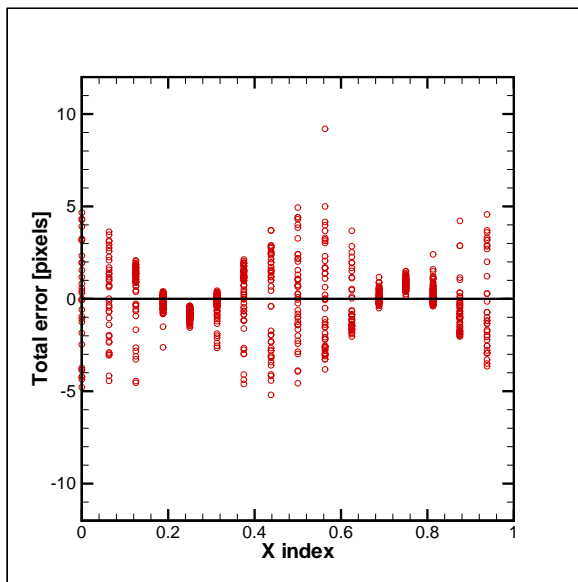
(a) Standard FFT
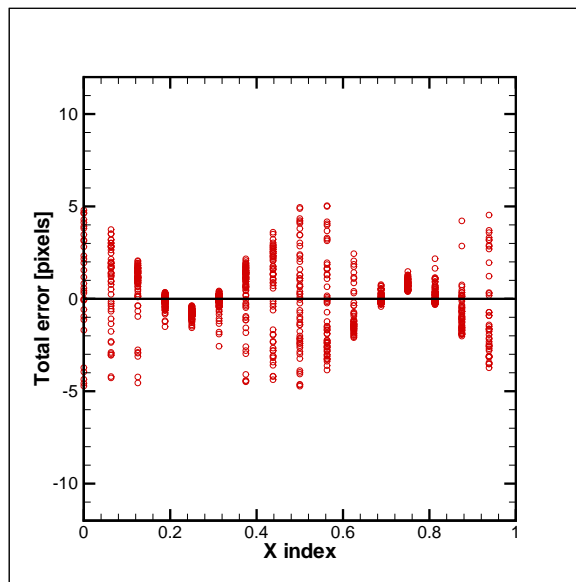
(b) Predictor Corrector FFT
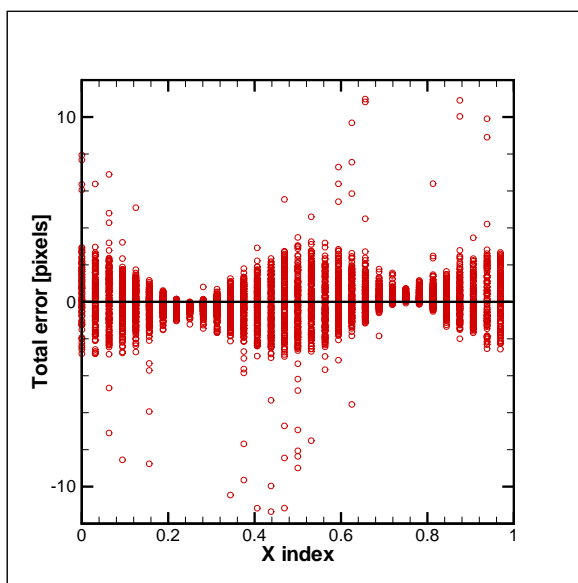
(c) Super Resolution FFT

(d) Deformed FFT

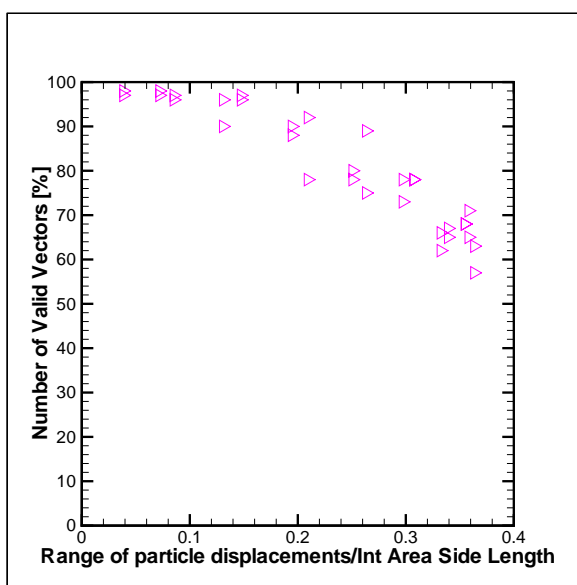Figure 5.22: Total error for validated measurements for sinusoid displacement function (a) Standard FFT (b) Predictor Corrector FFT (c) Super Resolution FFT (d) Deformed FFT

(a) Standard FFT

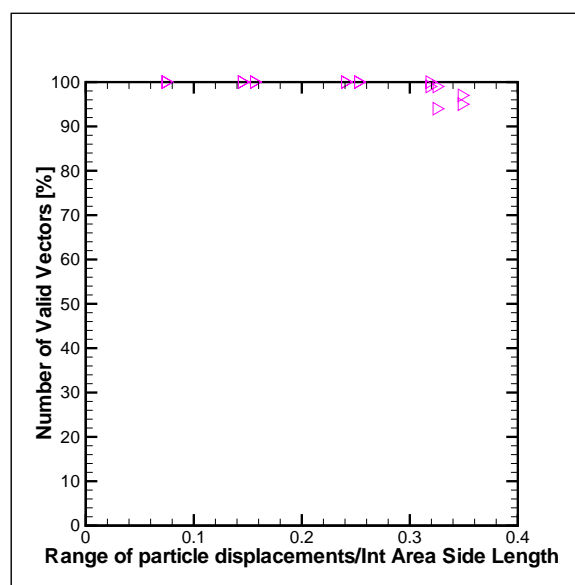(b) Predictor Corrector FFT

(c) Super Resolution FFT
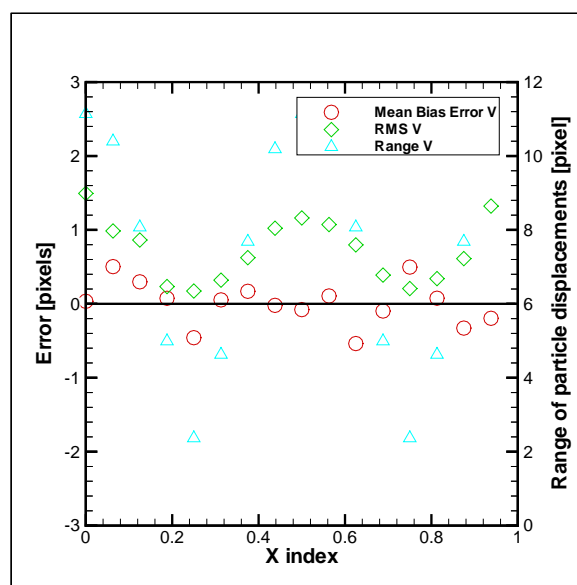
(d) Deformed FFT

Figure 5.23: Mean bias error, RMS error and range of displacements within an interrogation area for sinusoid displacement function (a) Standard FFT (b) Predictor Corrector FFT (c) Super Resolution FFT (d) Deformed FFT

The total error versus the range of displacements within the interrogation area was shown for the sinusoid images in Figure 5.24. The variation in the total error increases with the range of particle displacements within the interrogation area, for all four cross-correlation schemes. The rate of growth in the variance of the total error was smallest for the super resolution FFT algorithm while the other three methods were similar. Note, the scale for the range of particle displacements for the super resolution FFT method, Figure 5.24c, was different than the other three plots. This was due to the smaller range of particle displacements that existed within the interrogation area for the super resolution FFT method compared to the other three algorithms.

Also shown in Figure 5.24 is the connection between the size of the variation in the displacement measurement error and the range of particle displacements that existed within the interrogation area. For the standard FFT method the largest measurement error occurs when the range of particle displacement was 11 pixels and was approximately $\pm$ 5.5 pixels, or one-half the size of the range. This does not suggest that the measurement error was equal to one-half the range of particle displacements within the interrogation area, for the error was also influenced by the particle displacement profile in the interrogation area. However, the largest range of particle displacements occured at an $x_{index} = 0.5$, where the displacement gradient is almost constant across the interrogation area. The maximum difference in the particle displacements from the centre of the interrogation area was $\pm$ 5.5 pixels, due to the linear displacement gradient profile, which was the same error shown in Figure 5.24a. This relationship between the measurement error and the range of particle displacements indicates the error was not a result of the cross-correlation method, as the method was measuring a displacement that existed within the interrogation area. Rather the error was created because the displacement vector was located at the centre of the interrogation area. Similar results can be seen from the other three cross-correlation methods, including the super resolution FFT method which used a smaller interrogation area.

To account for the smaller range of particle displacements within the interrogation area for the super resolution FFT method the range of particle displacements was normalised with the interrogation area side length. Figure 5.25 shows the RMS error versus the normalised range of particle displacements within the interrogation area. Now the scales on the axes for all four plots in Figure 5.25 are the same. The RMS error increases with the range as expected, with the super resolution FFT method increasing the slowest. For the other three methods, the rate at which

(a) Standard FFT

(b) Predictor Corrector FFT
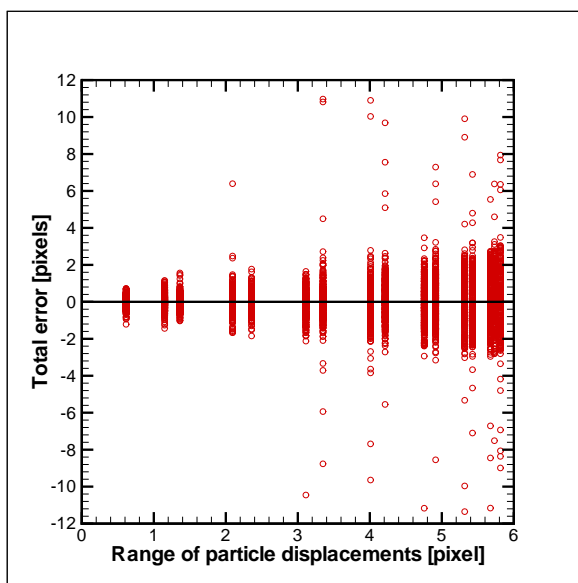
(c) Super Resolution FFT

(d) Deformed FFT

Figure 5.24: Total error for validated measurements vs range of displacements within an interrogation area for sinusoid displacement function (a) Standard FFT (b) Predictor Corrector FFT (c) Super Resolution FFT (d) Deformed FFT (Note: change in horizontal scale in (c))
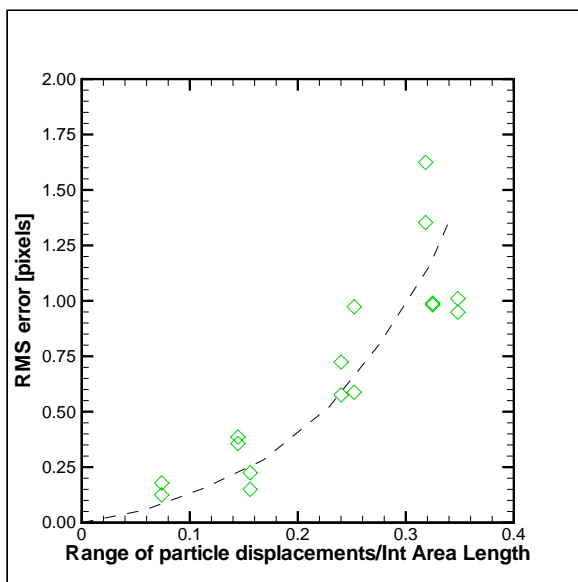
(a) Standard FFT
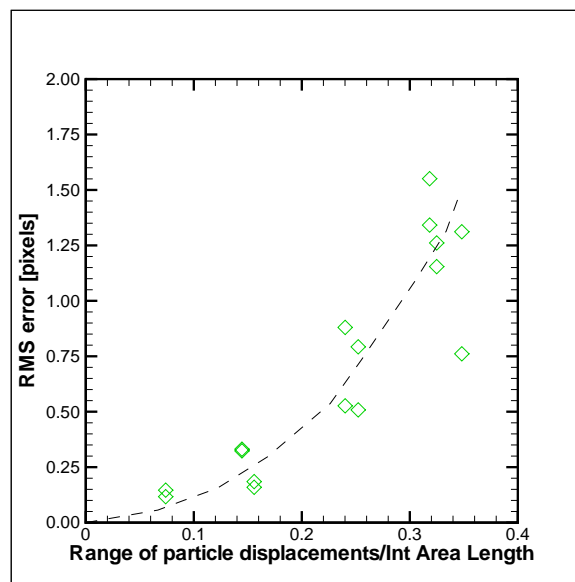
(b) Predictor Corrector FFT
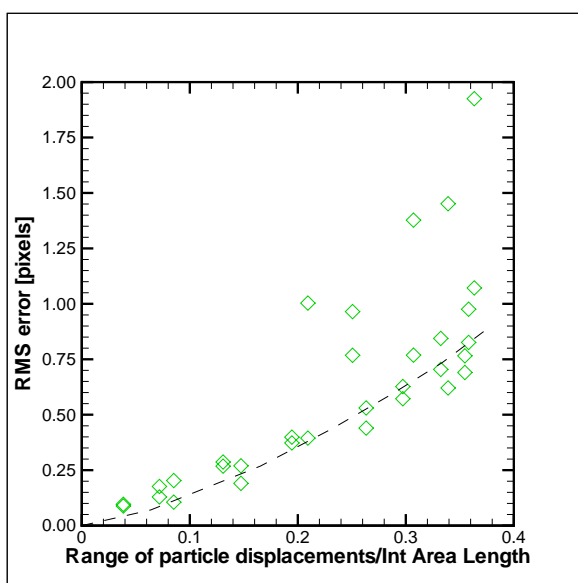
(c) Super Resolution FFT
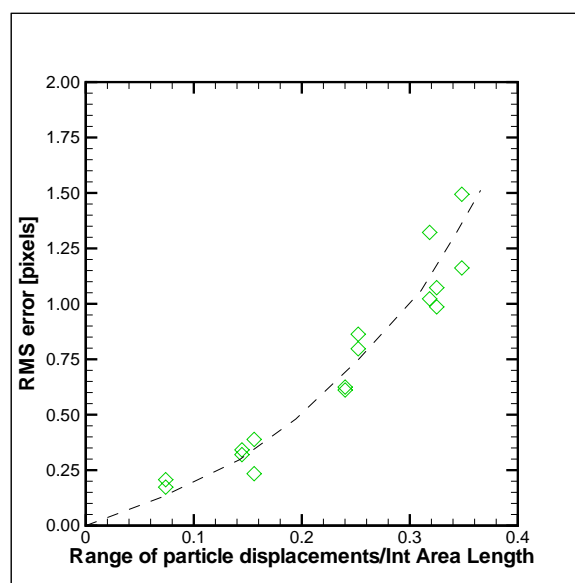
(d) Deformed FFT

Figure 5.25: RMS error vs the range of displacements within an interrogation area, normalised by the side length of the interrogation area for sinusoid velocity function (a) Standard FFT (b) Predictor Corrector FFT (c) Super Resolution FFT (d) Deformed FFT (Note: trend lines are for visual purposes only)

the RMS error increases was similar. However, from Figure 5.25, if the displacement gradient within the interrogation areas was below one-quarter of the side length of the interrogation area the RMS error will be less than 1 pixel for all four cross-correlation strategies.

Number of Valid Vectors

An important factor when investigating the robustness of the four cross-correlation strategies is the number of valid vectors. Figure 5.26 shows the percentage of valid vectors used in determining the ensemble average, the mean bias error and the RMS error, versus the x_{index}. The predictor corrector FFT showed a slight improvement over the standard FFT method with an increase from 35% to 40% in the lowest region. The super resolution FFT method increased the number of valid vectors to 60% compared to the deformed FFT which used over 90% of the displacement vectors for all values of x_{index}. The high number of valid vectors for the deformed FFT method resulted from the choice of validation strategy used, which was peak validation. The objective of the deformed FFT was to create a uniform displacement throughout the interrogation area, such that every particle moved with the same displacement, resulting in more particles contributing to the displacement peak relative to the other peaks. If another validation strategy were used, such as nearest neighbours as described in Section 2.3.2, the number of valid vectors may have decreased.

The number of valid vectors decreased in regions of high gradient, *i.e.* in areas where the displacement gradient was highest, *i.e.* $x_{index} = 0.5$. Figure 5.27 shows the percentage of valid vectors versus the range of displacements within the interrogation area normalised with the interrogation area side length. When the range of particle displacements increased the number of valid vectors decreased for all four cross-correlation methods. The standard FFT and predictor corrector FFT methods decreased the most with the range of displacements while the deformed FFT algorithm only showed a slight decrease.
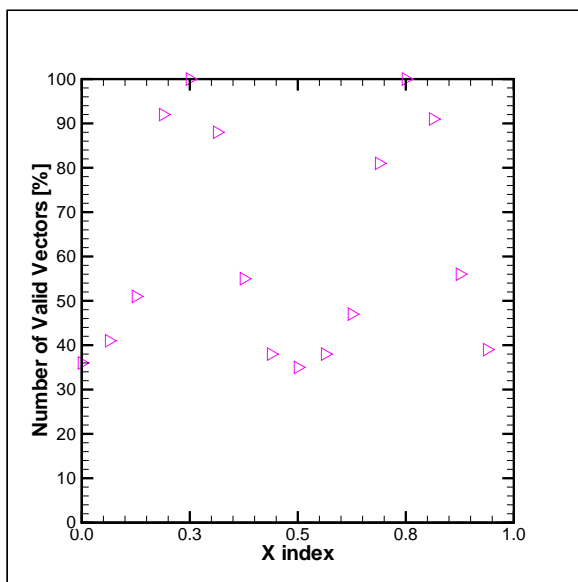
(a) Standard FFT
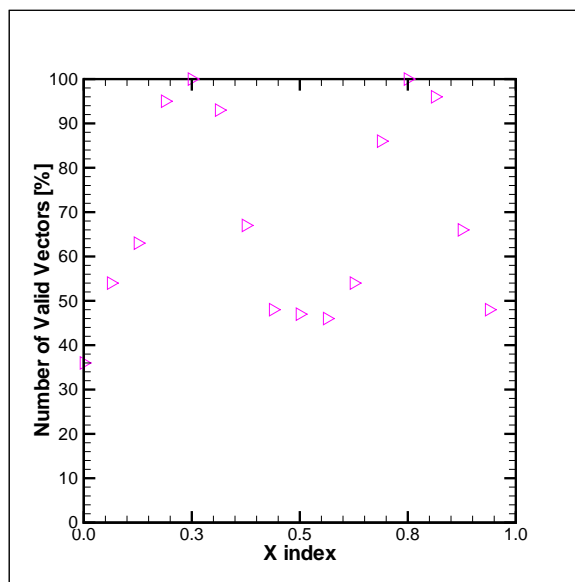
(b) Predictor Corrector FFT
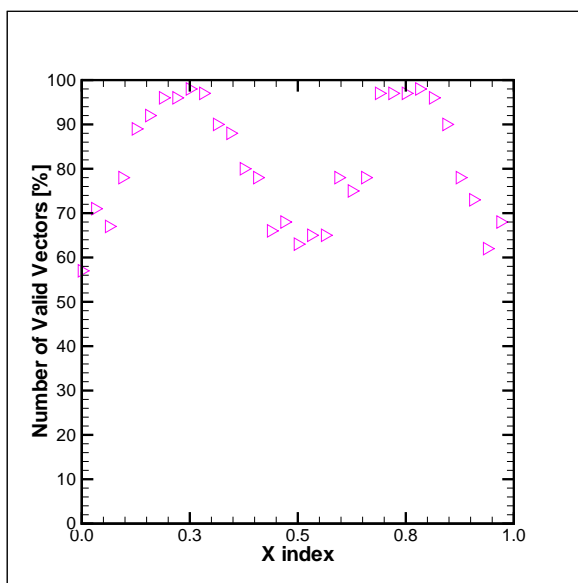
(c) Super Resolution FFT
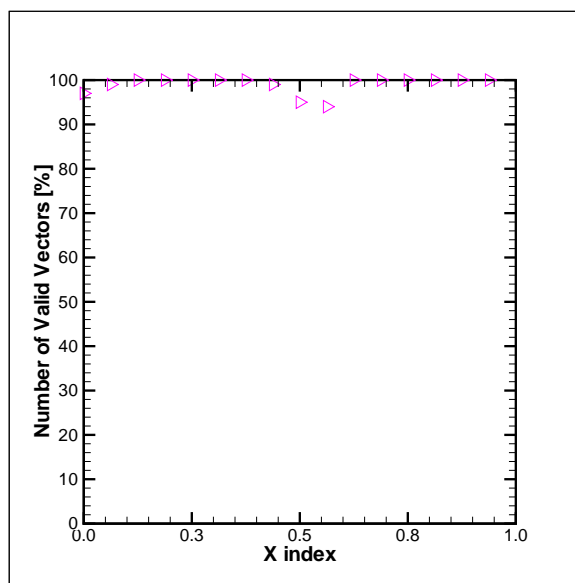
(d) Deformed FFT

Figure 5.26: Percentage of valid vectors for sinusoid displacement function (a) Standard FFT (b) Predictor Corrector FFT (c) Super Resolution FFT (d) Deformed FFT
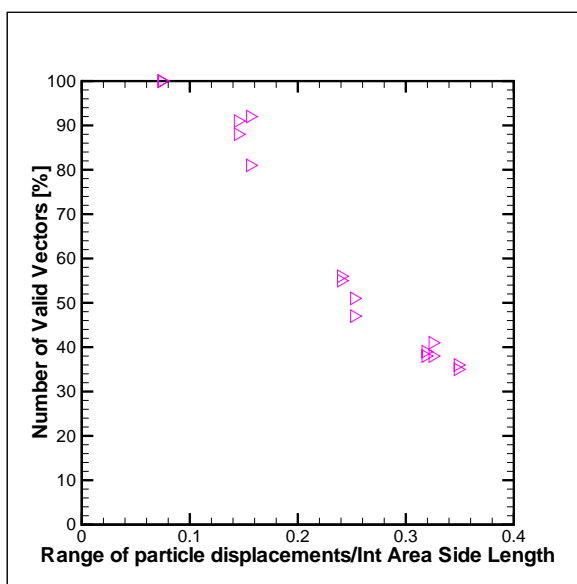
(a) Standard FFT
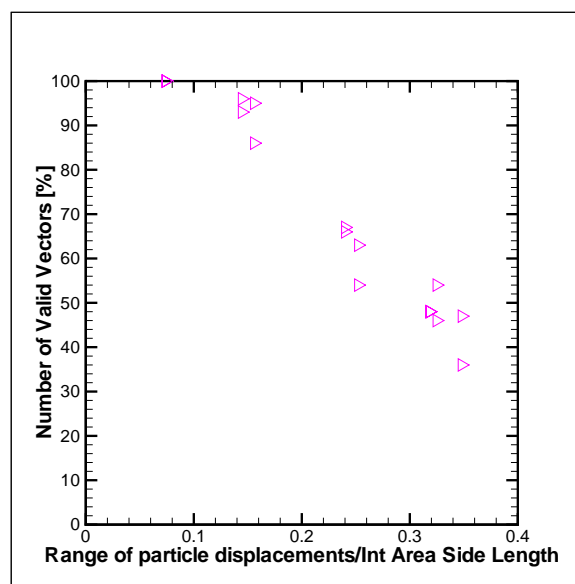
(b) Predictor Corrector FFT

(c) Super Resolution FFT

(d) Deformed FFT

Figure 5.27: Percentage of valid vectors vs the range of displacements within an interrogation area, normalised by the interrogation area side length for sinusoid displacement function with minimum and maximum displacements for each interrogation area (a) Standard FFT (b) Predictor Corrector FFT (c) Super Resolution FFT (d) Deformed FFT

5.5.3   Step, Sawtooth and Sinusoid Images Summary

Spatial Resolution

Unlike the uniform translation images, the step, sawtooth and sinusoid images contained displacement gradients, thus the spatial resolution of the displacement vectors was important. For the step images, the measurement error in the super resolution FFT and deformed FFT methods caused the ensemble average vector plot to inaccurately estimate the particle displacements near the step. The standard FFT and predictor corrector FFT methods both produced results that contained the actual sharp corners in the displacement profile.

For the averaged sawtooth and sinusoid displacement images, the definition of the displacement profile was best represented with the super resolution FFT strategy. This was due to the increase in the number of vectors (twice as many across the image as the other three cross-correlation methods) which was a result of the smaller interrogation areas used in the final iteration.

Dynamic Range

The dynamic range refers to the span of displacements each cross-correlation method was capable of measuring. Due to the one-quarter rule imposed on the maximum displacement, the super resolution FFT scheme had the largest dynamic range. The first iteration performed by the super resolution FFT method used a 64x64 pixel interrogation area, which was capable of accurately measuring a $\pm$ 16 pixel displacement, based on the one-quarter rule. The subsequent iterations reduced the interrogation area size until it reached a 16x16 pixel area. The other three cross-correlation strategies used the same size interrogation area, a 32x32 pixel area, for each iteration, which is capable of accurately measuring only an $\pm$ 8 pixel displacement. As well, none of the methods evaluated appeared to have difficulty with the resolution of small displacements, as shown in the uniform images. Therefore the super resolution FFT scheme had the best dynamic range of the four cross-correlation methods examined for the step, sawtooth and sinusoid images.

Accuracy

Similar to the spatial resolution, the method with the highest accuracy was not the same for the step, sawtooth and sinusoid images. For the step images the predictor corrector FFT method had the lowest mean bias error (0.1 pixels) throughout the image, as well as the lowest RMS error (0.02 pixels) compared to the other three cross-correlation methods.

In the sawtooth and sinusoid displacement images a bias in the measurements of the maximum displacements was seen in the standard FFT, predictor corrector FFT and the super resolution FFT scheme, as each method underestimated the displacement. The deformed FFT algorithm was the only measurement technique that had displacement vectors that were equal to or greater than the maximum displacements. This resulted in a smaller bias error for the deformed FFT method compared to the other three cross-correlation methods.

When examining the total error for every validated measurement, the range of the error for the super resolution FFT scheme was much smaller than for the other three cross-correlation strategies. This was a direct result of the smaller interrogation areas used in the super resolution FFT method which had a smaller range of displacements within the interrogation areas. Furthermore, when comparing the mean bias error and the RMS error for the entire image, the super resolution FFT method was slightly better than the deformed FFT scheme. Therefore, the super resolution FFT method was the most accurate of the four cross-correlation strategies evaluated for the sawtooth and sinusoid displacement images.

Robustness

The robustness of the cross-correlation strategies was judged by the number of validated vectors produced by each method. The deformed FFT scheme validated nearly all of the possible displacement vectors, suggesting it was the most robust method. The standard FFT method eliminated the most displacement vectors of the four cross-correlation schemes with the applied validation strategy. This shows the advantage of using multiple iterations. If an invalid displacement vector was discovered at a location, it could replaced with a valid displacement vector during the subsequent iterations.

However, the super resolution FFT method was less robust than the standard FFT scheme since it produced many displacement vectors that were validated but were clearly measuring an incorrect displacement. This was more detrimental than eliminating over half of the data through validation since erroneous displacement measurements were used in calculating the different flow statistics, such as the average displacement, *etc.*

5.6 Source and Vortex Images

Turbulent flows generally contain gradients in more than a single direction. Therefore, the source and vortex displacement functions were employed to generate images to investigate the effect that displacement gradients in both the horizontal and vertical directions have on the results from each cross-correlation algorithm. The source images contained a line source that scaled with the radius, *i.e.* the displacements were purely radial with the centre of the image as the origin. Figure 5.28 shows the displacement profile for a typical source image. The vortex images
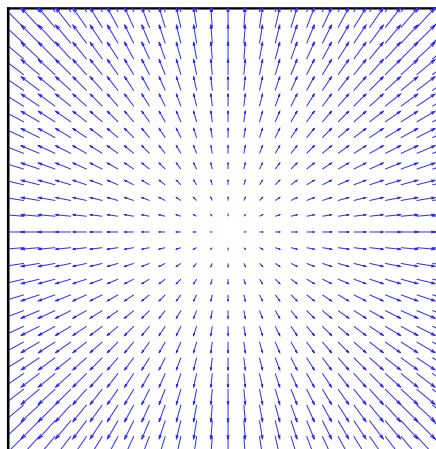
Figure 5.28: Vector plot for a source image

were created using only a rotational displacement which scaled with the distance from the centre of the vortex, as shown in Figure 5.29.

For the results shown, the maximum displacement for both types of images was 8 pixels, which occured at the corners of the images. Therefore, the displacement gradient, which was constant in the radial direction for both the source and vortex images, was 0.025 *pixels/pixel*. The displacement gradient experienced by particles in the source and vortex images was much smaller compared to the maximum 0.4 *pixels/pixel* gradient experienced by particles in the sinusoid images with a period of 128 pixels.

5.6.1 Source and Vortex Analysis

To reduce the number of plots, the results shown are for a particle diameter of 4 pixels and 15 particles per 32x32 pixel area. Since the source and vortex images were axisymmetric, the horizontal $[u]$ and vertical $[v]$ displacements were converted into radial $[v_r]$ and angular $[v_\theta]$
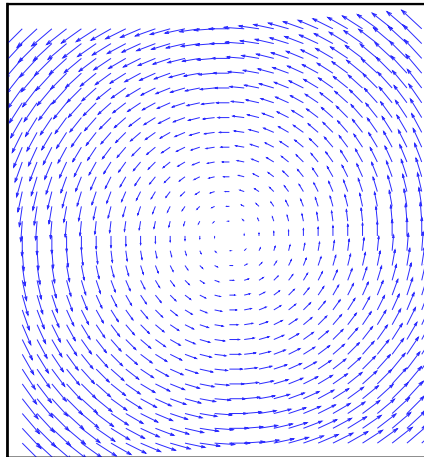
Figure 5.29: Vector plot for a vortex image

displacements using Equations 5.5 and 5.6, and were plotted versus the radius $[r]$.

$$v_r = u \cdot \frac{x}{r} + v \cdot \frac{y}{r} \qquad (5.5)$$

$$v_\theta = u \cdot \frac{y}{r} - v \cdot \frac{x}{r} \qquad (5.6)$$

Since the source images only contain angular displacements, the error in the radial direction was only result of the sub-pixel interpolation. Therefore, only the displacement results in the angular direction are discussed regarding the source images. Similarly, for the vortex images, only the radial displacement measurements are examined.

Since the displacement measurements occurred on a Cartesian grid, the conversion of the location of the displacement vector to polar co-ordinates resulted in vectors at different radii. Therefore, the results could not be averaged as was the case for the step, sawtooth and sinusoid displacement images, and the mean bias error and the RMS error could not be calculated as a function of the radius. Instead, the 10th, 50th and 90th percentiles were determined to evaluate the displacement measurement results. The 50th percentile represents the median displacement measurement and will represent the bias in the cross-correlation method. The difference between the 10th and 90th percentiles represents the amount of variation in the displacement measurements, *i.e.* the random error.

5.6.2   Source and Vortex Results

Figure 5.30 contains every individual validated displacement measurement along with the exact particle displacement as a function of the radius for the source images with a particle diameter of 4 pixels and a particle number density of 15 particles per 32x32 pixel area. The error in the displacement measurements was much lower than that of the step, sawtooth and sinusoid images, even though there were displacement gradients in two directions for the source images. This was due to the magnitude of the displacement gradients in the source and vortex images. As mentioned earlier, the maximum gradient within a single 32x32 pixel interrogation area was less than 0.025 pixel/pixel for the source images, compared to 0.4 pixel/pixel for the sinusoid images with a period of 128 pixels. Therefore the displacement gradient was very small across

(a) Standard FFT

(b) Predictor Corrector FFT

(c) Super Resolution FFT

(d) Deformed FFT
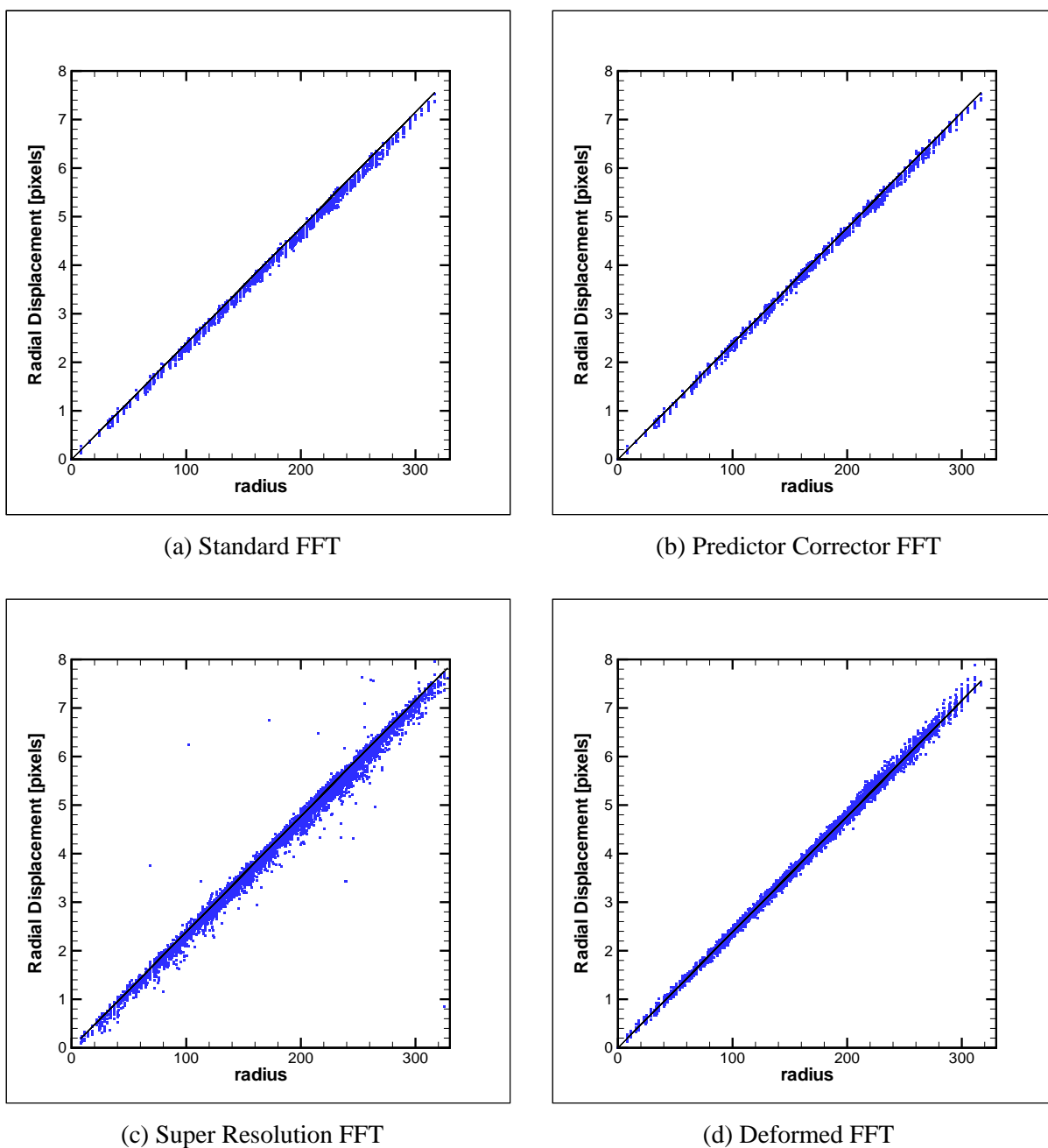
Figure 5.30: Every validated measurement for source displacement function with minimum and maximum displacements for each interrogation area with a particle size of 4 pixels in diameter and a particle number density of 15 particles per 32x32 pixel area (a) Standard FFT (b) Predictor Corrector FFT (c) Super Resolution FFT (d) Deformed FFT

the interrogation area for the source and vortex images. And as shown with the step, sawtooth and sinusoid images, the displacement measurement error was dependent on the range of the particle displacement within the interrogation area.

Similar to the results seen for the sinusoid displacement images, the super resolution FFT method produces displacement measurements which were validated, but were not measuring the correct particle displacement. Again, these outliers were a result of the smaller interrogation areas used by the super resolution FFT method. The smaller interrogation areas contained fewer particles than the other three cross-correlation strategies, approximately one-quarter. Therefore, fewer particles contributed to the true displacement peak. In the case of the outliers, the noise peak in the correlation plane was greater than 1.3 times (the value of the applied peak validation) the displacement peak. Similar to the results for the sinusoid images, the outliers may be removed with a higher peak validation or other validation strategies, as described in Section 2.3.2.

Also shown in Figure 5.30 were the tendencies of the standard FFT, predictor corrector FFT and super resolution FFT methods to underestimate the particle displacements while the deformed FFT method appeared to produce measurements both above and below the actual particle displacements. Similar results are shown for the vortex images in Figure 5.31.

To show the error in the displacement measurements for each cross-correlation strategy evaluated, Figure 5.32 shows the total error versus the radius for the source images. Lines representing the 10th, 50th and 90th percentiles of the total error in the displacement measurements are included in Figure 5.32. The exact values for the 10th, 50th and 90th percentiles are also shown in Table 5.2.

The bias towards measuring displacements less than the actual particle translation was evident for the standard FFT, predictor corrector FFT and the super resolution FFT methods with a 50th percentile of -0.102, -0.055 and -0.066 pixels respectively. However, the 50th percentile for the deformed FFT method was nearly zero with a value of -0.002 pixels, and thus there was almost no bias in the measurements.

The variation in the displacement measurements can be evaluated using the difference between the 10th and 90th percentiles. The super resolution FFT method had a much larger variation,
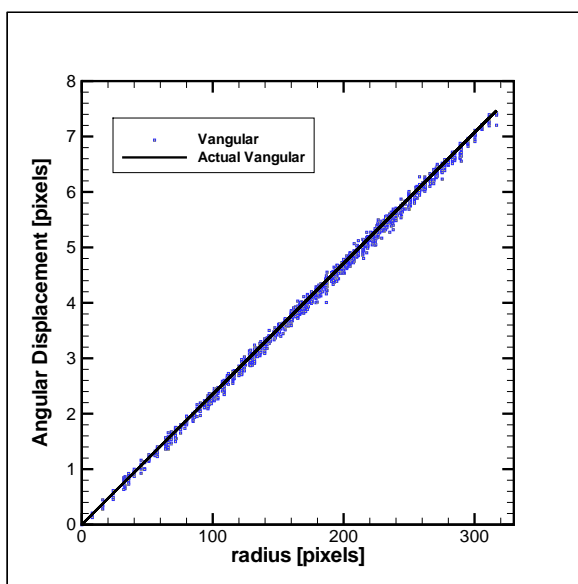
(a) Standard FFT
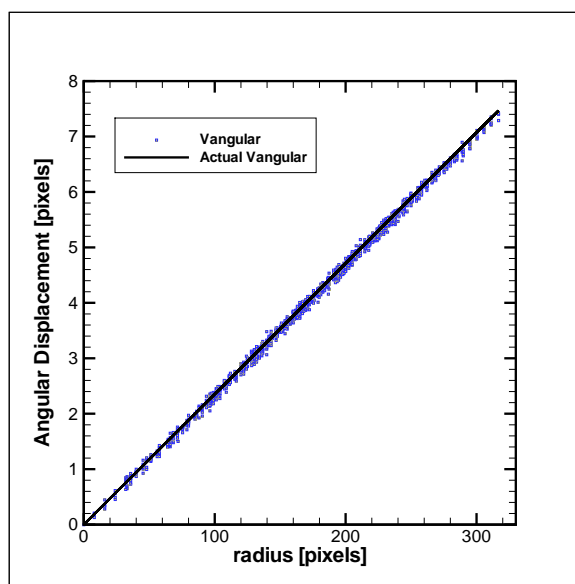
(b) Predictor Corrector FFT
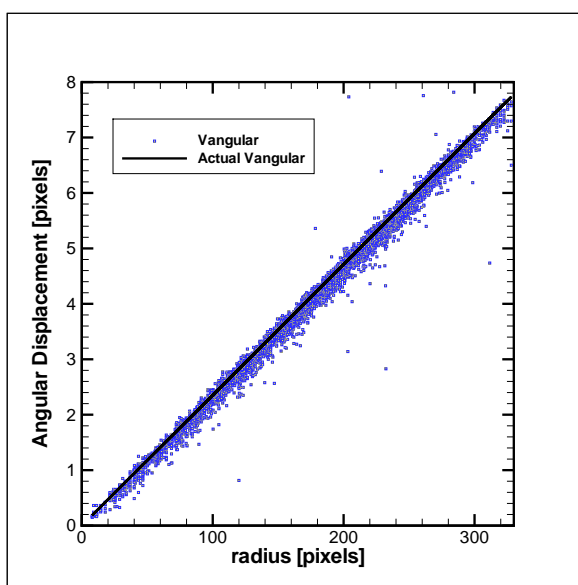
(c) Super Resolution FFT
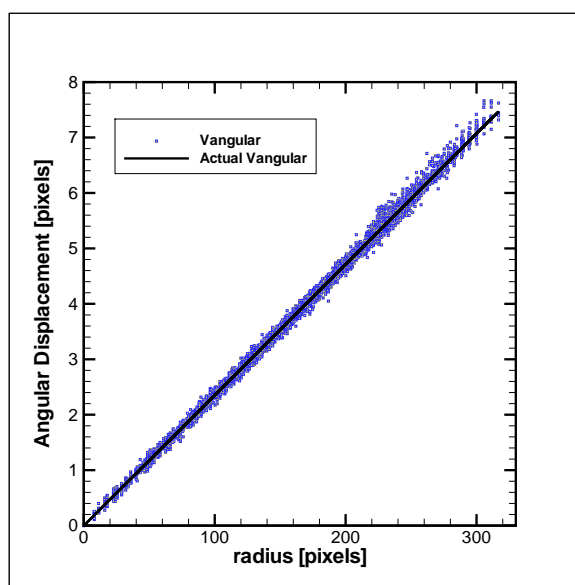
(d) Deformed FFT

Figure 5.31: Every validated measurement for vortex displacement function with minimum and maximum displacements for each interrogation area with a particle size of 4 pixels in diameter and a particle number density of 15 particles per 32x32 pixel area (a) Standard FFT (b) Predictor Corrector FFT (c) Super Resolution FFT (d) Deformed FFT
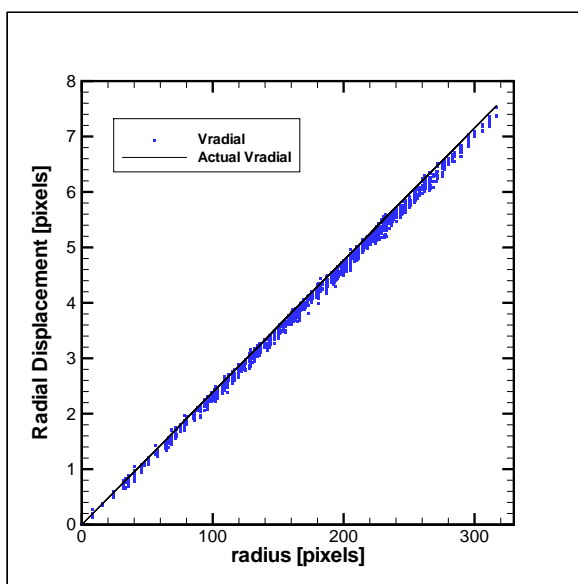
(a) Standard FFT
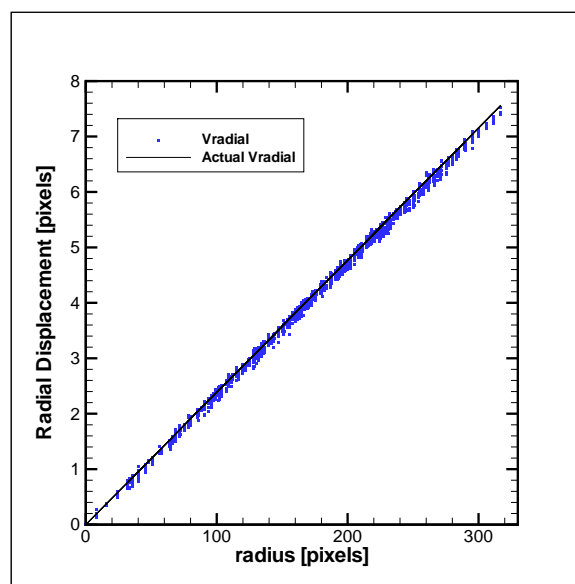
(b) Predictor Corrector FFT
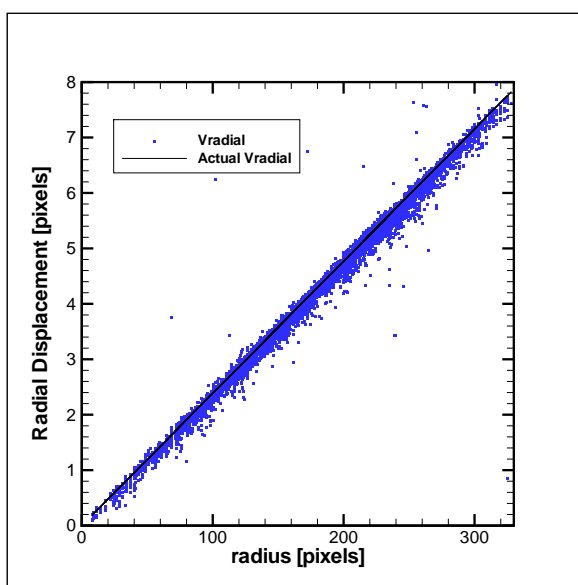
(c) Super Resolution FFT
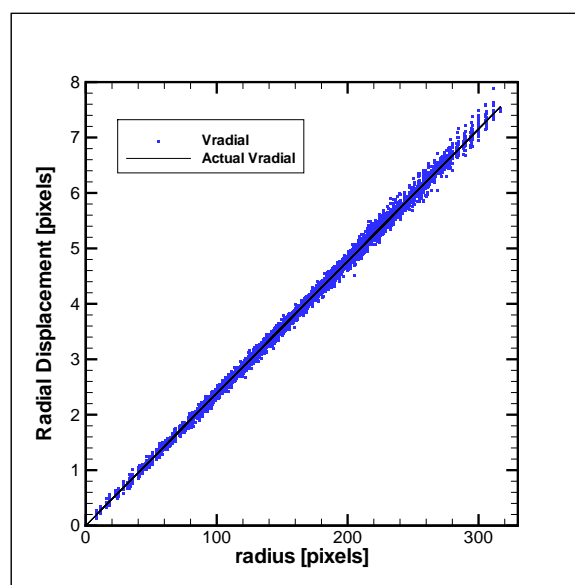
(d) Deformed FFT

Figure 5.32: Total error for validated measurements for source displacement function with minimum and maximum displacements for each interrogation area with a particle size of 4 pixels in diameter and a particle number density of 15 particles per 32x32 pixel area (a) Standard FFT (b) Predictor Corrector FFT (c) Super Resolution FFT (d) Deformed FFT

Cross-correlation method	10th percentile	50th percentile	90th percentile	Difference between 10th and 90th percentiles
Standard FFT	-0.194	-0.102	-0.019	0.176
Predictor Corrector FFT	-0.140	-0.055	0.024	0.164
Super Resolution FFT	-0.221	-0.066	0.034	0.256
Deformed FFT	-0.087	-0.002	0.085	0.172

Table 5.2: 10th, 50th and 90th percentile values for the source images with a particle size of 4 pixels in diameter and a particle number density of 15 particles per 32x32 pixel area

Cross-correlation method	10th percentile	50th percentile	90th percentile	Difference between 10th and 90th percentiles
Standard FFT	-0.132	-0.047	0.038	0.170
Predictor Corrector FFT	-0.115	-0.035	0.042	0.157
Super Resolution FFT	-0.206	-0.058	0.040	0.247
Deformed FFT	-0.084	0.005	0.094	0.178

Table 5.3: 10th, 50th and 90th percentile values for the vortex images with a particle size of 4 pixels in diameter and a particle number density of 15 particles per 32x32 pixel area

0.256 pixels, compared to the other three methods, which all had similar ranges between the 10th and 90th percentiles, approximately 0.17 pixels.

Also shown in Figure 5.32d was the increase in the total error for some displacement measurements produced using the deformed FFT method at a radius of approximately 300 pixels. This increase in the error occurs at the corners and edges of the image. Since there were no vectors beyond the corners or edges of the image, extrapolation was required to determine the amount to deform the interrogation area, which was less accurate than the bi-linear interpolation used everywhere else. This decrease in accuracy caused an increase in the error for some measurements at values of extreme radius. Similar results are shown for the vortex images in Figure 5.33 and Table 5.3.

(a) Standard FFT

(b) Predictor Corrector FFT

(c) Super Resolution FFT

(d) Deformed FFT
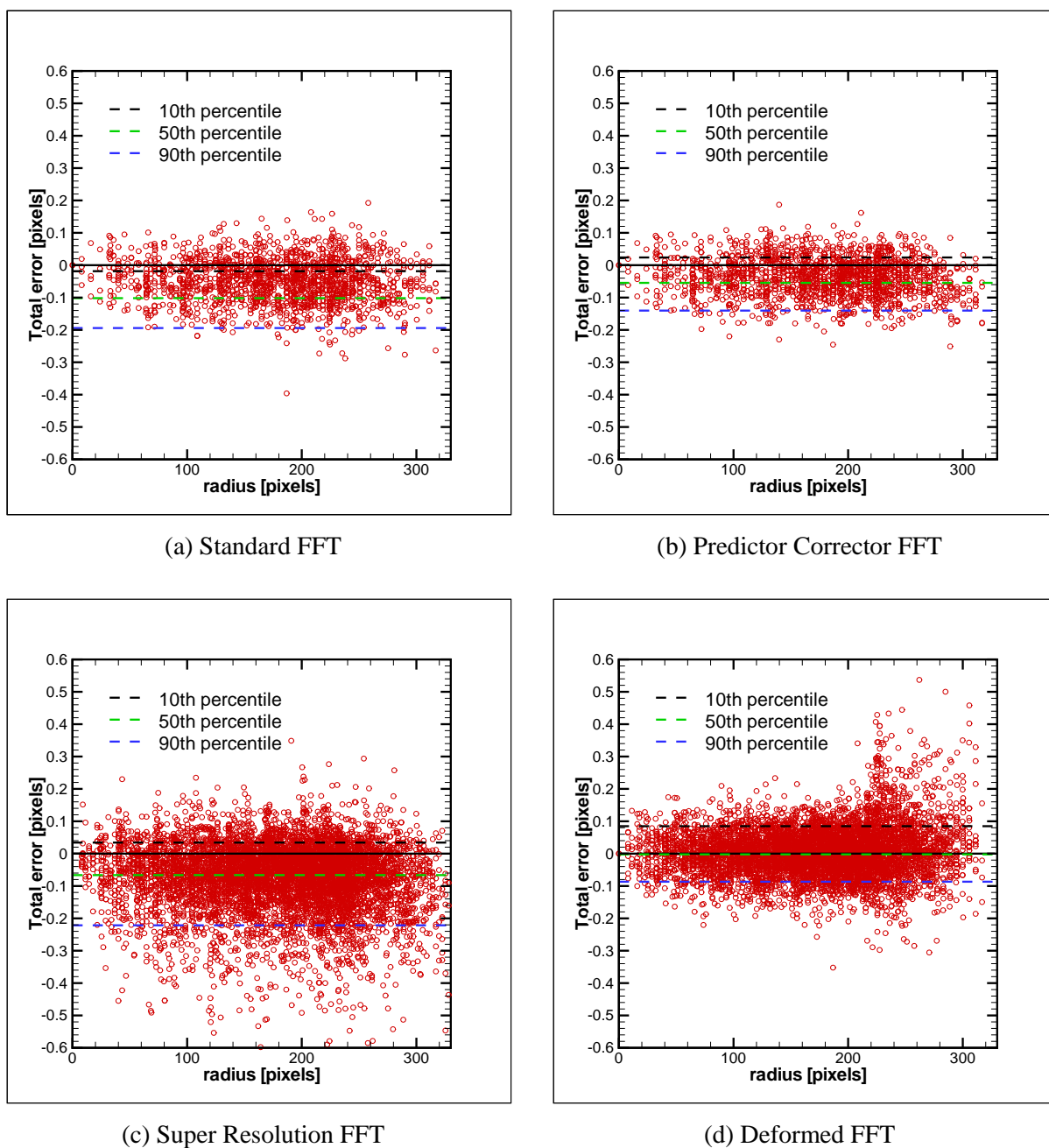
Figure 5.33: Total error for validated measurements for vortex displacement function with minimum and maximum displacements for each interrogation area with a particle size of 4 pixels in diameter and a particle number density of 15 particles per 32x32 pixel area a) Standard FFT b) Predictor Corrector FFT c) Super Resolution FFT d) Deformed FFT

5.6.3 Source and Vortex Images Summary

Spatial Resolution

The displacement profile in the source and vortex images are linear, unlike the step, sawtooth and sinusoid images. As a result, the spatial resolution was not as critical. However, the super resolution FFT method was able to produce displacement vectors closest to the centre of the image.

Dynamic Range

The dynamic range refers to the span of displacements the cross-correlation strategies were capable of measuring. Since the first iteration for the super resolution FFT method has an interrogation area twice as large as the other three methods, 64x64 versus 32x32 pixel area respectively, the super resolution FFT method is capable of measuring displacements twice as large. Therefore, the super resolution FFT method has the greatest dynamic range of the four cross-correlation algorithms evaluated.

Accuracy

The accuracy of the four cross-correlation strategies was evaluated by comparing the values of the 10th, 50th and 90th percentiles. The 50th percentile was the median displacement measurement and provided an estimate of the bias in the cross-correlation method. The magnitude of the difference between the 10th and 90th percentile provided an estimate of the amount of variation in the measurements, *i.e.* the random error. The deformed FFT method had a 50th percentile approximately equal to zero for both the source and vortex images, while the other three cross-correlation strategies each had a bias towards under-estimating the displacement, each greater than 0.05 pixels. Also, the difference between the 10th and 90th percentiles for the deformed FFT method was the second lowest of the four cross-correlation methods, only the standard FFT scheme was better. Overall, the deformed FFT method was the most accurate of the four cross-correlation strategies evaluated.

Displacement Function	Preferred Method	Reason
Uniform translation	Deformed FFT	Increased accuracy due to sub-pixel offsets
Step	Predictor Corrector FFT	No interpolation required near step
Sawtooth	Super Resolution FFT	Smaller range of displacements within interrogation area
Sinusoid	Super Resolution FFT	Smaller range of displacements within interrogation area
Source	Deformed FFT	Approximately zero bias error
Vortex	Deformed FFT	Approximately zero bias error

Table 5.4: Synthetic image results summary

Robustness

The robustness of the cross-correlation methods was judged by the number of valid displacement vectors produced by each strategy evaluated. Due to the small displacement gradients within the image nearly all the vectors were validated for each cross-correlation method. Therefore, no conclusions can be made regarding the robustness of the cross-correlation strategies from the results of the source and vortex images.

5.7   Summary of Synthetic Results

Table 5.4 shows a summary of the six types of synthetic images evaluated along with the cross-correlation method which produced the best estimates of particle displacements. The uniform translation images were used to determine the least amount of error possible with the cross-correlation strategies. The most accurate results had a mean bias error of 0.03 pixels and an RMS error of 0.03 pixels, both produced by the deformed FFT method. Larger interrogation areas were determined to be more accurate, although little improvement was seen between 32x32 and 64x64 pixel areas, due to the uniform nature of the flow. The deformed FFT algorithm

produced the least amount of error since it was capable of sub-pixel offsets of the interrogation areas between iterations.

The Gaussian sub-pixel interpolation scheme was determined to be more accurate than the parabolic scheme, due in part to the particles being modelled with a Gaussian distribution. It was also determined that a particle diameter of 3-5 pixels produced the smallest RMS error for all four methods, while each method gave better results at higher particle number densities.

The step images contained an infinite displacement gradient at the location of the step. The inability of the super resolution FFT and deformed FFT methods to interpolate in the area around the step reduced their accuracy in high displacement gradient situations. Since the other two methods, the standard FFT and predictor corrector FFT, did not use any interpolation they were able to measure the displacement near the step successfully. Therefore, in flows where a very high displacement gradient exists, the predictor-corrector FFT method should be employed, since it is more robust and slightly more accurate than the standard FFT method.

The sawtooth and sinusoid images contained large, but finite, displacement gradients in a single direction. The RMS error was found to increase with the range of displacements, *i.e.* due to the existence of more displacements within a single interrogation area a larger range of displacements were measured. As such, the displacements measured did not always exist at the centre of the interrogation area, as was assumed when the displacement vector was placed at the centre of the interrogation area. As a result, a positional bias error was introduced into the results. The smaller interrogation areas provided with the super resolution FFT method improved the accuracy of the results due to the smaller range of displacements and the fact that the maximum positional bias error was dependent on the interrogation area size.

When the range of displacements within a interrogation area was below one-quarter of the interrogation area size, the RMS error was below 1 pixel for each method examined. Also, all the methods consistently under predicted the maximum particle displacements except for the deformed FFT algorithm, which tended to have an equal number of results above and below the true maximum particle displacement.

The deformed FFT used the most vectors, after a peak validation was applied to the final results,

compared to the other cross-correlation methods tested. However, due to the increased spatial resolution, the higher dynamic range and the reduced range of particle displacements within an interrogation area, the super resolution FFT provided the best results for the sawtooth and sinusoid images. Therefore, in flows which contain high frequency displacement gradients the super resolution FFT method should be employed. However, if the deformed FFT method were combined with the super resolution FFT scheme, *i.e.* the interrogation areas in the super resolution FFT method were deformed based on the displacement vector field, the results may improve due to the robustness and accuracy of the deformed FFT algorithm.

In the analysis of the source and vortex images, the impact of displacement gradients in two directions was examined. All four methods showed no signs of difficulty with measuring the displacements in the source or vortex images, due to the relatively small displacement gradients within the interrogation areas. However, similar to the step, sawtooth and sinusoid images, each method consistently under-predicted the displacement except for the deformed FFT scheme, which again produced the same number of results above and below the true displacement. Therefore, due to the reduced bias error and small random error, the deformed FFT method produced the best results for the source and vortex images.

Chapter 6

Experimental Results

6.1 Introduction

Chapter 5 summarised the results from the synthetic images analysed with four different cross-correlation strategies. The synthetic images allowed parameters such as particle size, density of seed particles and particle displacements to be controlled, which was be beneficial when evaluating the cross-correlation methods. However, the parameters mentioned above can not always be controlled in an experimental environment. As a result, the images collected during experiments may not be as ideal and therefore as easy to process as the synthetic images. That is, the particle density may vary throughout the images, the particle intensity may vary between images, *etc.* Therefore it was important to verify the conclusions from the synthetic image results with images collected under realistic experimental conditions.

To confirm the results of Chapter 5, the flow was measured inside a multiple grooved channel using PIV. The multiple grooved channel was chosen since DNS calculations for the channel flow existed, as reported by Yang [1]. The DNS calculations were compared to the PIV velocity measurements to evaluate the success of the cross-correlation methods. This chapter provides an overview of the experimental setup, along with a discussion concerning the velocity measurements, which were collected using both water and air as the flow medium.

6.2   Multiple Grooved Channel

The turbulent flow in a multiple grooved channel was indicative of several industrial flows, including the flow over buildings and the flow between printed circuit boards on which computer chips are aligned. For the case studied, a channel with periodically repeating rectangular blocks which were placed perpendicular to the direction of the main flow was used, as is shown in Figure 6.1. The flow within the grooved channel was similar to that in a channel with a backwards facing step (BFS) where there exists a region of wall-shear on the top of the block as well as a recirculation zone behind the block. The difference between the BFS and the grooved channel was that in the latter, the flow was not fully developed along the top of the block, due to the short length of the block, thus affecting the characteristics of the flow downstream of the block.

The grooved channel was chosen to verify the cross-correlation methods due to the large flow structures that existed within the flow. Regions of wall-shear, free-shear and recirculation all existed within the flow, and were similar to the displacement functions applied to the particles in the synthetic images evaluated in Chapter 5.

Two experiments were performed, one with water as the fluid inside the grooved channel and

Flow Direction
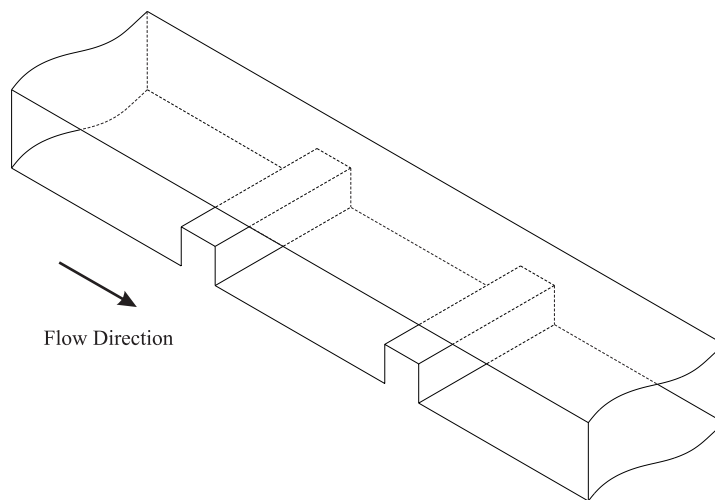
Figure 6.1: Multiple grooved channel setup

the other using air. The properties of each fluid were very different and necessitated the use of different seed particles, thus each medium produced distinct images, as shown in Figure 1.2 and repeated here in Figure 6.2.

6.2.1 Flow Conditions

To perform the experiment using two different fluids, water and air, the concept of Reynolds similarity was applied. This states that two geometrically similar flows using different flow mediums will give the same flow characteristics provided that the Reynolds number is the same for each flow, and the Reynolds number is the dominant parameter of the flow. For the grooved channel, the Reynolds number was based on the mean bulk velocity $[U_m]$ between the upper wall of the channel and the top of the block, as well as the distance between these two walls $[H - h]$.

$$Re = \frac{\rho \cdot U_m \cdot (H - h)}{\mu} \tag{6.1}$$

A Reynolds number of 6900 was used for all the experiments since this was the value used for the DNS calculations reported by Yang [1]. This produced volume flow rates of $Q_w = 0.555 \ litre/s$ and $Q_a = 8.28 \ litre/s$ for the experiments conducted with water and air as the fluid media, respectively.

6.3 Experimental Setup and Components

Schematics of the full experimental setups for the grooved channel are shown in Figures 6.3 and 6.4 for water and air respectively. The setup consisted of a clear acrylic channel with plastic grooves and a flowmeter to monitor the flow rate. Each component will be discussed in the following sections.

6.3.1 Acrylic Channel

The measurements in water and air were made using the same acrylic channel as is shown in Figure 6.5. The floor of the channel was constructed of grey PVC plastic to reduce the amount
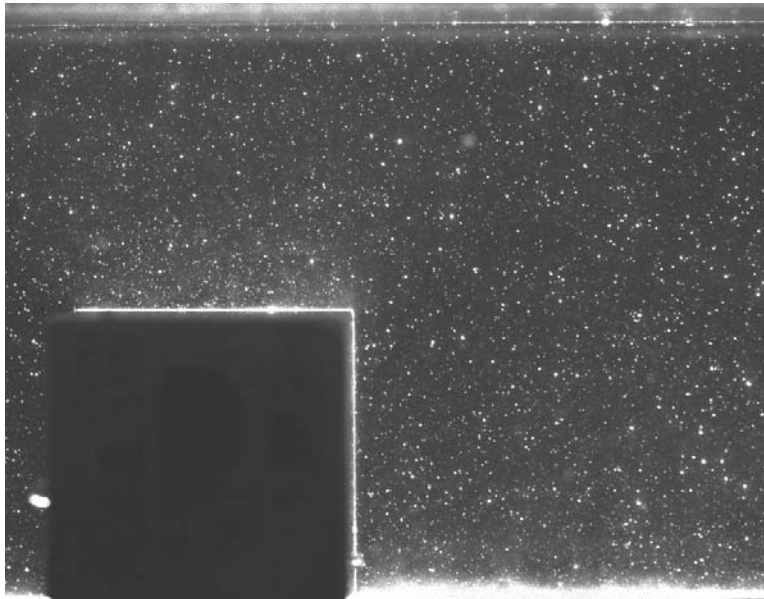
(a) Water
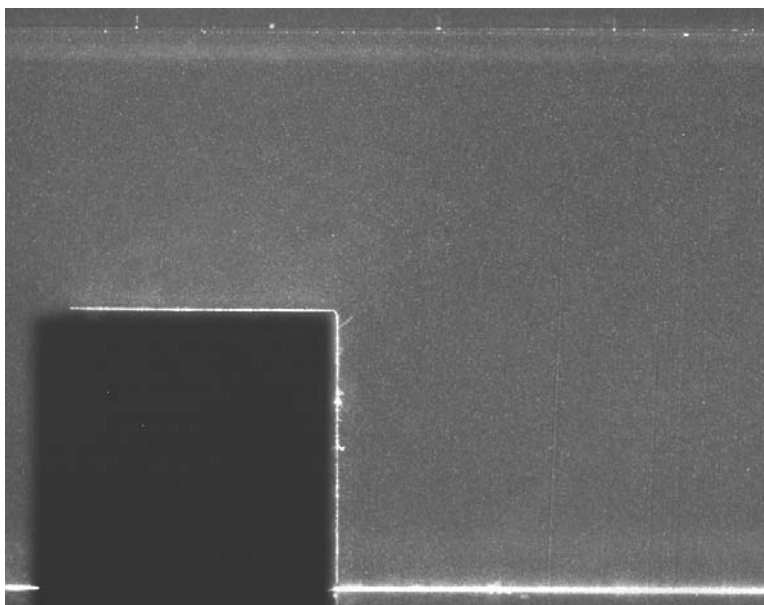
(b) Air

Figure 6.2: Typical seeded PIV images (60mm x 40mm) for (a) water using Pliolite as seed particles and (b) air using mineral oil for seed particles
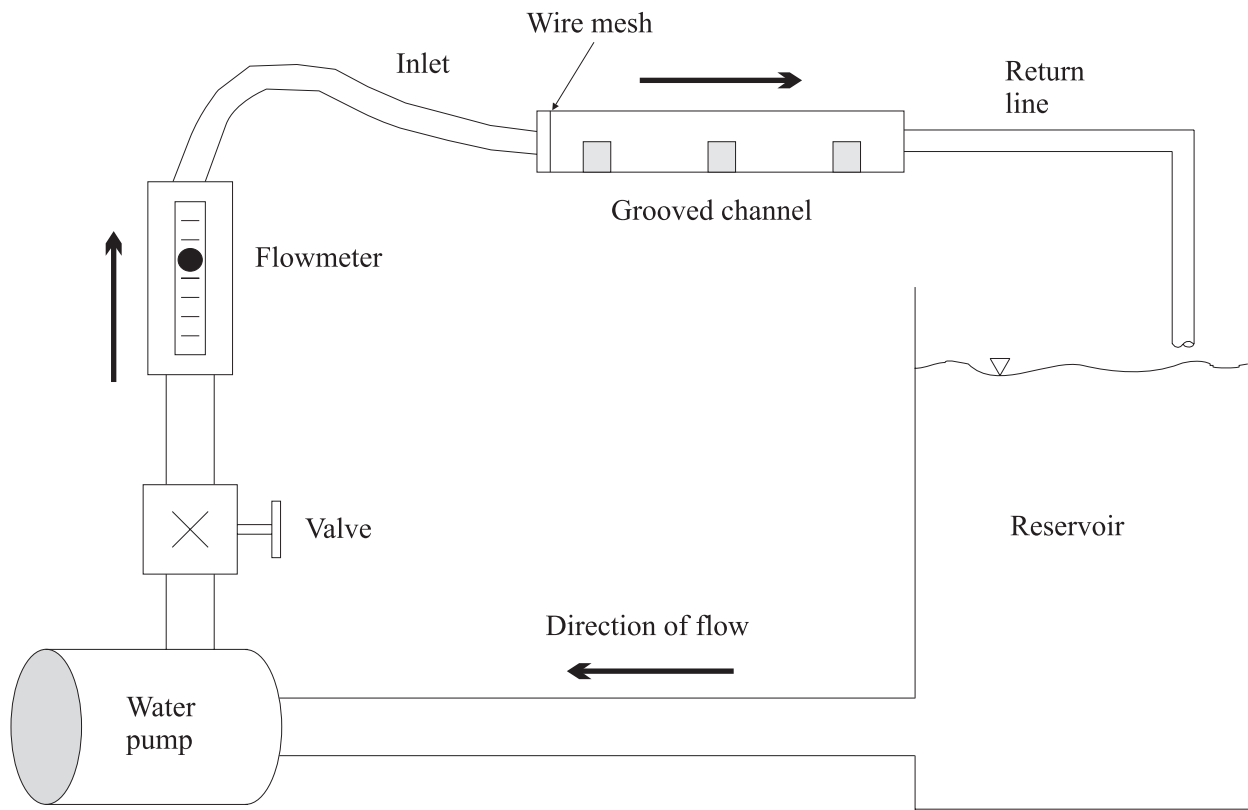
Figure 6.3: Schematic of the experimental setup for water
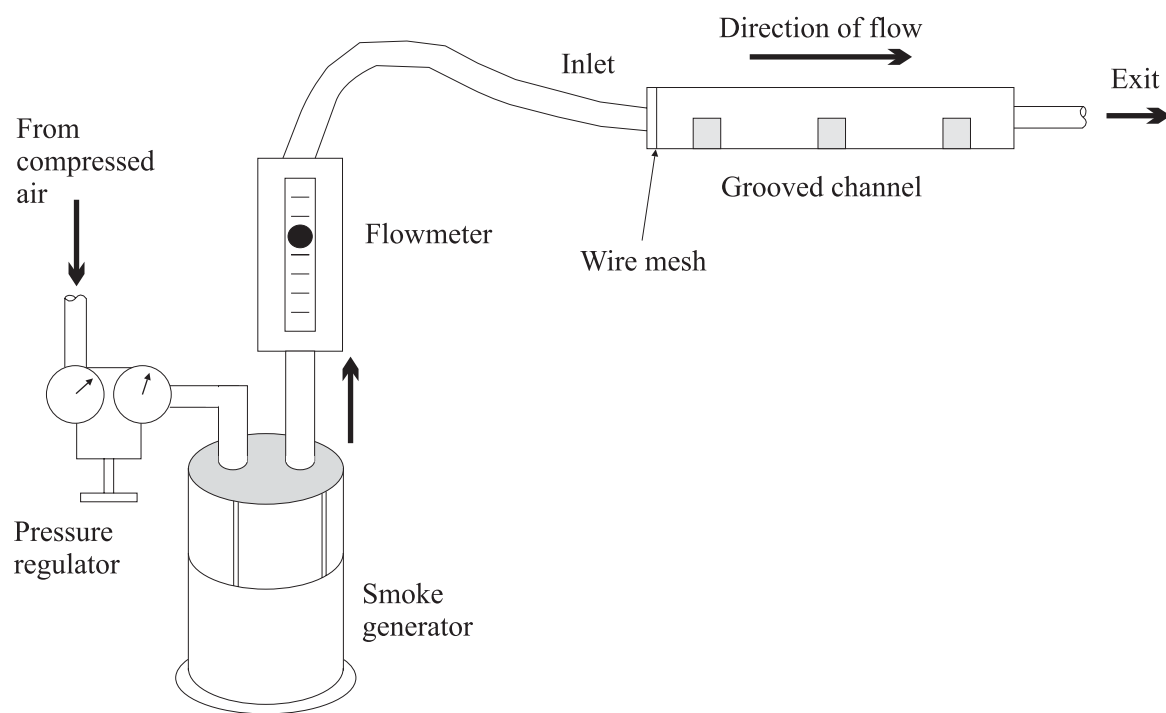
Figure 6.4: Schematic of the experimental setup for air
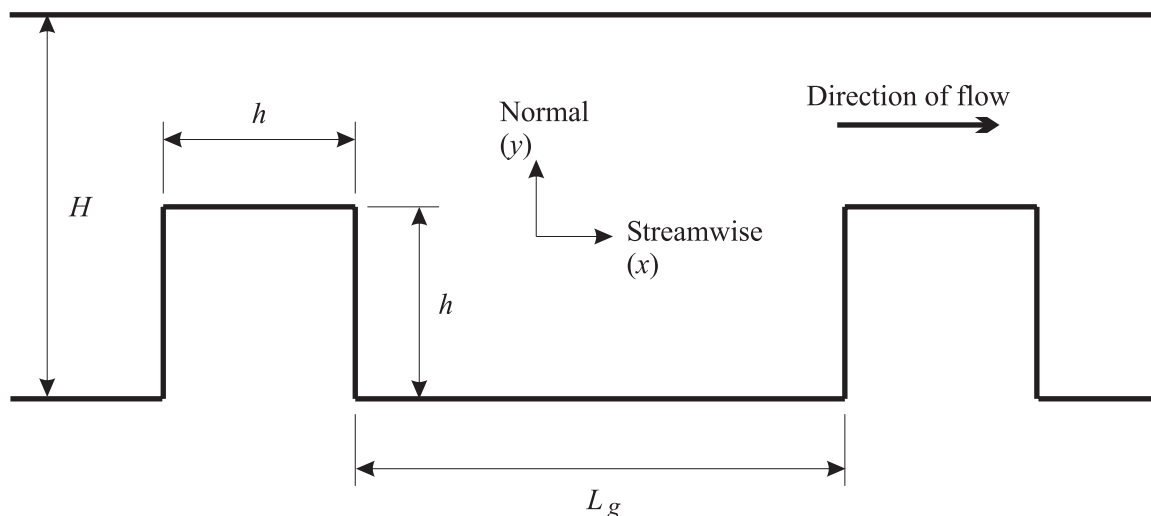
Figure 6.5: Acrylic channel used for experiments

	Dimension
H	4 cm
h	2 cm
W	8 cm
L_g	28 cm

Table 6.1: Multiple grooved channel dimensions

of laser reflection at the surface, and to improve the near wall measurements. The dimensions of the channel are listed in Table 6.1. The channel had an inner cross-section of 8 cm by 4 cm [WxH], with a length of 86 cm. One inch barbed fittings were placed at either end of the channel to connect the inlet and outlet hoses.

Three PVC rectangular blocks created the repeating *grooves*, each 2 cm by 2 cm [hxh] and extended the entire width of the channel. They were placed inside the channel with a spacing of 28 cm between them [L_g]. All measurements were conducted between the second and third grooves to ensure that the flow was fully developed, *i.e.* the effects from the entrance of the

channel had smoothed out. To reduce the inlet effects a 2 *mm* by 2 *mm* wire mesh was placed 1 *cm* from the entrance of the channel to help break up the larger turbulent length scales generated from the flow entrance. The edges of the grooves contained a very slight chamfer compared to the sharp 90° corners used in the DNS calculations.

6.3.2   Water-Based Setup

For the experiments that used water as the fluid, a centrifugal pump was employed to move the water through the channel. The water was pumped from a large reservoir through a valve that was used to control the flow rate, which was monitored with a variable area flowmeter (Omega FL7401). After the flow passed through the channel it returned to the reservoir.

As the water was recirculated through the channel, it was possible for the temperature of the water to rise during the experiment, due to the energy added by the pump, and thus the water temperature was monitored with a thermometer. Due to the relatively large volume of the reservoir ($\sim 1\ m^3$), there was no recorded temperature change for the duration of the experiment.

6.3.3   Air-Based Setup

Although the channel used for the water experiment was identical to that used for the air-based experiments, the method of *pumping* the flow was different. For the air-based experiments compressed air at a pressure of 100 kPa was used as the fluid medium with a pressure regulator to control the amount of flow through the channel. The compressed air first traveled through a smoke generator (where the seed particles were created by burning the mineral oil) before entering the variable area flowmeter (Omega FL7314) and then into the grooved channel. Mineral oil smoke is commonly used for seed particles in air-based PIV experiments [39]. To prevent the temperature of the air from increasing with time due to the smoke generator, the air was not recycled after it passed through the channel. Instead, it was vented to the atmosphere.
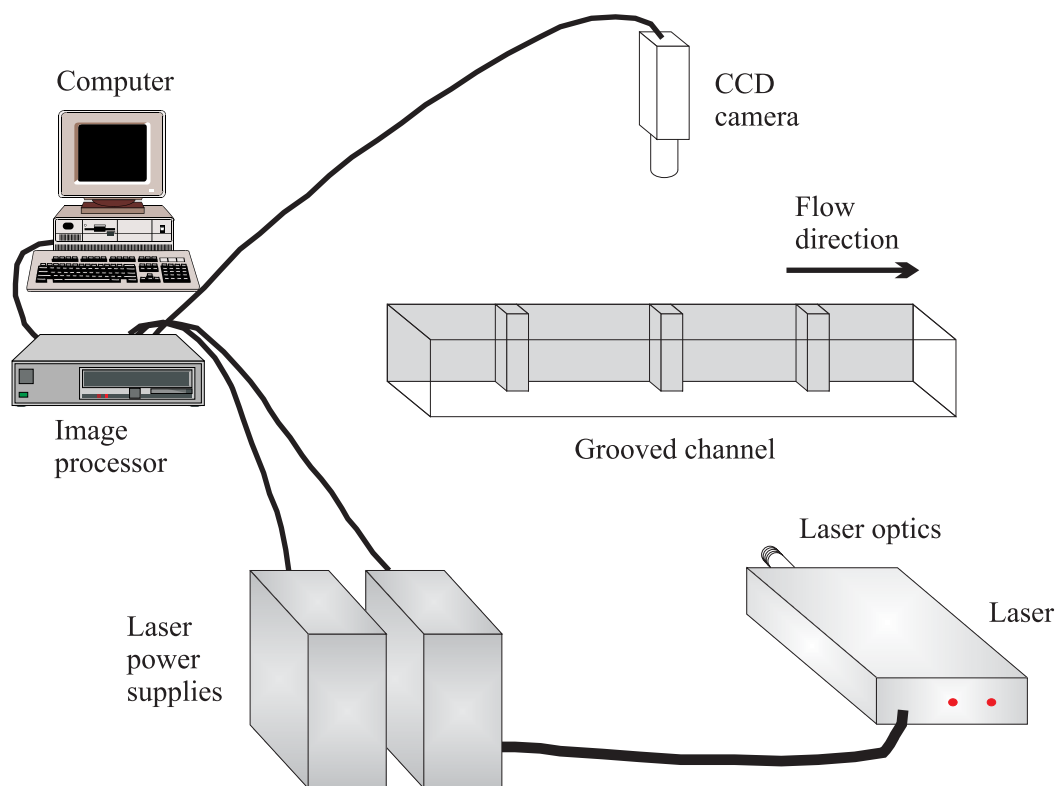
Figure 6.6: PIV Experimental Setup

6.4 PIV Experimental Setup and Components

The PIV experimental setup and its relation to the grooved channel is shown in Figure 6.6. The PIV setup comprised of a laser and laser beam optics, a camera and an image processor. Each component will be described in detail below.

6.4.1 The Laser and Laser Beam Optics

To illuminate the flow for all the experiments, a New Wave Gemini/15Hz dual cavity Nd-YAG laser was used and was capable of generating two $500mJ/5ns$ pulses at a wavelength of $532nm$.

The power used during the experiments was dictated by the intensity of the images, and was always much less than the maximum available.

To create the light sheet, a cylindrical lens was attached to the output of the laser along with a focusing lens. The cylindrical lens spread the beam into a 2-D sheet while the focusing lens controlled the thickness of the laser sheet. The laser sheet thickness was between 1-2 mm for the experiments conducted using both the water and air.

6.4.2   The CCD Camera and Image Processor

To record the location of the seed particles within the laser sheet a Kodak Megaplus ES1.0 CCD camera with 1008x1018 pixel resolution was used. The Kodak Megaplus ES1.0 camera used a combination of light sensitive cells and an equal number of storage cells, the latter are not exposed to light. The light from the first laser pulse was exposed to the light sensitive cells to record the first image. The intensity of the light sensitive cells was then transferred to the storage cells immediately such that the light sensitive cells were ready to record the second image [25, 28]. The data from both types of cells were then transferred to the computer, where the two images were saved.

It was necessary to synchronise the transfer of data from the light sensitive cells to the storage cells with the timing of the laser pulses. This was done using an image processor. For the grooved channel experiments the image processor used was the Dantec 1100 Flow Processor.

6.5   Seed Particles

The Pliolite (by Goodyear) particles used to seed the water-based experiments were polymer based and ranged from 44 to 74 microns in diameter. Before the experiment began, the seed particles were *mixed* into the reservoir and allowed to come to rest overnight. The seed particles that had a specific gravity greater than unity sank to the bottom of the reservoir, while those less with a specific gravity less than unity floated to the top. The remaining seed particles, which

were pumped through the channel, had the same density as the water. It was important that the seed particles be the approximate density of the fluid otherwise they would not follow the flow properly, thus influencing the measurements.

The seed particles used for the air experiment were very different from those used in the water trial. Due to the relatively low density of air the choice of seed particles was limited. For the grooved channel experiments, mineral oil smoke was employed, since it has been shown produce good measurements in air [39]. Mineral oil was heated using a smoke generator, which was placed in line with the air supply before the channel inlet, as shown in Figure 6.4.

6.6 Results

For the experiments conducted, 1000 images were recorded for each of the experiments performed using water and air. The images recorded the motion of the particles in the region before the flow reached the leading edge of the block to approximately one and a half block heights from the trailing edge of the block, as shown in Figure 6.7. The image size was 60 *mm* by 60 *mm* and
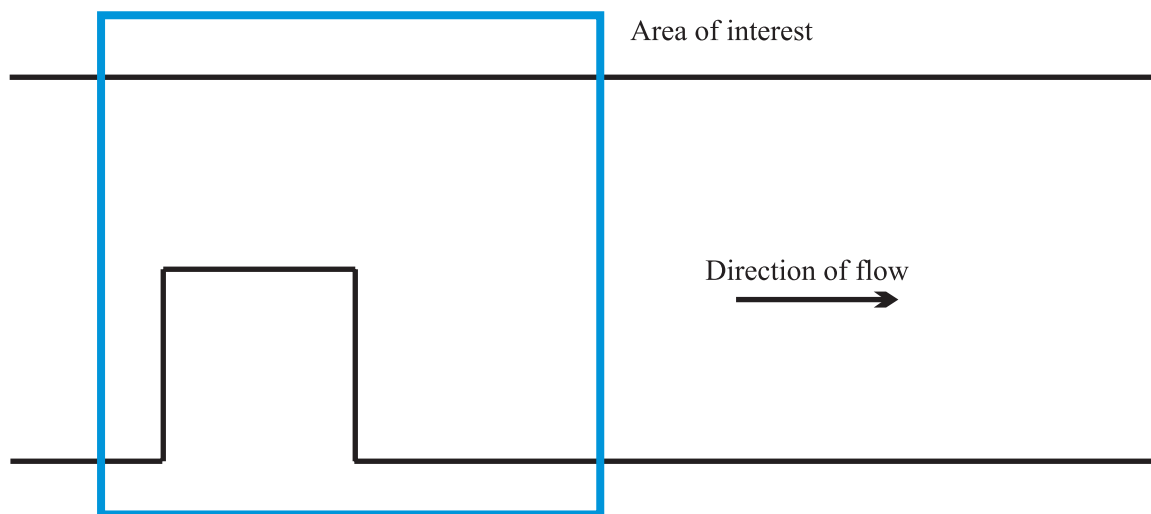
Figure 6.7: Measurement location in relation to the grooved channel

62 *mm* by 62 *mm* for the water and air-based experiments, respectively. The small difference in the image sizes was due to the actual setup of the experiments.

6.6.1 Parameters used in PIV Processing

Before discussing the results from the grooved channel experiments it is important to outline the values of the parameters used for each of the four methods. Table 6.2 shows the values used for the processing of the experimental images for each of the four cross-correlation algorithms. The same parameters were used for both the water and air images to allow for comparisons of the results.

Parameter	Standard FFT	Predictor Corrector FFT	Super Resolution FFT	Deformed FFT
Horizontal interrogation area overlap [%]	75	75	75	75
Vertical interrogation area overlap [%]	75	75	75	75
Sub-pixel interpolation	Gaussian	Gaussian	Gaussian	Gaussian
Number of iterations	1	4	3	4
Type of validation between iterations	-	Peak	Peak	Peak
Value of validation between iterations	-	1.3	1.3	1.3
Initial size of interrogation area	32x32	32x32	64x64	32x32
Super resolution factor	-	-	2	-
Type of validation of results	Peak	Peak	Peak	Peak
Value of validation of results	1.4	1.4	1.4	1.4

Table 6.2: Parameters used for each cross-correlation algorithm for both water and air experiments

6.6.2 Non-dimensionalisation of Results

To maintain the same Reynolds number for the water and air experiments the flow rates through the channel were different, as described in Section 6.2.1. Therefore to make comparisons between the experiments and the DNS calculations, the results were non-dimensionalised. The length dimensions were non-dimensionalised using the difference between the height of the channel and the block $[H - h]$, which was 2 cm for both the water and air experiments. The velocity results were non-dimensionalised by the mean velocity of the flow $[U_m]$ as it passed over the block, 0.3467 m/s and 5.175 m/s for the water and air trials, respectively. The non-dimensional parameters then became:

$$x* = \frac{x}{H - h} \tag{6.2}$$

$$y* = \frac{y}{H - h} \tag{6.3}$$

$$u* = \frac{u}{U_m} \tag{6.4}$$

$$v* = \frac{v}{U_m} \tag{6.5}$$

6.6.3 Vector Velocity Field

Figure 6.8 shows the non-dimensionalised average vector velocity field for both the water and air experiments compared to the DNS results reported by Yang [58]. The results shown in Figure 6.8 were determined using the standard FFT method. The other three cross-correlation methods produced similar vector plots and are not shown.

The average velocity vector field produced from both experiments appears to agree with the DNS results. As the flow approaches the block it began to move upwards, especially at the corner of the block. This caused a small separation region on the top of the block, which was evident from the vector direction. As the flow moved past the trailing edge of the block a shear gradient formed between the faster moving flow at the top of the channel and slower moving flow behind the block. A large recirculation zone also existed behind the block. Due to this large recirculation zone, a region of near zero average velocity appeared at the bottom of the channel immediately after the block.
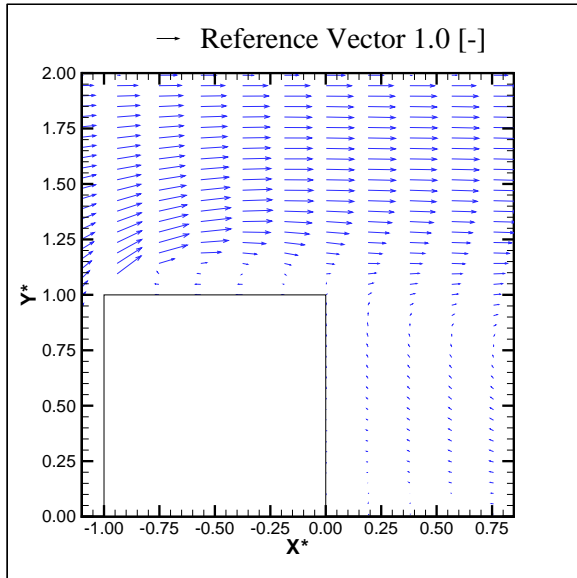
(a) Water Experiment - Standard FFT
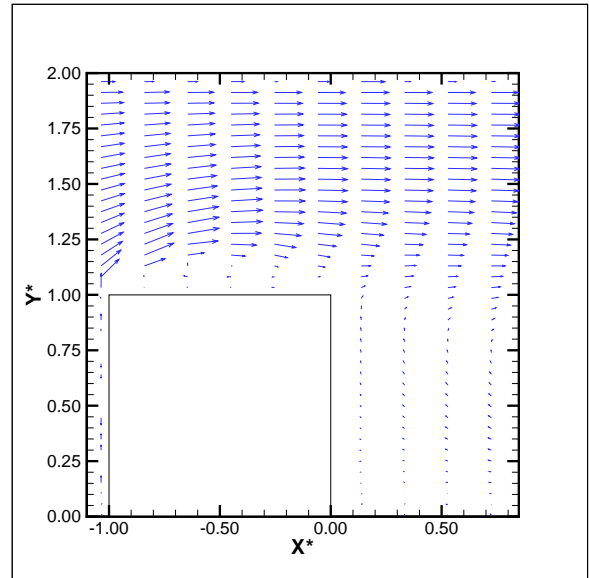
(b) Air Experiment - Standard FFT
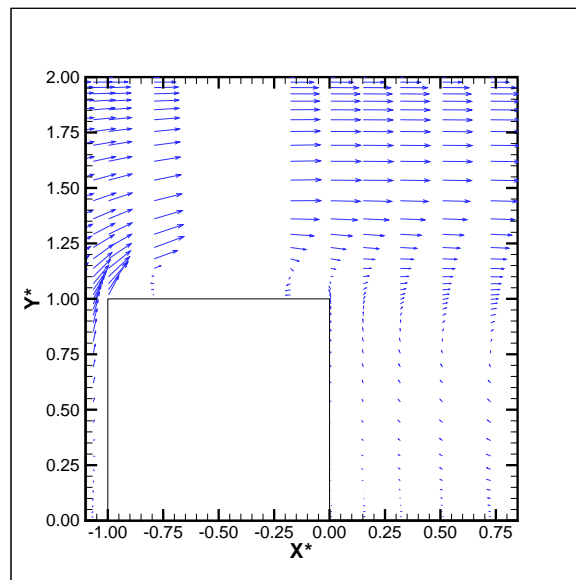
(c) DNS Results

Figure 6.8: Average velocity vector field within grooved channel (a) Water (b) Air (c) DNS results [58]

The results from the average of 1000 images produced important information regarding the general motion of the flow within the channel, but did not give any insight into the turbulence or steadiness of the flow. Figure 6.9 shows the non-dimensionalised velocity vector field, produced using the four cross-correlation strategies, for the same *single* image pair in water, *i.e.* the velocity of the flow at an instant in time. The sizes of the recirculation region can be seen to vary from those indicated from the average velocity field. As well, there was a large variaton in the magnitude of the velocity in the stagnation region immediately behind the block on the channel floor. Figure 6.10 shows similar results for the experiments performed with air, at a single instance in time.

The velocity vector fields in Figures 6.9 and 6.10 were not validated to show the number of the erroneous velocity measurements produced by each cross-correlation method. The number of erroneous measurements appears to be the highest for the super resolution FFT method, compared to the other three schemes, although the relative number of erroneous measurements was low. However, it is important not to form any conclusions regarding the robustness of the four cross-correlation strategies from Figures 6.9 and 6.10 since they only represent one image pair from each experiment. The robustness of the cross-correlation methods will be discussed below.

6.6.4   Robustness

The method used to evaluate the robustness of the four cross-correlation schemes for the synthetic images compared the number of validated vectors. A similar procedure was used for the water and air experiments. Figures 6.11 and 6.12 contain contour plots of the percentage of 1000 possible vectors used at each location for each cross-correlation algorithm. For all four cross-correlation strategies, in both the water and air trials, the lowest number of validated vectors occured immediately above the block surface. This may be due to reflections from the block surface as well as the existence of high velocity gradients in this region, which is consistent with the results seen using the synthetic images. For the synthetic images, as the displacement gradients increased, the number of valid vectors decreased.

Also shown in Figures 6.11 and 6.12 was the improvement in the number of validated vectors between the standard FFT and predictor corrector FFT methods. This was due to the repeated

(a) Standard FFT

(b) Predictor Corrector FFT

(c) Super Resolution FFT
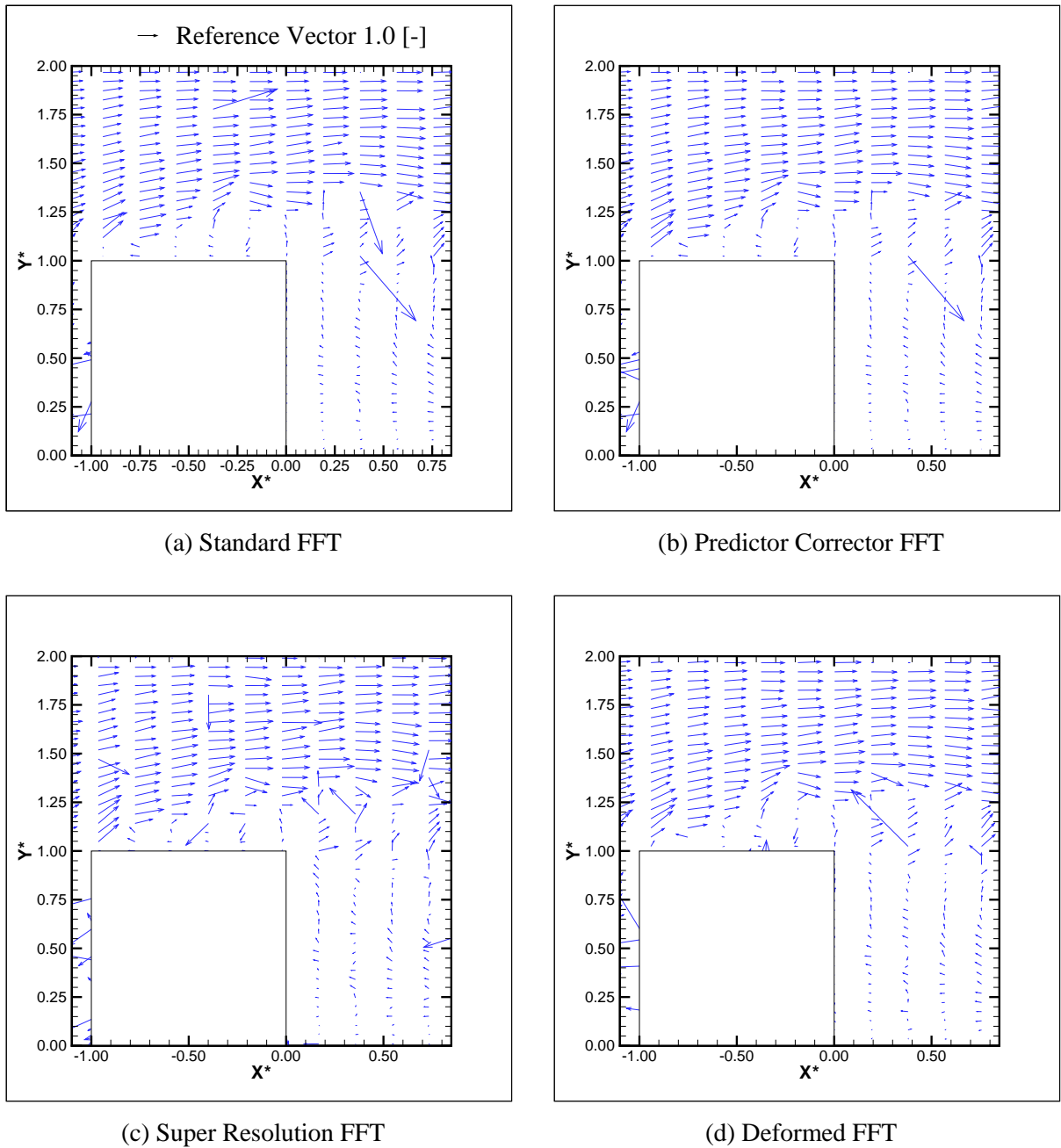
(d) Deformed FFT

Figure 6.9: Unvalidated instantaneous velocity vector field for water (a) Standard FFT (b) Predictor Corrector FFT (c) Super Resolution FFT (d) Deformed FFT

(a) Standard FFT

(b) Predictor Corrector FFT
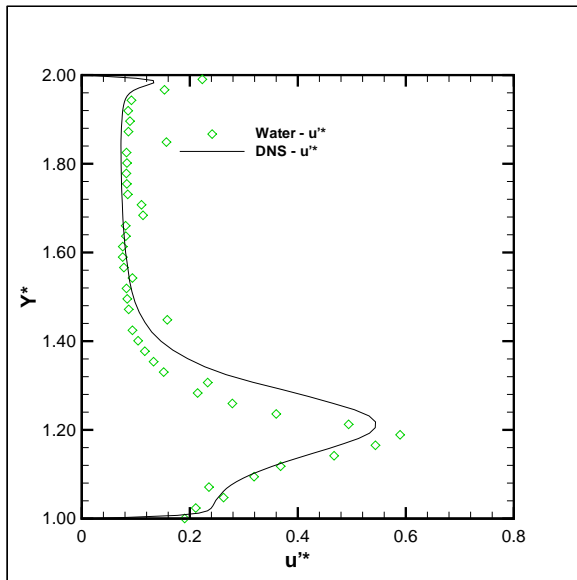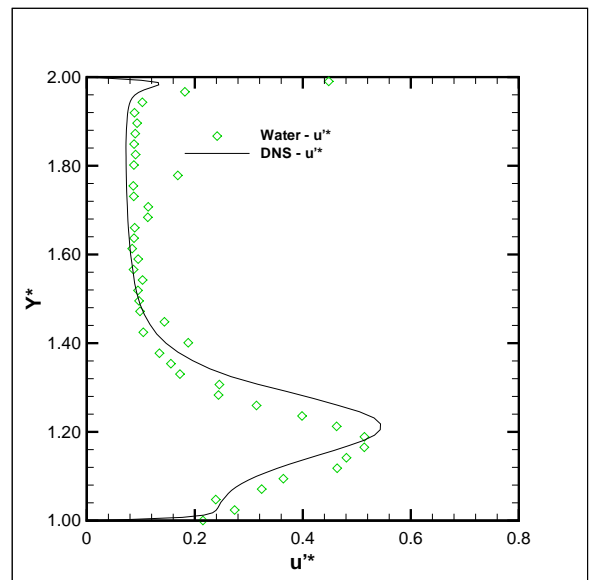
(c) Super Resolution FFT
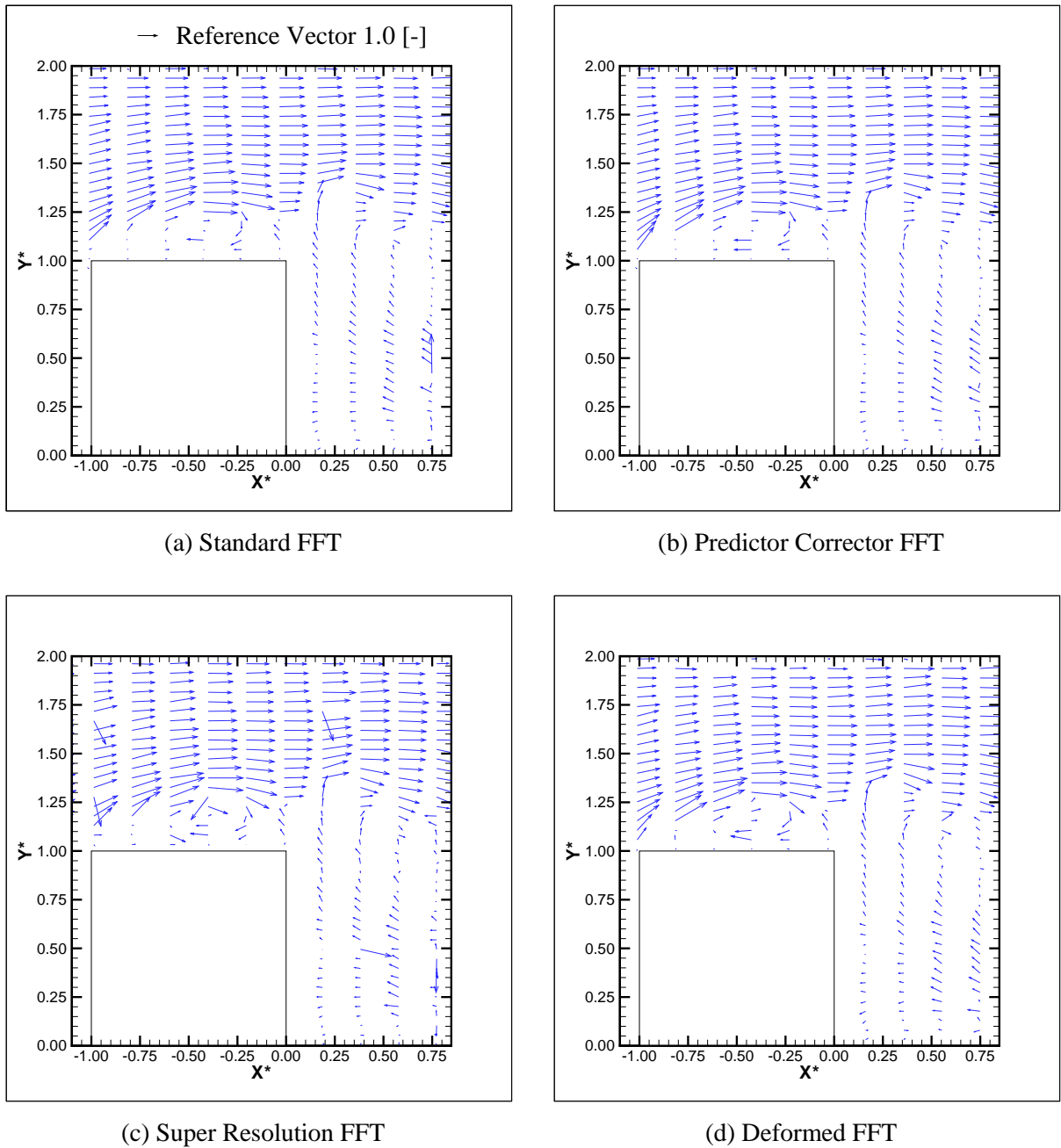
(d) Deformed FFT

Figure 6.10: Unvalidated instantaneous velocity vector field for air (a) Standard FFT (b) Predictor Corrector FFT (c) Super Resolution FFT (d) Deformed FFT

(a) Standard FFT

(b) Predictor Corrector FFT

(c) Super Resolution FFT
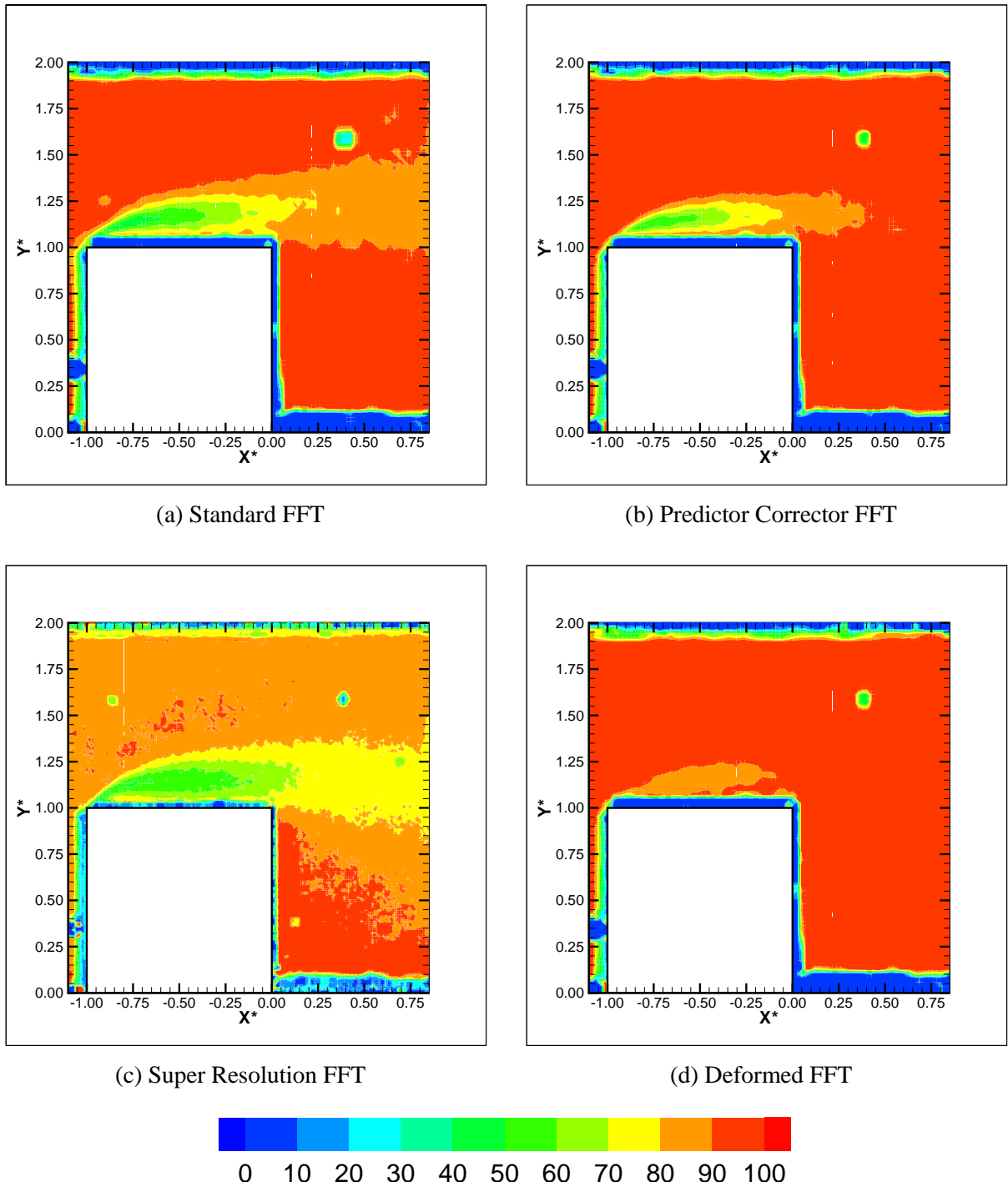
(d) Deformed FFT

Figure 6.11: Contour plot of the percentage of validated vectors in the water based experiment (a) Standard FFT (b) Predictor Corrector FFT (c) Super Resolution FFT (d) Deformed FFT

(a) Standard FFT

(b) Predictor Corrector FFT

(c) Super Resolution FFT
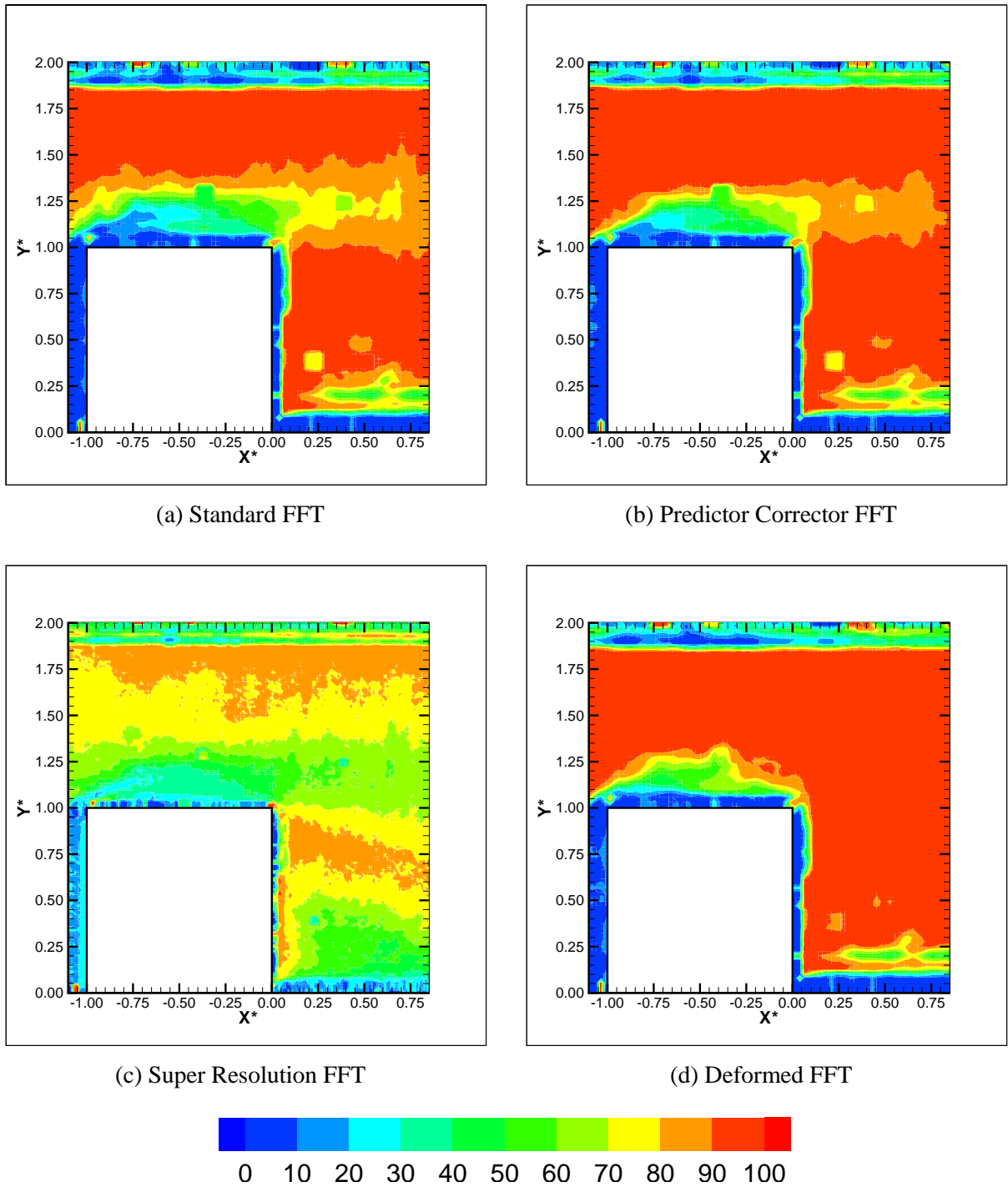
(d) Deformed FFT

Figure 6.12: Contour plot of the percentage of validated vectors in the air based experiment (a) Standard FFT (b) Predictor Corrector FFT (c) Super Resolution FFT (d) Deformed FFT

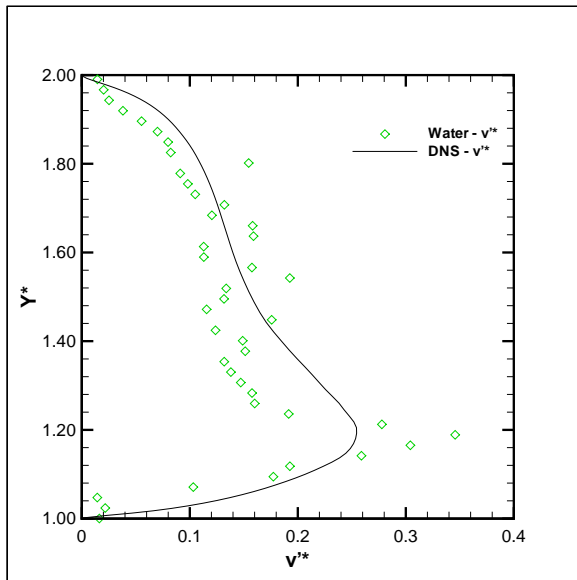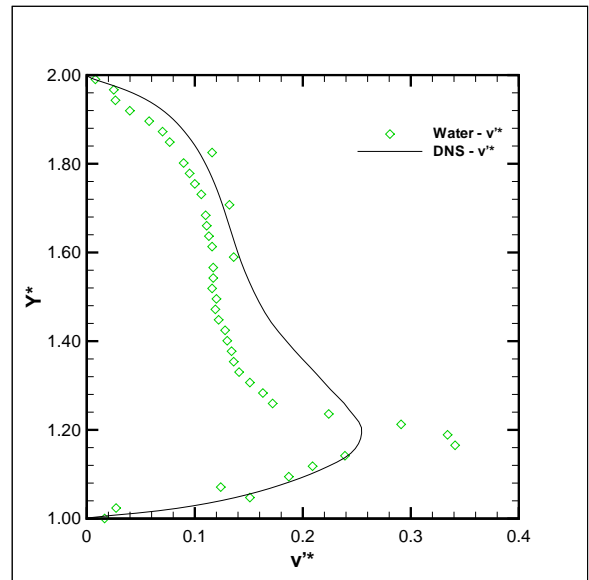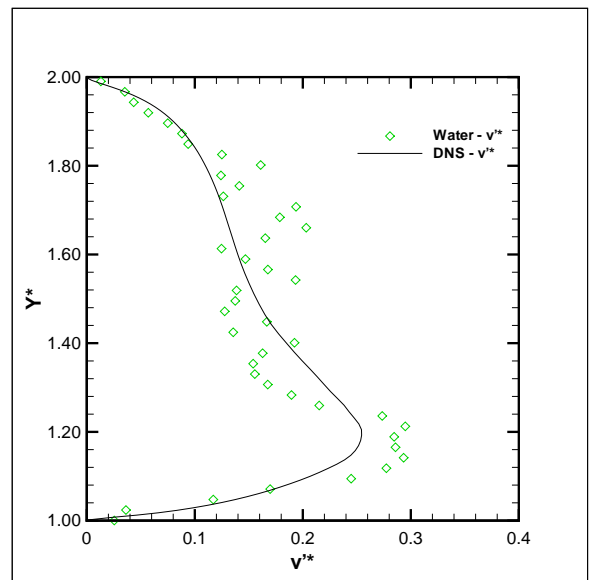iterations of the predictor corrector FFT which allows initially invalid vectors to be *re-evaluated* on subsequent iterations. However, repeated iterations did not benefit the robustness of the super resolution FFT method, which produced the least number of valid vectors of the four cross-correlation algorithms evaluated. This was a result of the smaller interrogation areas which will contain less particles to contribute to the displacement peak in the correlation plane. Yet, the smaller interrogation areas did allow the super resolution FFT scheme to obtain more valid velocity vectors closer to the walls of the block and channel than the other three cross-correlation strategies, for both the water and air trials. Overall, of the four cross-correlation methods evaluated, the deformed FFT scheme produced the largest percentage of valid velocity vectors for both the water and air experiments.

6.6.5 Derived Flow Characteristics

From the validated vector velocity field it is possible to determine other flow characteristics, *i.e.* the wall shear stress, flow streamlines, *etc.* One such flow characteristic which was derived from the velocity vector field to evaluate the rotation of the flow within the cross section created by the 2-D laser sheet was vorticity. The non-dimensionalised 2-D vorticity $[\omega*]$ was calculated using Equation 6.6.

$$\omega* = \frac{\partial v*}{\partial x*} - \frac{\partial u*}{\partial y*} \tag{6.6}$$

Figures 6.13 and 6.14 contain contour plots of the average vorticity field for the water trial for the four cross-correlation algorithms compared to the DNS results. Figures 6.15 and 6.16 show the contour plots for the average vorticity field for the air trial.

Of the four cross-correlation strategies applied, the deformed FFT produced results most similar to those of the DNS, based on qualitative analysis. However, the average vorticity field calculated from both experiments for all methods appeared to match the DNS results in both shape and magnitude, including the high negative vorticity at the leading edge of the block. As well, the amount the magnitude of the vorticity decreased as the flow spreads beyond the block to fill the entire channel was similar between the experimental and the DNS results. On the bottom of the
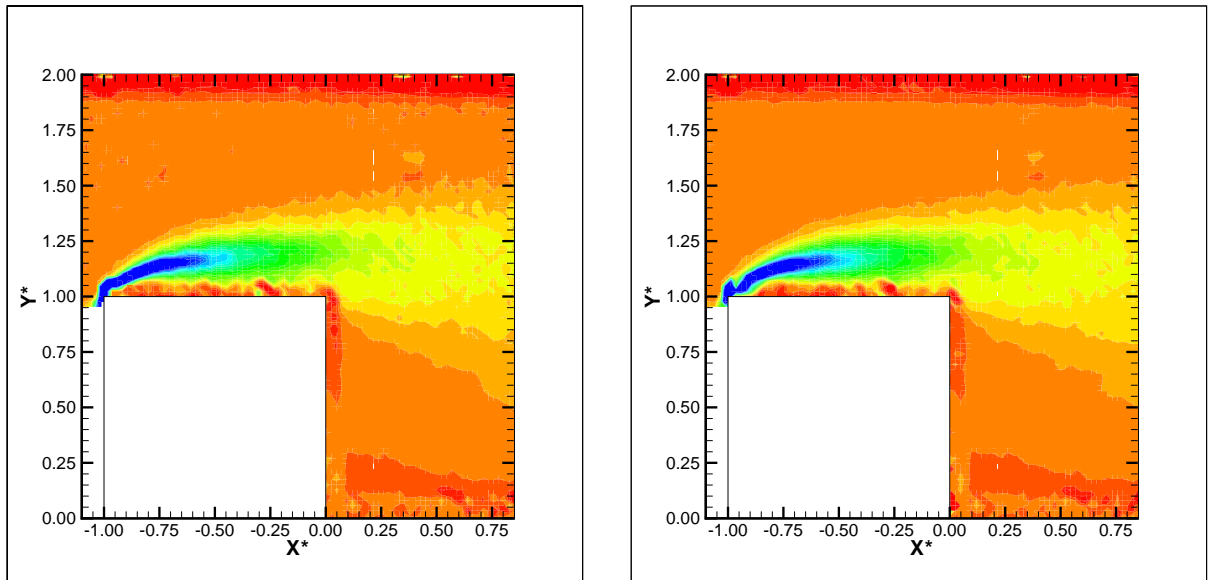
(a) Standard FFT

(b) Predictor Corrector FFT
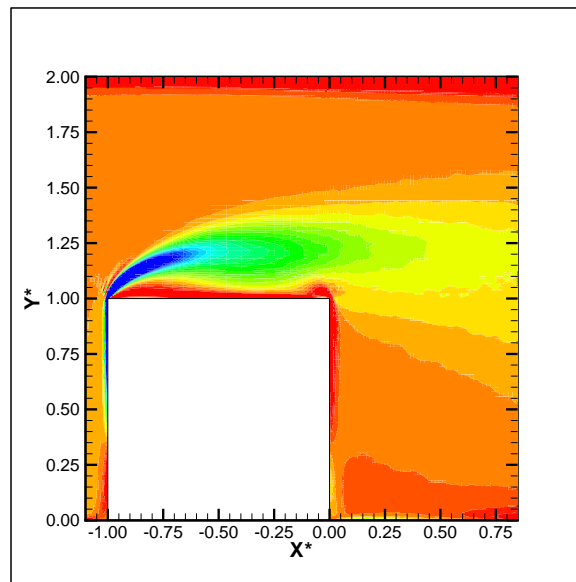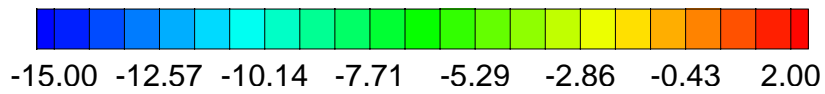
(c) DNS Results

Figure 6.13: Contour plot of average vorticity in water (a) Standard FFT (b) Predictor Corrector FFT (c) DNS Results
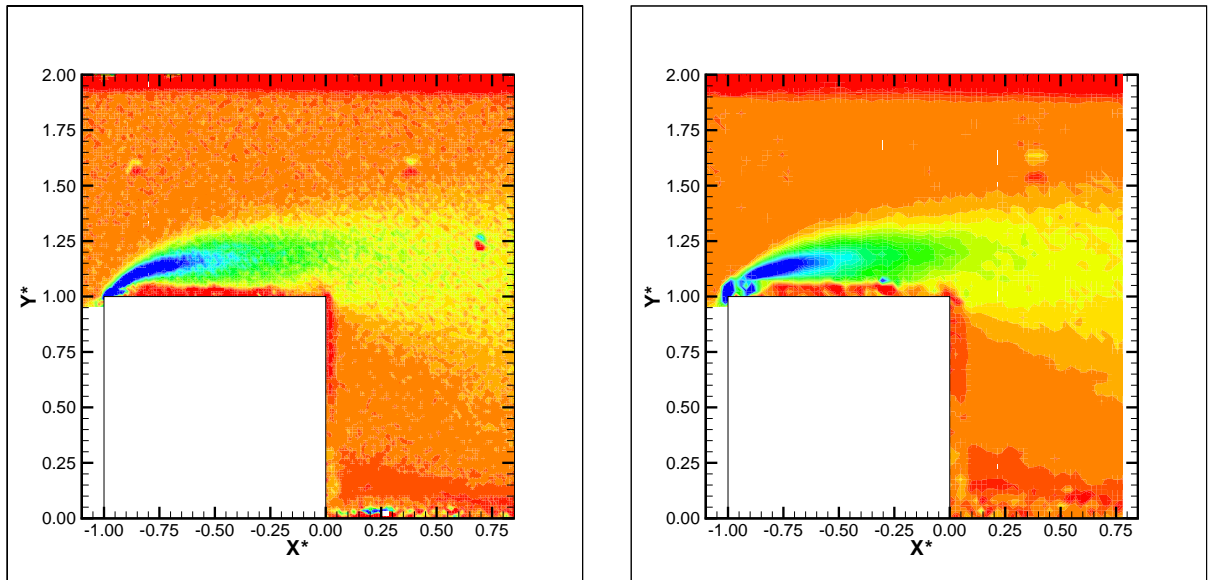
(a) Super Resolution FFT
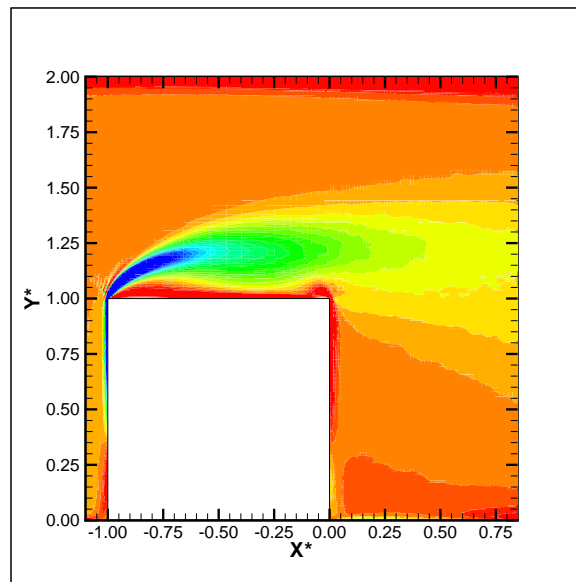
(b) Deformed FFT
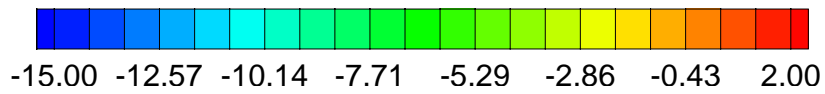
(c) DNS Results

Figure 6.14: Contour plot of average vorticity in water (a) Super Resolution FFT (b) Deformed FFT (c) DNS Results
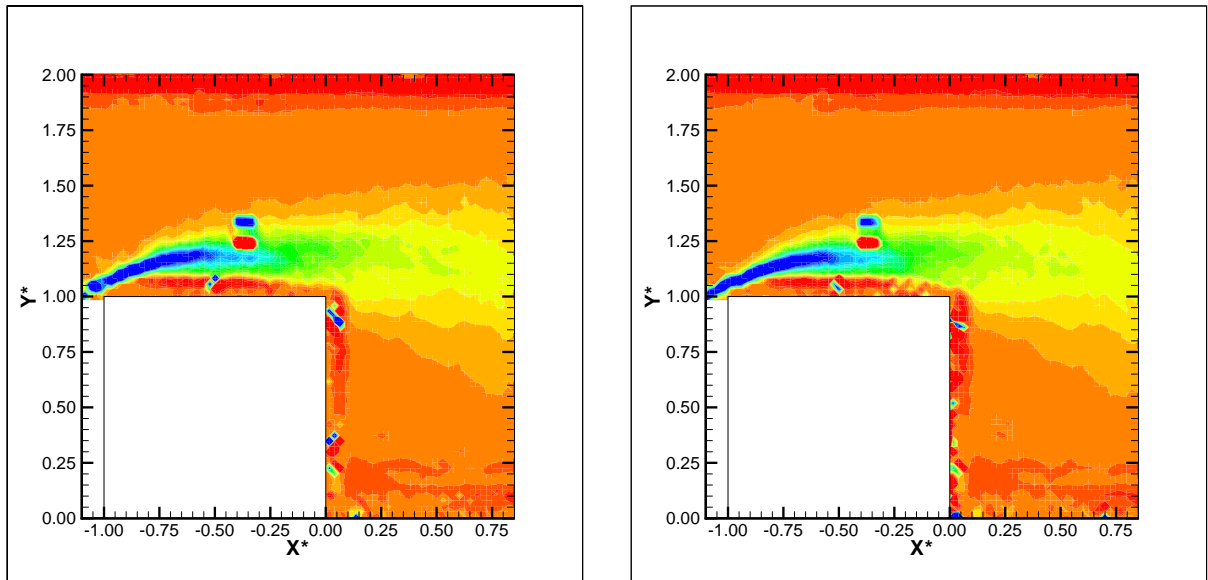
(a) Standard FFT

(b) Predictor Corrector FFT
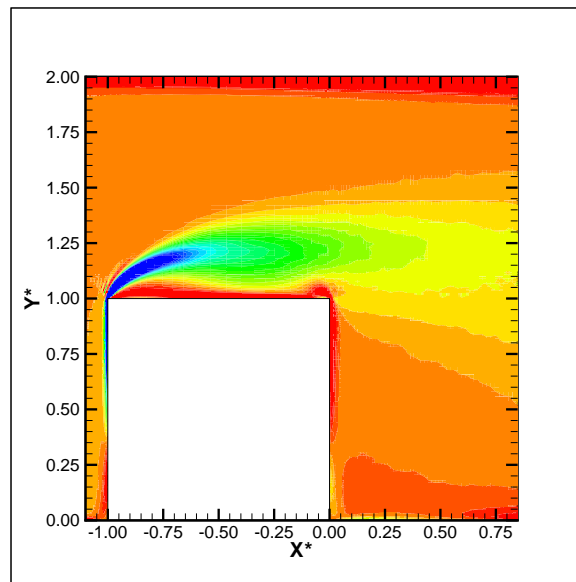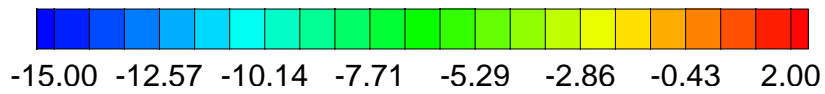
(c) DNS Results

Figure 6.15: Contour plot of average vorticity in air (a) Standard FFT (b) Predictor Corrector FFT (c) DNS Results
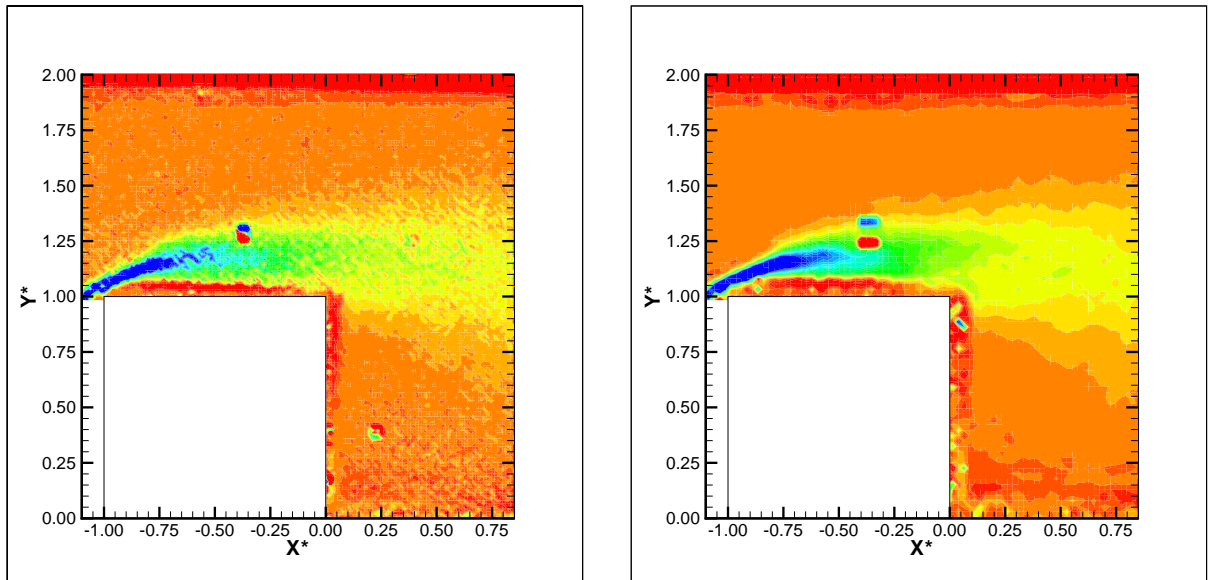
(a) Super Resolution FFT
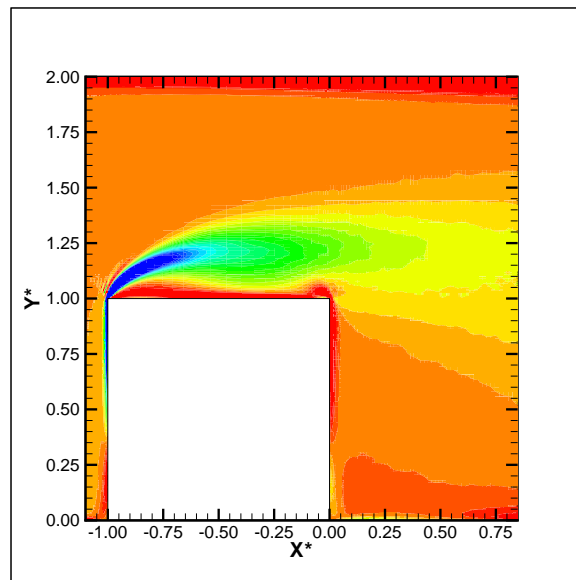
(b) Deformed FFT
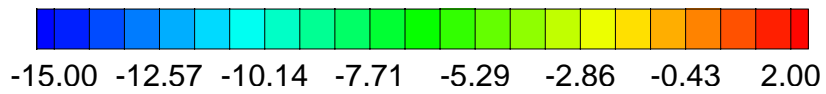
(c) DNS Results

Figure 6.16: Contour plot of average vorticity in air (a) Super Resolution FFT (b) Deformed FFT (c) DNS Results

channel behind the block exists a region of positive vorticity as is shown in the contour plots in Figures 6.13 - 6.16.

6.6.6   2-D Turbulent Kinetic Energy

The average velocity vector and vorticity field are both dependent on the mean flow characteristics and do not provide insight into the turbulence in the flow. The amount the flow fluctuates can be seen in the non-dimensionalised 2-D turbulent kinetic energy $[k*]$ contour plot. The 2-D turbulent kinetic energy is defined as:

$$k* = \frac{\overline{u'*^2} + \overline{v'*^2}}{2} \tag{6.7}$$

where $u'*$ and $v'*$ are the non-dimensionalised fluctuating component of the velocity, obtained by subtracting the average velocity from each instantaneous velocity measurement. Only the 2-D turbulent kinetic energy can be evaluated since the flow in the third dimension could not be measured with the chosen experimental setup.

Figures 6.17 and 6.18 contain contour plots of the 2-D turbulent kinetic energy for the water experiments as determined using the 1000 validated velocity vector fields produced with the four cross-correlation strategies as well as the DNS results. Figures 6.19 and 6.20 contain the 2-D turbulent kinetic energy contour plots determined for the air trial.

For both the water and air experiments the shape and magnitude of the 2-D turbulent kinetic energy contours agreed with the DNS results, independent of the cross-correlation methodology. The sudden increase in the turbulent kinetic energy at the leading edge of the block compared well with DNS simulation by Yang [58]. Also, the decrease in the turbulent kinetic energy when the flow area expands to fill the entire height of the channel as it moved beyond the block matched the DNS results well.

The turbulent kinetic energy was greater for the experimental results than the DNS results in the region immediately above the block. This may be due to the lower number of validated vectors used in determining the turbulent kinetic energy here than in other areas of the flow field, as shown in Figures 6.11 and 6.12. Of the four cross-correlation strategies applied, the deformed FFT produced results that matched the shape of DNS simulation the best.
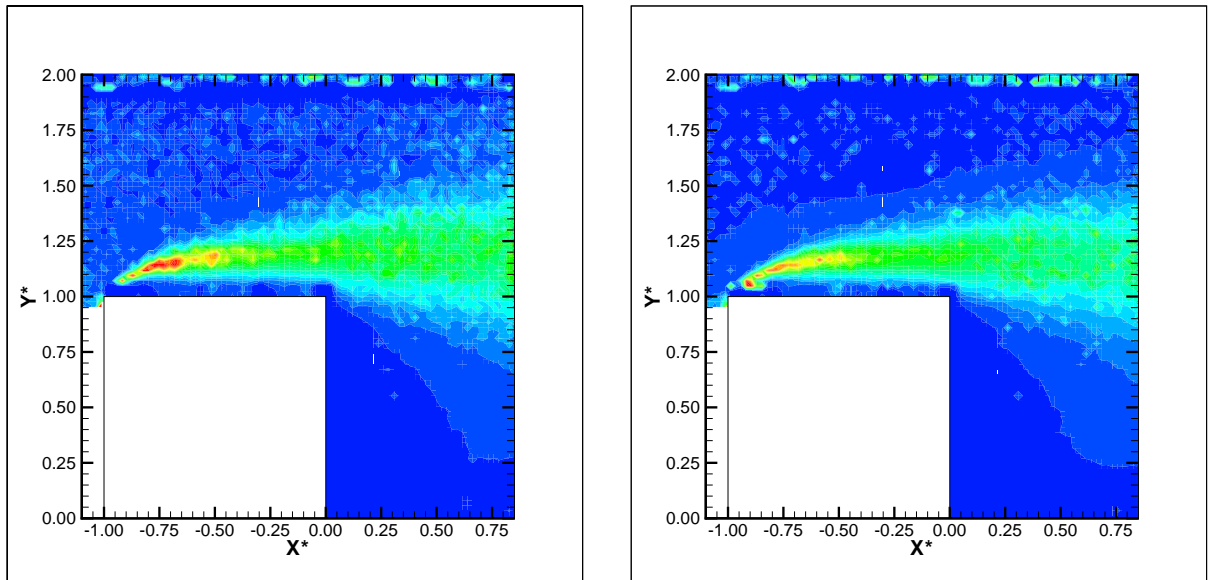
(a) Standard FFT

(b) Predictor Corrector FFT
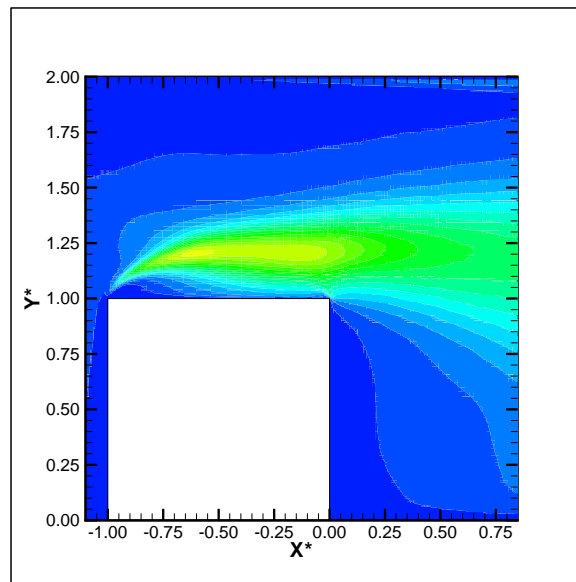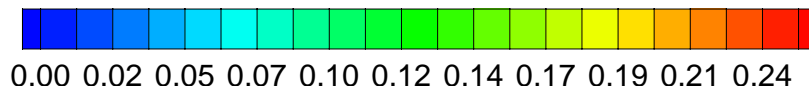
(c) DNS Results

Figure 6.17: Contour plot of 2-D turbulent kinetic energy in water (a) Standard FFT (b) Predictor Corrector FFT (c) DNS Results
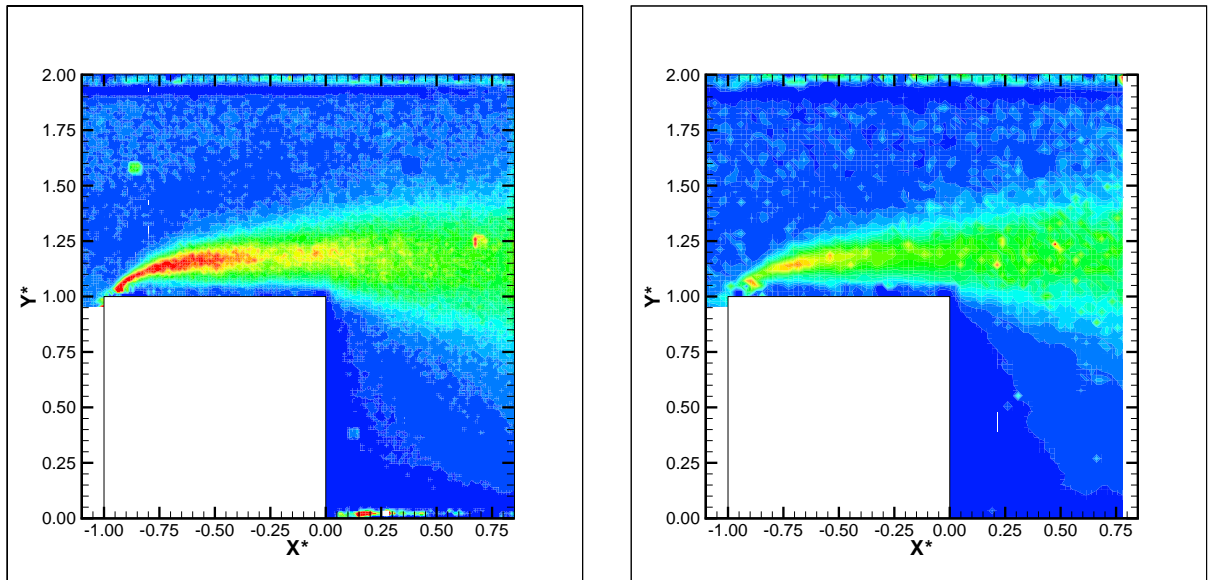
(a) Super Resolution FFT
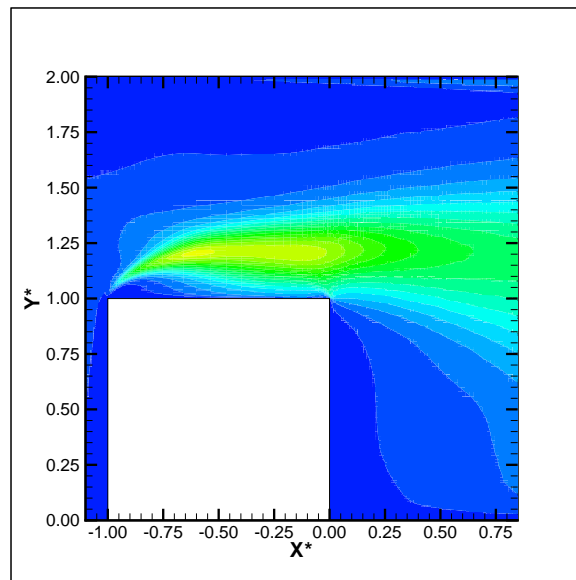
(b) Deformed FFT
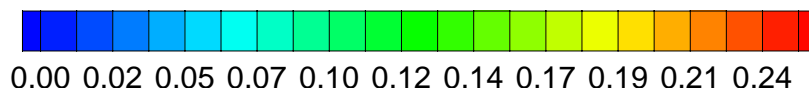
(c) DNS Results

Figure 6.18: Contour plot of 2-D turbulent kinetic energy in water (a) Super Resolution FFT (b) Deformed FFT (c) DNS Results
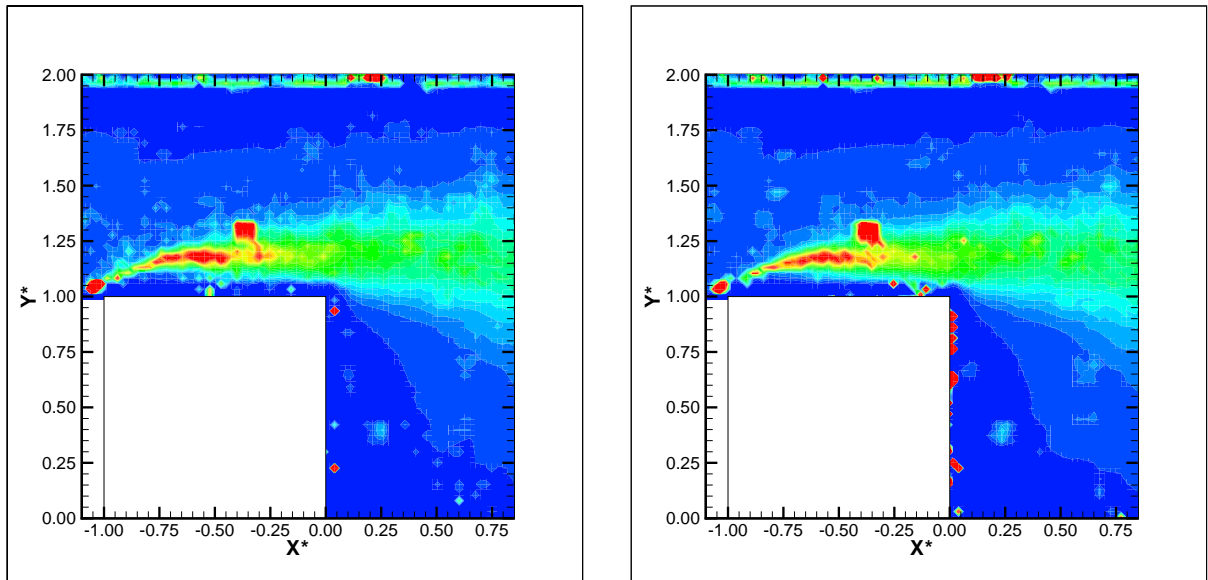
(a) Standard FFT

(b) Predictor Corrector FFT
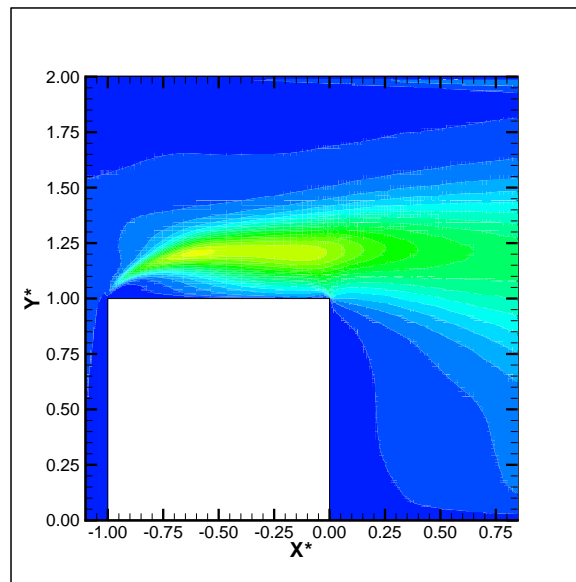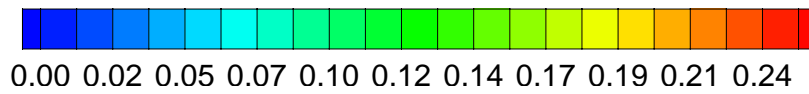
(c) DNS Results

Figure 6.19: Contour plot of 2-D turbulent kinetic energy in air (a) Standard FFT (b) Predictor Corrector FFT (c) DNS Results
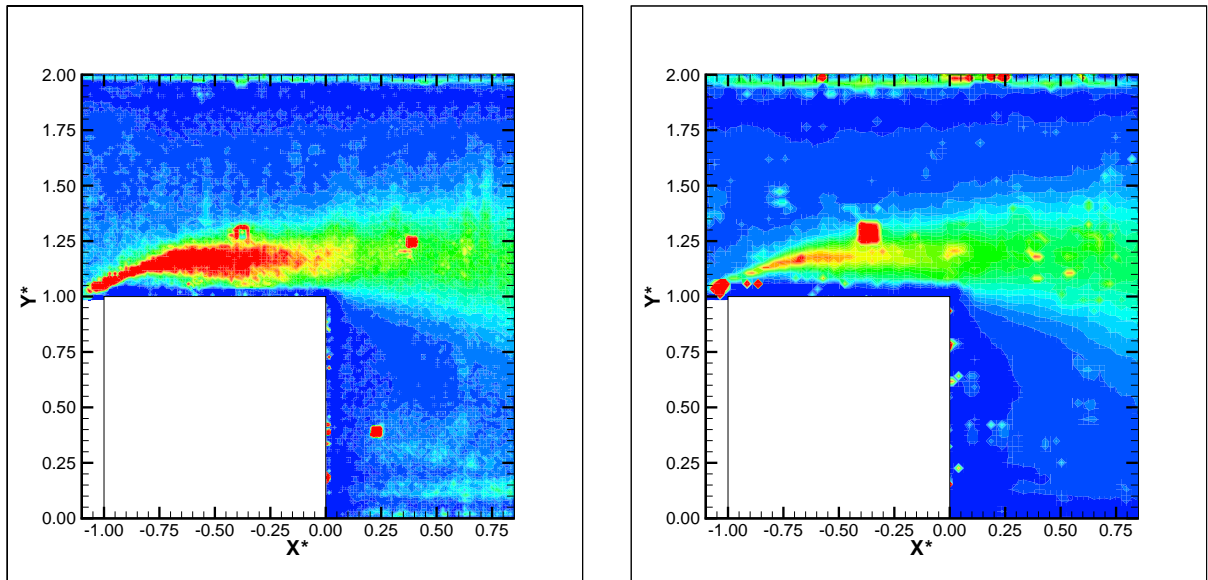
(a) Super Resolution FFT
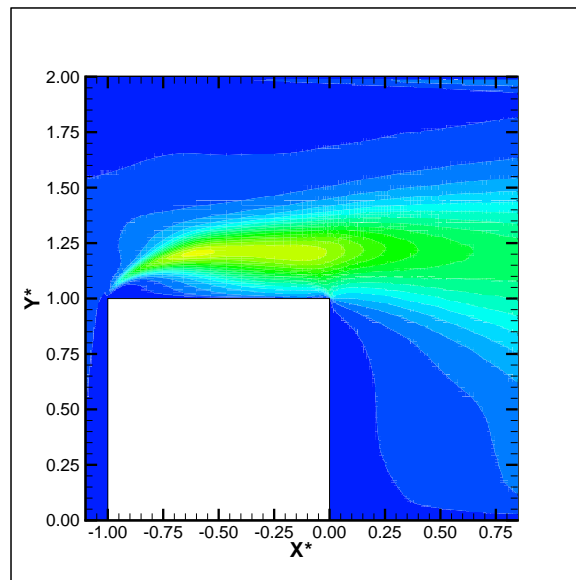
(b) Deformed FFT

(c) DNS Results

Figure 6.20: Contour plot of 2-D turbulent kinetic energy in air (a) Super Resolution FFT (b) Deformed FFT (c) DNS Results

6.6.7 Streamwise and Normal Profiles at $x_{index} = -0.5$

Average Velocity Profile

The velocity vector and contour plots allowed the comparison of the experimental and DNS results on a qualitative scale by visually comparing the shape of the flow characteristics. To quantify the comparison of the experimental and DNS results, profiles of flow characteristics were used at different sections within the flow.

Figures 6.21 and 6.22 show line profiles of the average streamwise velocity at $x* = $ -0.5 for the water and air experiments respectively. Since $x* = $ -0.5 occurred at the middle of the block, the range for $y*$ in the plots was from 1 to 2. Each plot shows a comparison of a cross-correlation scheme with the DNS results. The shape of the streamwise velocity profiles were very similar between each cross-correlation algorithm and the DNS results for both the water and the air trials, with the differences from the DNS simulation approximately 4% and 0%, respectively, based on the maximum velocity.

In Figures 6.21 and 6.22, the average streamwise velocity profile produced by each cross-correlation method for both the water and air experiments shifted downwards closer to the top of the block, compared to the DNS results. This shift was a result of the difference in the measured velocity and DNS results of the average normal velocity at $x* = $ -0.5, which was much smaller than the average streamwise velocity, as shown in Figures 6.23 and 6.24. The estimated normal velocity was consistently smaller than the DNS calculations, approximately 50%, for both the water and air experiments and for each of the four cross-correlation algorithms. Assuming the DNS simulation is correct, the difference in the results was probably due to the presence of a chamfer at the corner of the block, compared to the DNS simulation where the block had a sharp 90° corner. The chamfer allowed for a smoother transition of the flow at the leading edge of the block, thus reducing the magnitude of the average normal velocity. This reduced positive normal velocity caused the average streamwise velocity profile to shift downwards toward the top of the block surface, as observed in the experimental results. However, the shape of the normal velocity profile produced by the cross-correlation algorithms matched well with the DNS simulation.
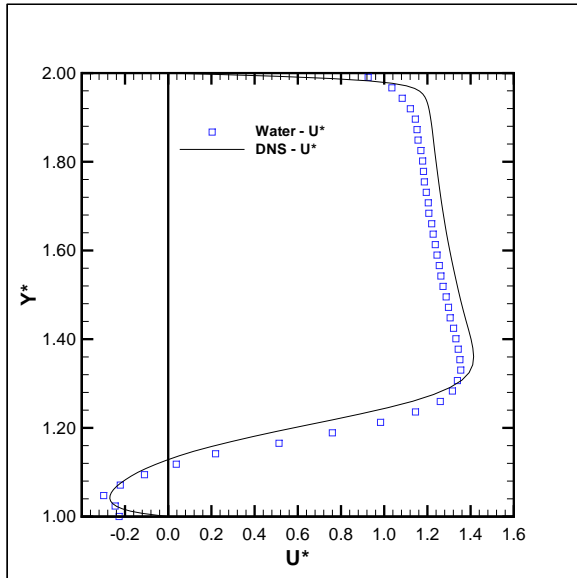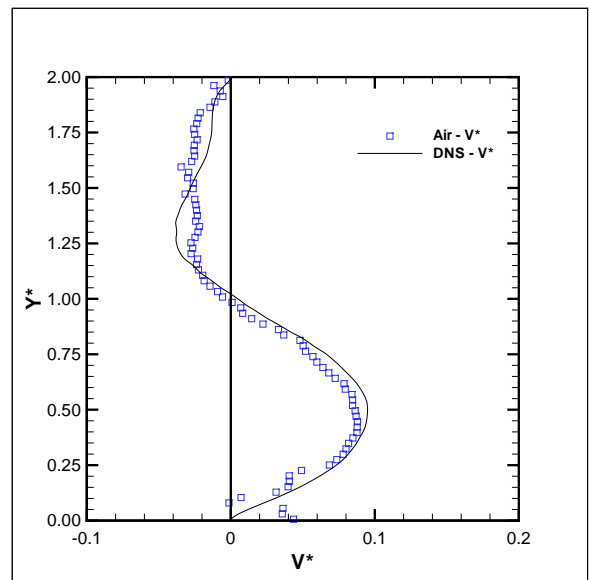
(a) Standard FFT
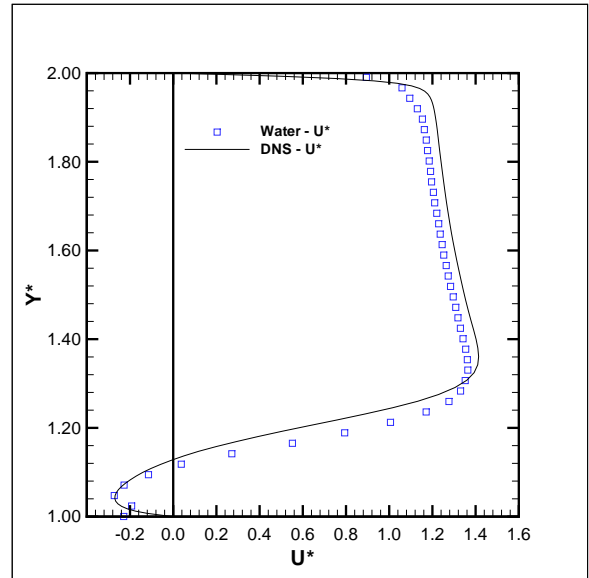
(b) Predictor Corrector FFT
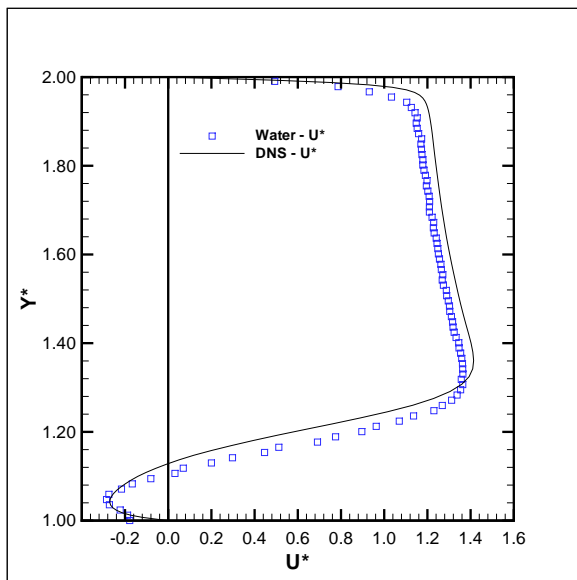
(c) Super Resolution FFT
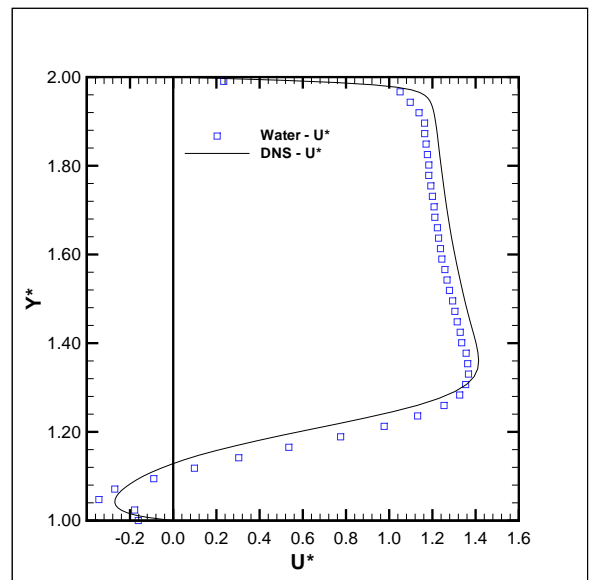
(d) Deformed FFT
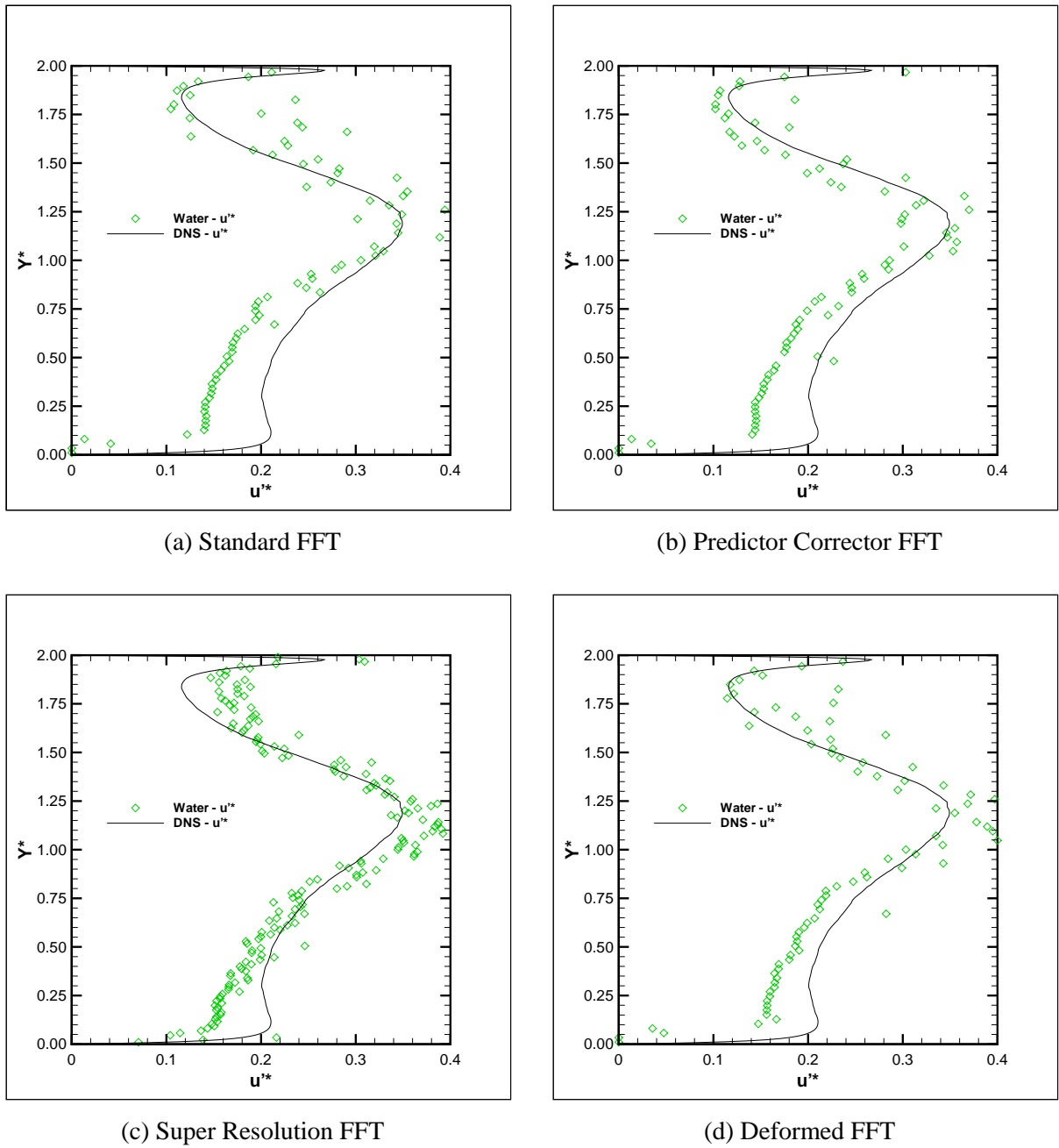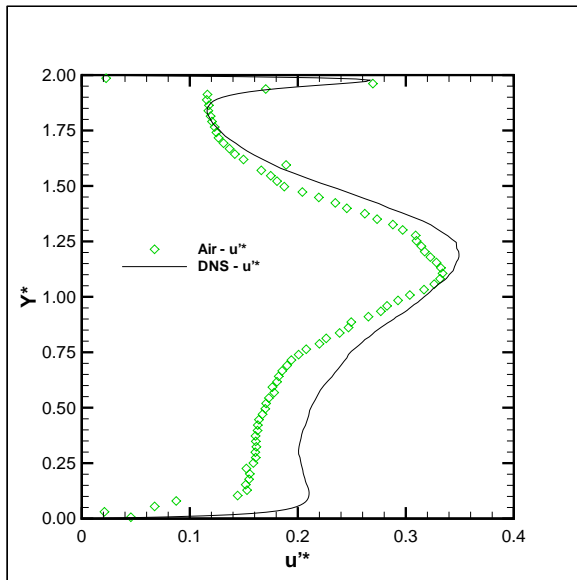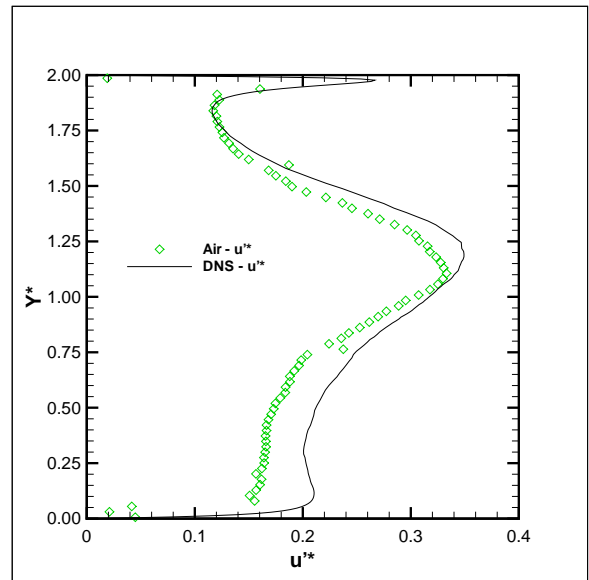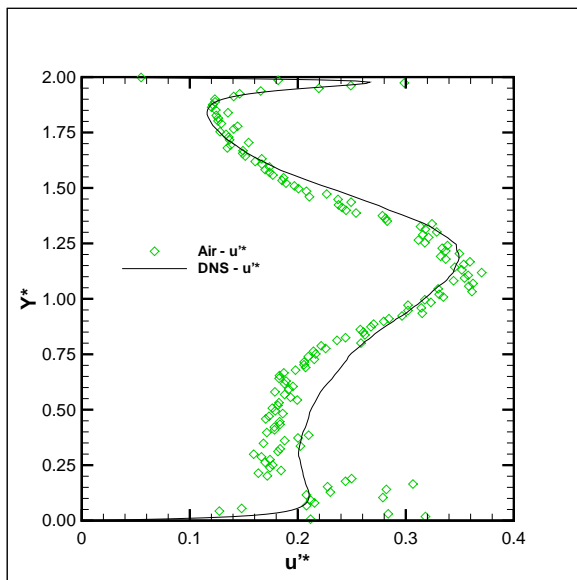
Figure 6.21: Profile of averaged non-dimensionalised streamwise velocity in water at $x* = -0.5$ (a) Standard FFT (b) Predictor Corrector FFT (c) Super Resolution FFT (d) Deformed FFT
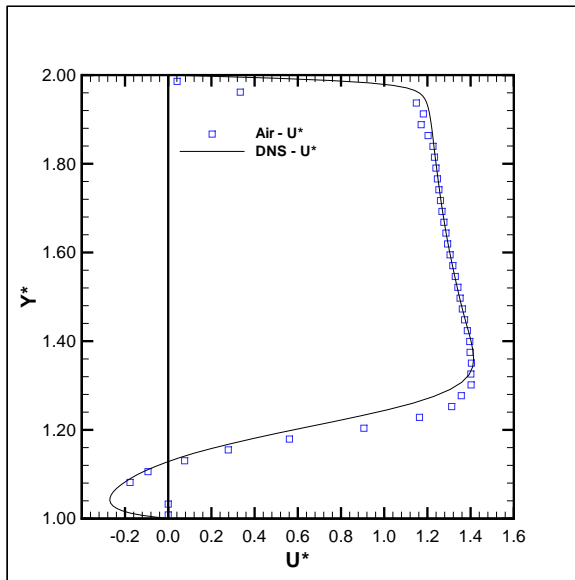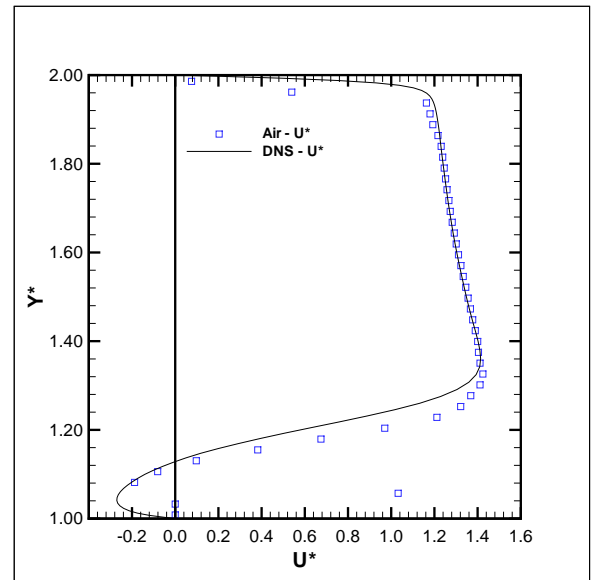
(a) Standard FFT

(b) Predictor Corrector FFT
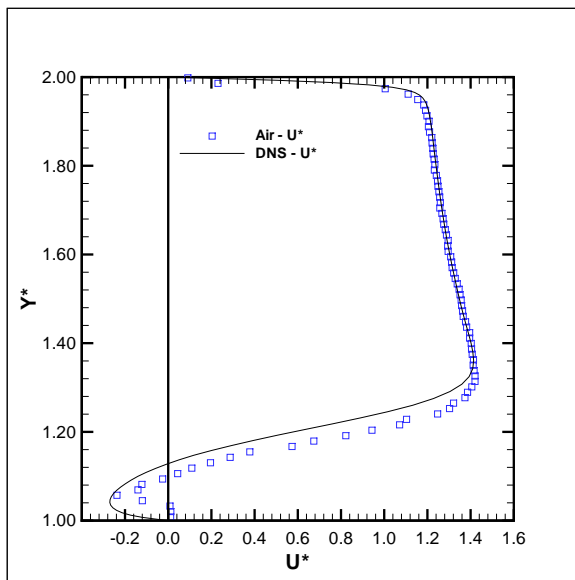
(c) Super Resolution FFT
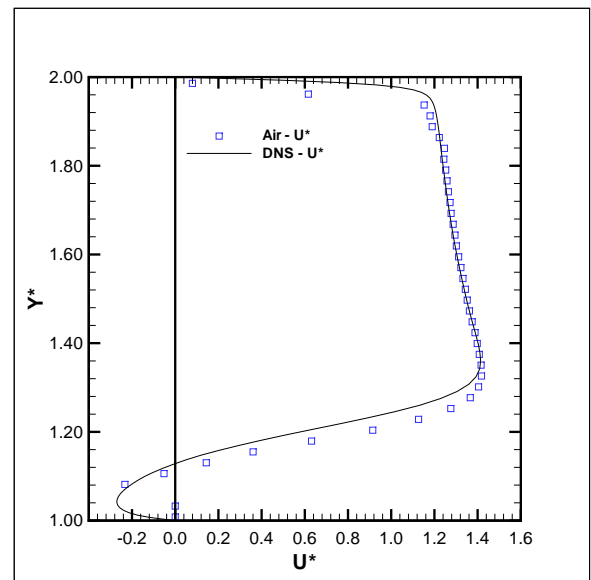
(d) Deformed FFT

Figure 6.22: Profile of averaged non-dimensionalised streamwise velocity in air at $x* = -0.5$ (a) Standard FFT (b) Predictor Corrector FFT (c) Super Resolution FFT (d) Deformed FFT
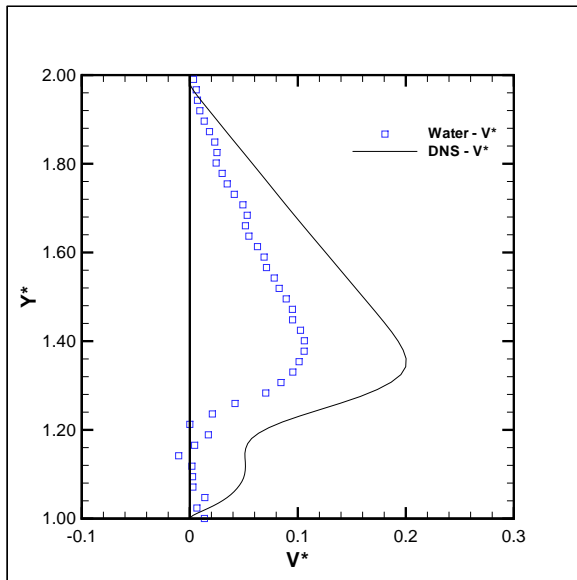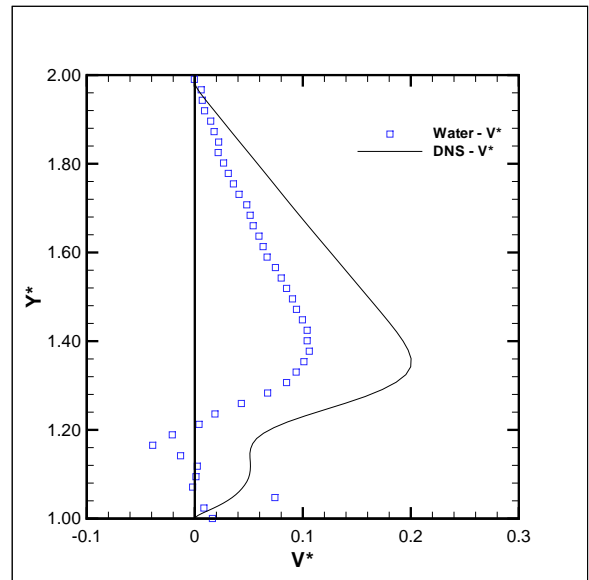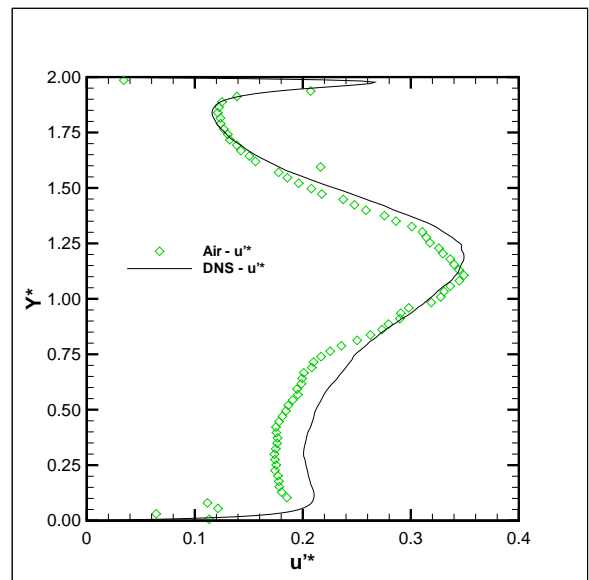
(a) Standard FFT

(b) Predictor Corrector FFT
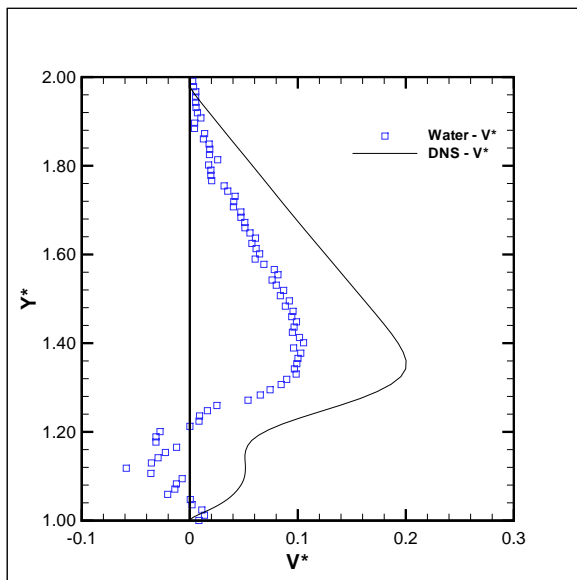
(c) Super Resolution FFT
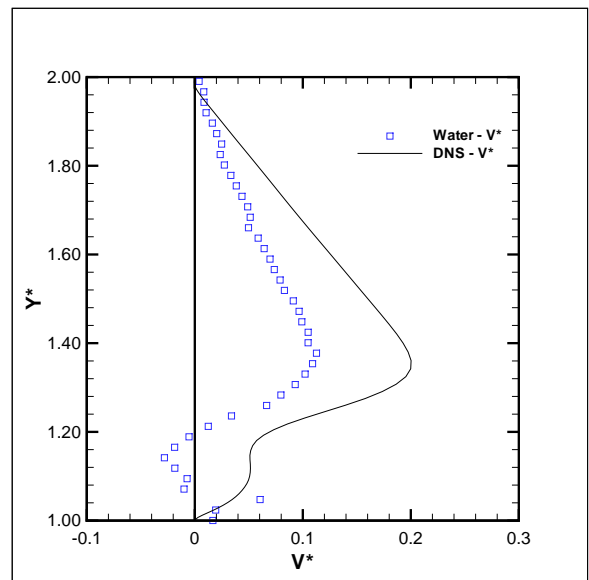
(d) Deformed FFT

Figure 6.23: Profile of averaged non-dimensionalised streamwise velocity in water at $x* = -0.5$ (a) Standard FFT (b) Predictor Corrector FFT (c) Super Resolution FFT (d) Deformed FFT
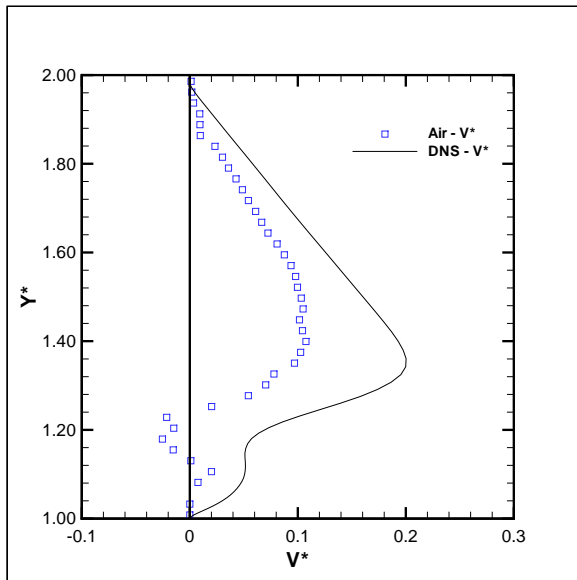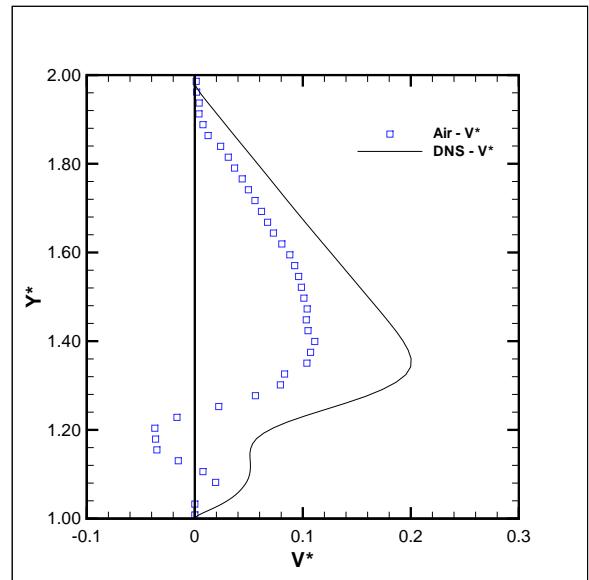
(a) Standard FFT
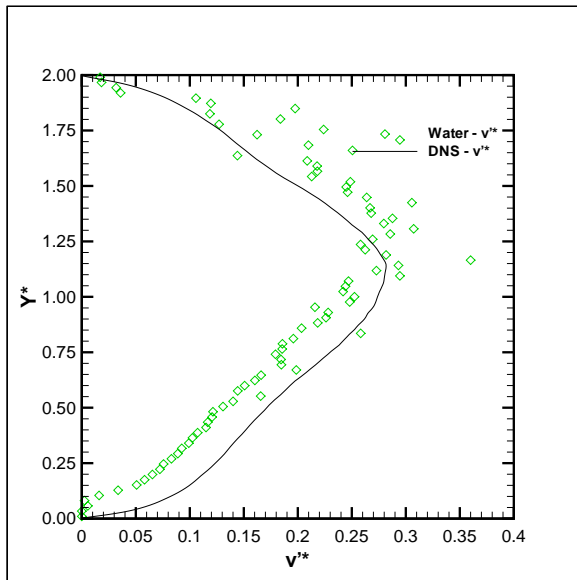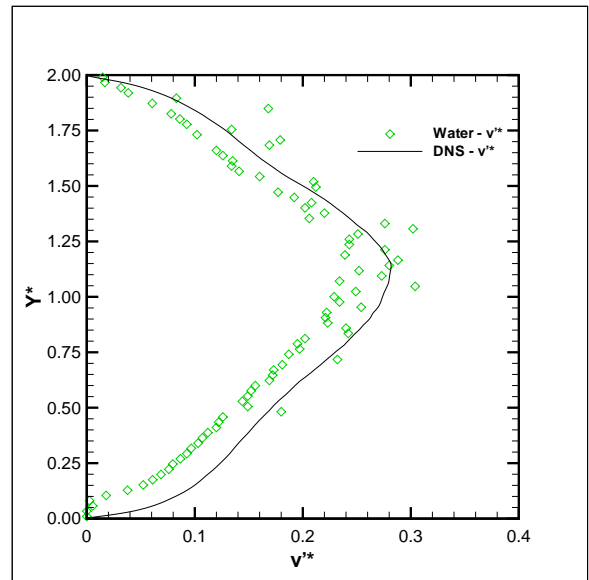
(b) Predictor Corrector FFT
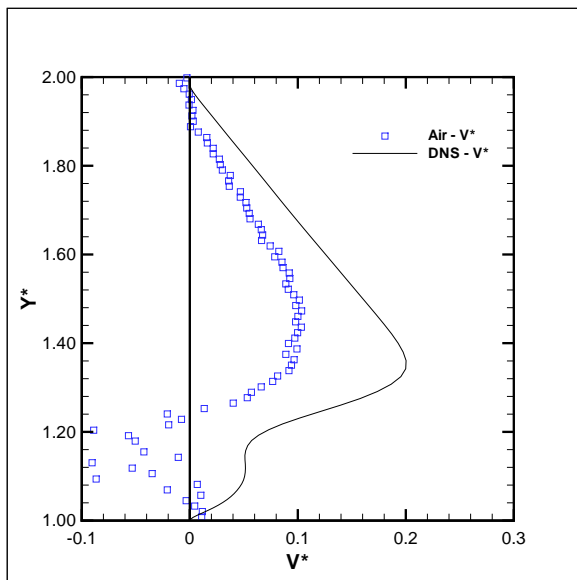
(c) Super Resolution FFT
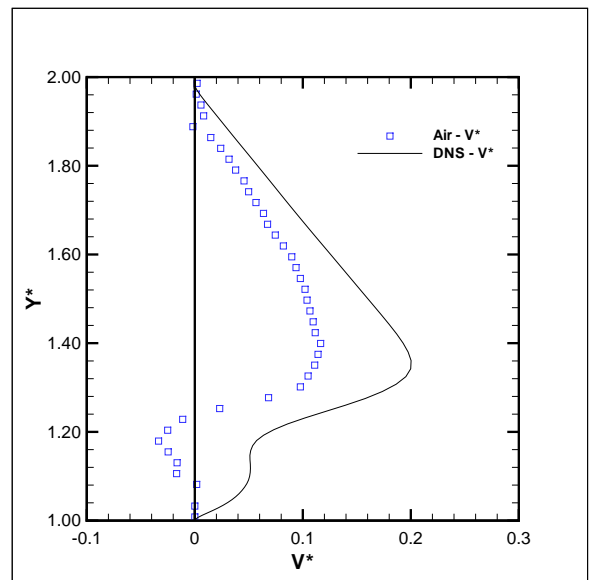
(d) Deformed FFT

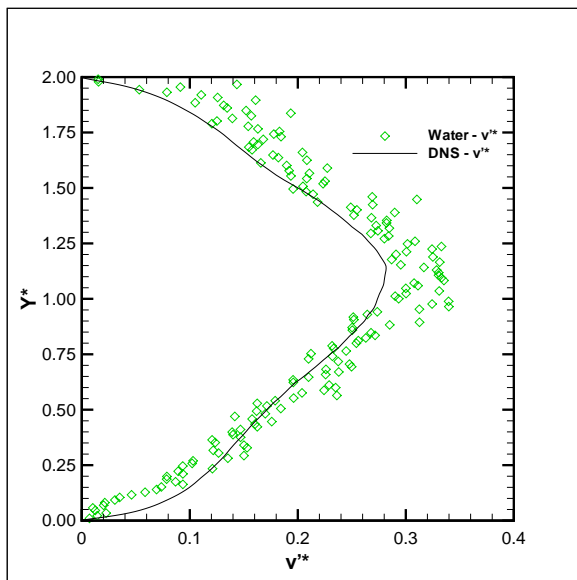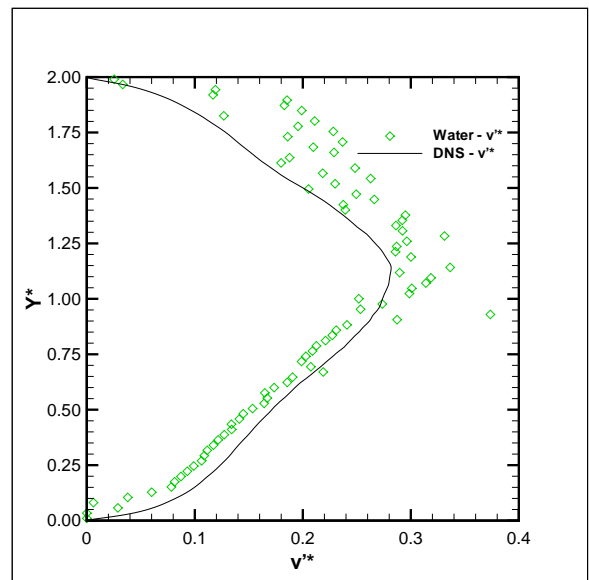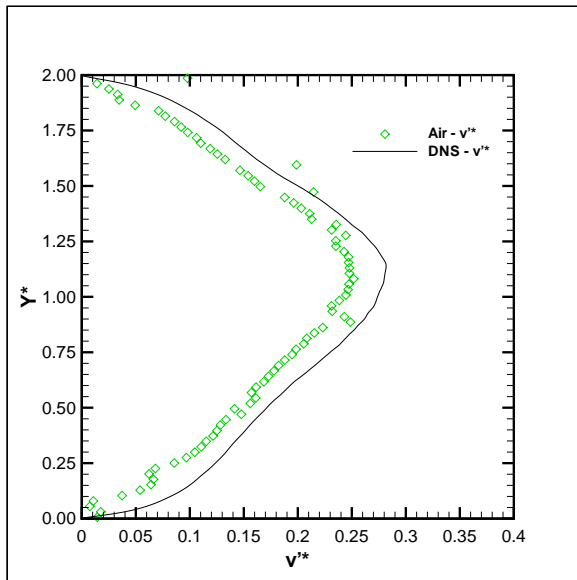Figure 6.24: Profile of averaged non-dimensionalised streamwise velocity in air at $x* = -0.5$ (a) Standard FFT (b) Predictor Corrector FFT (c) Super Resolution FFT (d) Deformed FFT

Velocity Fluctuations Profile

Typically it is easier to measure the correct average velocity, which is a first order statistic, than to accurately measure the turbulent fluctuations of a flow, which is a second order statistic [40]. A comparison of the fluctuations in the streamwise velocity at $x* = $ -0.5 for the water and air trials respectively, for each cross-correlation method applied, is shown in Figures 6.25 and 6.26. The shift of the experimental results towards the top of the block was evident due to the reduced velocity in the normal direction in comparison to the DNS results. However, the difference between the measured streamwise fluctuation and the DNS simulation was very small for each cross-correlation method applied. The results produced by the water trial were closer to the DNS simulation than the air trial, other than the larger fluctuation measured with the super resolution FFT method above $y* = 1.5$. Of the four cross-correlation algorithms applied, the deformed FFT method matched the streamwise fluctuations of the DNS simulation the closest with differences of -5.5% and 6.8% of the maximum displacement for the water and air experiments, respectively.

Line profiles of the fluctuations in the normal velocity are shown in Figures 6.27 and 6.28 for the water and air trials, respectively. Between the water and air trials, the fluctuations in the normal velocity produced from the air experiment better matched the DNS results. However, both trials produced similar results, in shape and magnitude, compared to the DNS simulation even though the magnitude of the normal velocity was different between the experiment and the DNS simulation. Of the four cross-correlation methods, the normal velocity fluctuations produced with the deformed FFT scheme matched the DNS simulation the best. However, the normal velocity fluctuation measurements obtained using the super resolution FFT method are larger near the top of the block, $1.0 < y* < 1.3$, compared to the other three cross-correlation schemes and the DNS results. It is unclear if this was a result of the flow characteristics or the reduced number of valid vectors produced with the super resolution FFT method near the top of the block.

(a) Standard FFT
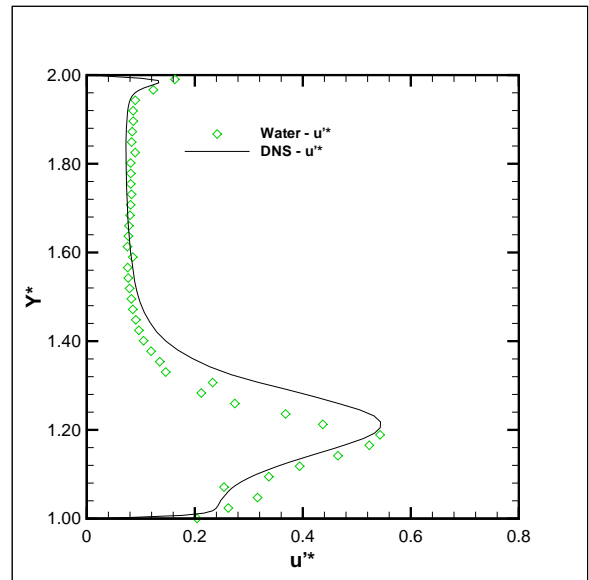
(b) Predictor Corrector FFT
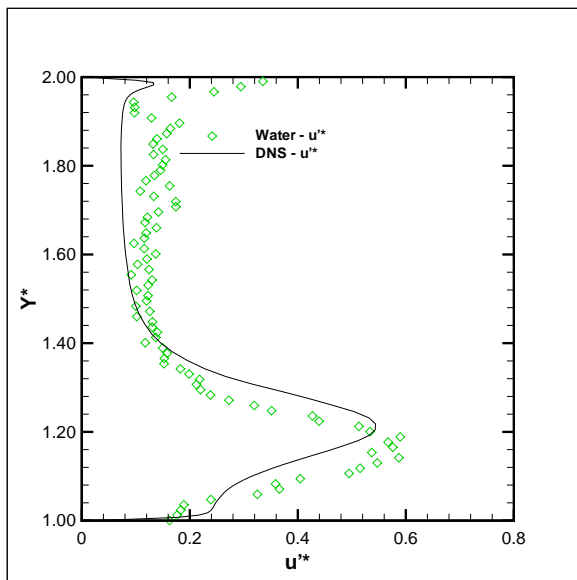
(c) Super Resolution FFT
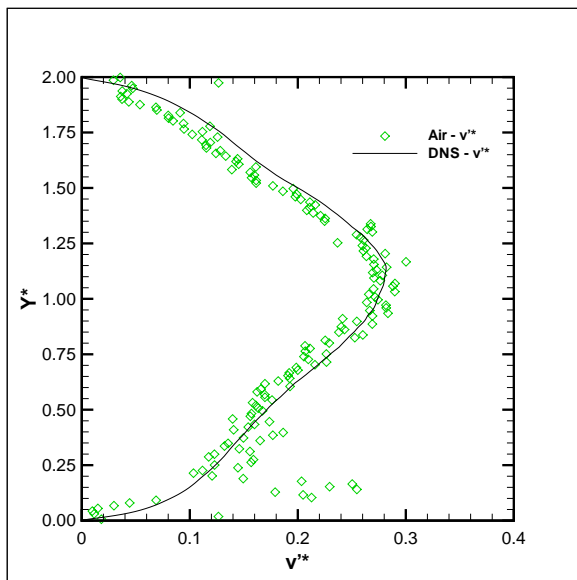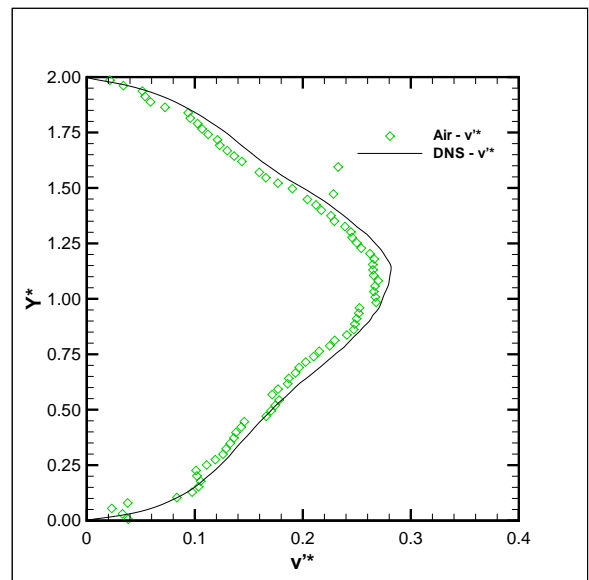
(d) Deformed FFT

Figure 6.25: Profile of averaged non-dimensionalised streamwise turbulent fluctuations in water at $x* = $ -0.5 (a) Standard FFT (b) Predictor Corrector FFT (c) Super Resolution FFT (d) Deformed FFT
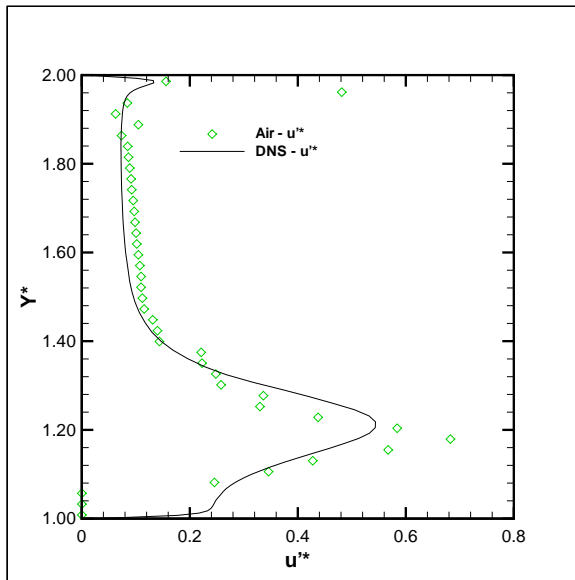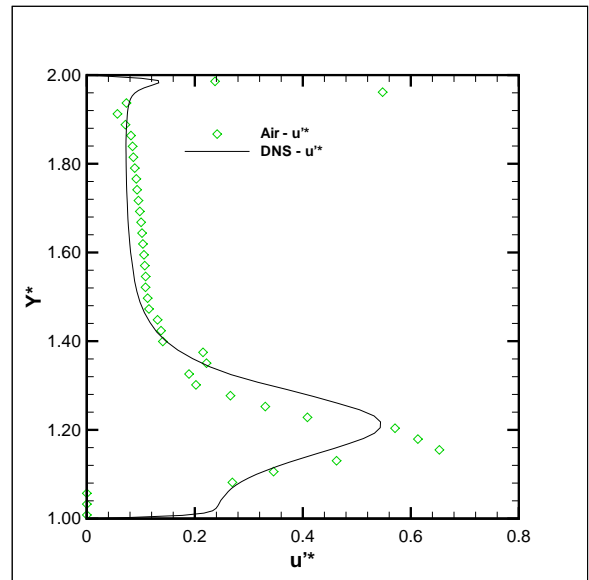
(a) Standard FFT

(b) Predictor Corrector FFT
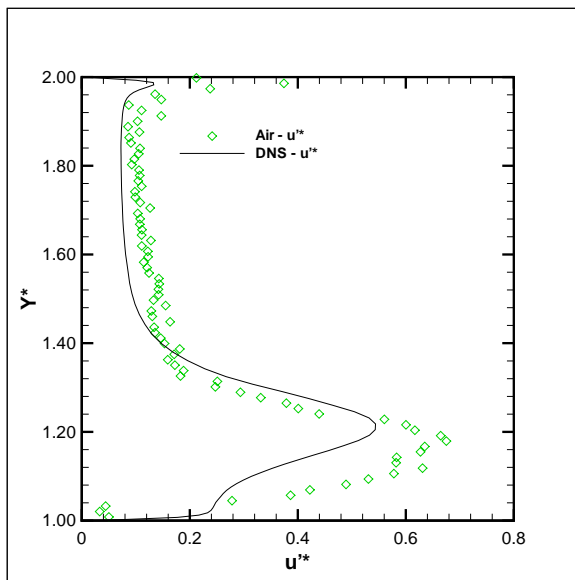
(c) Super Resolution FFT
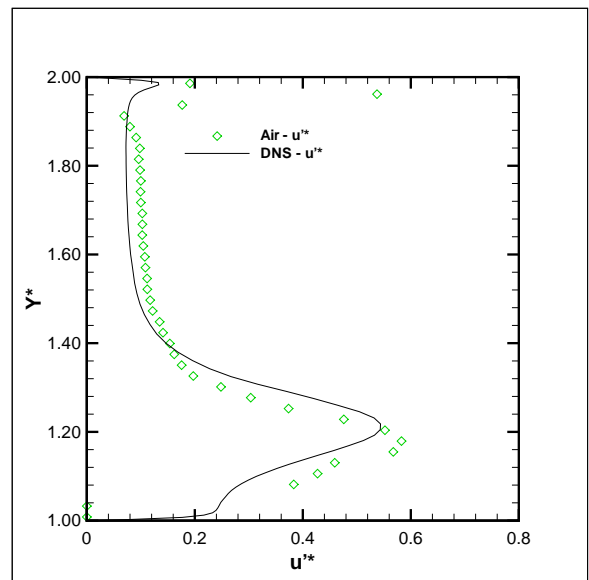
(d) Deformed FFT

Figure 6.26: Profile of averaged non-dimensionalised streamwise turbulent fluctuations in air at $x*$ $= -0.5$ (a) Standard FFT (b) Predictor Corrector FFT (c) Super Resolution FFT (d) Deformed FFT

(a) Standard FFT

(b) Predictor Corrector FFT
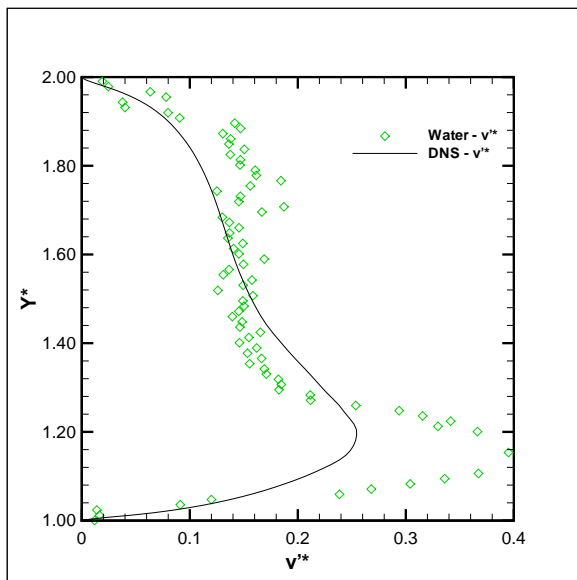
(c) Super Resolution FFT

(d) Deformed FFT

Figure 6.27: Profile of averaged non-dimensionalised normal turbulent fluctuations in water at $x*$ = -0.5 (a) Standard FFT (b) Predictor Corrector FFT (c) Super Resolution FFT (d) Deformed FFT
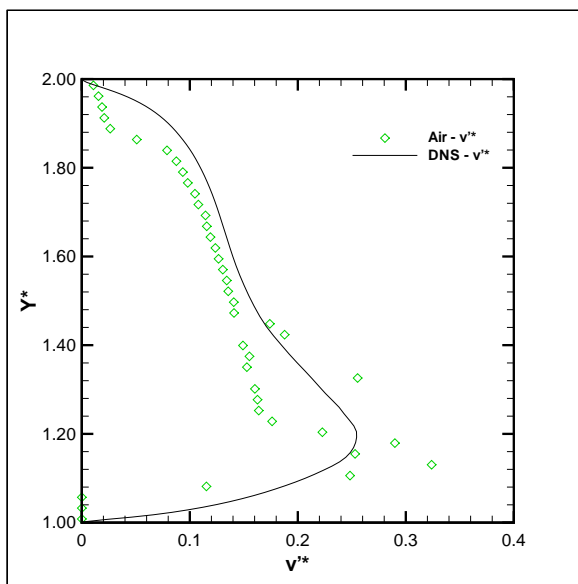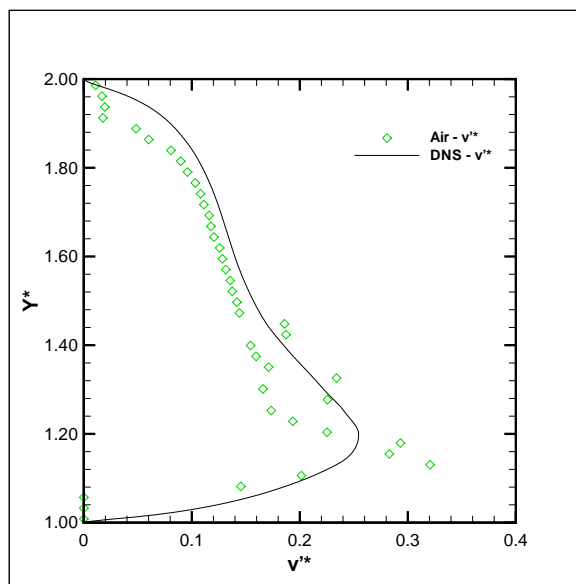
(a) Standard FFT

(b) Predictor Corrector FFT
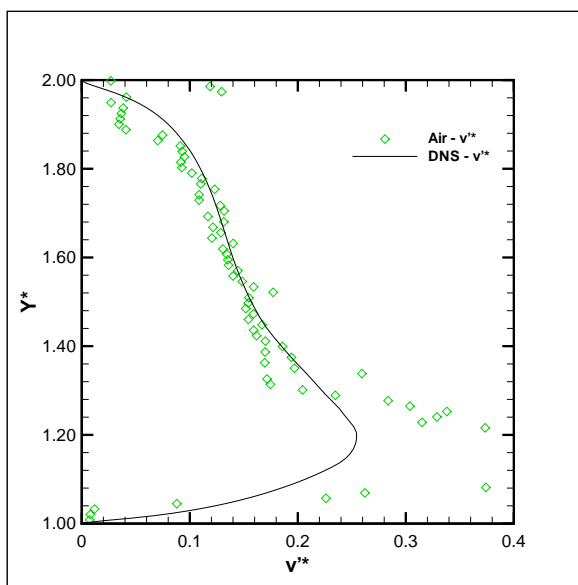
(c) Super Resolution FFT
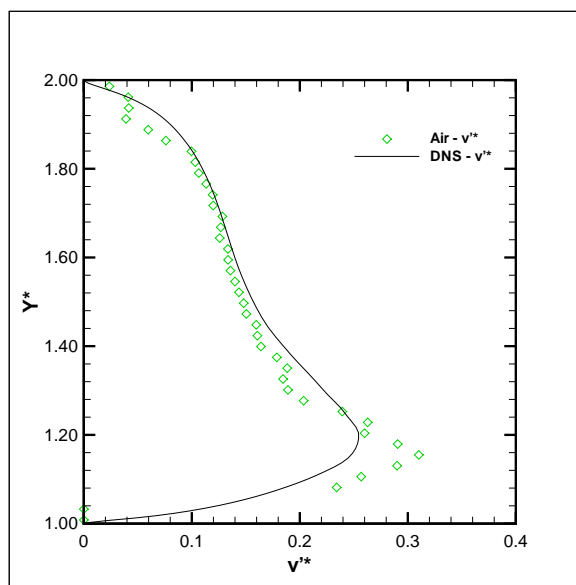
(d) Deformed FFT

Figure 6.28: Profile of averaged non-dimensionalised normal turbulent fluctuations in air at $x*$ $= -0.5$ (a) Standard FFT (b) Predictor Corrector FFT (c) Super Resolution FFT (d) Deformed FFT

6.6.8 Streamwise and Normal Profiles at $x_{index} = 1.0$

Average Velocity Profile

The flow characteristics at $x* = $ -0.5, which was located above the middle of the block, were presented in Figures 6.21 - 6.28. The non-dimensionalised average streamwise velocity profile at $x* = 1.0$, which was downstream of the block, was shown in Figures 6.29 and 6.30 for the water and air experiments, respectively. The measurements from the air experiment more closely match the DNS results than those from the water trial, although the difference was small. The maximum difference between the average streamwise velocity for the water and DNS results occurs between $1.5 < y* < 2$, and is approximately 0.1, or -8% different from the DNS simulation. The non-dimensionalised difference in the velocity can be converted into a pixel displacement $[(\Delta x, \Delta y)_{image}]$ by multiplying by the time separation $[\Delta t]$ and the mean velocity above the block $[U_m]$ and then dividing by the spatial scaling $[M]$ to convert from meters to pixels, as shown in Equations 6.8 and 6.9.

$$\Delta x_{image} = \frac{u* \cdot \Delta t \cdot U_m}{M} \tag{6.8}$$

$$\Delta y_{image} = \frac{v* \cdot \Delta t \cdot U_m}{M} \tag{6.9}$$

Therefore a difference in the non-dimensionalised velocity of 0.1 was less than a displacement of 0.4 pixels between the first and second images. It was difficult to determine how the error was divided among the cross-correlation scheme, the sub-pixel interpolation scheme, particle dynamics or even the experimental error. Nonetheless, the measurements for the water and the air experiments were similar to the DNS simulation results.

The average normal velocity profiles at $x* = 1.0$ are shown in Figures 6.31 and 6.32 for the water and air experiments, respectively. The measured normal velocity matched the DNS simulation well, with less than a 10% difference from the DNS simulation for the deformed FFT method. The shape and magnitude of the velocity was similar for both experiments, as was the point where the sign of the velocity switches, regardless of the cross-correlation scheme applied. However, of the four cross-correlation strategies employed, the deformed FFT method measured the average normal velocity profile closest to the DNS calculations.
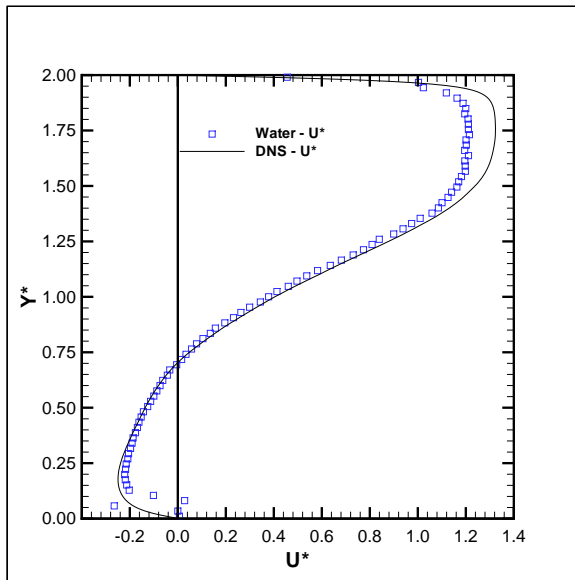
(a) Standard FFT
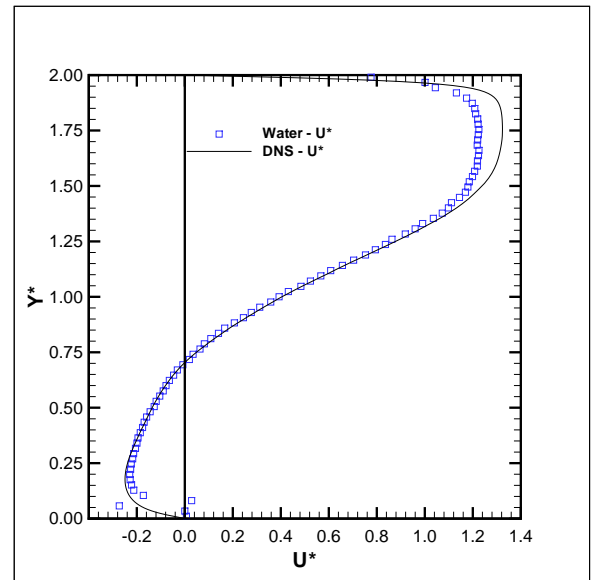
(b) Predictor Corrector FFT
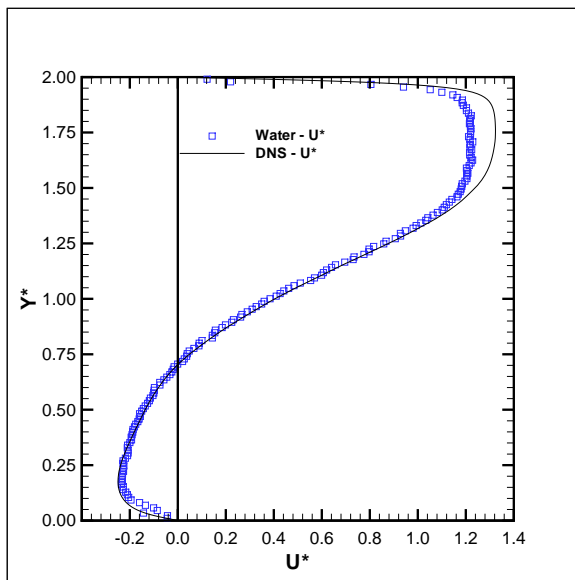
(c) Super Resolution FFT
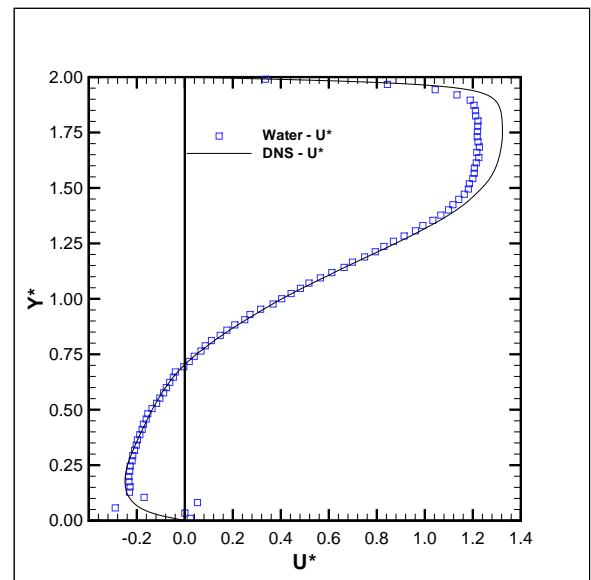
(d) Deformed FFT

Figure 6.29: Profile of averaged non-dimensionalised streamwise velocity in water at $x* = 1.0$ (a) Standard FFT (b) Predictor Corrector FFT (c) Super Resolution FFT (d) Deformed FFT
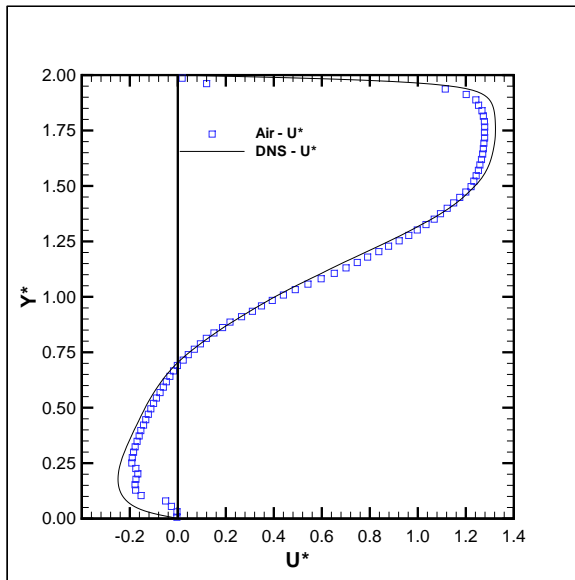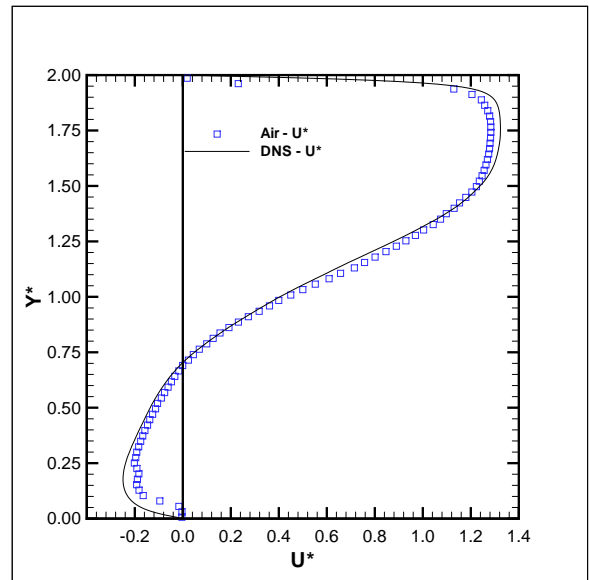
(a) Standard FFT

(b) Predictor Corrector FFT
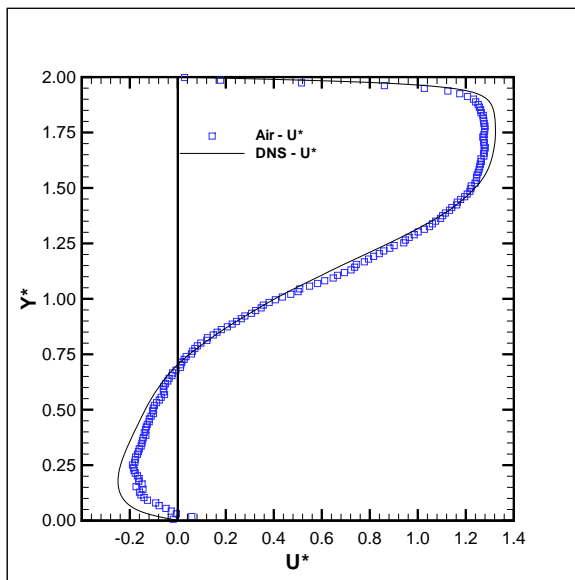
(c) Super Resolution FFT
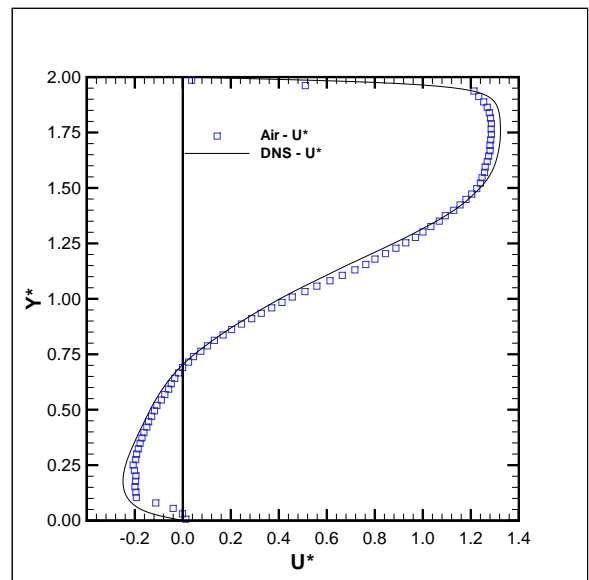
(d) Deformed FFT

Figure 6.30: Profile of averaged non-dimensionalised streamwise velocity in air at $x* = 1.0$ (a) Standard FFT (b) Predictor Corrector FFT (c) Super Resolution FFT (d) Deformed FFT
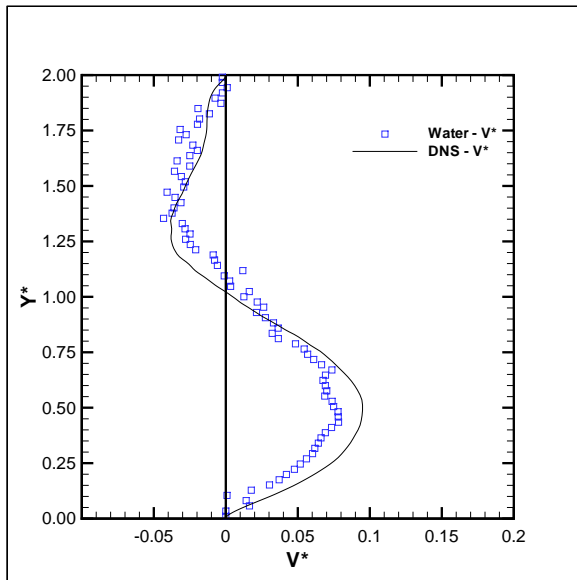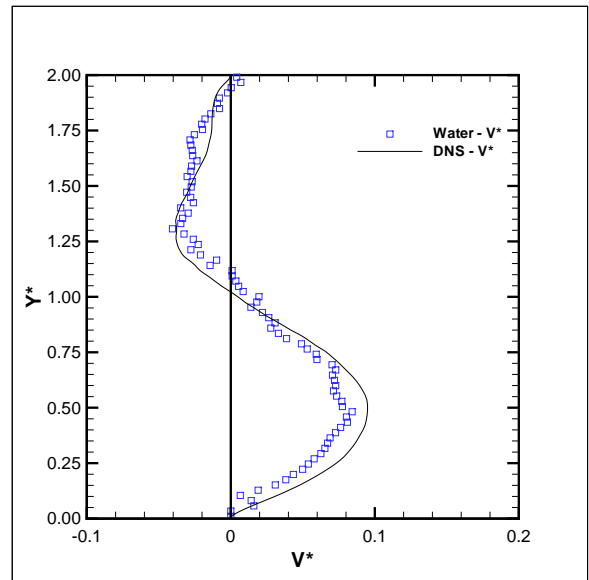
(a) Standard FFT

(b) Predictor Corrector FFT
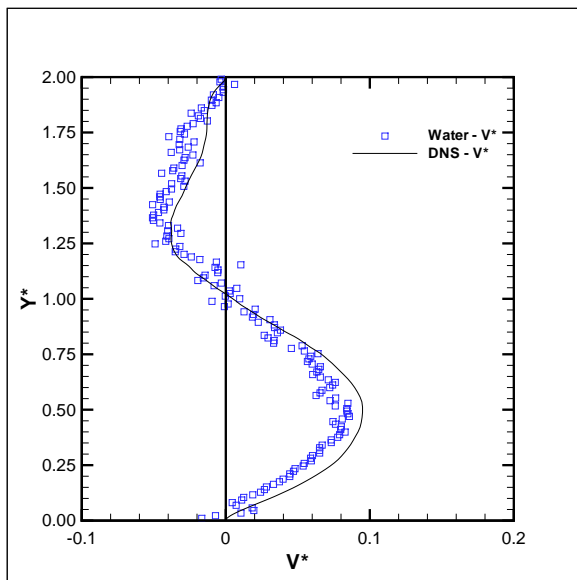
(c) Super Resolution FFT
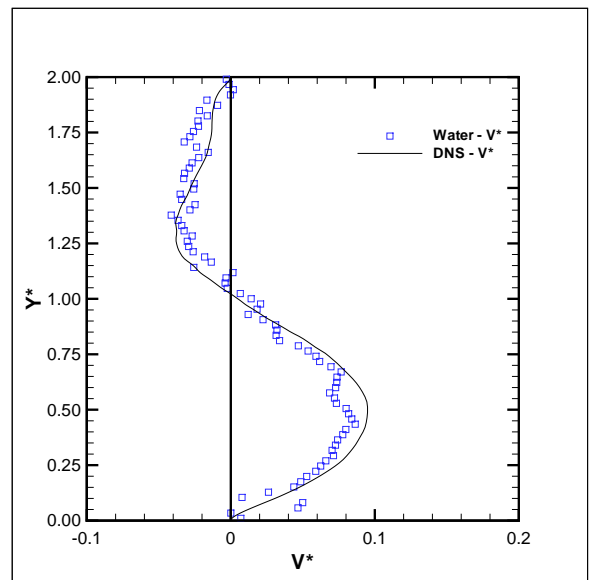
(d) Deformed FFT

Figure 6.31: Profile of averaged non-dimensionalised normal velocity in water at $x* = 1.0$ (a) Standard FFT (b) Predictor Corrector FFT (c) Super Resolution FFT (d) Deformed FFT
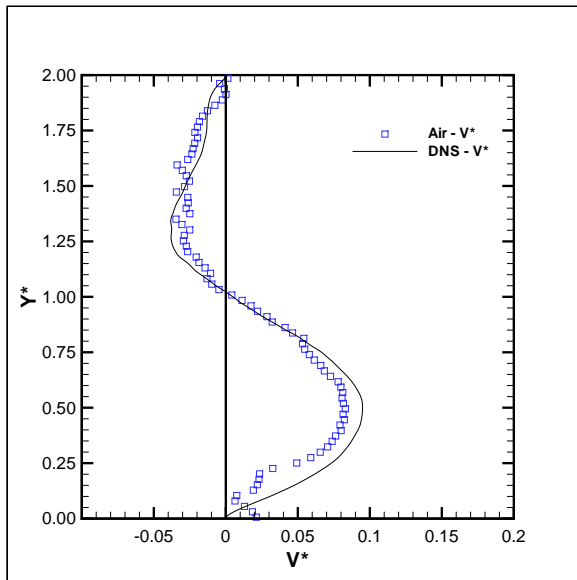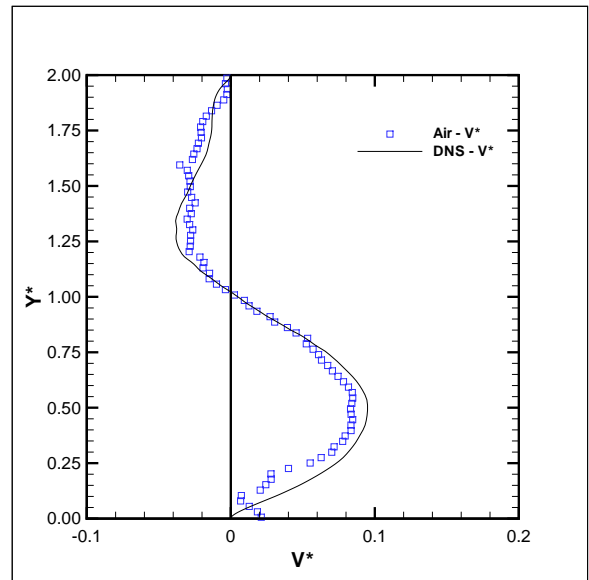
(a) Standard FFT

(b) Predictor Corrector FFT
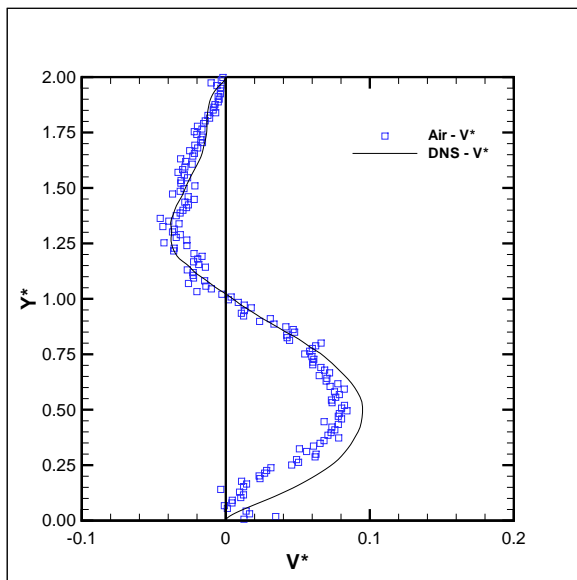
(c) Super Resolution FFT

(d) Deformed FFT

Figure 6.32: Profile of averaged non-dimensionalised normal velocity in air at $x* = 1.0$ (a) Standard FFT (b) Predictor Corrector FFT (c) Super Resolution FFT (d) Deformed FFT

Velocity Fluctuations Profile

The streamwise velocity fluctuations are shown in Figures 6.33 and 6.34 for the water and air trials, respectively. The measurements from the air experiment are closer to the DNS results than those from the water trial, especially when $y*$ was greater than 1. However, for both the water and air trials the measured magnitude of the fluctuations in the streamwise direction was less than that predicted by the DNS simulation when $y*$ was less than 0.75. The difference was very small, approximately 0.02 for the deformed FFT method, which was the closest to the DNS simulation of the four cross-correlation methods evaluated.

The comparisons between the water and air normal fluctuating velocity measurements and the DNS simulation are shown in Figures 6.35 and 6.36, respectively. The measurements for the water experiment when $y*$ was greater than 1.0 contained more error as they had more variation than the air trial. However, the measurements were very similar to the results of the DNS simulation, with the deformed FFT method producing the closest results.

6.7 Summary

The flow inside a multiple grooved channel was measured using each of the four cross-correlation strategies. Experiments were performed to verify if the conclusions drawn from the analysis of the synthetic images were more widely applicable than to only the ideal synthetic images. The difficulty with experiments was that rarely the exact answer was known, making it difficult to determine the errors of a measurement technique. For the multiple grooved channel, DNS calculations were available and allowed comparison of the vector velocity field, derived flow characteristics (such as the average vorticity) as well as some turbulent statistics, although the uncertainty of these statistics was unknown. As well, multiple experiments were performed using both water and air as the flow medium in the channel. This was done to verify that the cross-correlation methods were capable of measuring the motion of the seed particles in both water and air, which produced very different images.

(a) Standard FFT

(b) Predictor Corrector FFT

(c) Super Resolution FFT

(d) Deformed FFT

Figure 6.33: Profile of averaged non-dimensionalised streamwise turbulent fluctuations in water at $x* = 1.0$ (a) Standard FFT (b) Predictor Corrector FFT (c) Super Resolution FFT (d) Deformed FFT

(a) Standard FFT

(b) Predictor Corrector FFT

(c) Super Resolution FFT

(d) Deformed FFT

Figure 6.34: Profile of averaged non-dimensionalised streamwise turbulent fluctuations in air at $x* = 1.0$ (a) Standard FFT (b) Predictor Corrector FFT (c) Super Resolution FFT (d) Deformed FFT

(a) Standard FFT

(b) Predictor Corrector FFT

(c) Super Resolution FFT

(d) Deformed FFT

Figure 6.35: Profile of averaged non-dimensionalised normal turbulent fluctuations in water at $x*$ = 1.0 (a) Standard FFT (b) Predictor Corrector FFT (c) Super Resolution FFT (d) Deformed FFT
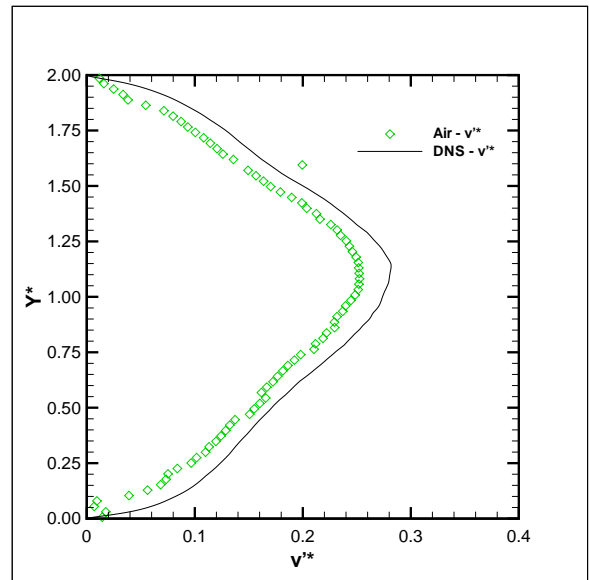
(a) Standard FFT

(b) Predictor Corrector FFT

(c) Super Resolution FFT

(d) Deformed FFT

Figure 6.36: Profile of averaged non-dimensionalised normal turbulent fluctuations in air at $x*$ = 1.0 (a) Standard FFT (b) Predictor Corrector FFT (c) Super Resolution FFT (d) Deformed FFT

The measured average velocity vector field and the derived average vorticity field were very similar to those predicted by the DNS calculations independent of which cross-correlation method was used, for both the water and air trials. As well, the second order statistics, the turbulent fluctuations, were similar to those predicted by the DNS simulation. The only comparison where there was a significant difference between the measured and the DNS results occured for the average normal velocity at the leading edge of the block. However, this difference could possibly be attributed to the slight chamfer on the edges of the block used for the experiments as compared to the sharp 90° corners used in the DNS simulation.

Of the four cross-correlation schemes evaluated, the deformed FFT was the most robust method since it produced the highest percentage of valid velocity vectors. As well, the measurements produced using the deformed FFT method matched the DNS simulation the best of the cross-correlation algorithms.

Chapter 7

Conclusions and Recommendations

7.1 Summary

PIV is a powerful tool used in fluid mechanics to measure the velocity of a flow field within a 2-D plane. PIV can provide estimates of both the instantaneous and average velocity vectors through an entire flow field. As a result, its popularity among researchers as the preferred flow measuring technique is growing, along with expectations of increased accuracy, improved vector resolution and the ability to measure the finer details of a flow.

The objective of this work was to compare the most common particle displacement extraction strategies in PIV against each other without bias and to determine their individual strengths and weaknesses. In the literature, when a PIV method is evaluated it was typically compared only to one other method, usually the simplest PIV algorithm, and applied to a specific flow. In this work, each PIV algorithm was applied to many different types of flows.

The four most common cross-correlation based strategies were chosen: (1) standard FFT (2) predictor corrector FFT (3) super resolution FFT and (4) deformed FFT. Each method uses a fast Fourier transform to perform the cross-correlation to estimate a representative particle displacement within the interrogation areas. The difference between the methods is how the

interrogation areas were selected. The standard FFT method was the simplest scheme examined and correlates the interrogation area in the first image to a corresponding interrogation area in the second image that was located in the same part of the image.

The predictor corrector FFT method was an extension of the standard FFT method where after the first cross-correlation was calculated in the standard manner, the cross-correlation was repeated with the interrogation area in the second image offset by an integer value equal to the displacement initially found using the standard FFT method. The advantage of the predictor corrector method was the ability to measure displacements less than 0.5 pixels, where the FFT based cross-correlation was most accurate.

The super resolution FFT scheme was very similar to the predictor corrector FFT method except the size of the interrogation area was reduced by a factor of two between iterations. Along with measuring displacements less than 0.5 pixels, the super resolution FFT allowed a higher resolution of velocity vectors without increasing the interrogation area overlap.

The final algorithm evaluated was the deformed FFT. Similar to the previous two methods, the deformed FFT method was an extension of the standard FFT algorithm where it repeated the cross-correlation for multiple iterations. However, the interrogation area in the second image was *constructed* by determining the offset of each pixel in the interrogation area of the first image. The advantage of the deformed FFT method was the cross-correlation measured a uniform particle displacement throughout the interrogation area, regardless of the actual flow. The uniform flow condition was important since it was a necessary assumption when using a cross-correlation to measure particle displacement.

The four cross-correlation algorithms were evaluated through analysis of both computer generated synthetic images and images collected from two experiments, one with water and the other with air as the fluid medium. The synthetic images were created using a MATLAB [55] computer program, which controlled the particle size, particle number density and the motion of the particles. Six different types of image displacement functions were used to *move* the particles; (1) uniform linear translation (2) step displacement profile (3) sawtooth displacement profile (4) sinusoid displacement profile (5) line source displacement and (6) line vortex displacement. The synthetic images were used since the exact particle displacement was known.

The experimental images were used to verify the conclusions drawn from the results of the analysis of the synthetic images. The flow in a multiple grooved channel was measured using both water and air as the working fluid. This was done since the images collected in the experiments using water as the fluid medium were very different from those obtained using air, due to the individual seeding requirements of each fluid. The difficulty with using experimental images to examine the errors in a cross-correlation strategy is that the exact answer is generally unknown. However, in the case of the grooved channel, the measured results could be compared to DNS calculations, which were considered to be highly accurate.

7.1.1 Conclusions based on the Analysis of the Synthetic Images

Standard FFT Algorithm

The standard FFT method, which the other three algorithms are adaptions of, performed well for the analysis of all of the synthetic images. The relative error for the standard FFT method was comparable to the other cross-correlation algorithms evaluated and the algorithm was able to estimate the step displacement much better than the super resolution FFT and deformed FFT methods. However, the robustness of the standard FFT method consistently ranked third of the four cross-correlation schemes since the method only used one iteration. The standard FFT method should be applied to experiments where a high degree of accuracy is not required, *i.e.* most industrial flow applications.

Predictor Corrector FFT Algorithm

The predictor corrector FFT algorithm displayed very little improvement in accuracy compared to the standard FFT method although the robustness of the predictor corrector FFT method consistently ranked second best of the four cross-correlation algorithms evaluated. The improved robustness over the standard FFT method was attributed to the repeated iterations. The predictor corrector FFT scheme was able to estimate the displacements in the step images the best of the four cross-correlation algorithms, slightly better than the standard FFT method. The

predictor corrector FFT method should be applied to flows where a sharp discontinuity exists within the flow, *i.e.* a co-flow with two fluids of high viscosity, or in a flow with very uniform flow, *i.e.* flow in a pipe.

Super Resolution FFT Algorithm

The super resolution FFT method consistently ranked the worst of the four cross-correlation algorithms for robustness. This was due to the smaller interrogation areas used for the final iteration which contained fewer particles compared to the other algorithms. The results for the images generated with the step displacement function contained large errors around the step due to the interpolation used to offset the interrogation areas between iterations. However, the super resolution FFT method was able to estimate the particle displacements in the sinusoid images the best of four cross-correlation algorithms. The increased accuracy was attributed to the smaller interrogation areas used for the final iteration. The smaller interrogation areas contained a smaller range of displacements and the maximum positional bias was smaller. The super resolution FFT method produced the best spatial resolution of the four cross-correlation algorithms since the spacing between vectors was smaller, also due to the smaller interrogation areas. The super resolution FFT method should be applied to flows which contain a high frequency of velocity gradients, *i.e.* multiple jets in a line.

Deformed FFT Algorithm

The deformed FFT algorithm was the most accurate of the four cross-correlation algorithms for the uniform translation algorithms since the interrogation areas were capable of sub-pixel offsets between iterations. Similar to the super resolution FFT method, the deformed FFT scheme had difficulty properly measuring the step images due to the interpolation required in generating the interrogation areas. However, the deformed FFT was consistently the most robust of the four cross-correlation algorithms and produced the most accurate results for the images generated with the source and vortex displacement functions. The deformed FFT algorithm should be applied

to flows which contain large velocity gradients in two directions, *i.e.* swirling flows, or when a high degree of accuracy is required from the displacement results.

7.1.2   Summary of the Analysis of the Experimental Images

To verify that the results from the synthetic images were not specific to the computer generated images, experiments were conducted to measure the flow in a multiple grooved channel. The multiple grooved channel was chosen since DNS calculations for the flow were available. The experiments were conducted using both water and air as the fluid medium since the seed particles are very different, thus producing different images.

The measured average velocity vector field, the derived average vorticity and the turbulent fluctuation data were very similar to the DNS calculations for all cross-correlation methods for both the water and air trials. The only comparison where there was a significant difference between the measured and the DNS results occured for the average normal velocity at the leading edge of the block. However, differences here could be attributed to the slight chamfer on the leading edge of the block, compared to the sharp 90° corner used in the DNS simulation.

Overall, the PIV experiments produced results that were similar to the DNS simulation, proving the capability of PIV to measure complex flows. Of the four cross-correlation schemes evaluated the deformed FFT consistently produced measurements closest to the DNS simulation, which agrees with the results from the synthetic image analysis.

7.2   Recommendations for Future Work

The current comparison between the four FFT based cross-correlation techniques did not investigate the effect of altering the parameters associated with the peak validation scheme used between iterations. Also, using different validation schemes, such as a nearest neighbour comparison, may improve the results for some of the methods in certain applications, especially for the methods that interpolate the displacement vector field and where a *smooth* vector field is beneficial.

Only the super resolution FFT and deformed FFT methods used interpolation as a part of their algorithms when determining interrogation area offsets between iterations. The interpolation scheme applied for this study was the simplest method to implement, bi-linear interpolation. Higher order interpolation schemes, *i.e.* bi-cubic, spline, *etc.*, may improve the accuracy of these interpolated offset values, thus improving the accuracy of the results.

Any future investigations should explore the combination of the super resolution FFT and deformed FFT methods. The combined method would use the deformed FFT algorithm to construct the interrogation areas but the size of the interrogation areas would reduce by a factor of 2 between iterations, similar to the super resolution FFT scheme.

Finally, the placement of the vector at a location other than the centre of the interrogation area should be investigated with the iterative cross-correlation algorithms. The results from the synthetic images, especially the sawtooth and sinusoid images, displayed how each method was capable of measuring a displacement that existed somewhere within the interrogation area. However, the displacement measured did not always occur at the centre of the interrogation area. By placing the velocity vector in the correct location within the interrogation area, the interpolation used to determine the offset values for each of the methods using iterations would improve, leading to more accurate results. As well, the accuracy of the final velocity vector field would increase, regardless of which method was applied since the positional bias error would be removed/minimised.

References

[1] K.-S. Yang, "Large eddy simulation of turbulent flows in periodically grooved channel," *J. Wind Eng. Ind. Aerodyn.*, vol. 84, pp. 47–64, 2000.

[2] P. Buchhave, J. M. Delhaye, F. Durst, W. K. George, K. Refslud, and J. H. Whitelaw, eds., *Proceedings of the LDA-Symposium in Copenhagen*, (Denmark), 1975.

[3] F. Durst, A. Melling, and J. H. Whitelaw, *Principles and Practice of Laser-Doppler Anemometry*. New York, New York: Academic Press Inc., 1976.

[4] H. D. Thompson and W. H. Stevenson, *Laser Velocimetry and Particle Sizing*. New York: Hemisphere Publishing Corporation, 1979.

[5] R. J. Adrian, "Particle-imaging techniques for experimental fluid mechanics," *Annu. Rev. Fluid Mech.*, vol. 23, pp. 261–304, 1991.

[6] C. J. D. Pickering and N. A. Halliwell, "Laser speckle photography and particle image velocimetry: photographic film noise," *Applied Optics*, vol. 23, pp. 2961–2969, 1984.

[7] K. Takehara, R. J. Adrian, G. T. Etoh, and K. T. Christensen, "A Kalman tracker for super-resolution PIV," *Experiments in Fluids [Suppl.]*, pp. S34–S41, 2000.

[8] E. A. Cowen and S. G. Monismith, "A hybrid digital particle tracking velocimetry technique," *Experiments in Fluids*, vol. 22, pp. 199–211, 1997.

[9] J. E. Rehm and N. T. Clemens, "An improved method for enhancing the resolution of conventional double-exposure single-frame particle image velocimetry," *Experiments in Fluids*, vol. 26, pp. 497–504, 1999.

[10] R. D. Keane, R. J. Adrian, and Y. Zhang, "Super-resolution particle imaging velocimetry," *Meas. Sci. Technol.*, vol. 6, pp. 754–768, 1995.

[11] Y. A. Hassan, T. K. Blanchat, and C. H. S. Jr., "PIV flow visualization using particle tracking techniques," *Meas. Sci. Technol.*, vol. 3, pp. 633–642, 1992.

[12] Y. G. Guezennec and N. Kiritsis, "Statistical investigation or errors in particle image velocimetry," *Experiments in Fluids*, vol. 10, pp. 138–146, 1990.

[13] I. Grant, "Particle image velocimetry: a review," *Proc. Instn. Mech. Engrs.*, vol. 211, pp. 55–76, 1997.

[14] C. Brucker, "3D scanning PIV applied to an air flow in a motored engine using digital high-speed video," *Meas. Sci. Technol.*, vol. 8, pp. 1480–1492, 1997.

[15] T. P. Chang, N. A. Wilcox, and G. B. Tatterson, "Application of image processing to the analysis of three-dimensional flow fields," *Opt. Engng*, vol. 23, pp. 283–287, 1984.

[16] N. J. Lawson and J. Wu, "Three-dimensional particle image velocimetry: error analysis of stereoscopic techniques," *Meas. Sci. Technol.*, vol. 8, pp. 894–900, 1997.

[17] S. K. Sinha, "Improving the accuracy and resolution of particle image or laser speckle velocimetry," *Experiments in Fluids*, vol. 6, pp. 67–68, 1988.

[18] www.dantecmt.com, "Dantec Dynamics website." Internet.

[19] W. T. Lai, "Particle image velocimetry: a new approach in experimental fluid research," in *Three-Dimensional Velocity and Vorticity Measuring and Image Analysis Techniques*, pp. 61–92, Kluwer Academic Publishers, 1996. TSI Incorparted.

[20] C. E. Willert and M. Gharib, "Digital particle image velocimetry," *Experiments in Fluids*, vol. 10, pp. 181–193, 1991.

[21] C. Willert, "The fully digital evaluation of photographic PIV recordings," *Applied Scientific Research*, vol. 56, pp. 79–102, 1996.

[22] R. D. Keane and R. J. Adrian, "Optimization of particle image velocimeters. Part 1: Double pulsed systems," *Meas. Sci. Technol.*, vol. 1, pp. 1205–1215, 1990.

[23] R. D. Keane and R. J. Adrian, "Optimization of particle image velocimeters. Part 2: Multiple pulsed systems," *Meas. Sci. Technol.*, vol. 2, pp. 963–974, 1991.

[24] P. Buchhave, "Particle image velocimetry — status and trends," *Experimental Thermal and Fluid Science*, vol. 5, pp. 586–604, 1992.

[25] M. Raffel, C. Willert, and J. Kompenhans, *Particle Image Velocimetry – A Practical Guide*. Berlin, Germany: Springer, 1998.

[26] R. D. Keane and R. J. Adrian, "Theory of cross-correlation analysis of PIV images," *Applied Scientific Research*, vol. 49, pp. 191–215, 1992.

[27] L. Gui and W. Merzkirch, "Generating arbitrarily sized interrogation windows for correlation-based analysis of particle image velocimetry recordings," *Experiments in Fluids*, vol. 24, pp. 66–69, 1998.

[28] Dantec Measurement Technology, *FlowMap Particle Image Velocimetry Instrumentation, Installation and User's Guide*, 1999.

[29] J. Westerweel, "Fundamentals of digital particle image velocimetry," *Meas. Sci. Technol.*, vol. 8, pp. 1379–1392, 1997.

[30] J. Nogueria, A. Lecuona, and P. A. Rodriguez, "Local field correction PIV: on the increase of accuracy of digital PIV systems," *Experiments in Fluids*, vol. 27, pp. 107–116, 1999.

[31] L. Lourenco and A. Krothapalli, "On the accuracy of velocity and vorticity measurements with PIV," *Experiments in Fluids*, vol. 18, pp. 421–428, 1995.

[32] J. Westerweel, "Theoretical analysis of the measurement precision in particle image velocimetry," *Experiments in Fluids [Suppl.]*, pp. S3–S12, 2000.

[33] J. Nogueria, A. Lecuona, and P. A. Rodriguez, "Identification of a new source of peak locking, analysis and its removal in conventional and super-resolution PIV techniques," *Experiments in Fluids*, vol. 30, pp. 309–316, 2001.

[34] C. N. Young, *Quantification of the flow structure in pool fires*. Ph. D research proposal, University of Waterloo, 2000.

[35] M. Muste, Z. Xiong, A. Kruger, and I. Fujita, "Error estimation in PIV applied to large-scale flows," in *The 3rd International Workshop on PIV'99*, (Santa Barbara, USA), September 1999.

[36] A. K. Prasad, R. J. Adrian, C. C. Landreth, and P. W. Offutt, "Effect of resolution on the speed and accuracy of particle image velocimetry interrogation," *Experiments in Fluids*, vol. 13, pp. 105–116, 1992.

[37] R. J. Adrian, "Dynamic ranges of velocity and spatial resolution of particle image velocimetry," *Meas. Sci. Technol.*, vol. 8, pp. 1393–1398, 1997.

[38] H. Huang, D. Dabiri, and M. Gharib, "On errors of digital particle image velocimetry," *Meas. Sci. Technol.*, vol. 8, pp. 1427–1440, 1997.

[39] A. Melling, "Tracer particles and seeding for particle image velocimetry," *Meas. Sci. Technol.*, vol. 8, pp. 1406–1416, 1997.

[40] J. O. Hinze, *Turbulence*. New York, USA: McGraw-Hill, 2nd ed., 1975.

[41] A. Boillot and A. K. Prasad, "Optimization procedure for pulse separation in cross-correlation PIV," *Experiments in Fluids*, vol. 21, pp. 87–93, 1996.

[42] R. J. Adrian, "Limiting resolution of particle image velocimetry for turbulent flow," in *Advances in Turbulence Research*, pp. 1–19, Pohang, Korea: Postech, 1995.

[43] S. T. Wereley and C. D. Meinhart, "Accuracy improvements in particle image velocimetry algorithms," in *Proceedings of the 10th Applications of Laser Techniques to Fluid Mech.*, (Lisbon, Portugal), July 2000.

[44] M. L. Jakobsen, T. P. Dewhirst, and C. A. Greated, "Particle image velocimetry for predictions of acceleration fields and force within fluid flows," *Meas. Sci. Technol.*, vol. 8, pp. 1502–1516, 1997.

[45] H. T. Huang and H. E. Fielder, "Deformed particle image pattern matching in particle image velocimetry," *Applied Scientific Research*, vol. 51, pp. 179–183, 1993.

[46] H. T. Huang, H. E. Fielder, and J. J. Wang, "Limitation and improvement of PIV - Part 1: Limitation of conventional techniques due o deformation of particle image patterns," *Experiments in Fluids*, vol. 15, pp. 168–174, 1993.

[47] C. N. Young, R. Gilbert, D. A. Johnson, and E. J. Weckman, "Vector placement to reduce positional bias and improve PIV results." To be published in ASME symposium on Experimental and Numerical flow visualization and Laser Anemometry, June 2002.

[48] J. Westerweel, D. Dabiri, and M. Gharib, "The effect of a discrete window offset on the accuracy of cross-correlation analysis of digital PIV recordings," *Experiments in Fluids*, vol. 23, pp. 20–28, 1997.

[49] F. Scarano and M. L. Riethmuller, "Iterative multigrid approach in PIV image processing with discrete window offset," *Experiments in Fluids*, vol. 26, pp. 513–523, 1999.

[50] H. T. Huang, H. E. Fielder, and J. J. Wang, "Limitation and improvement of PIV - Part 2: Particle image distortion, a novel technique," *Experiments in Fluids*, vol. 15, pp. 263–273, 1993.

[51] S. Ashforth-Frost, B. N. Dobbins, K. Jambunathan, X. P. Wu, and Y. Ju, "A comparison of interrogation methods for particle image velocimetry," *SPIE*, vol. 2005, pp. 478–489, 1993.

[52] K. Jambunathan, X. Y. Ju, B. N. Dobbins, and S. Asforth-Frost, "An improved cross correlation technique for particle image velocimetry," *Meas. Sci. Technol.*, vol. 6, pp. 507–514, 1995.

[53] W. Weng, G. Liao, and W. Fan, "An improved cross-correlation method for (digital) particle image velocimetry," in *Proceedings of the 10th Applications of Laser Techniques to Fluid Mech.*, (Lisbon, Portugal), July 2000.

[54] W. H. Press, S. A. Teukolsky, W. T. Vetterling, and B. P. Flannery, *Numerical Recipes in C*. United Kingdom: Cambridge University Press, 2nd ed., 1992.

[55] The Mathworks, *MATLAB Reference Manual*.

[56] C. Y. Young, 2001. Synthetic Image Generator Computer Program.

[57] R. J. Adrian, "Statistical properties of particle image velocimetry measurements in turbulent flow," *Laser Anemometry in Fluid Mechanics*, vol. 3, pp. 115–129, 1988.

[58] K. S. Yang, April 2000. Personal correspondance.

Appendix A

Step Results

In this Appendix the results for the images generated with the step displacement function are presented for the different periods of 64, 128 and 256 pixels to show the conclusions in Chapter 5 were independent of step displacement function period. For all the results shown, the mean particle size was 4 pixels in diameter with a particle density of 15 particles per 32x32 pixel area.

Every validated measurement from the four cross-correlation methods are shown in Figures A.1, A.2 and A.3 for a period of 64, 128 and 256 pixels, respectively. The results for all three periods were similar with the standard FFT and predictor corrector FFT algorithms accurately estimating the step function. The super resolution FFT and deformed FFT schemes both had difficulty near the location of the step.

The displacement results were averaged and are shown in Figures A.4, A.5 and A.6 for periods of 64, 128 and 256 pixels, respectively. The error in the super resolution FFT and deformed FFT algorithms when measuring the step displacement is shown in the rounding of the measurements, regardless of the period.

The mean bias and random errors are shown in Figures A.7, A.8 and A.9 for periods of 64, 128 and 256 pixels, respectively. As expected the mean bias and random errors were independent of the period of the step displacement.
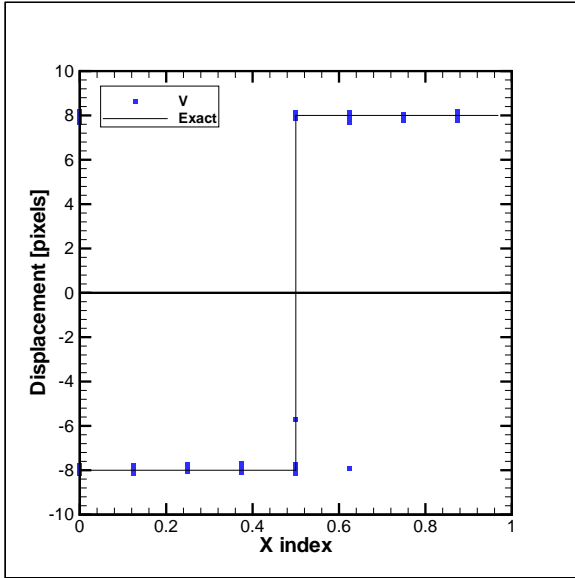
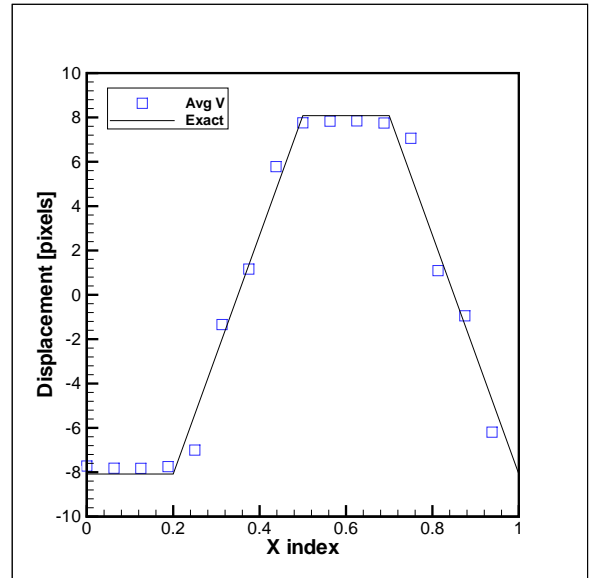(a) Standard FFT
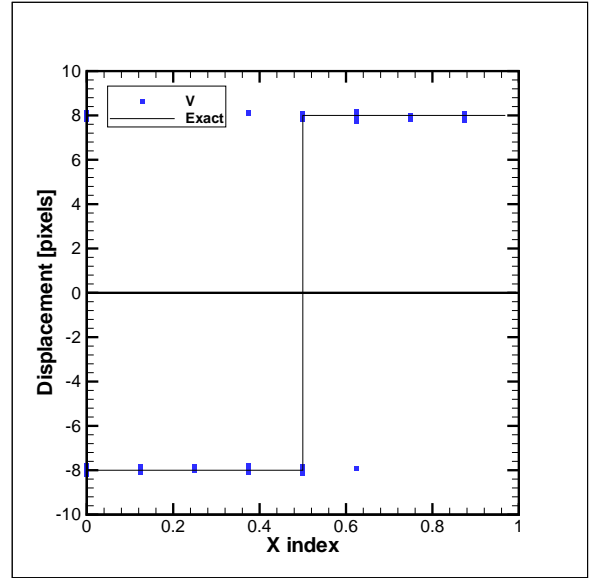
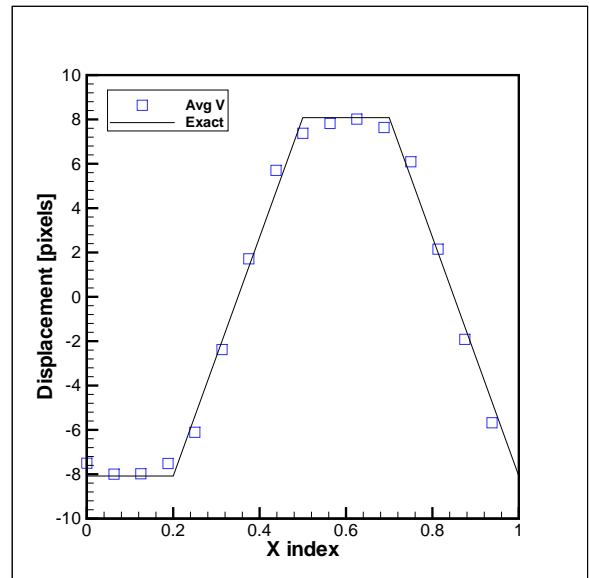(b) Predictor Corrector FFT
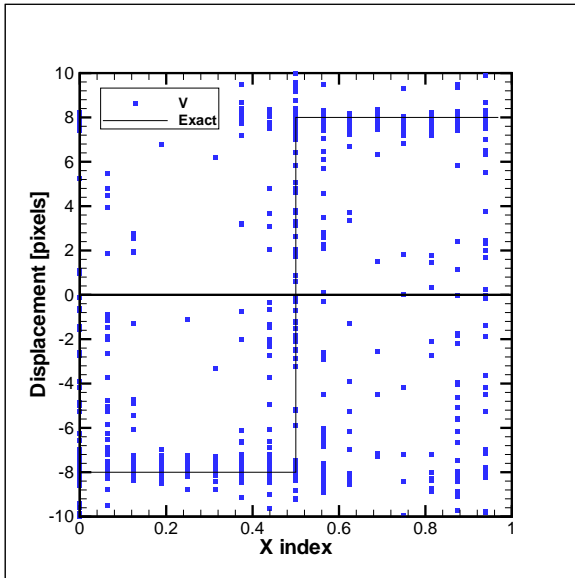
(c) Super Resolution FFT
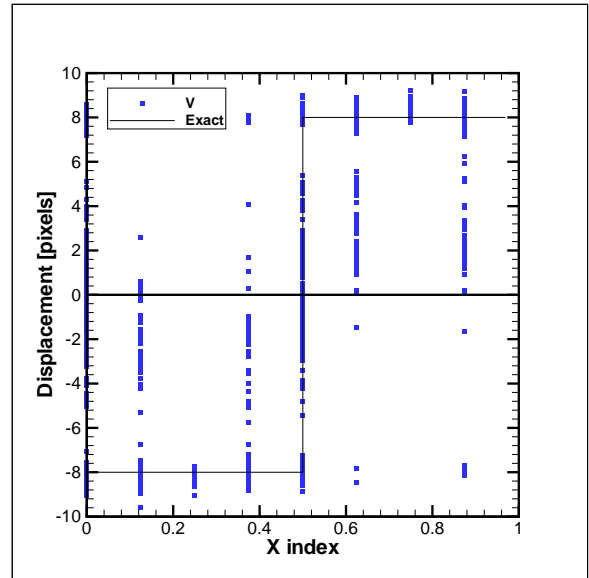
(d) Deformed FFT

Figure A.1: Validated displacement measurements for step displacement function of period 64, particle size 4 pixels in diameter and a particle number density of 15 particles per 32x32 pixel area (a) Standard FFT (b) Predictor Corrector FFT (c) Super Resolution FFT (d) Deformed FFT
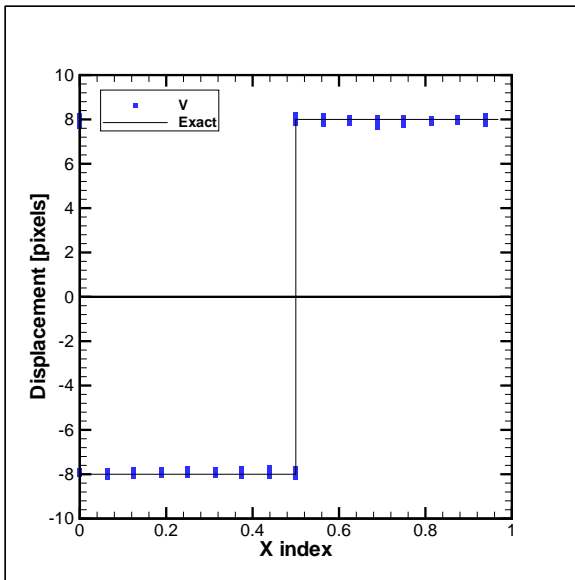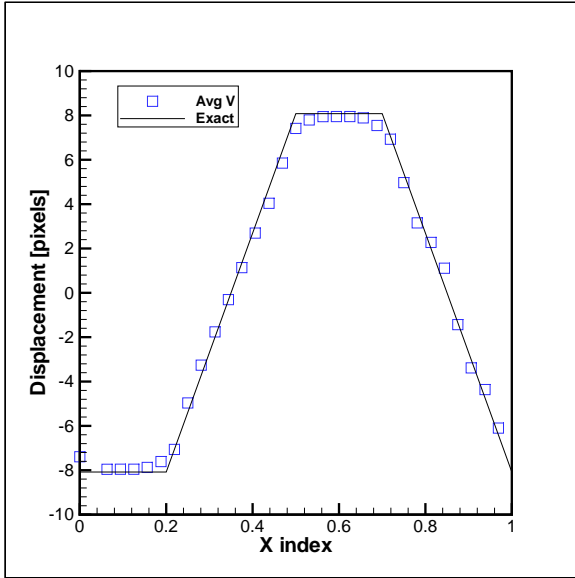
(a) Standard FFT
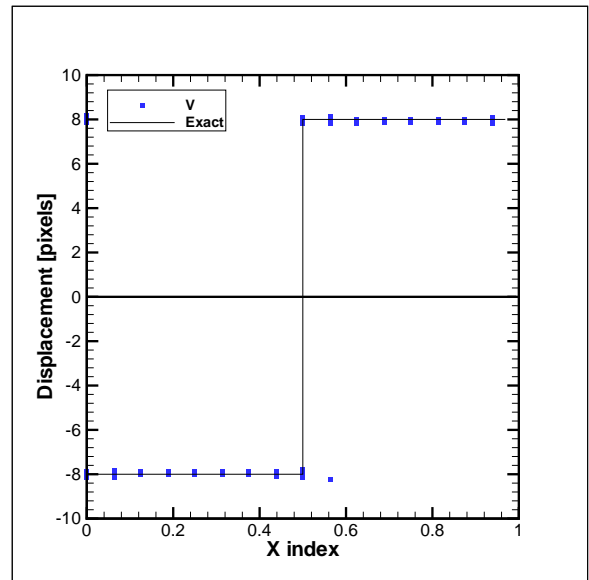
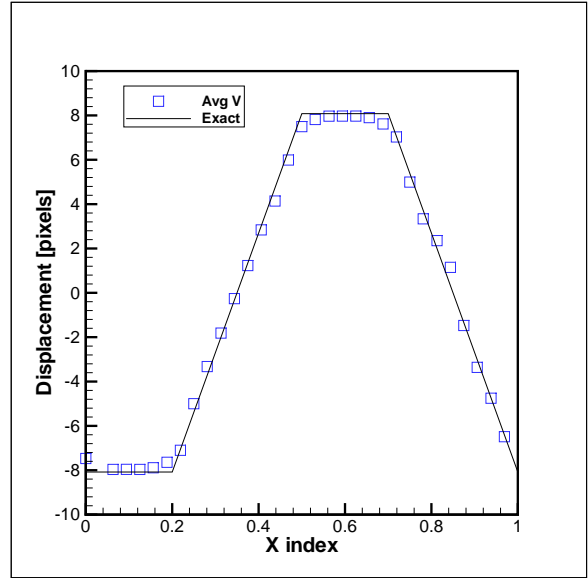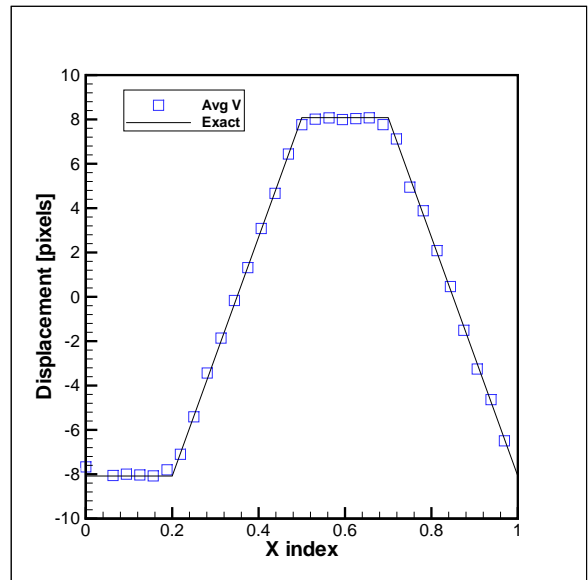(b) Predictor Corrector FFT
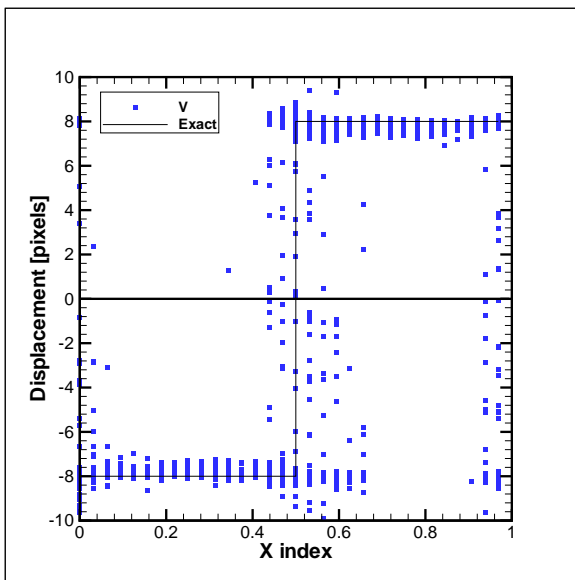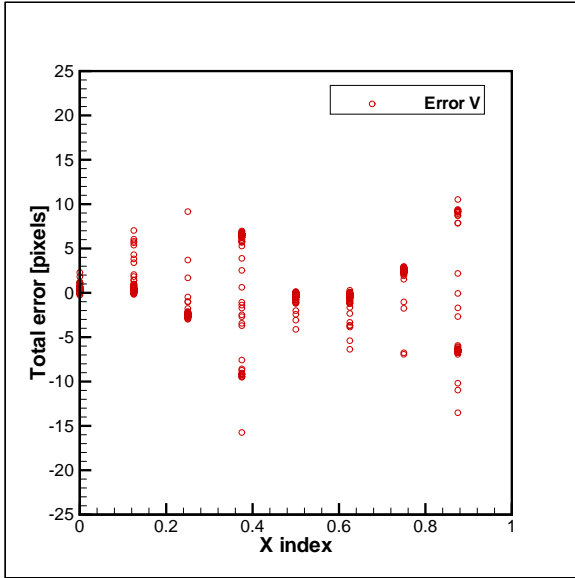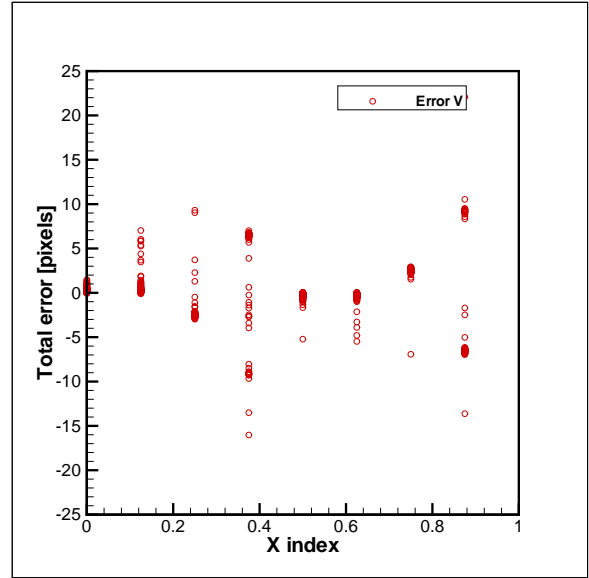
(c) Super Resolution FFT
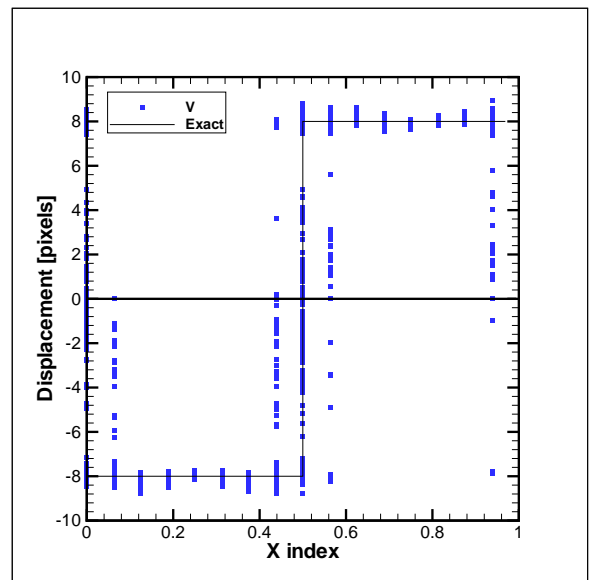
(d) Deformed FFT

Figure A.2: Validated displacement measurements for step displacement function of period 128, particle size 4 pixels in diameter and a particle number density of 15 particles per 32x32 pixel area (a) Standard FFT (b) Predictor Corrector FFT (c) Super Resolution FFT (d) Deformed FFT
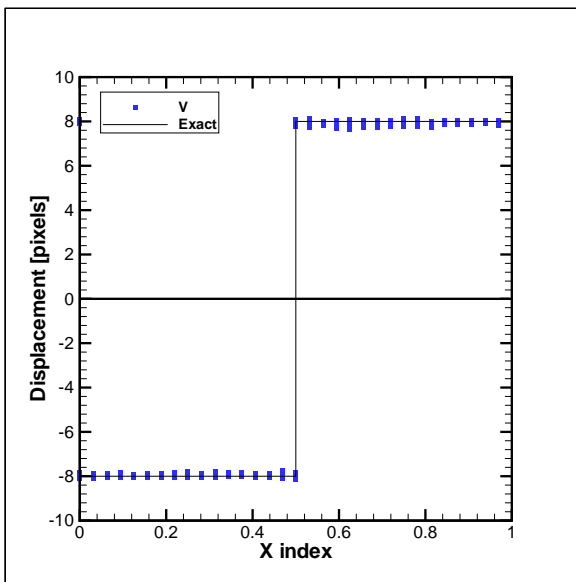
(a) Standard FFT
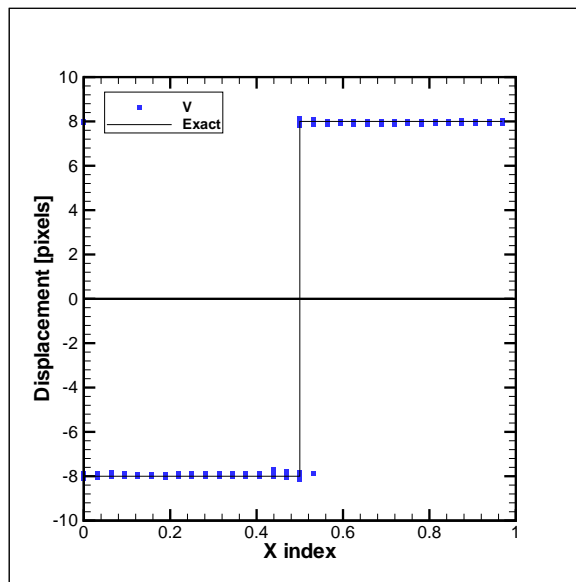
(b) Predictor Corrector FFT
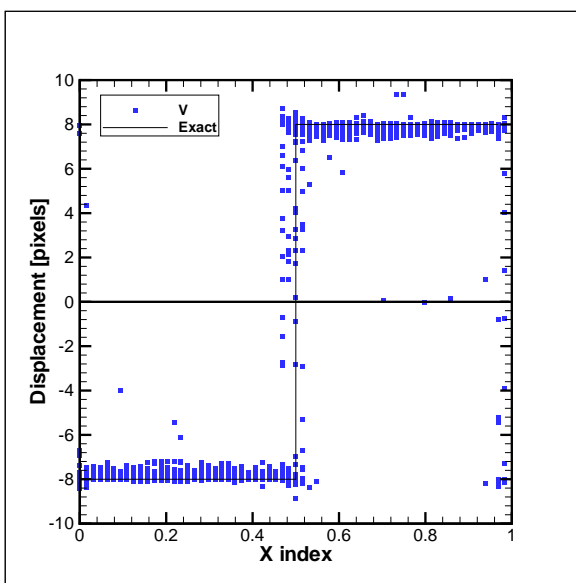
(c) Super Resolution FFT
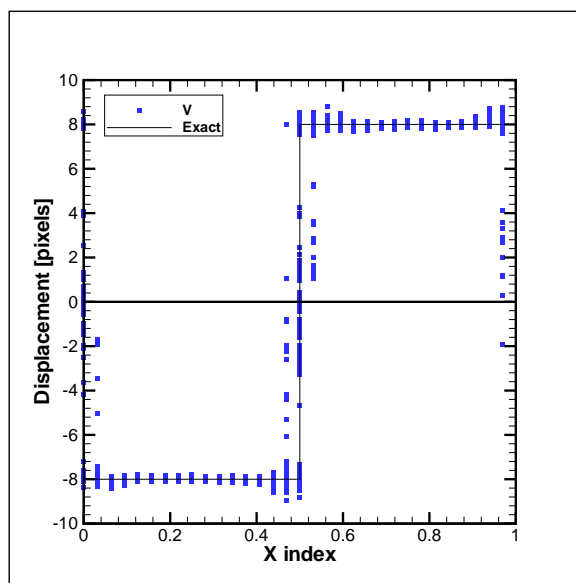
(d) Deformed FFT

Figure A.3: Validated displacement measurements for step displacement function of period 256, particle size 4 pixels in diameter and a particle number density of 15 particles per 32x32 pixel area (a) Standard FFT (b) Predictor Corrector FFT (c) Super Resolution FFT (d) Deformed FFT
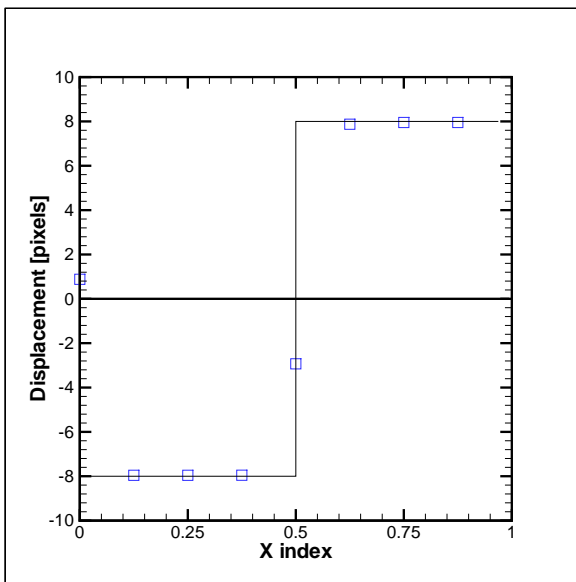
(a) Standard FFT
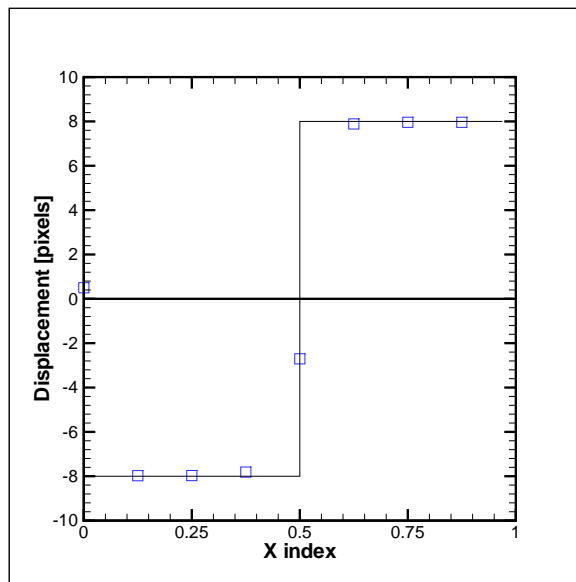
(b) Predictor Corrector FFT
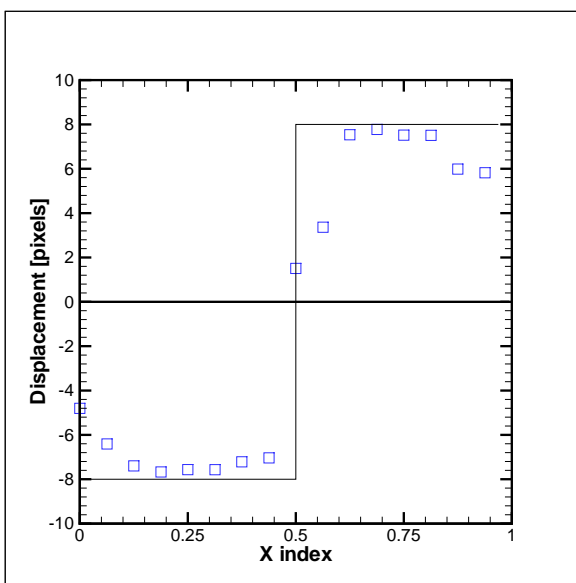
(c) Super Resolution FFT
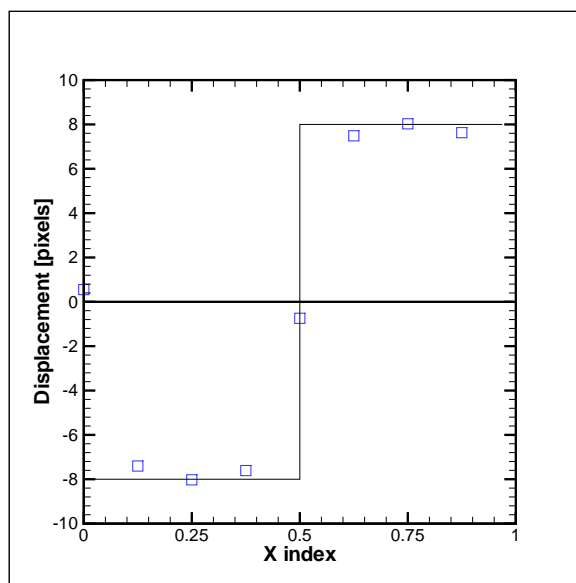
(d) Deformed FFT

Figure A.4: Ensemble averaged measurements for step displacement function of period 64, particle size 4 pixels in diameter and a particle n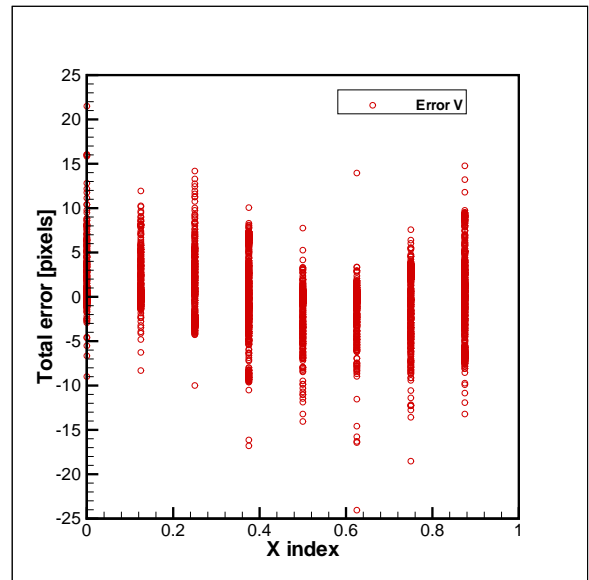umber density of 15 particles per 32x32 pixel area (a) Standard FFT (b) Predictor Corrector FFT (c) Super Resolution FFT (d) Deformed FFT
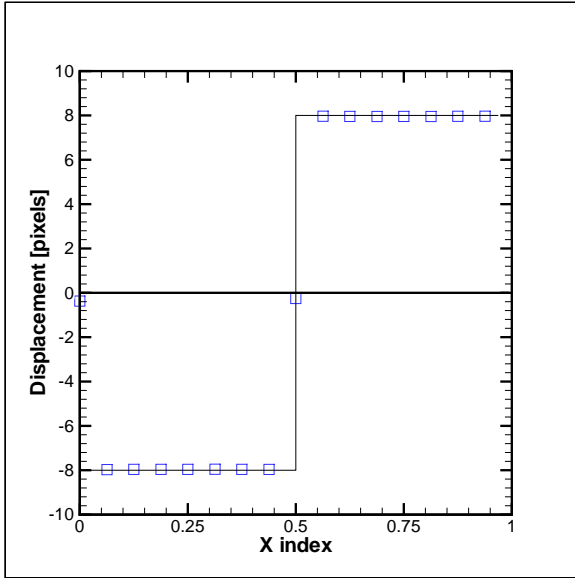
(a) Standard FFT
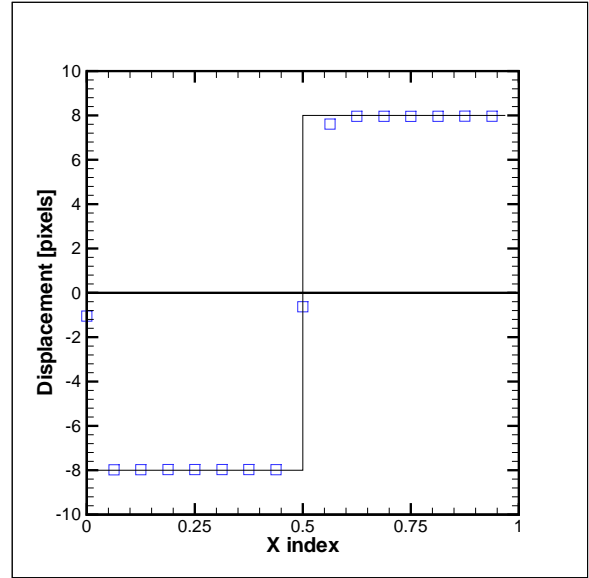
(b) Predictor Corrector FFT
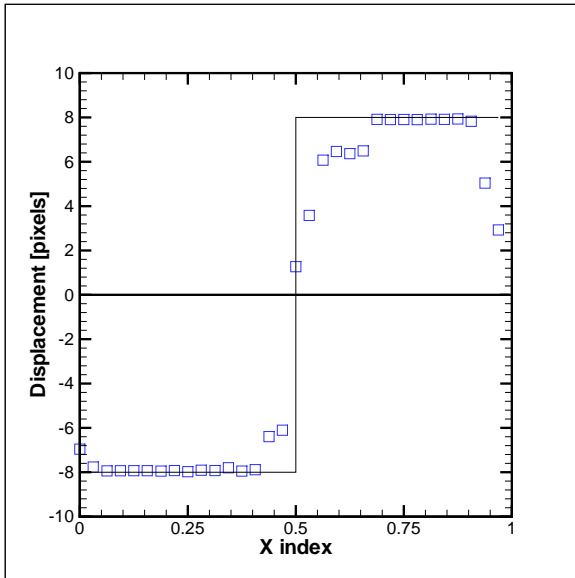
(c) Super Resolution FFT
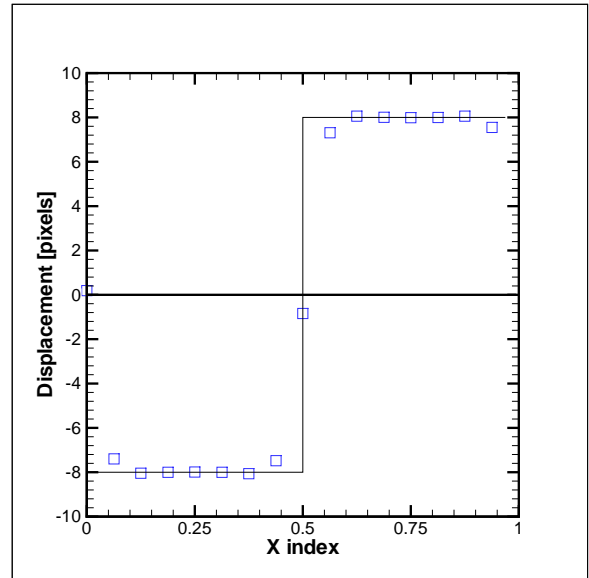
(d) Deformed FFT

Figure A.5: Ensemble averaged measurements for step displacement function of period 128, particle size 4 pixels in diameter and a particle number density of 15 particles per 32x32 pixel area (a) Standard FFT (b) Predictor Corrector FFT (c) Super Resolution FFT (d) Deformed FFT
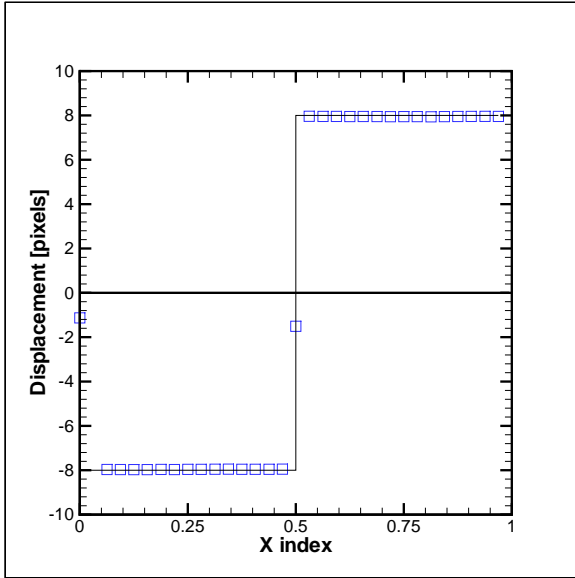
(a) Standard FFT
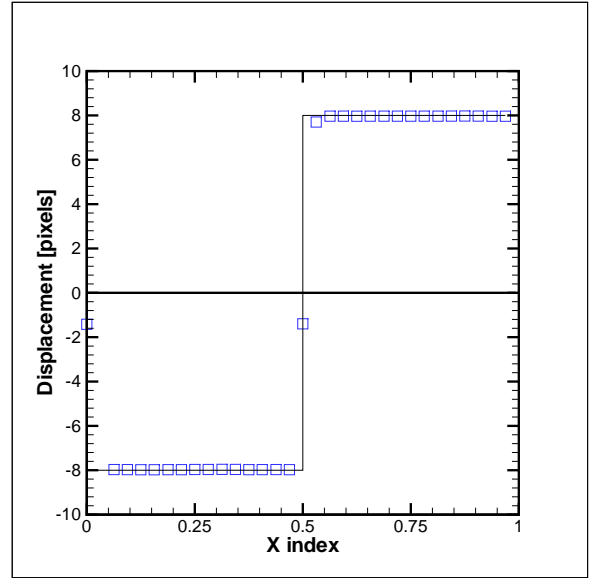
(b) Predictor Corrector FFT
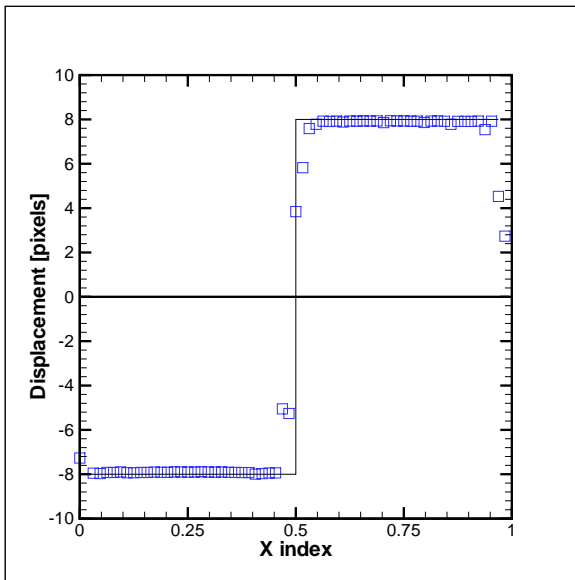
(c) Super Resolution FFT
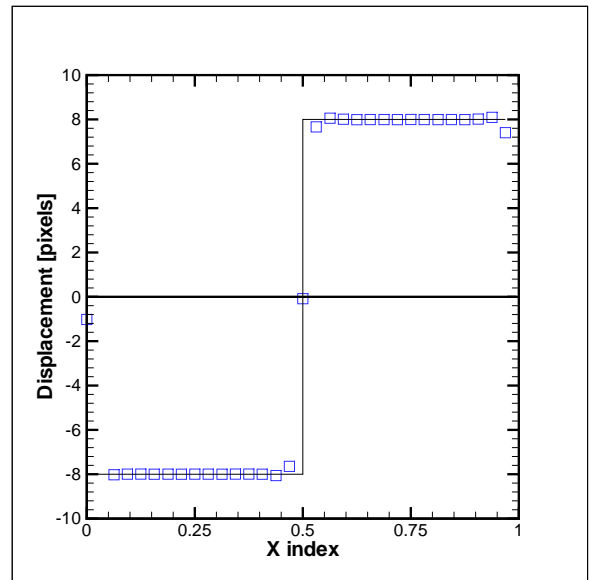
(d) Deformed FFT

Figure A.6: Ensemble averaged measurements for step displacement function of period 256, particle size 4 pixels in diameter and a particle 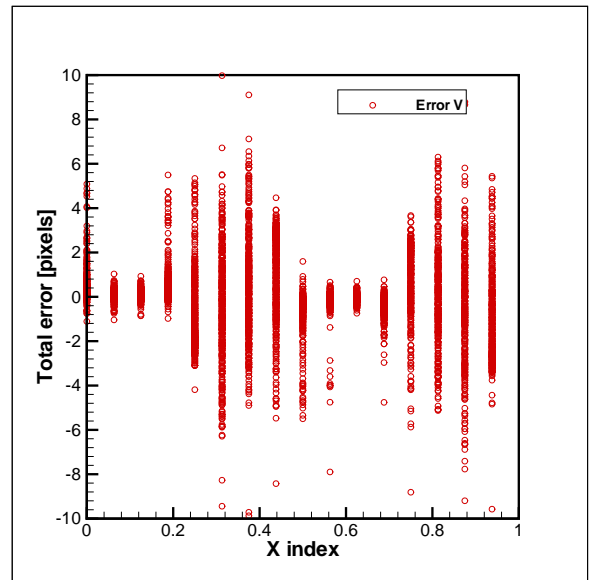number density of 15 particles per 32x32 pixel area (a) Standard FFT (b) Predictor Corrector FFT (c) Super Resolution FFT (d) Deformed FFT
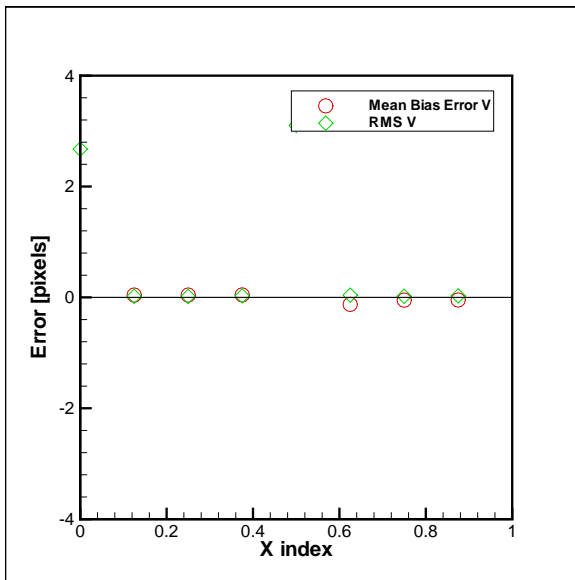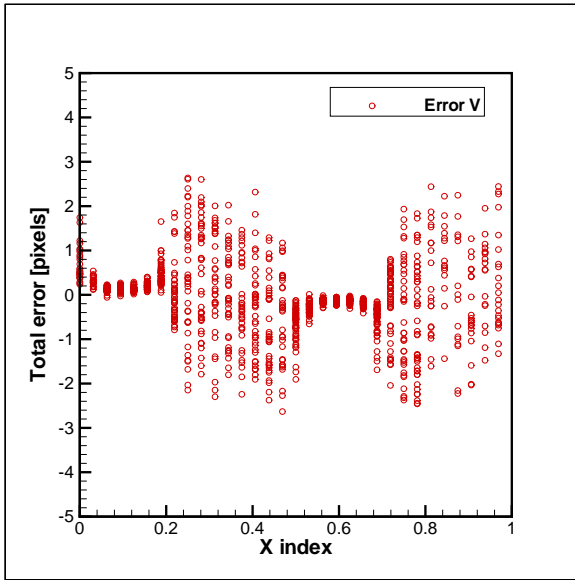
(a) Standard FFT
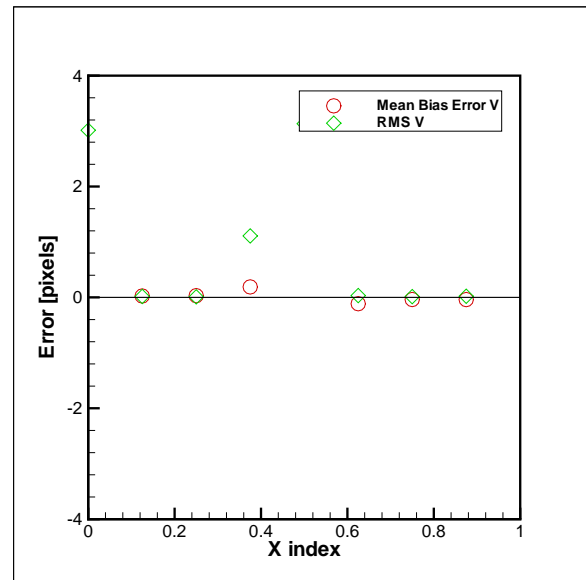
(b) Predictor Corrector FFT
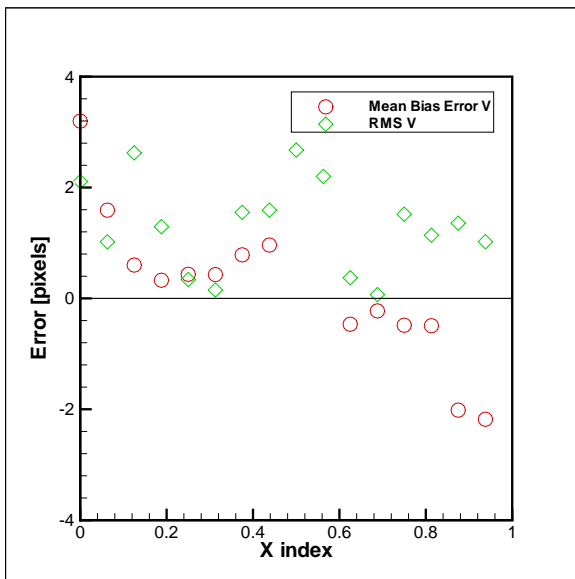
(c) Super Resolution FFT
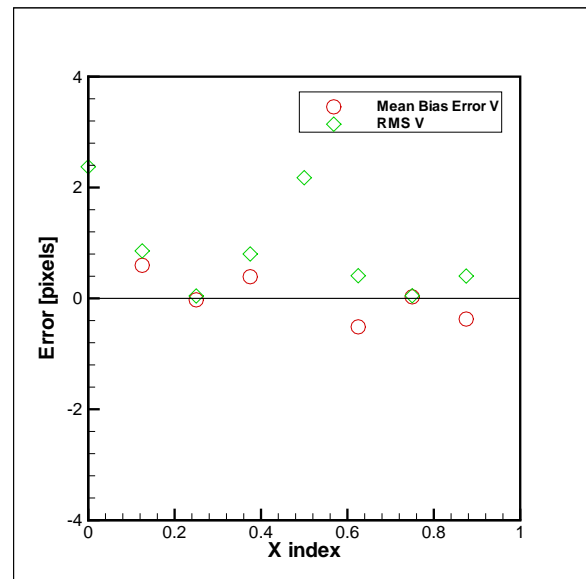
(d) Deformed FFT

Figure A.7: Mean bias and RMS error for step displacement function of period 64, particle size 4 pixels in diameter and a particle number density of 15 particles per 32x32 pixel area (a) Standard FFT (b) Predictor Corrector FFT (c) Super Resolution FFT (d) Deformed FFT
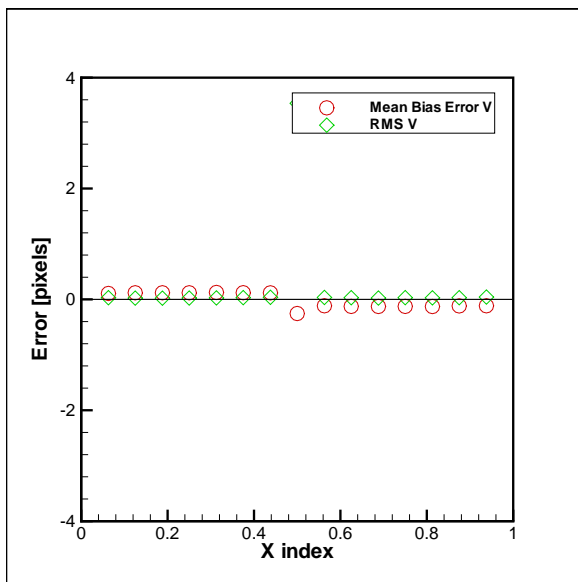
(a) Standard FFT
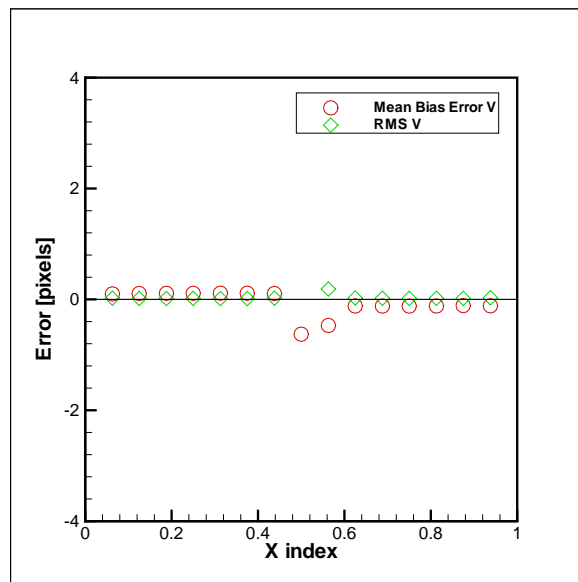
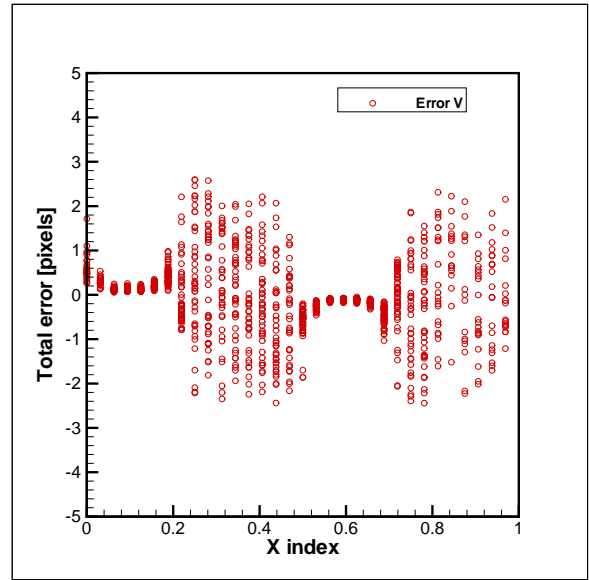(b) Predictor Corrector FFT
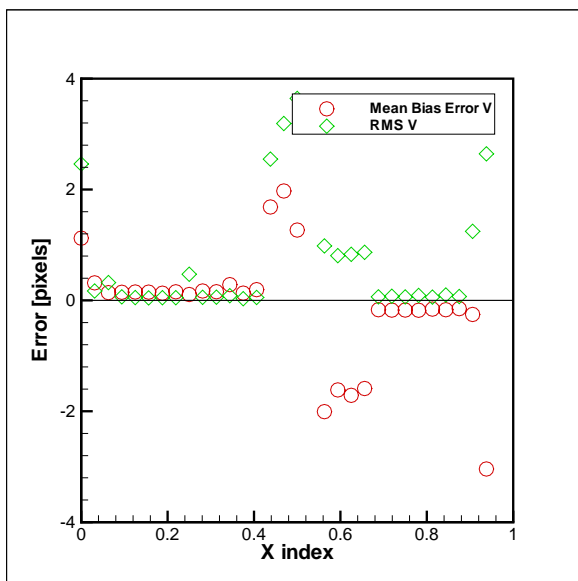
(c) Super Resolution FFT
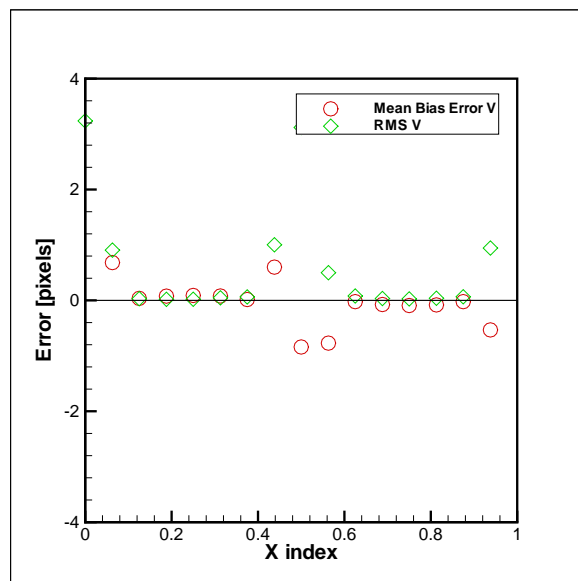
(d) Deformed FFT

Figure A.8: Mean bias and RMS error for step displacement function of period 128, particle size 4 pixels in diameter and a particle number 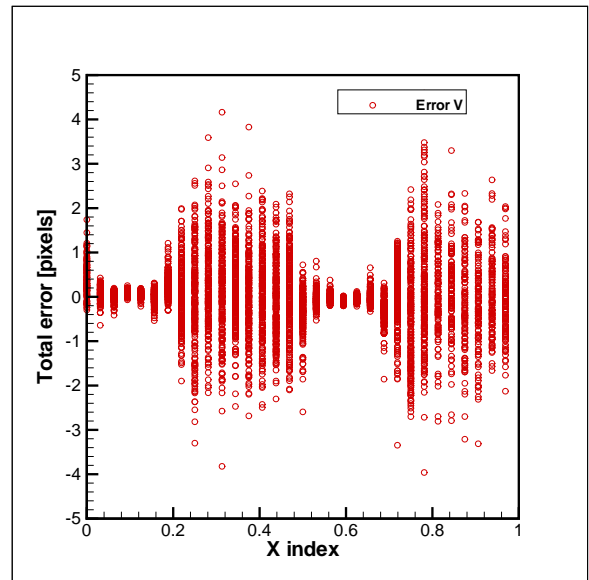density of 15 particles per 32x32 pixel area (a) Standard FFT (b) Predictor Corrector FFT (c) Super Resolution FFT (d) Deformed FFT
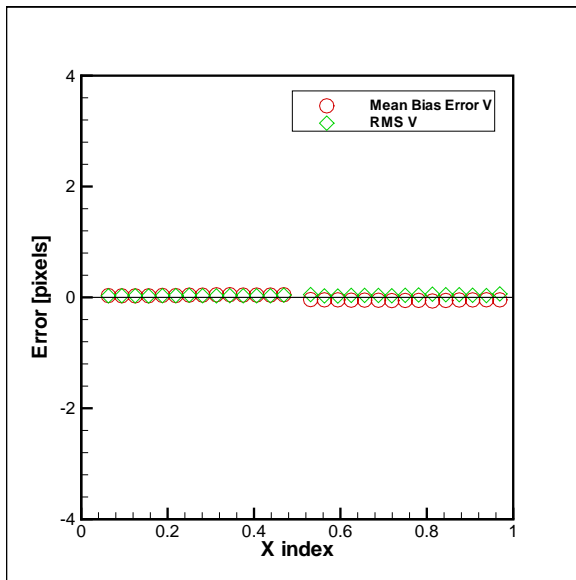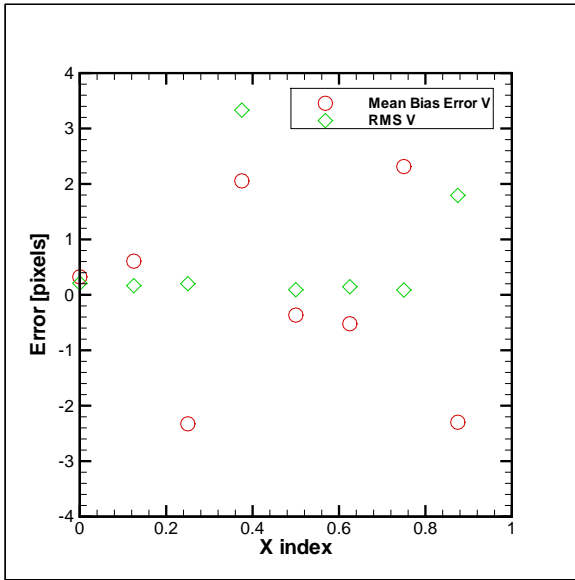
(a) Standard FFT
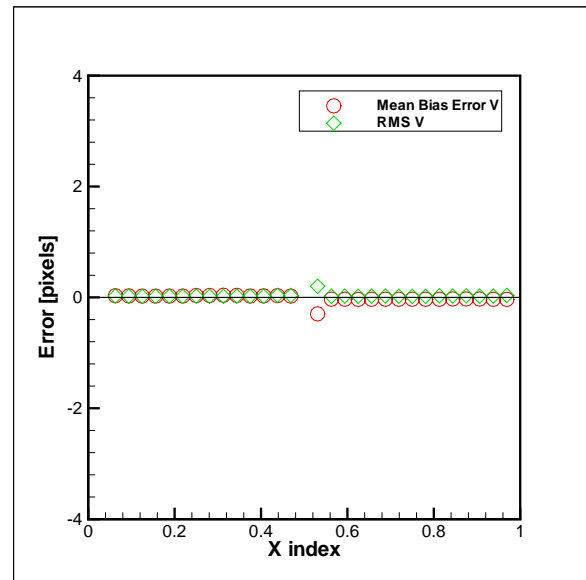
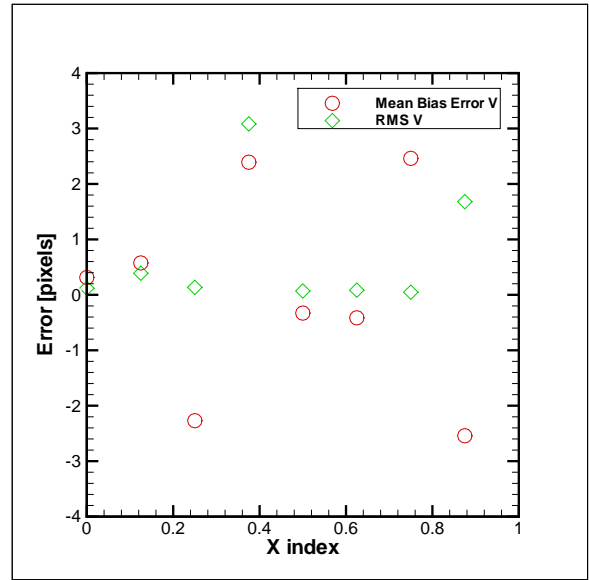(b) Predictor Corrector FFT
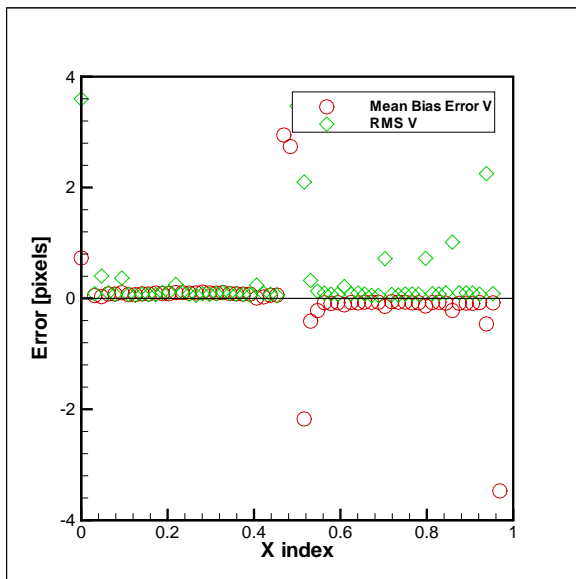
(c) Super Resolution FFT
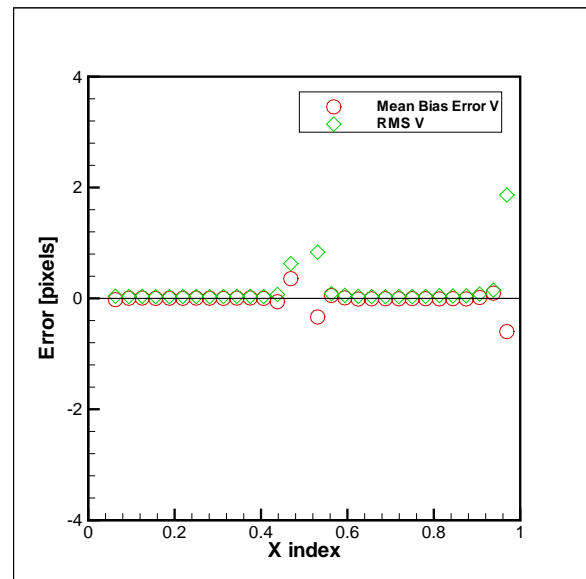
(d) Deformed FFT

Figure A.9: Mean bias and RMS error for step displacement function of period 256, particle size 4 pixels in diameter and a particle number density of 15 particles per 32x32 pixel area (a) Standard FFT (b) Predictor Corrector FFT (c) Super Resolution FFT (d) Deformed FFT

Appendix B

Sawtooth Results

In this Appendix the results for the images generated with the sawtooth displacement function are presented for the different periods of 64, 128 and 256 pixels to show the conclusions in Chapter 5 were independent of sawtooth displacement function period. For all the results shown, the mean particle size was 4 pixels in diameter with a particle density of 15 particles per 32x32 pixel area.

Every validated measurement from the four cross-correlation methods are shown in Figures B.1, B.2 and B.3 for a period of 64, 128 and 256 pixels, respectively. As the length of the period increased the measurement results improved. This was a result of the smaller range of displacement that existed within the interrogation areas. Figures B.4, B.5 and B.6 also contain every validated measurement point along with lines representing the maximum and minimum displacements which existed within the interrogation area at each measurement point. As the length of the period increased, the displacement gradient decreased and the range of displacements within each interrogation area also decreased. This resulted in displacement measurements which contained a smaller range of measurements.

The displacement results were averaged and are shown in Figures B.7, B.8 and B.9 for periods of 64, 128 and 256 pixels, respectively. As the period increased the resolution of the displacement function increased. This was a result of more displacement vectors being used due to the larger period.
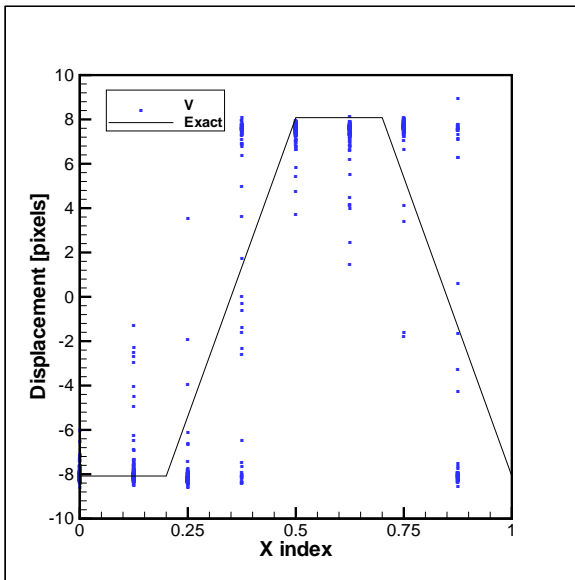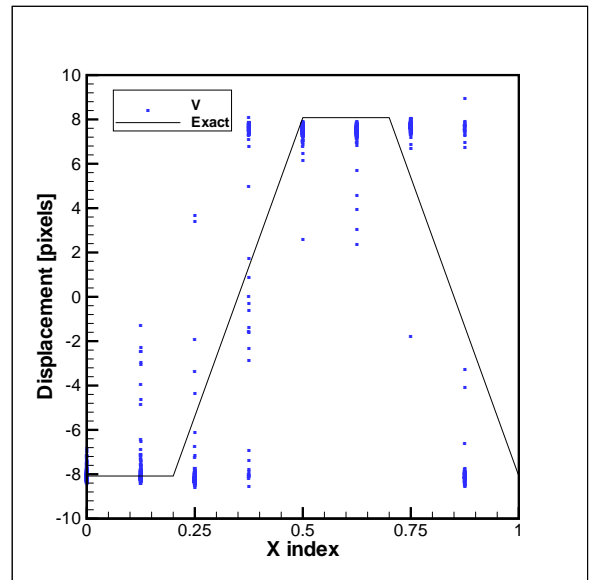
(a) Standard FFT

(b) Predictor Corrector FFT
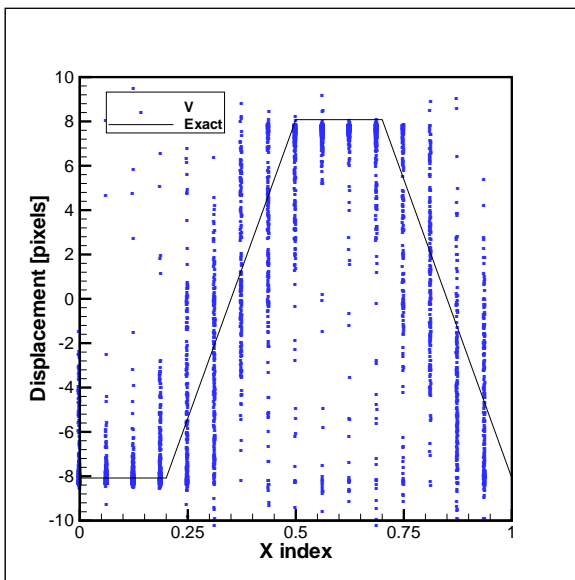
(c) Super Resolution FFT
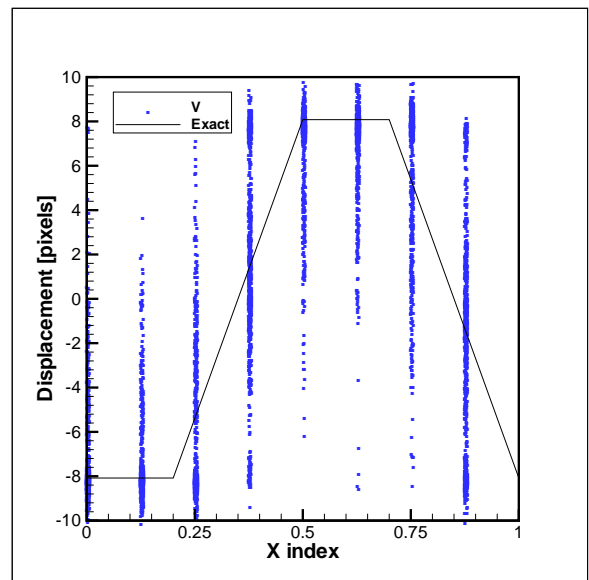
(d) Deformed FFT

Figure B.1: Validated displacement measurements for sawtooth displacement function for a period of 64 pixels (a) Standard FFT (b) Predictor Corrector FFT (c) Super Resolution FFT (d) Deformed FFT
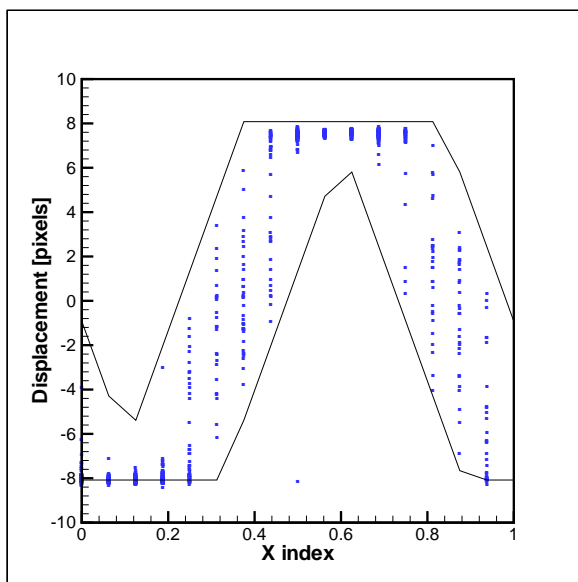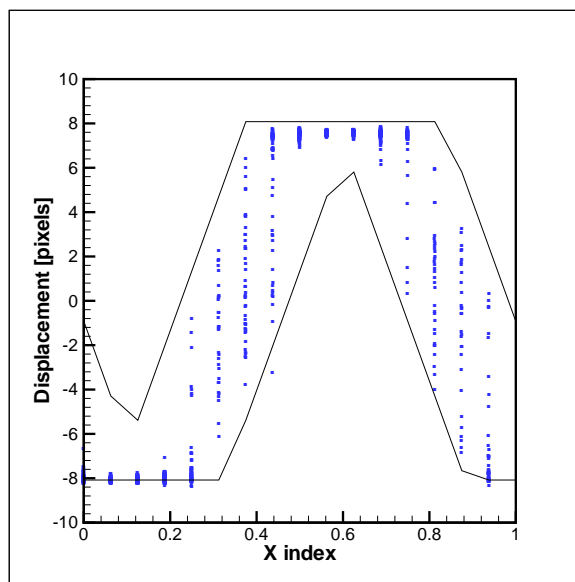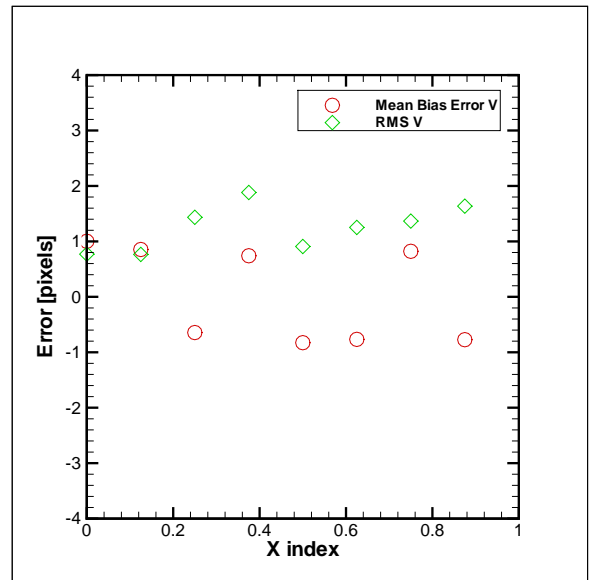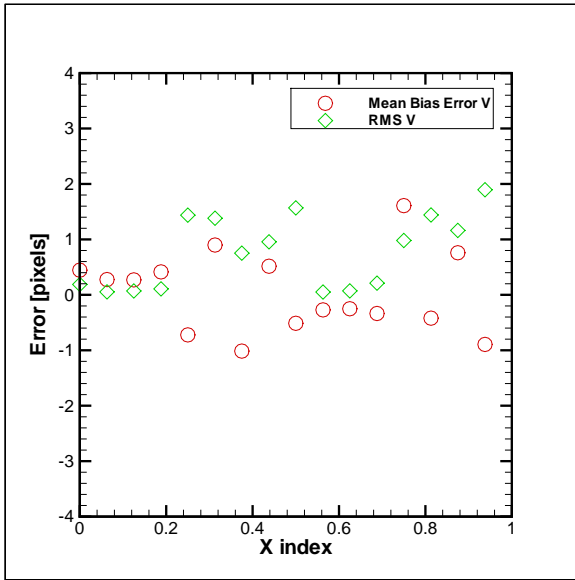
(a) Standard FFT

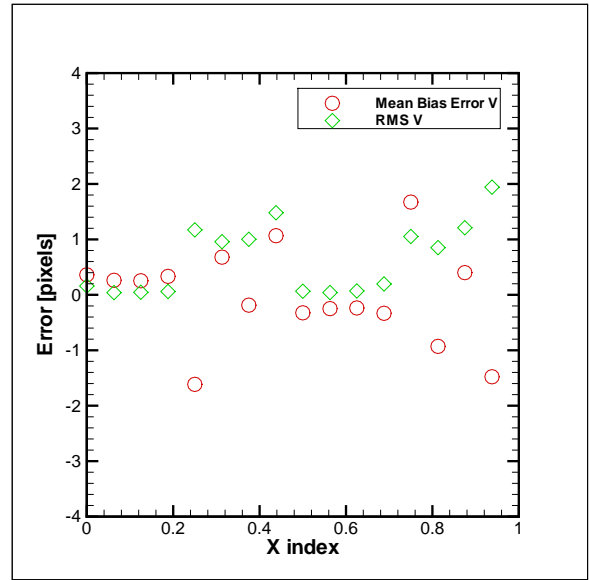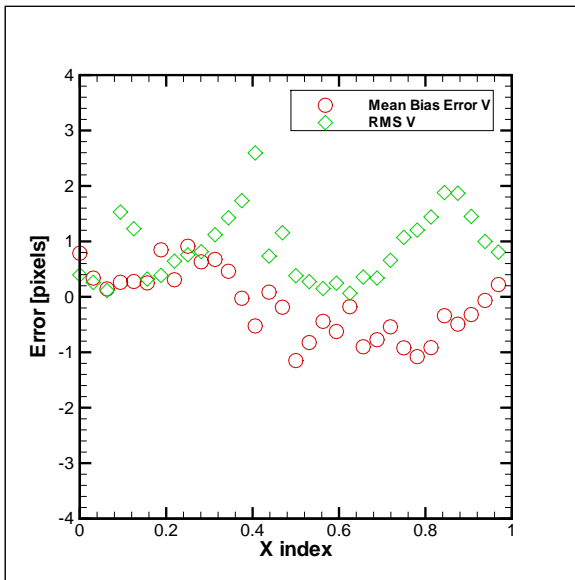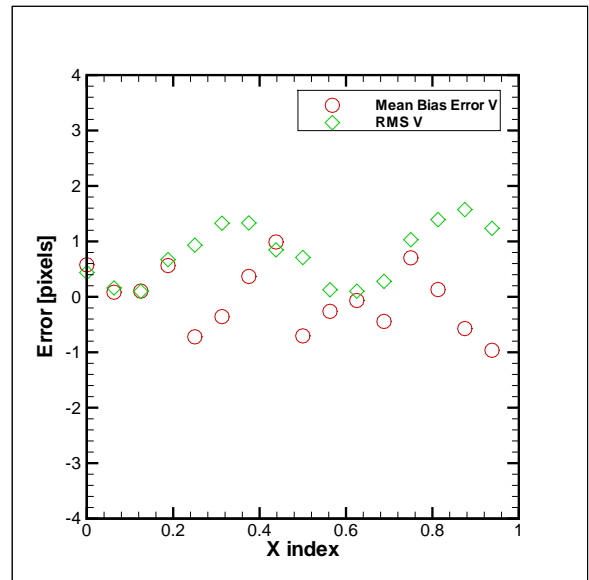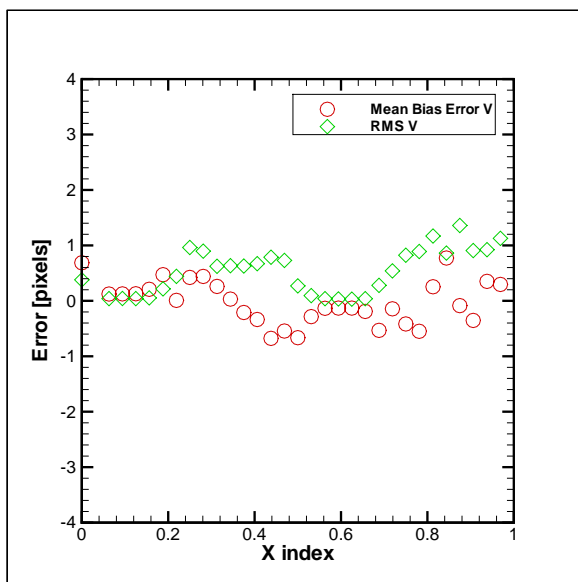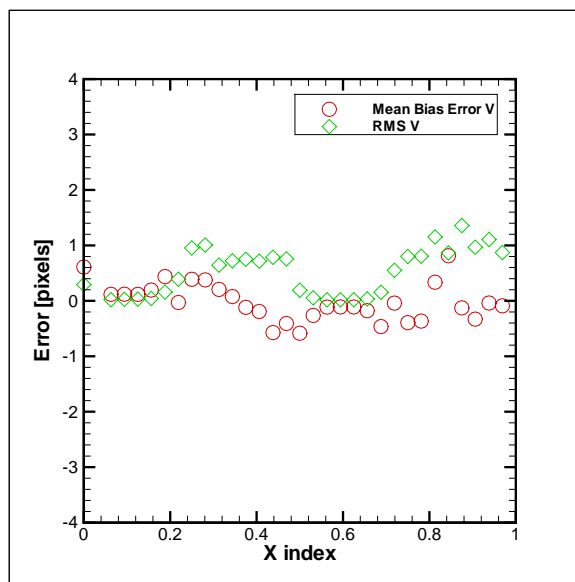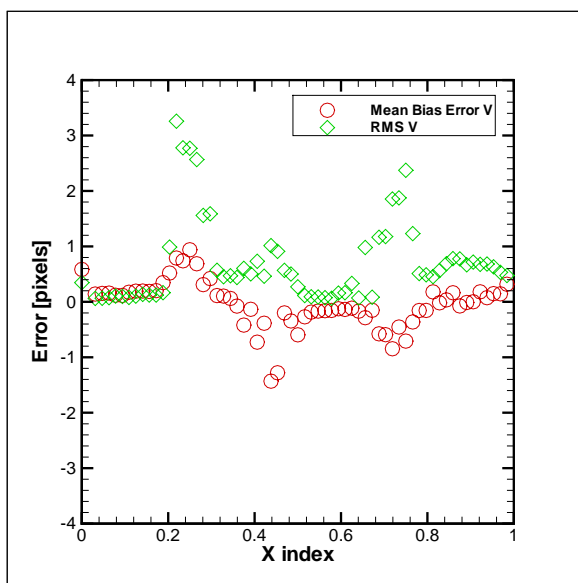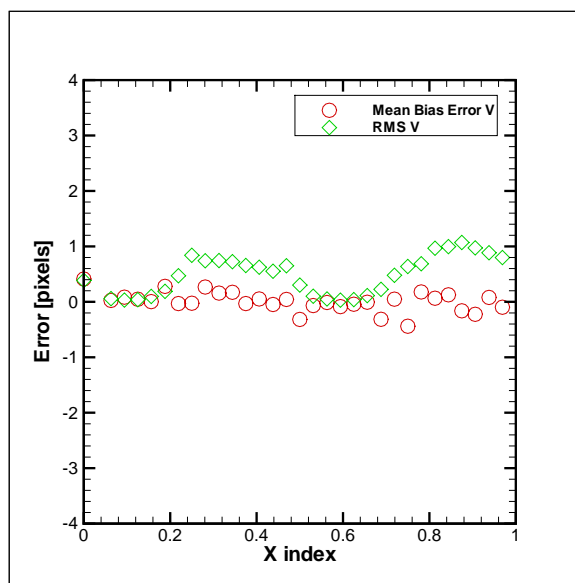(b) Predictor Corrector FFT
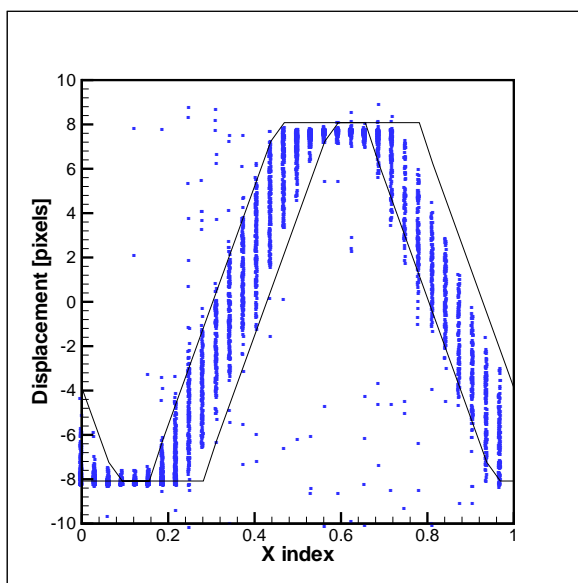
(c) Super Resolution FFT
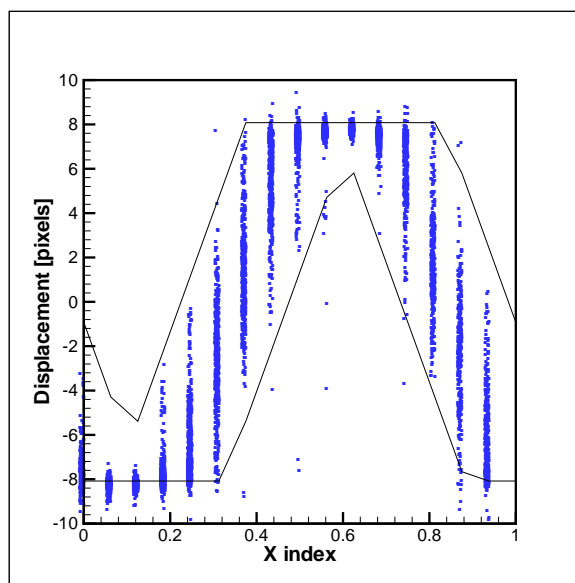
(d) Deformed FFT

Figure B.2: Validated displacement measurements for sawtooth displacement function for a period of 128 pixels (a) Standard FFT (b) Predictor Corrector FFT (c) Super Resolution FFT (d) Deformed FFT
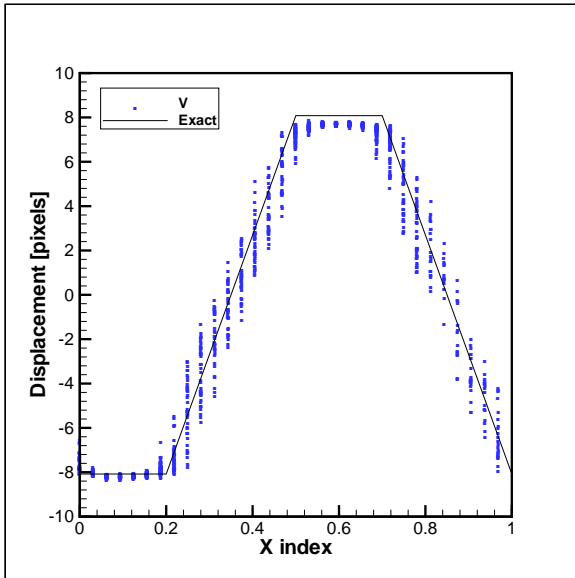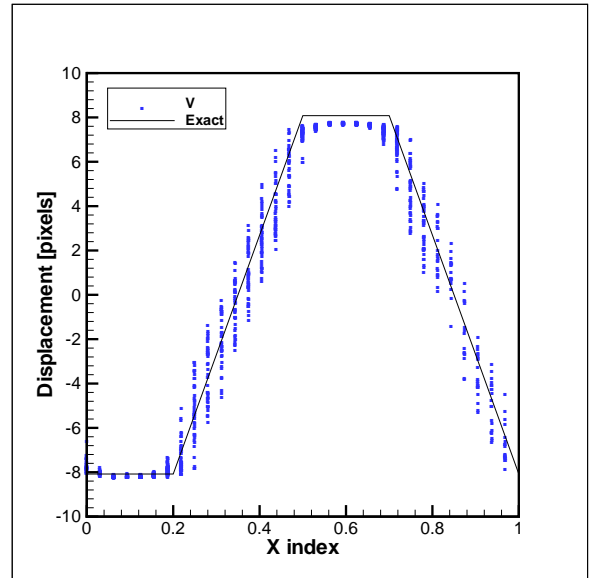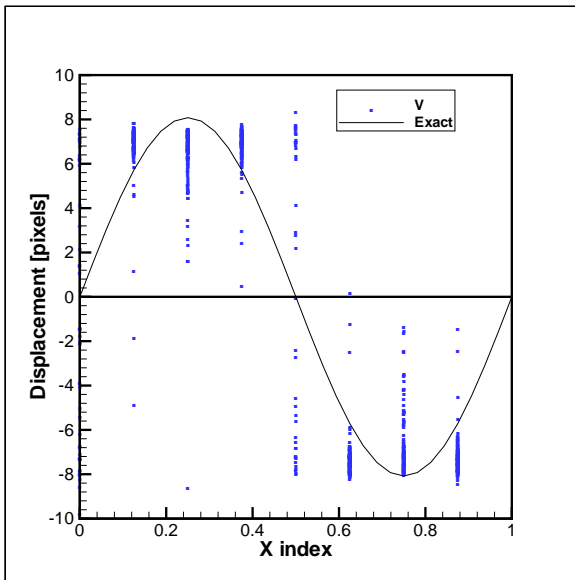
(a) Standard FFT

(b) Predictor Corrector FFT
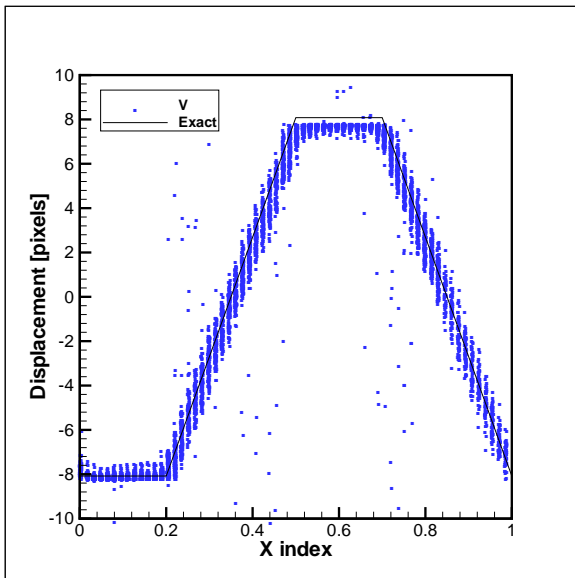
(c) Super Resolution FFT
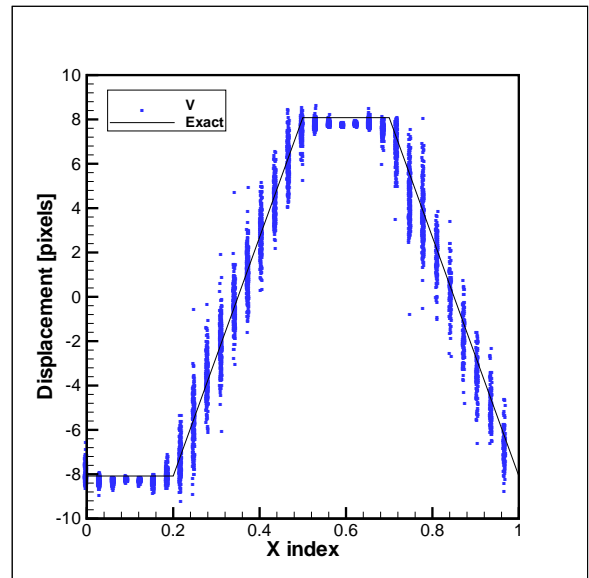
(d) Deformed FFT

Figure B.3: Validated displacement measurements for sawtooth displacement function for a period of 256 pixels (a) Standard FFT (b) Predictor Corrector FFT (c) Super Resolution FFT (d) Deformed FFT
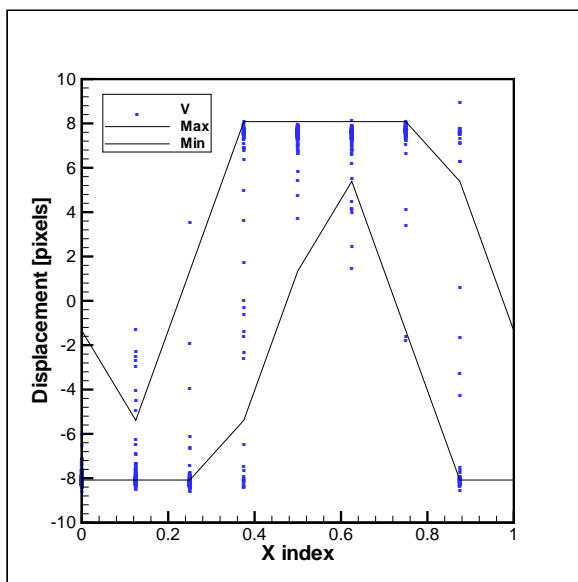
(a) Standard FFT
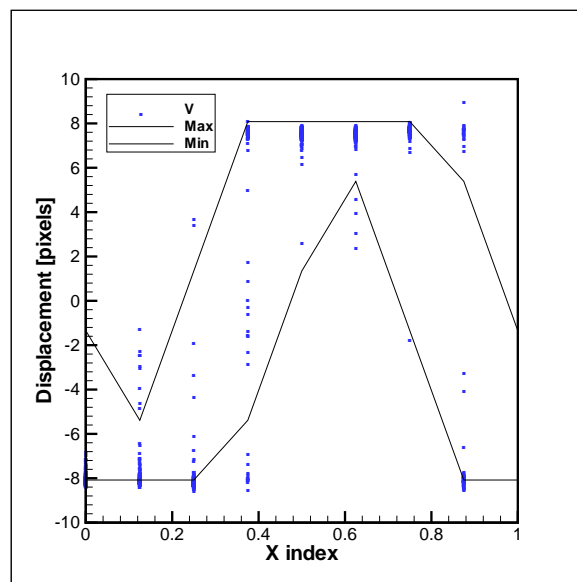
(b) Predictor Corrector FFT
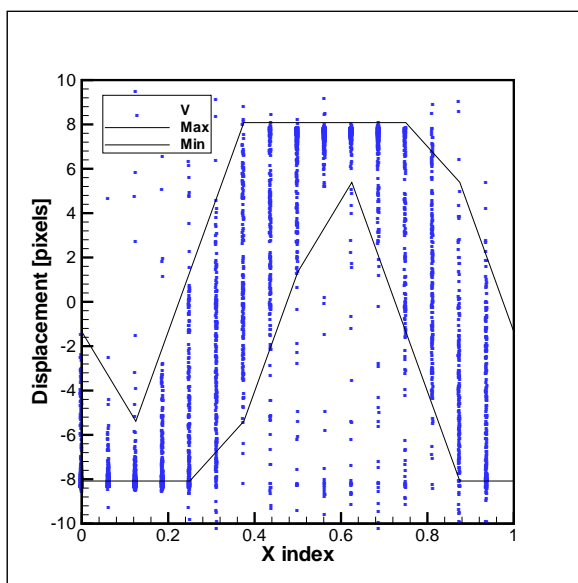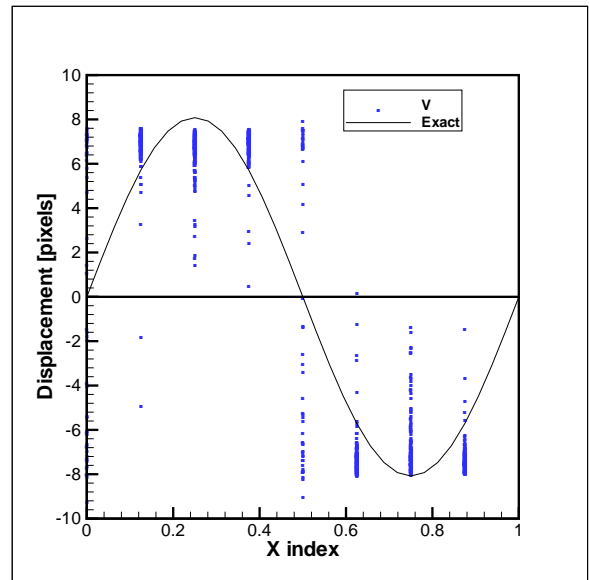
(c) Super Resolution FFT
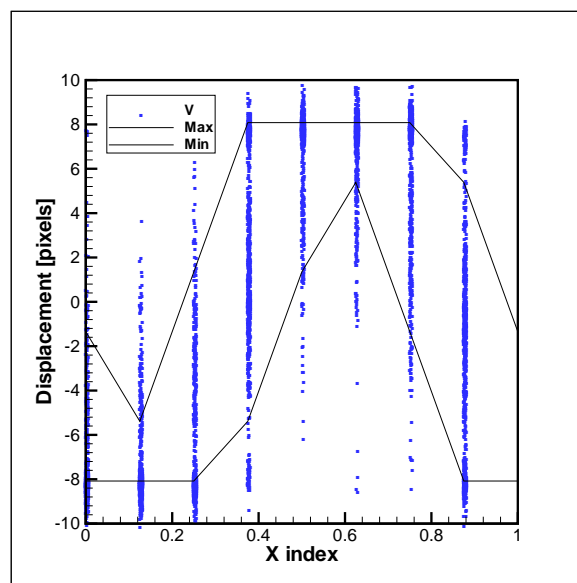
(d) Deformed FFT

Figure B.4: Validated displacement measurements for sawtooth displacement function for a period of 64 pixels with the minimum and maximum values in the each interrogation area (a) Standard FFT (b) Predictor Corrector FFT (c) Super Resolution FFT (d) Deformed FFT
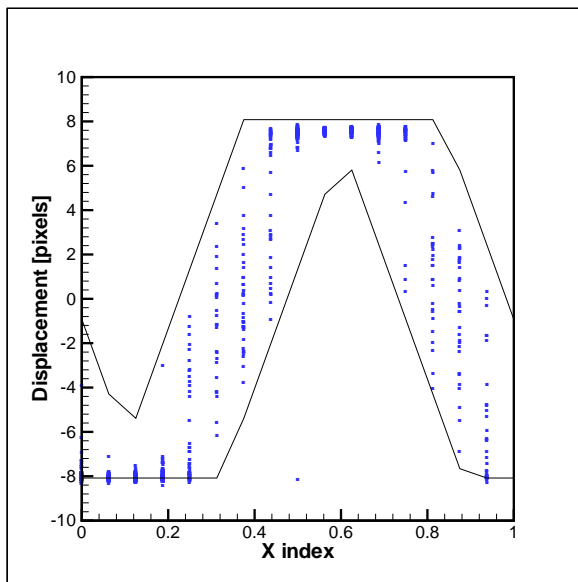
(a) Standard FFT
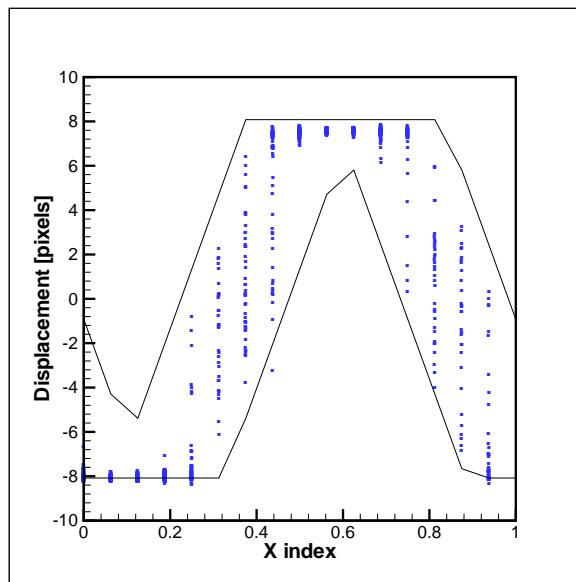
(b) Predictor Corrector FFT
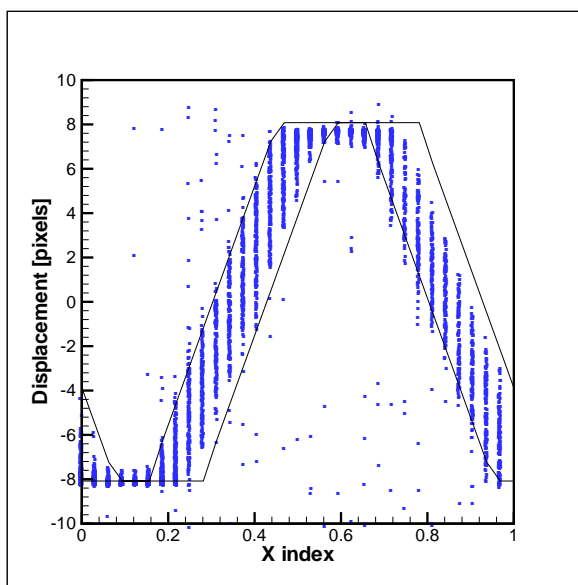
(c) Super Resolution FFT
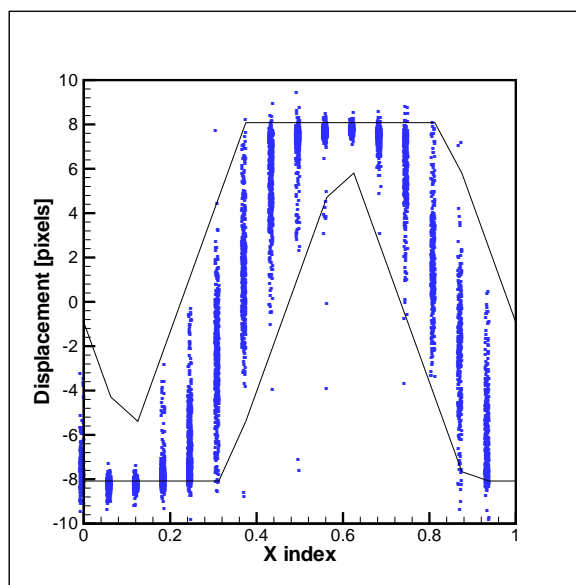
(d) Deformed FFT

Figure B.5: Validated displacement measurements for sawtooth displacement function for a period of 128 pixels with the minimum and maximum values in the each interrogation area (a) Standard FFT (b) Predictor Corrector FFT (c) Super Resolution FFT (d) Deformed FFT
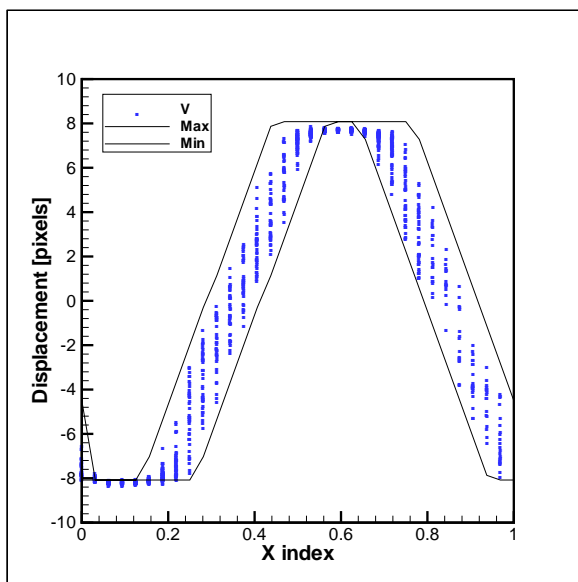
(a) Standard FFT
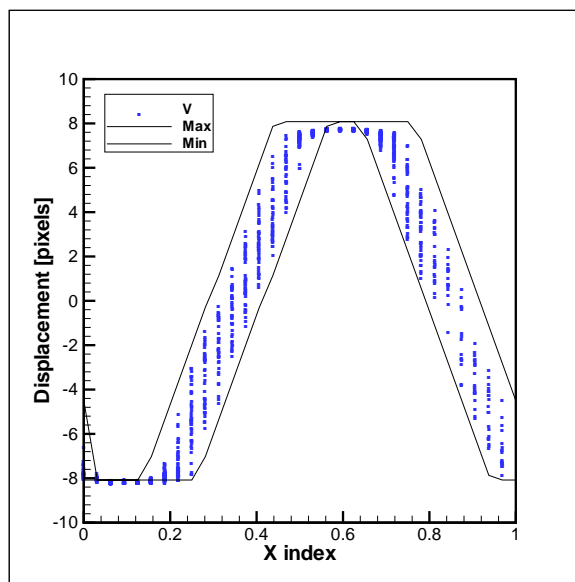
(b) Predictor Corrector FFT
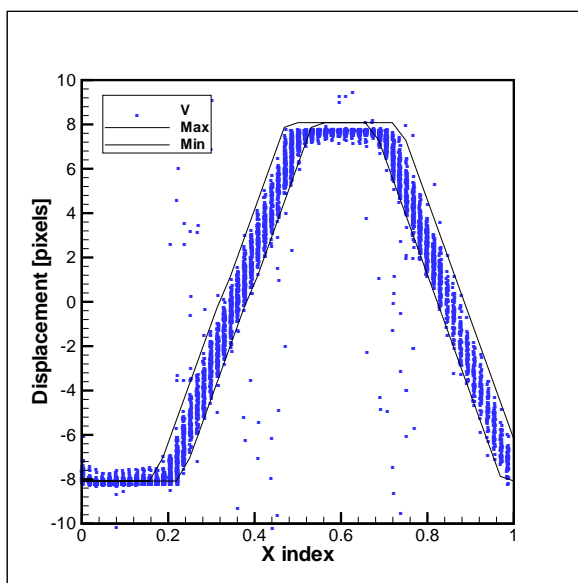
(c) Super Resolution FFT
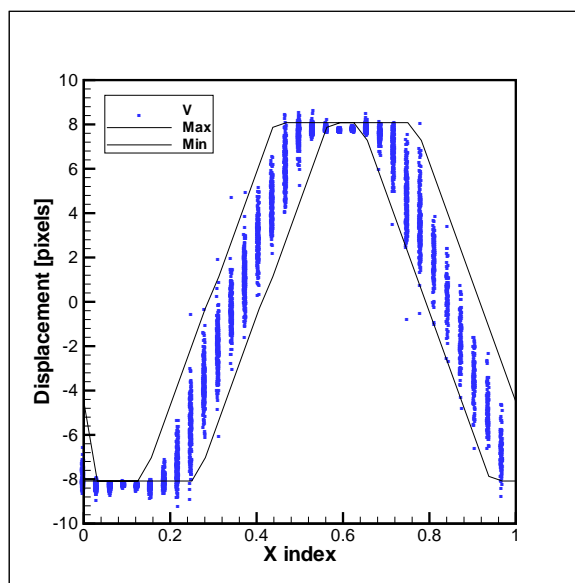
(d) Deformed FFT

Figure B.6: Validated displacement measurements for sawtooth displacement function for a period of 256 pixels with the minimum and maximum values in the each interrogation area (a) Standard FFT (b) Predictor Corrector FFT (c) Super Resolution FFT (d) Deformed FFT
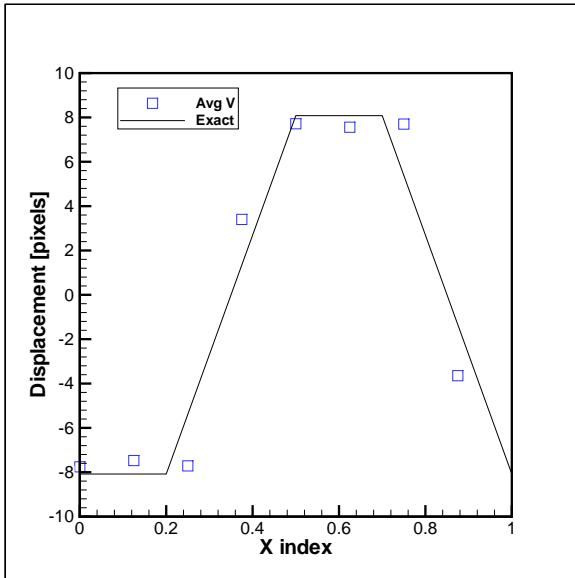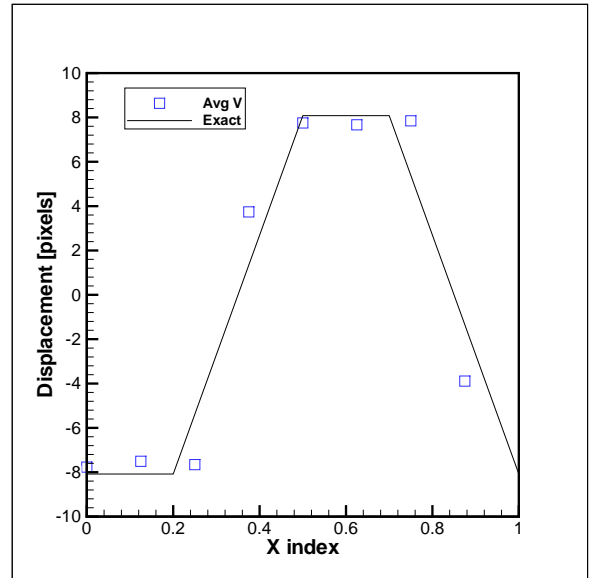
(a) Standard FFT

(b) Predictor Corrector FFT
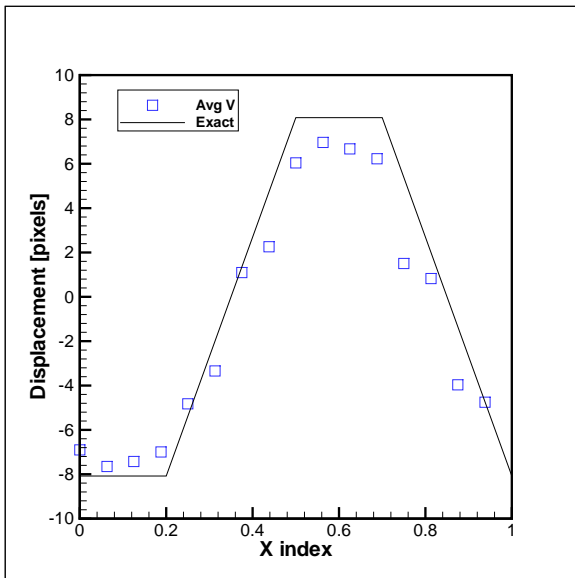
(c) Super Resolution FFT
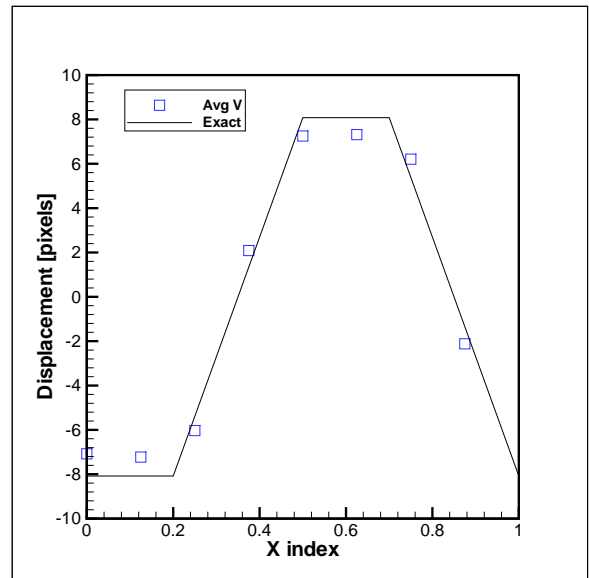
(d) Deformed FFT

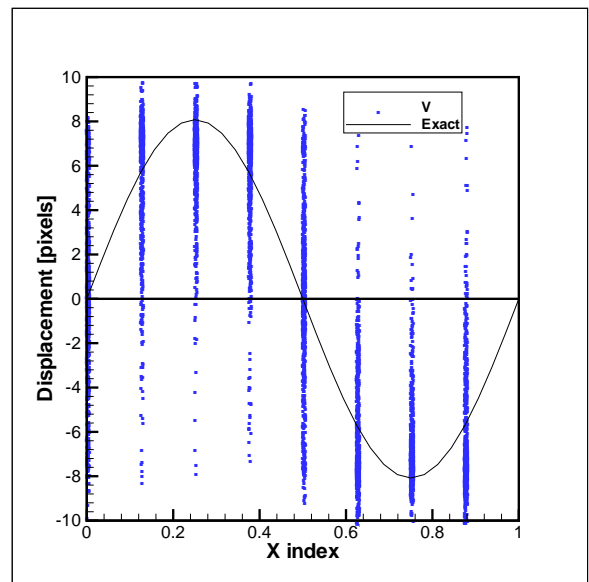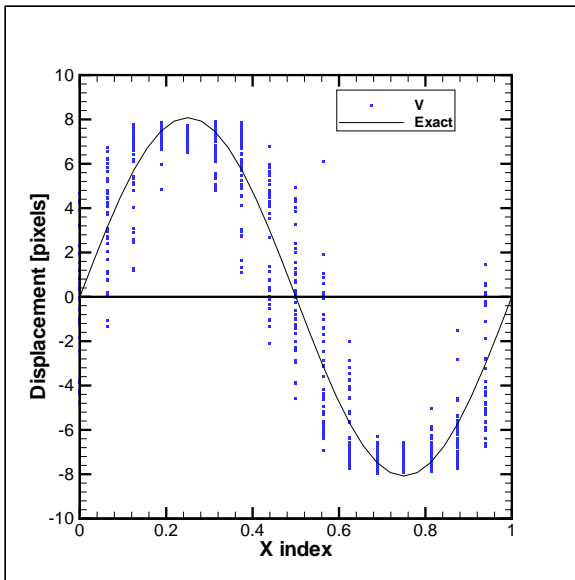Figure B.7: Ensembled averaged displacement measurements for sawtooth displacement function for a period of 64 pixels (a) Standard FFT (b) Predictor Corrector FFT (c) Super Resolution FFT (d) Deformed FFT
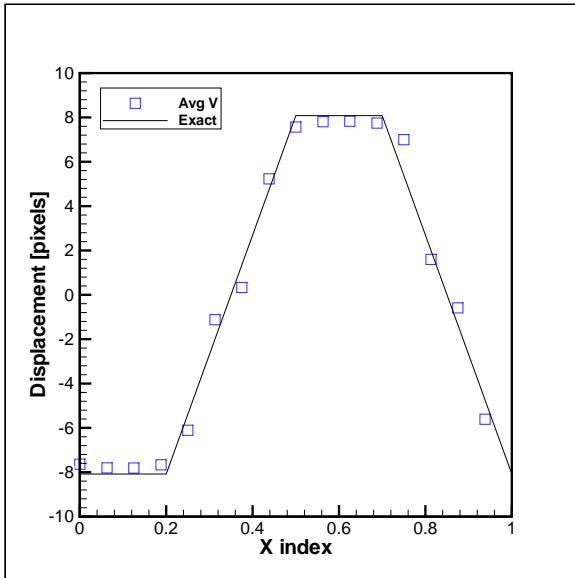
(a) Standard FFT

(b) Predictor Corrector FFT
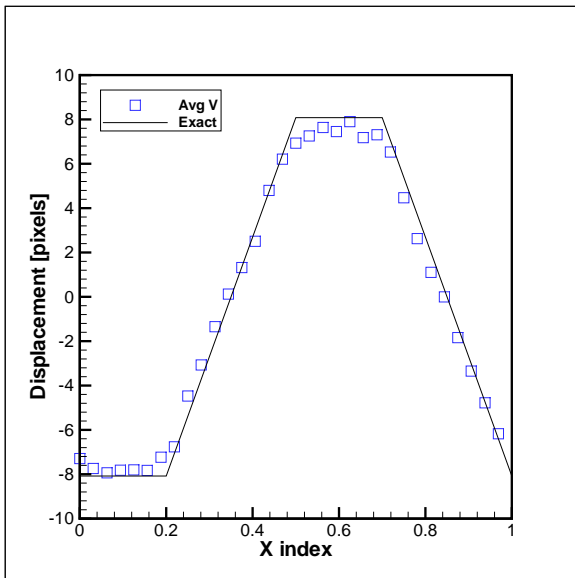
(c) Super Resolution FFT

(d) Deformed FFT

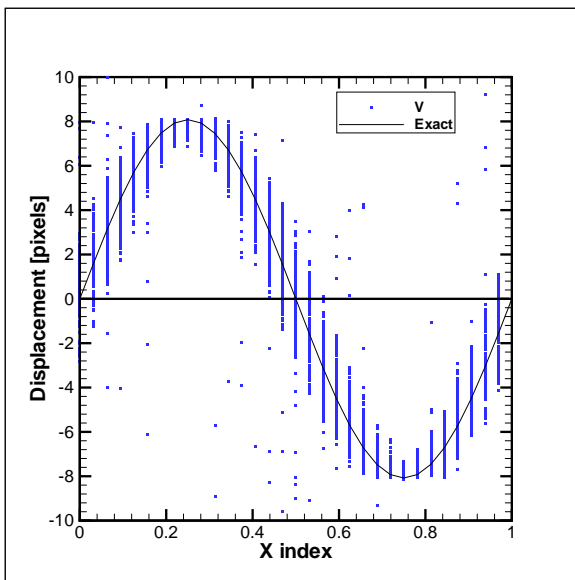Figure B.8: Ensembled averaged displacement measurements for sawtooth displacement function for a period of 128 pixels (a) Standard FFT (b) Predictor Corrector FFT (c) Super Resolution FFT (d) Deformed FFT

(a) Standard FFT

(b) Predictor Corrector FFT
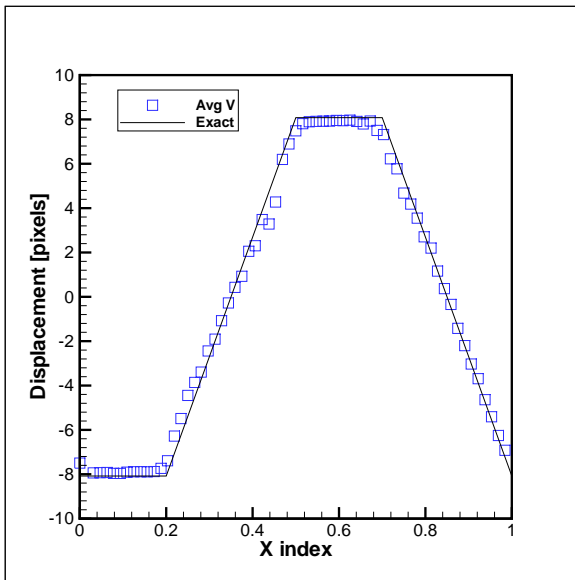
(c) Super Resolution FFT

(d) Deformed FFT

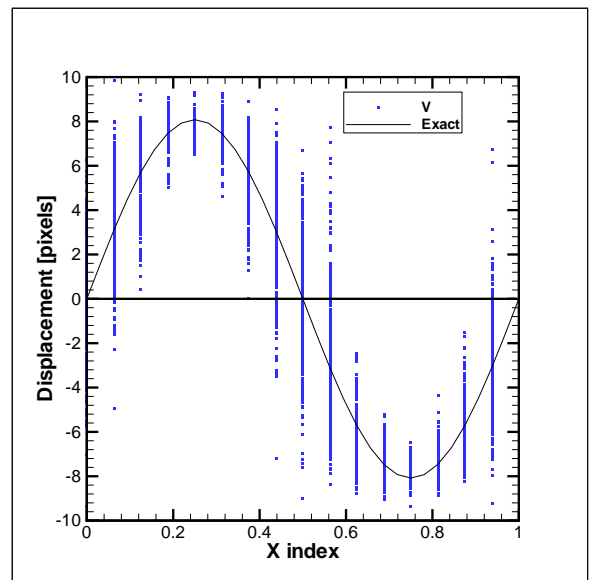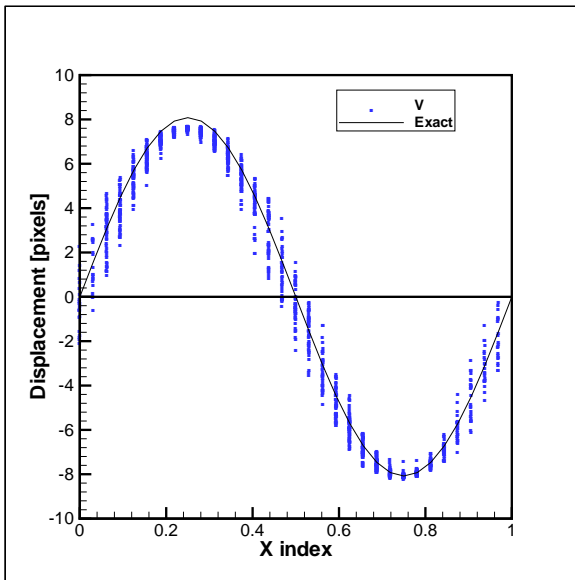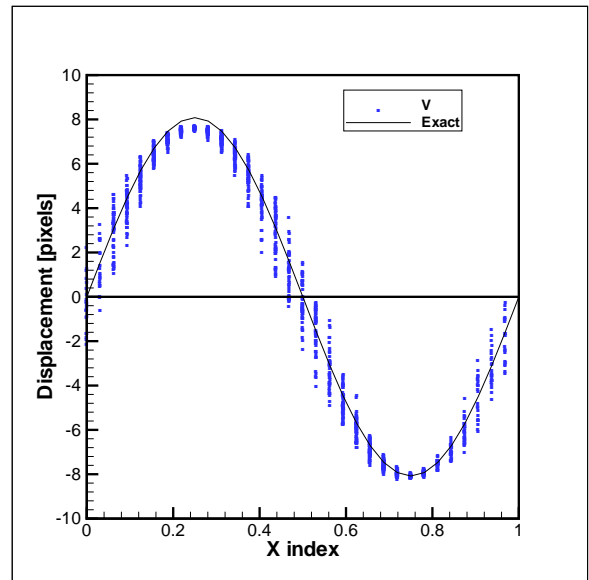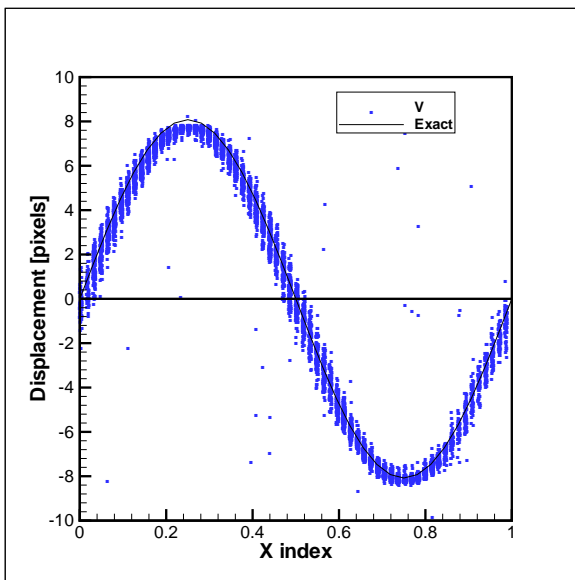Figure B.9: Ensembled averaged displacement measurements for sawtooth displacement function for a period of 256 pixels (a) Standard FFT (b) Predictor Corrector FFT (c) Super Resolution FFT (d) Deformed FFT

The total error within the measurements for the different cross-correlation algorithms evaluated is shown in Figures B.10, B.11 and B.12 for periods of 64, 128 and 256 pixels, respectively. The characteristics of the total error in the sawtooth displacement images were independent of the period length. In the regions of the constant displacement, only the deformed FFT method produced measurements above and below the exact particle displacement. While in regions of constant displacement gradients, all four methods produced measurements above and below the exact particle displacement at that x_{index} location.

The mean bias and random errors are shown in Figures B.13, B.14 and B.15 for periods of 64, 128 and 256 pixels, respectively. As expected the mean bias and random errors were independent of the period of the sawtooth displacement.
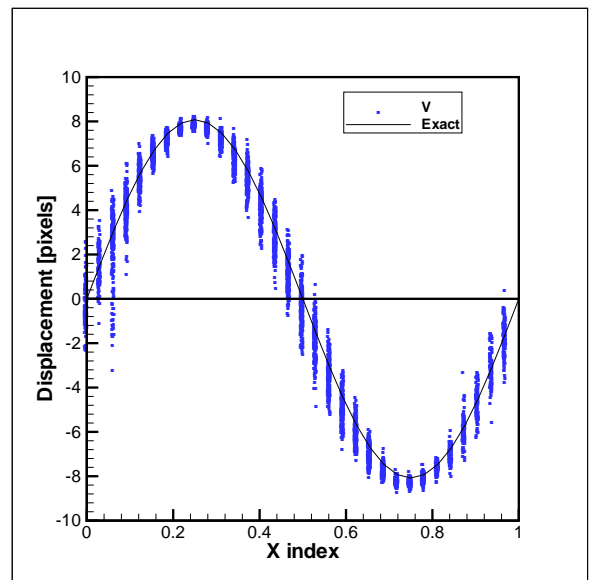
(a) Standard FFT

(b) Predictor Corrector FFT
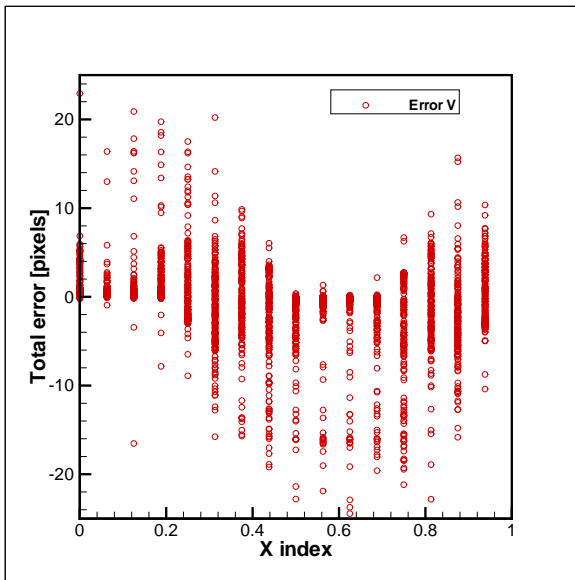
(c) Super Resolution FFT

(d) Deformed FFT

Figure B.10: Total error for every validated displacement measurement for sawtooth displacement function for a period of 64 pixels (a) Standard FFT (b) Predictor Corrector FFT (c) Super Resolution FFT (d) Deformed FFT
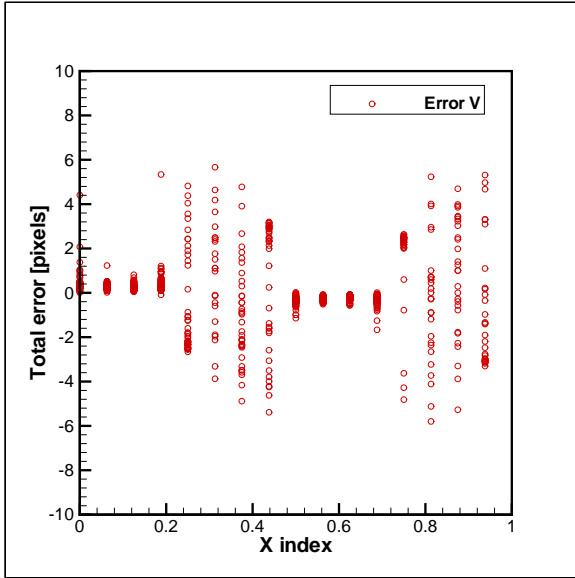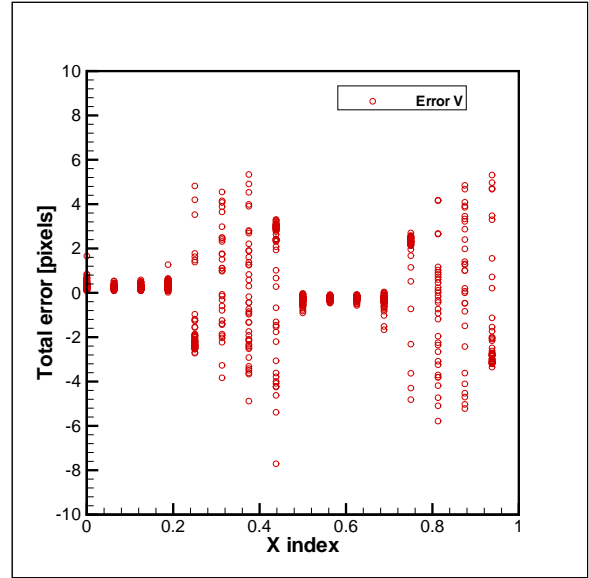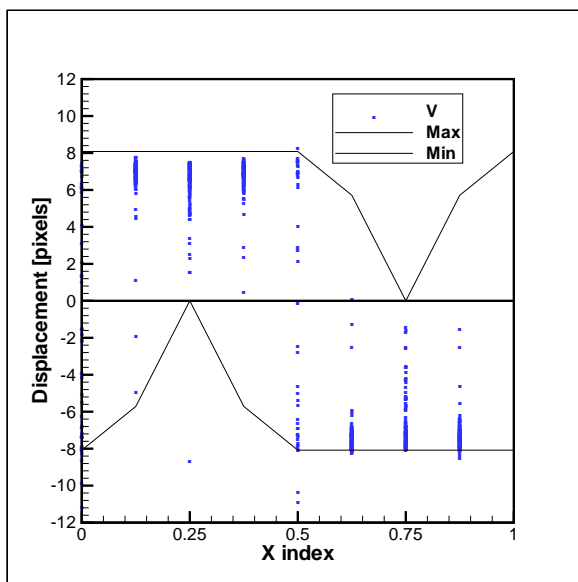
(a) Standard FFT

(b) Predictor Corrector FFT
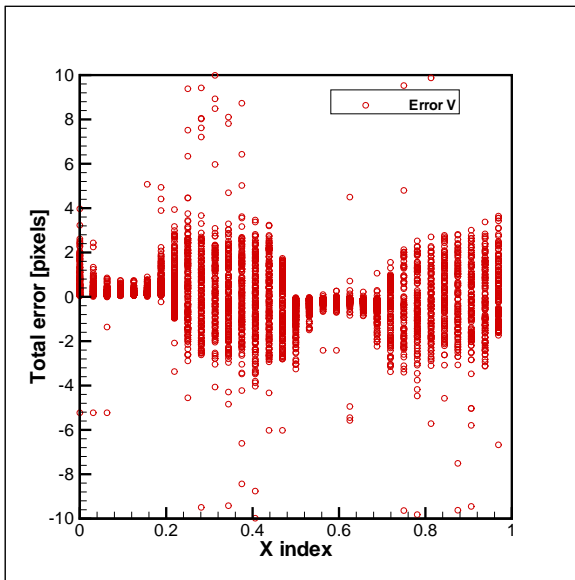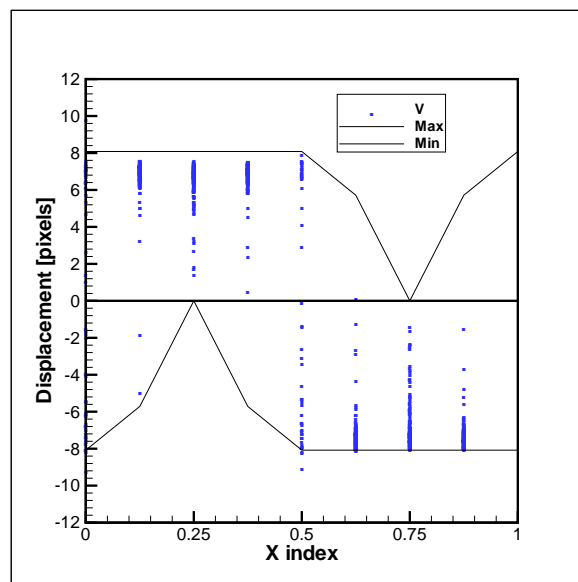
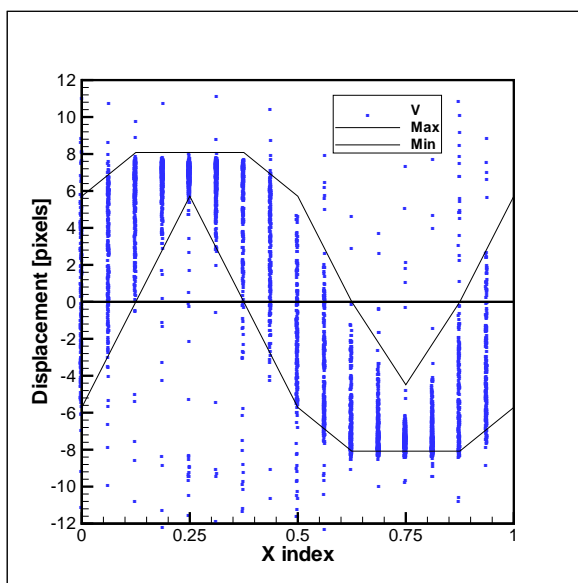(c) Super Resolution FFT

(d) Deformed FFT

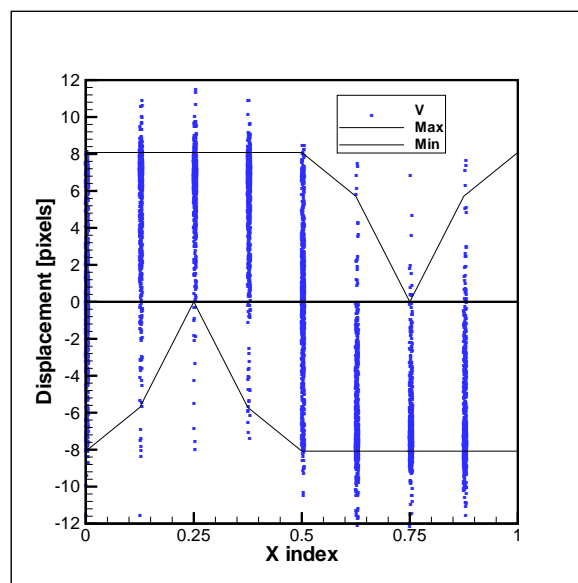Figure B.11: Total error for every validated displacement measurements for sawtooth displacement function for a period of 128 pixels (a) Standard FFT (b) Predictor Corrector FFT (c) Super Resolution FFT (d) Deformed FFT

(a) Standard FFT

(b) Predictor Corrector FFT
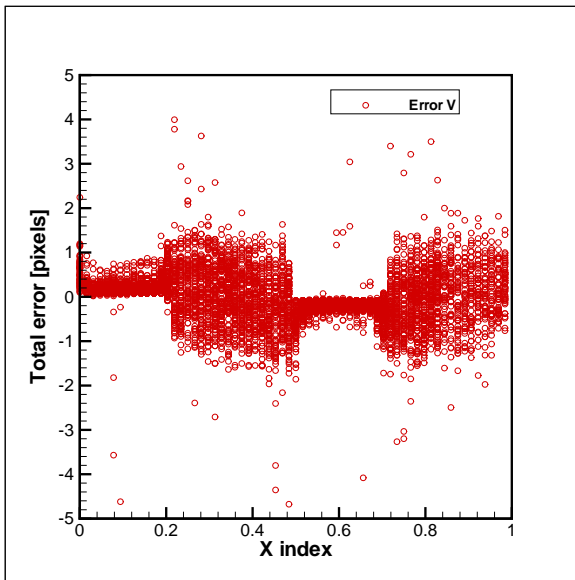
(c) Super Resolution FFT

(d) Deformed FFT

Figure B.12: Total error for every validated displacement measurements for sawtooth displacement function for a period of 256 pixels (a) Standard FFT (b) Predictor Corrector FFT (c) Super Resolution FFT (d) Deformed FFT

(a) Standard FFT
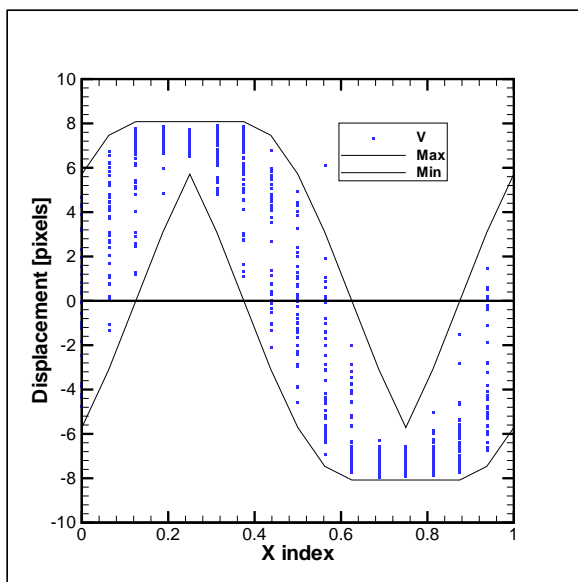
(b) Predictor Corrector FFT
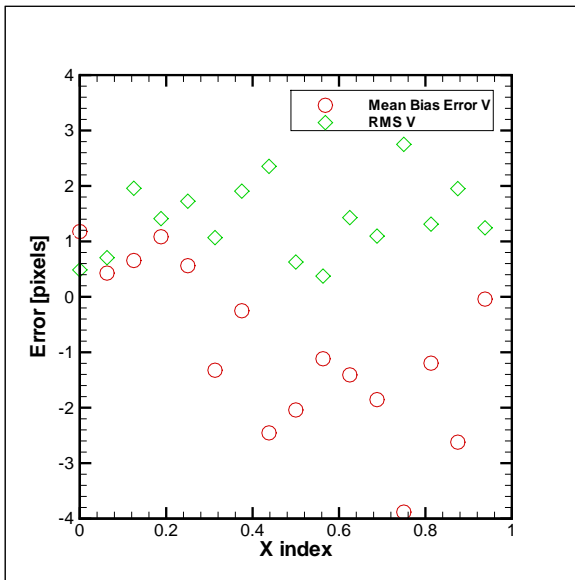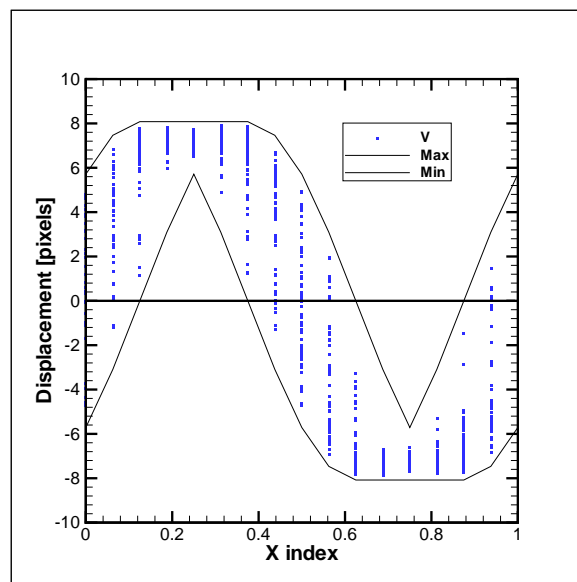
(c) Super Resolution FFT

(d) Deformed FFT

Figure B.13: Ensembled averaged error for sawtooth displacement function for a period of 64 pixels (a) Standard FFT (b) Predictor Corrector FFT (c) Super Resolution FFT (d) Deformed FFT

(a) Standard FFT

(b) Predictor Corrector FFT

(c) Super Resolution FFT

(d) Deformed FFT

Figure B.14: Ensembled averaged error for sawtooth displacement function for a period of 128 pixels (a) Standard FFT (b) Predictor Corrector FFT (c) Super Resolution FFT (d) Deformed FFT
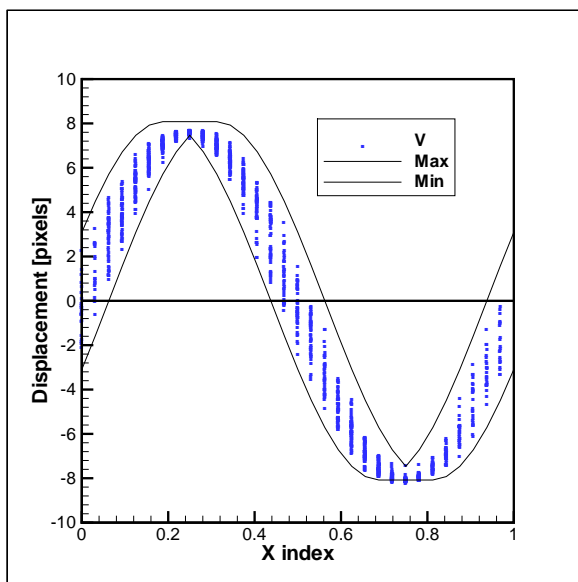
(a) Standard FFT

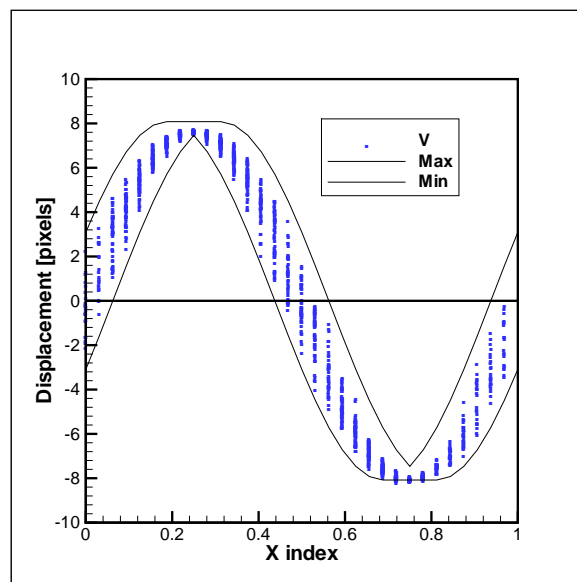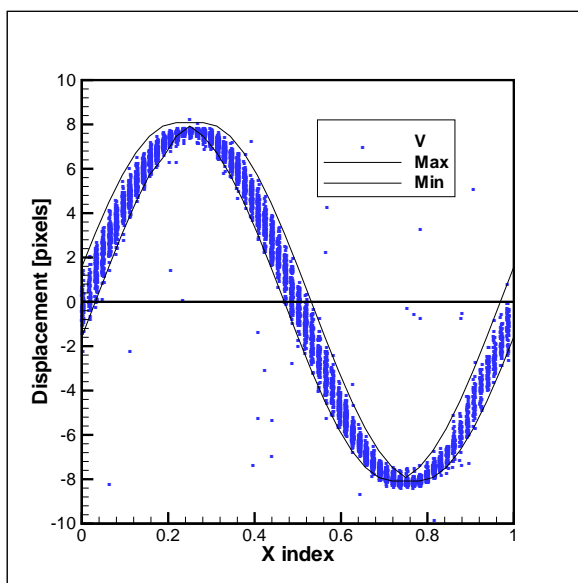(b) Predictor Corrector FFT

(c) Super Resolution FFT

(d) Deformed FFT

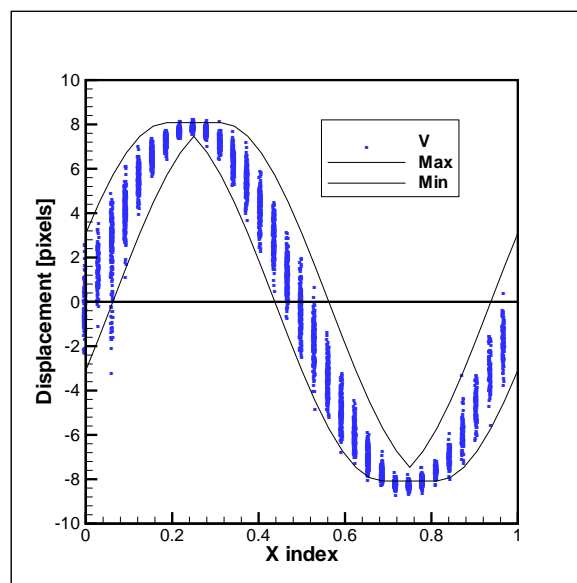Figure B.15: Ensembled averaged error for sawtooth displacement function for a period of 256 pixels (a) Standard FFT (b) Predictor Corrector FFT (c) Super Resolution FFT (d) Deformed FFT

Appendix C

Sinusoid Results

In this Appendix the results for the images generated with the sinsoid displacement function are presented for the different periods of 64, 128 and 256 pixels to show the conclusions in Chapter 5 were independent of sawtooth displacement function period. For all the results shown, the mean particle size was 4 pixels in diameter with a particle density of 15 particles per 32x32 pixel area.

Every validated measurement from the four cross-correlation methods are shown in Figures C.1, C.2 and C.3 for a period of 64, 128 and 256 pixels, respectively. As the length of the period increased the measurement results improved. This was a result of the smaller range of displacement that existed within the interrogation areas. Figures C.4, C.5 and C.6 also contain every validated measurement point along with lines representing the maximum and minimum displacements which existed within the interrogation area at each measurement point. As the length of the period increased, the displacement gradient decreased and the range of displacements within each interrogation area also decreased. This resulted in displacement measurements which contained a smaller range of measurements.

The displacement results were averaged and are shown in Figures C.7, C.8 and C.9 for periods of 64, 128 and 256 pixels, respectively. As the period increased the resolution of the displacement function increased. This was a result of more displacement vectors being used due to the larger period.
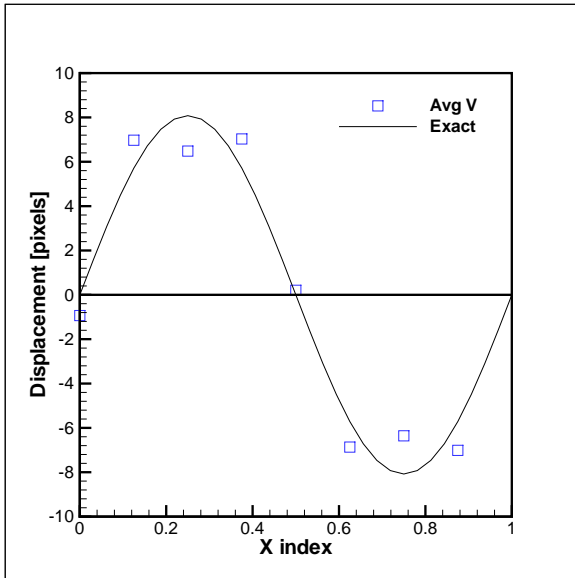
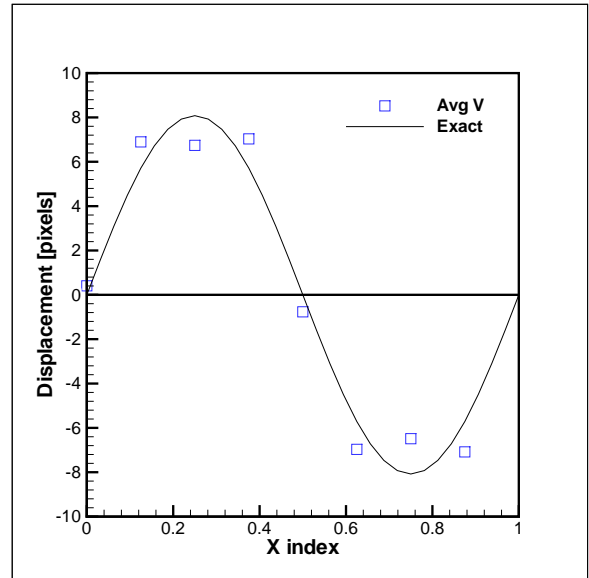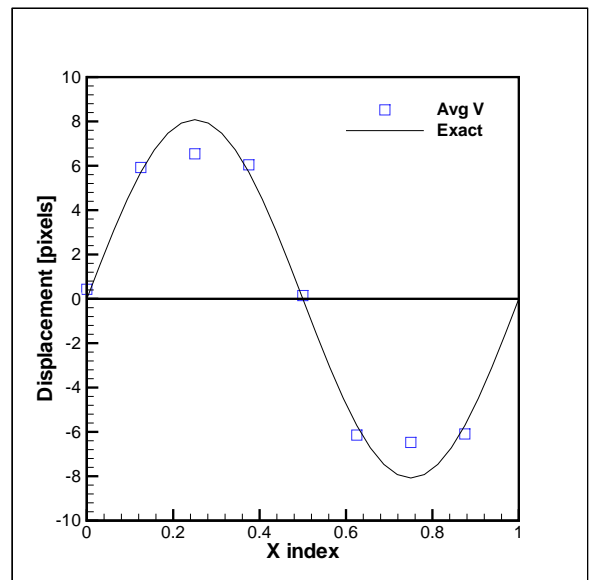(a) Standard FFT

(b) Predictor Corrector FFT
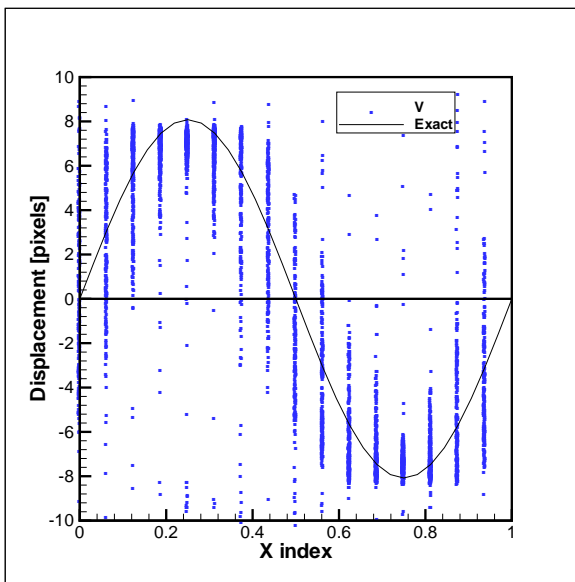
(c) Super Resolution FFT

(d) Deformed FFT

Figure C.1: Validated displacement measurements for sinusoid displacement function for a period of 64 pixels (a) Standard FFT (b) Predictor Corrector FFT (c) Super Resolution FFT (d) Deformed FFT
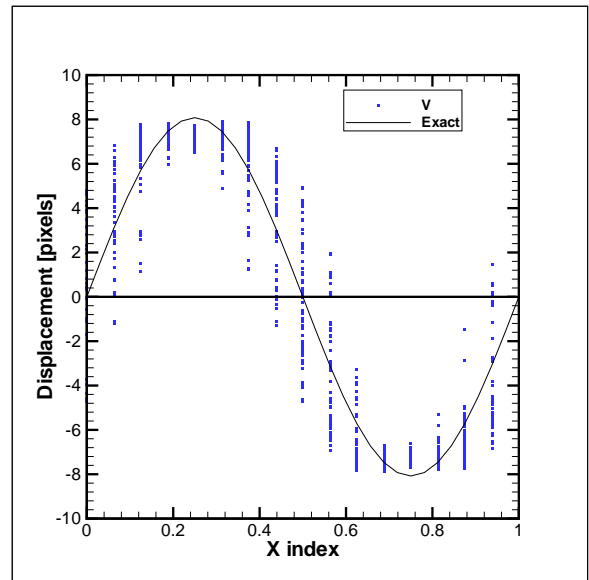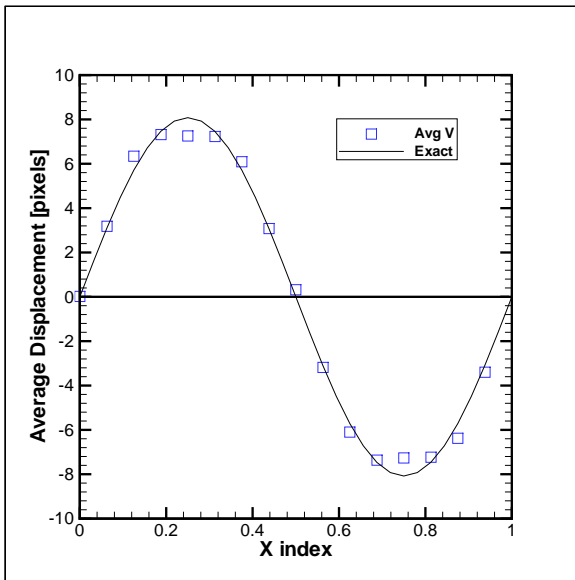
(a) Standard FFT

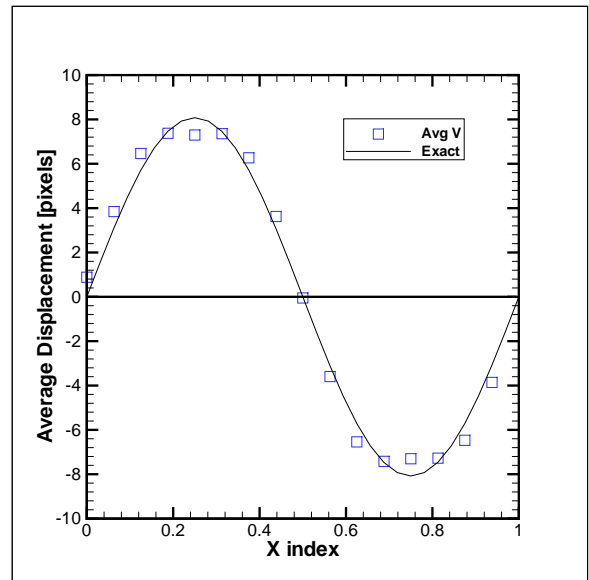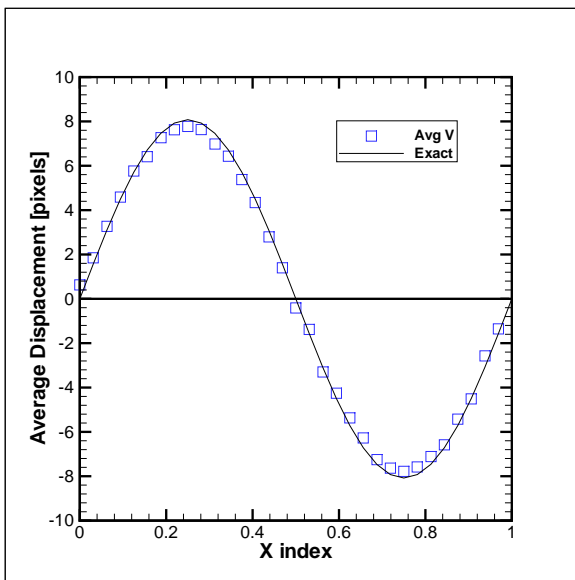(b) Predictor Corrector FFT

(c) Super Resolution FFT

(d) Deformed FFT

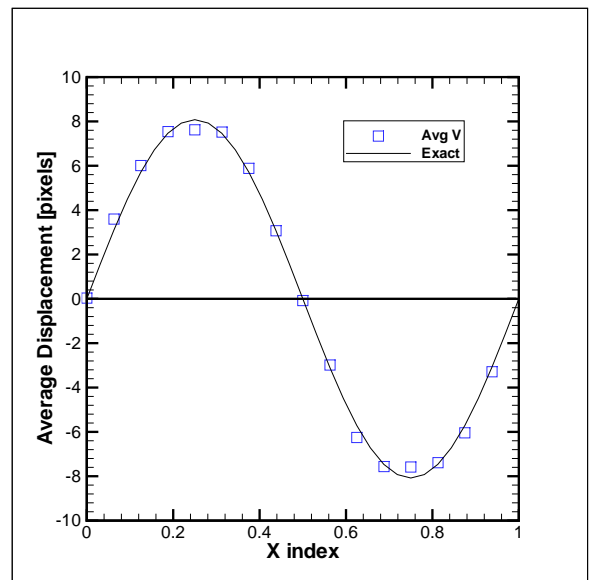Figure C.2: Validated displacement measurements for sinusoid displacement function for a period of 128 pixels (a) Standard FFT (b) Predictor Corrector FFT (c) Super Resolution FFT (d) Deformed FFT

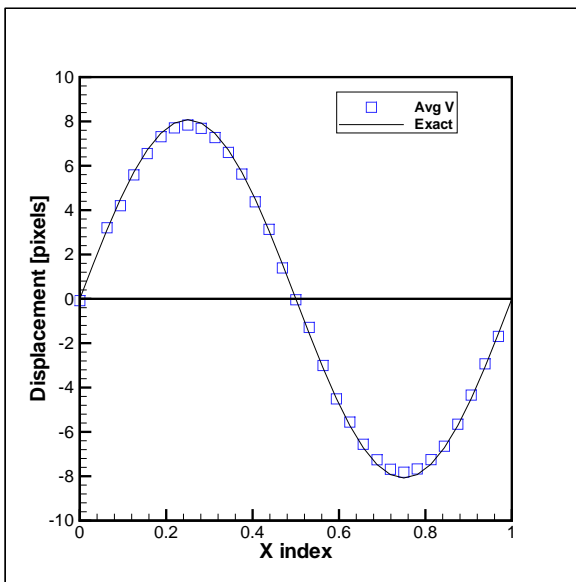(a) Standard FFT

(b) Predictor Corrector FFT

(c) Super Resolution FFT

(d) Deformed FFT

Figure C.3: Validated displacement measurements for sinusoid displacement function for a period of 256 pixels (a) Standard FFT (b) Predictor Corrector FFT (c) Super Resolution FFT (d) Deformed FFT

(a) Standard FFT

(b) Predictor Corrector FFT
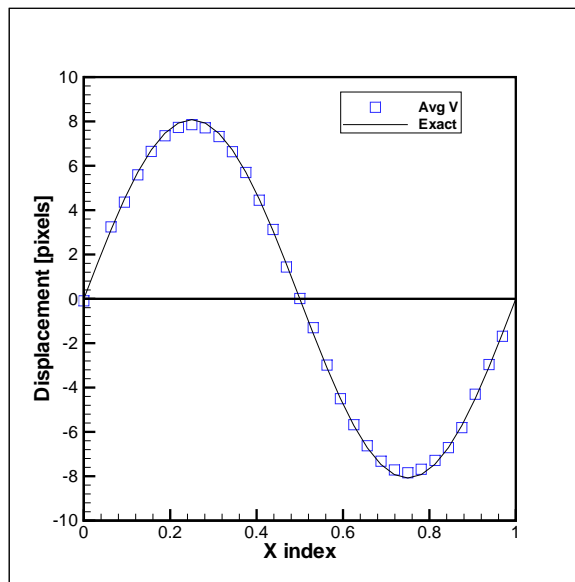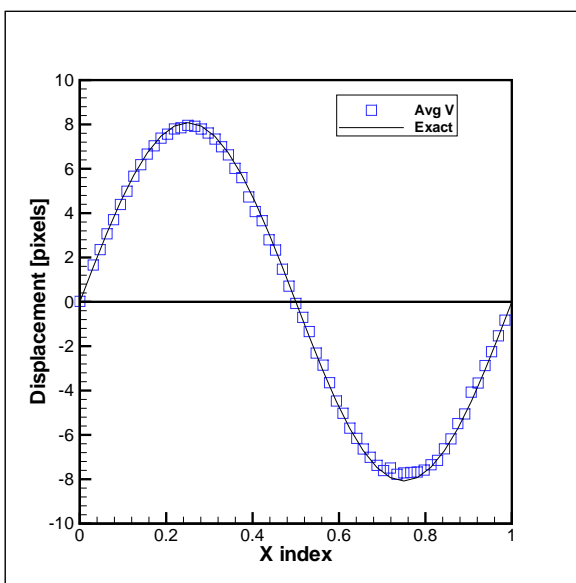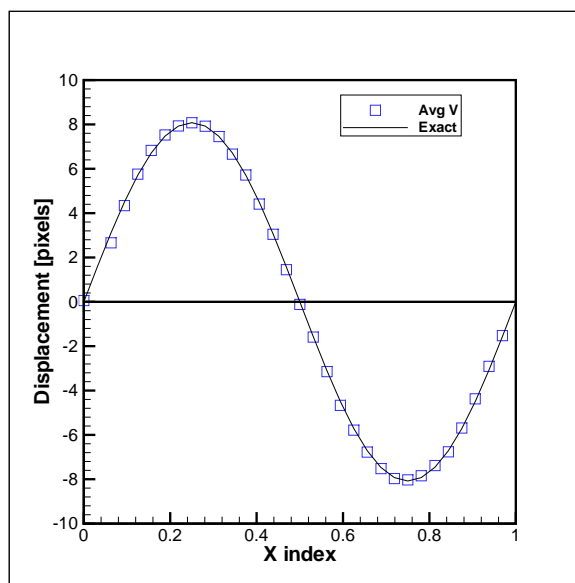
(c) Super Resolution FFT

(d) Deformed FFT

Figure C.4: Validated displacement measurements for sinusoid displacement function for a period of 64 pixels with the minimum and maximum values in the each interrogation area (a) Standard FFT (b) Predictor Corrector FFT (c) Super Resolution FFT (d) Deformed FFT

(a) Standard FFT

(b) Predictor Corrector FFT
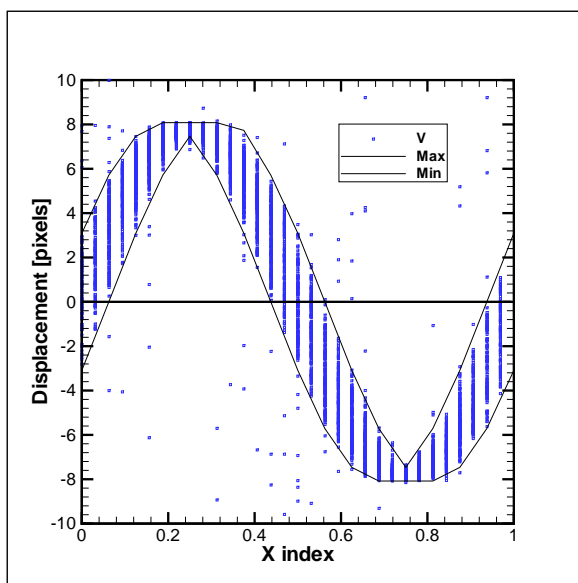
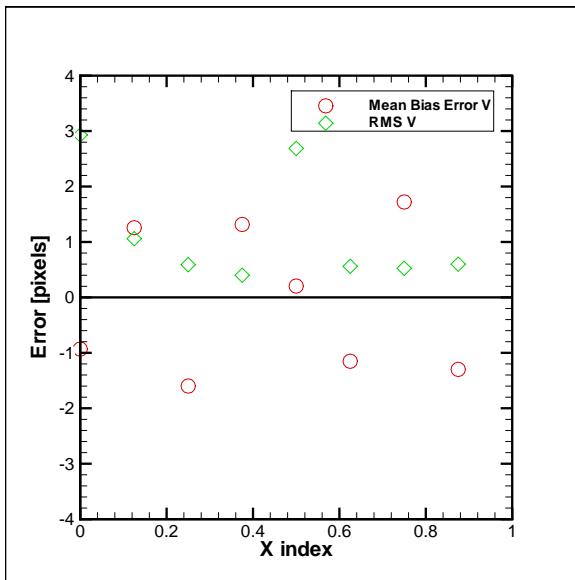(c) Super Resolution FFT
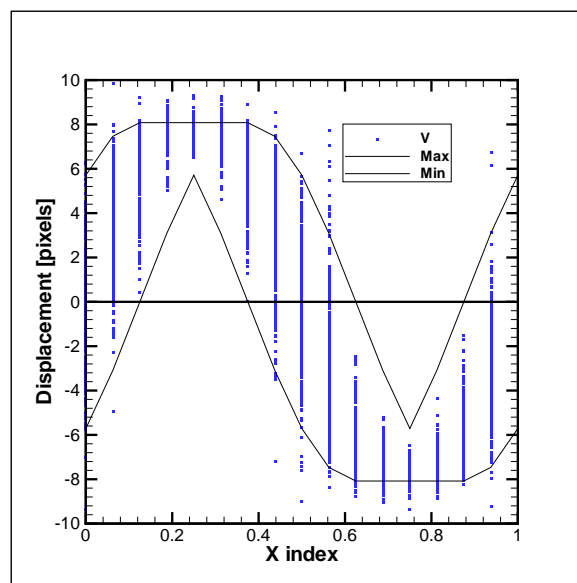
(d) Deformed FFT

Figure C.5: Validated displacement measurements for sinusoid displacement function for a period of 128 pixels with the minimum and maximum values in the each interrogation area (a) Standard FFT (b) Predictor Corrector FFT (c) Super Resolution FFT (d) Deformed FFT

(a) Standard FFT

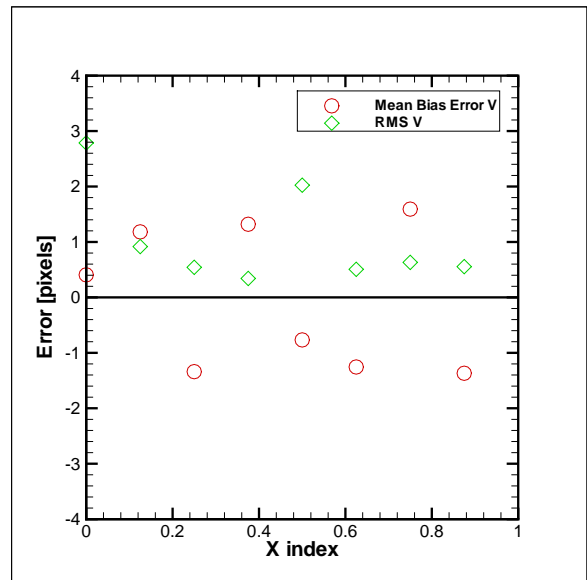(b) Predictor Corrector FFT

(c) Super Resolution FFT

(d) Deformed FFT

Figure C.6: Validated displacement measurements for sinusoid displacement function for a period of 256 pixels with the minimum and maximum values in the each interrogation area (a) Standard FFT (b) Predictor Corrector FFT (c) Super Resolution FFT (d) Deformed FFT

(a) Standard FFT

(b) Predictor Corrector FFT
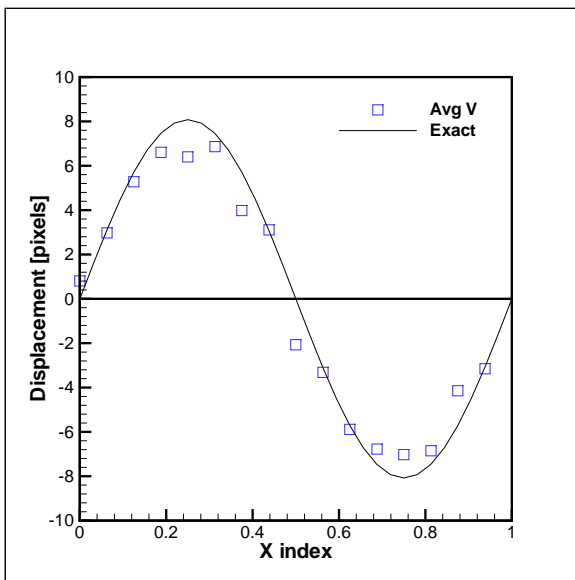
(c) Super Resolution FFT

(d) Deformed FFT

Figure C.7: Ensembled averaged displacement measurements for sinusoid displacement function for a period of 64 pixels (a) Standard FFT (b) Predictor Corrector FFT (c) Super Resolution FFT (d) Deformed FFT
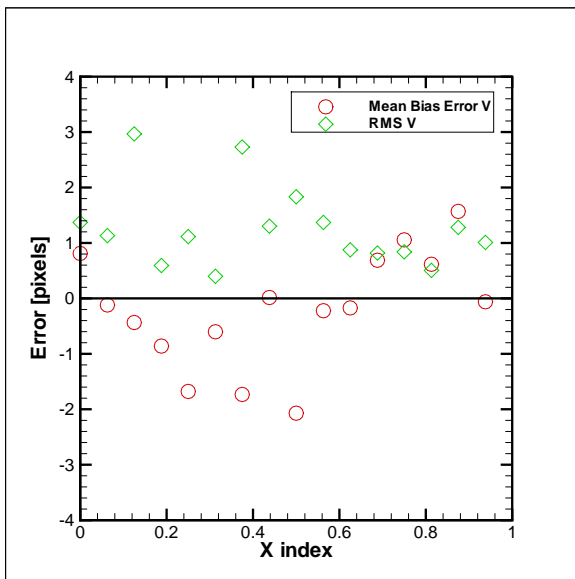
(a) Standard FFT

(b) Predictor Corrector FFT

(c) Super Resolution FFT

(d) Deformed FFT

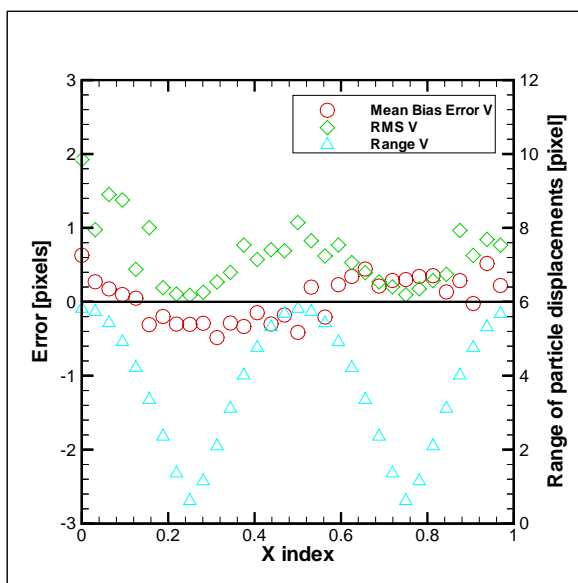Figure C.8: Ensembled averaged displacement measurements for sinusoid displacement function for a period of 128 pixels (a) Standard FFT (b) Predictor Corrector FFT (c) Super Resolution FFT (d) Deformed FFT

(a) Standard FFT

(b) Predictor Corrector FFT

(c) Super Resolution FFT

(d) Deformed FFT

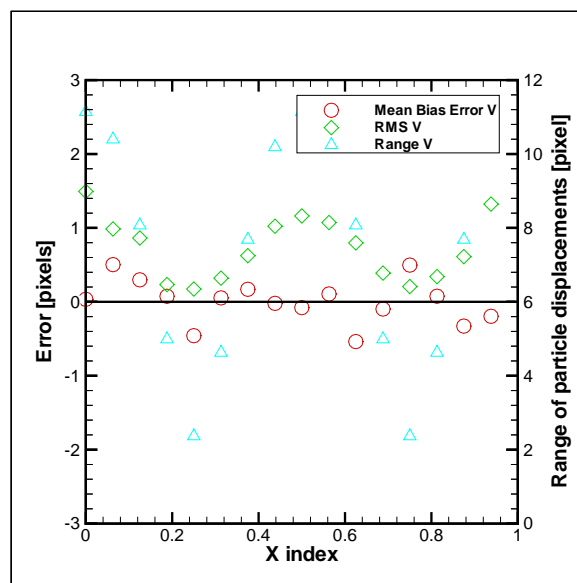Figure C.9: Ensembled averaged displacement measurements for sinusoid displacement function for a period of 256 pixels (a) Standard FFT (b) Predictor Corrector FFT (c) Super Resolution FFT (d) Deformed FFT

The mean bias and random errors are shown in Figures C.10, C.11 and C.12 for periods of 64, 128 and 256 pixels, respectively. As expected the mean bias and random errors were independent of the period of the sinusoid displacement.

(a)

(b)

(c)
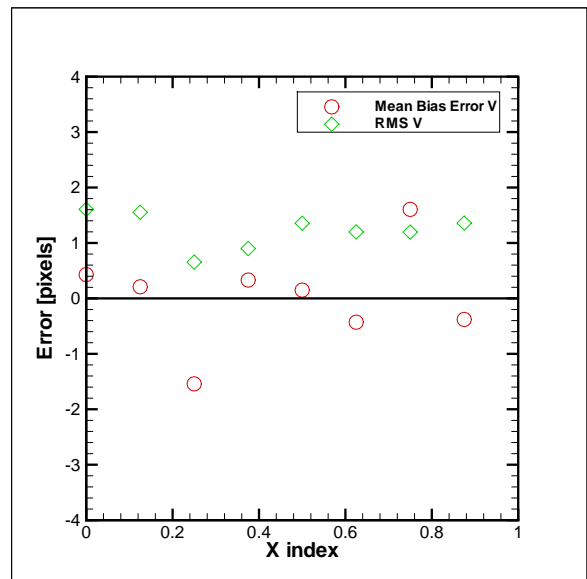
(d)

Figure C.10: Ensembled averaged error for sinusoid displacement function for a period of 64 pixels (a) Standard FFT (b) Predictor Corrector FFT (c) Super Resolution FFT (d) Deformed FFT
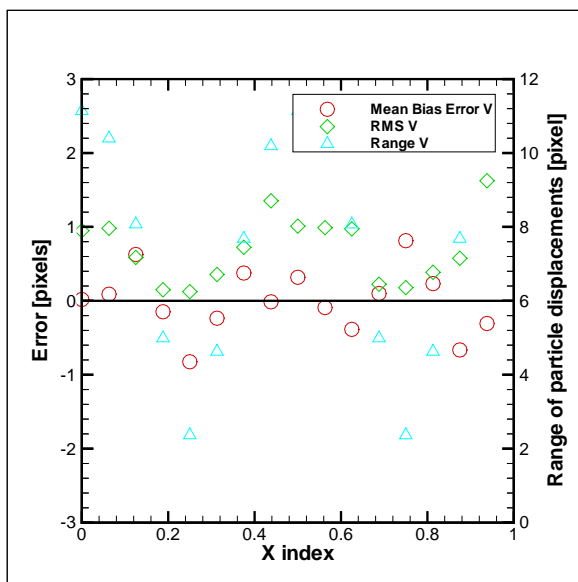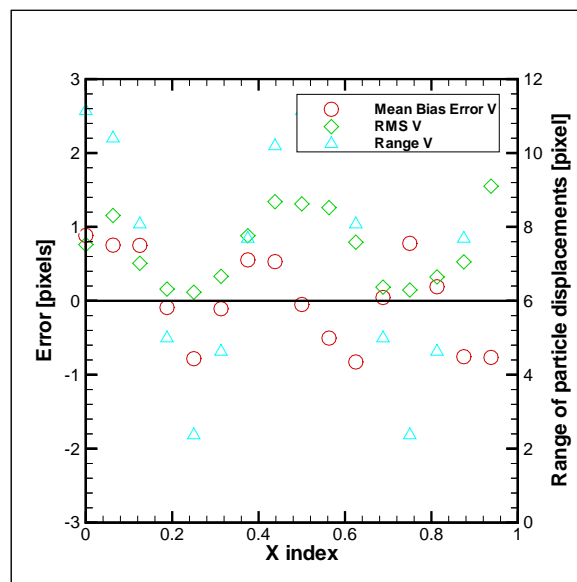
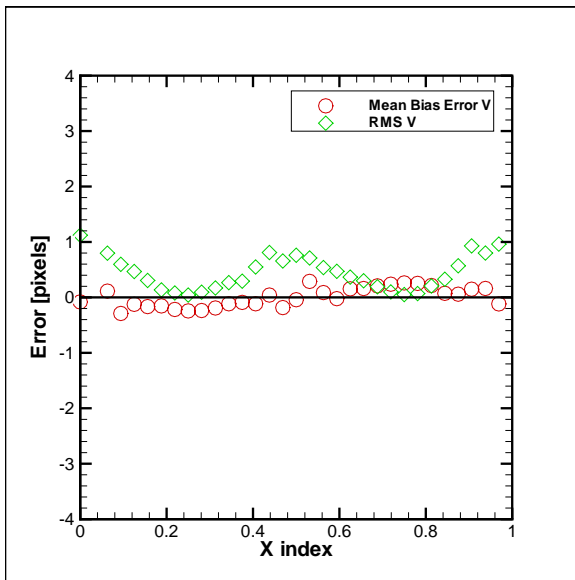(a) Standard FFT

(b) Predictor Corrector FFT
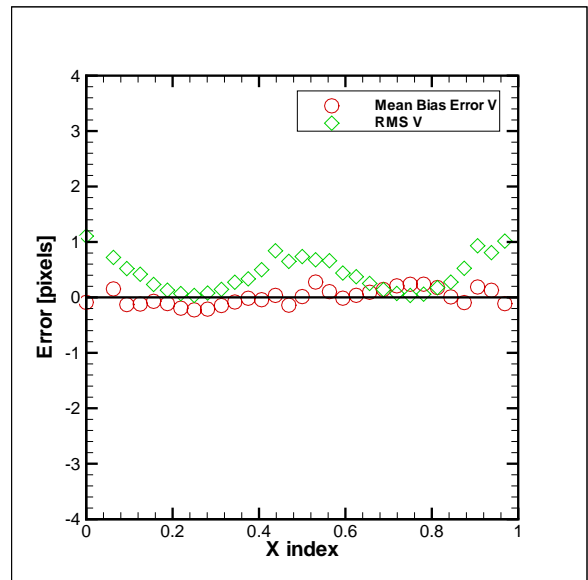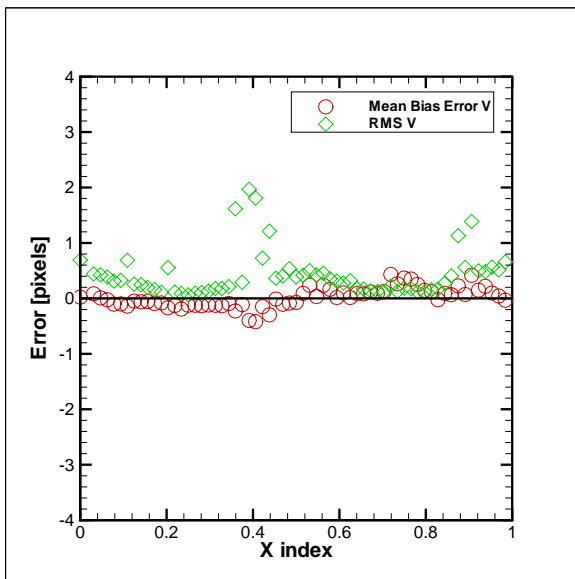
(c) Super Resolution FFT

(d) Deformed FFT

Figure C.11: Ensembled averaged error for sinusoid displacement function for a period of 128 pixels (a) Standard FFT (b) Predictor Corrector FFT (c) Super Resolution FFT (d) Deformed FFT
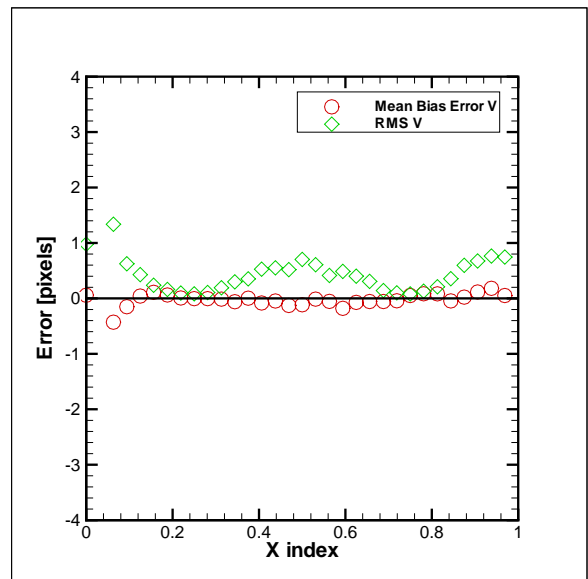
Figure C.12: Ensembled averaged error for sinusoid displacement function for a period of 256 pixels (a) Standard FFT (b) Predictor Corrector FFT (c) Super Resolution FFT (d) Deformed FFT